# Mirror-Coupled Nanoantennas with Hexagonal-Boron Nitride Spacers

**Alexander Casalis de Pury**

Department of Physics
University of Cambridge

This dissertation is submitted for the degree of
*Doctor of Philosophy*

Darwin College September 2020

I dedicate this thesis to my family and my friend Aleix Gorchs Rovira

# Declaration

This thesis is the result of my own work and includes nothing which is the outcome of work done in collaboration except as declared in the preface and specified in the text. It is not substantially the same as any work that has already been submitted before for any degree or other qualification except as declared in the preface and specified in the text. It does not exceed the prescribed word limit for the Physics and Chemistry Degree Committee of 60,000 words.

Alexander Casalis de Pury
September 2020

# Acknowledgements

I feel so fortunate and privileged to finally have the chance to write on these sacred pages, the one part that more than about five people will actually look at. A few months ago I sat down and looked at that empty page entitled, ‘*Acknowledgements*’ and thought "Wow, wouldn’t it feel amazing to have finished and finally be able to write the *Acknowledgements*!". I have to say, it feels every bit as great as I had hoped.....how often do you get to write something like this!? To the people in these acknowledgements, you have made the last few years the best of my life so far.

The first person I’d like to thank is my supervisor, Jeremy Baumberg, for letting me join the group and putting up with me for almost three and half years[1]. I feel so lucky to have ended up working with someone so utterly brimming with raw energy and fascinated by science every day. Whatever I do next in life I will try to find what you have found, it is a very high goal. Thank you also for being supportive of my visit to the Berkeley. Just as you had promised, it was disruptive, but I had to give it a try all the same.

I’d like also to thank the Cambridge Graphene Centre for putting your trust in me and funding this PhD. Thank you for introducing me to the world of two-dimensional materials.

Thank you so much to everyone in the NanoPhotonics centre for all the laughs and interesting conversations. Without being surrounded by so many friends as I was, my PhD would have been so much harder. I highly doubt I will ever find a more welcoming environment. Thanks to Dean Kos, the great ‘builder of nanophotonics’, for being a great friend also and to Femi Ojambati for all of the help and enthusiastic discussions about my work. In the end we never managed to properly meet face-to-face, but I owe a lot to my collaborator Xuezhi Zheng at KU Leuven for his feedback and brilliant calculations.

Then, every day after cycling back from that office full of friends, I got to arrive home at the outstanding 27 Clarendon Street. Cyan, Millie, Conor, Paddy, Peter, Beverly, together we will forever be the Clarendon crew. We were the number one PhD house in town and we knew it. We made the basement slugs, peeling paint and holes in the wall look like one giant

---

[1] Although it was more like two and a half in the end!

artwork. Also thanks to Ollie Batey and Cyan Williams (again!), my joint Darwin college and Graphene CDT pals, for all the fun times and complaining we did together.

To the final key remnants of the Darwin Masters year crew, Dan Ott, Gio Zenati, Lucy Rodrick and Corinna Hornwall, thanks for making me get off my butt to do things all the time and reminding me that there is so much fun to be had out there!

An extra special thanks goes to Cloudy Carnegie for supporting me and being my closest friend over the last few years. All the adventures we went on, all those sunny days out and nights about Cambridge were the best times I had.

Lastly and most importantly I get to thank my family, without whom I couldn't ever have gotten this far. To my mum, Amanda, who went to my college and fought to sign me up for A-levels when I messed up my IB, and always cares more for everybody else than herself. To my dad, Robert, who inspired me to apply here in the first place and in whose footsteps I have had the privilege to follow. To my brothers Richard and George, who are my best friends and my inspiration in life. To my wonderful Aunt Caroline, the Delacours, my Grandparents and everyone, for all the great family meals, walks along the cliffs and beaches, music, dancing, holidays and tea times, thank you for everything.

Anyway, here I am at the end of my time as a PhD student. It feels bittersweet because I have loved every minute, but I guess it is time to move on to the next thing.

# Abstract

Transparent dielectric materials are employed in a wide range of optical resonators. Combining plasmonic nanoantennas with such resonators enables the formation of nanoscale optical resonances. The novel nano-optics observed by combining these heterostructures with optically active media is laying the foundations for devices such as ultra-high efficiency optical switches. In this thesis, mirror-coupled nanoantennas consisting of the layered dielectric hexagonal-Boron Nitride encapsulated between gold nanoparticles and a gold substrate, are probed using high-angle optical scattering measurements. During illumination of individual nanoparticles, light is trapped at the nanoscale inside the hBN, between particle and gold beneath. As the thickness of hBN is decreased, the coupling between nanoparticle and substrate changes dramatically. Here, the inert properties of hBN are used to remove extraneous influences on scattering spectra, thereby revealing new nanoscale light confinement mechanisms and sub-nanometre structural changes.

In the first experiment presented, submicron-thick hBN crystals embedded in gold form planar Fabry-Perot half-microcavities. Gold nanoparticles on top of these microcavities form previously unidentified angle- and polarization-sensitive nanoresonator modes that are tightly laterally confined by the nanoparticle. Comparing dark-field scattering with reflection spectroscopies shows plasmonic and Fabry-Perot-like enhancements magnify subtle interference contributions, which lead to unexpected redshifts in the dark-field spectra, explained by the presence of these new modes.

In the second experiment presented, the thickness of hBN is reduced down to a single-atom-thick layer leading to greatly enhanced field intensities and confinement when compared to thicker layers, via plasmonic coupling. By comparing results to an analytic model, resultant ultra-sensitive scattering signals from nanoparticles atop these thinner layers reveal field interactions sub-nanometre structural changes.

Finally, photoluminescence measurements on defects in as-grown monolayer $WS_2$ on gold lead to clear emission despite significant substrate quenching. Measurements using nanoplatelets of the metal halide perovskite methyl-ammonium lead-iodide, lead to suppression of resonant modes and a blue-shifting behaviour correlated with light emission.

# Publications

1. A. Casalis de Pury, X. Zheng, O. S. Ojambati, A. Trifonov, C. Grosse, M-E. Kleemann, V. Babenko, D. Purdie, T. Taniguchi, K. Watanabe, A. Lombardo, G. A. E. Vandenbosch, S. Hofmann, and J. J. Baumberg, **Localized Nanoresonator Mode in Plasmonic Microcavities**, *Physical Review Letters*, (2020)
2. M-E. Kleemann, R. Chikkaraddy, E. M. Alexeev, D. Kos, C. Carnegie, W. Deacon, A. Casalis de Pury, C. Große, B. de Nijs, J. Mertens, A. I. Tartakovskii, J. J. Baumberg, **Strong-coupling of WSe2 in Ultra-Compact Plasmonic Nanocavities at Room Temperature**, *Nature Communications*, (2017)

# Table of contents

# List of figures

# List of tables

# Abbreviations

1. NPoM - Nanoparticle on Mirror
2. NP - Nanoparticle
3. NRM - Nanoresonator Mode
4. hBN - hexagonal Boron Nitride
5. TMD - Transition Metal Dichalcogenide
6. $WS_2$ - Tungsten Disulphide
7. $WSe_2$ - Tungsten Diselenide
8. MAPI - Methyl-Ammonium Lead Iodide
9. NPoMC - Nanoparticle on Microcavity
10. CVD - Chemical Vapour Deposition
11. AFM - Atomic Force Microscopy
12. SEM - Scanning Electron Microscope
13. SP - Surface Plasmon
14. LSP - Localised Surface Plasmon
15. LSPR - Localised Surface Plasmon Resonance
16. FWHM - Full Width Half-Maximum
17. FOM - Figure of Merit
18. MIM - Metal-Insulator-Metal
19. vdW - van der Waals
20. BS - Beam Splitter
21. FS - Focal Stop
22. NA - Numerical Aperture

23. NIR - Near Infra-red
24. IR - Infra-red
25. DF - Dark field
26. BF - Bright Field
27. TE - Transverse Electric
28. TM - Transverse Magnetic
29. PC - PolyCarbonate
30. RMS - Root Mean Squared

## Symbols

1. $C$ - Optical cross-section, Capacitance
2. $\alpha$ - Polarizability
3. $\varepsilon$ - Dielectric permittivity
4. $R$ - Radius, Reflection matrix
5. $E$ - Electric field, energy
6. $k$ - Wave-vector
7. $\omega$ - Angular frequency
8. $t$ - Time
9. $p$ - Dipole moment
10. $q$ - $kR$
11. $m$ - Mass
12. $\gamma$ - Damping constant
13. $N$ - Charge carrier density
14. $\mu$ - Magnetic permeability

15. $Q$ - Optical interaction efficiency, Q-factor
16. $F$ - Cavity finesse
17. $I$ - Optical intensity
18. $L$ - Cavity length/width
19. $\lambda$ - Wavelength
20. $d$ - Nanoparticle on Mirror gap distance
21. $\sigma$ - Penetration depth
22. $w$ - Mode width
23. $\beta$ - Phase thickness
24. $V$ - Mode volume

# Chapter 1

# Introduction

A principle aim in nanoscience is to take ideas from current technologies and adapt them, so that they can be shrunk down to their smallest possible size. In doing so, not only are we able to make smaller and more compact machines, but we are also able to access new realms of physics, chemistry and biology. Nanoscientists dream of robots that can manipulate and build molecules, ships that can swim between cells and nano-materials that can self-assemble into macroscale structures. Broadly speaking, nanoscientists are still building the components of these machines, and in this thesis the component is the nanoantenna. As will be seen, by combining the nanoantenna into a resonator structure the nanoscale fields generated can be manipulated to enable the detection single molecules, measure atom-scale distances and access the quantum mechanical regime with light. These heterostructures are one of the most promising candidates candidates for ultra-high efficiency optical switches [9, 11]. These structures are so small that the rules which normally describe antenna behaviour must be modified to understand their interactions with light. These rules are still being fully described and there is much more to be understood. This thesis aims to build on some of the missing rules.

An antenna is a conductive metal structure which translates light into the flow of electrical current and vice versa. In an antenna, light energy is converted into the motion of individual electrons with the shape, size and constituents of the antenna dictating this motion. Just as light is able to move electrons, the acceleration of electrons leads to radiation of light. The symbiotic relationship between electron flow and radiation means that signals on a circuit board are directly correlated with the motion of electrons and the radiated light as a result [12, 13]. An electrical signal sent to an antenna from a circuit board, leads to radiation of the signal in the form of light which is received at a second antenna and converted back into the same electrical signal. From television and mobile phones, to bluetooth and WiFi, most of our communication technologies at some stage rely on antennas and their ability to transfer information from free-space to a circuit board and vice versa.

A typical dipole antenna will have a length-scale on the order of half of the incident wavelength of light and is made of conductive metal, allowing efficient flow of electrons[13]. Televisions for example, pick up light with a wavelength of about 1mm to 10m, thus TV antennas range in scale from about 0.5mm to 5m. At this scale, electrons resonate within the antenna, propagating back and forth according to the frequency of incident light and the dimensions of the antenna. This allows signals from broadcasters to be translated into the motion of electrons along the antenna and, via a lot of clever electronics, convert the resulting current into images and sound.

The density of information that can be transferred in the form of a signal is limited by the wavelength of light, because a signal is just a variation in the electrical or light wave over a time period. Lower frequencies and therefore longer wavelengths allow for a reduced number variations in the wave over a given time period, and therefore reduced information density. For this reason large antennas, such as antennas for radios, are not able pick up information of the density required for television which have much shorter antennas. Correspondingly, as the demand for faster information transfer continues to increase and devices require information of higher density, the frequency of signals needs to be increased and antennas need to be made smaller and smaller[12]. This is all fine up to a point, but the efficiency of coupling to electrons in antennas drops rapidly as antenna size is reduced. Below the diffraction limit in particular, resonant excitation of electrons is highly inefficient.

Nanoantennas offer a method of confining light to nanoscale geometries, well below the diffraction limit[14]. This is because they operate via propagation of plasmons, rather than of electrons. Plasmons are are quasi-particles representing the collective motion of electrons (see next chapter). They resonate at a much lower frequencies for the same frequency of light and therefore nanoantennas are able to couple to light with wavelengths as short as 400 nm. In Fig.1.1(b,c) nanorods, grown in solution act as nanoscale dipole antennas scattering and re-radiating visible light.

This thesis examines two possible ways to create nanoantennas which confine light down to nanoscale geometries using highly localised plasmonic enhancements generated by spherical gold nanoparticles. These plasmonic systems show great promise for a number of future applications such as low-power nanoswitches, compact ultrafast light sources, nanosensors and efficient energy harvesting systems [14, 9, 15]. My hope is that it might help to provide potential routes or useful information to help in the creation of novel and scalable nano-optical devices of the future.

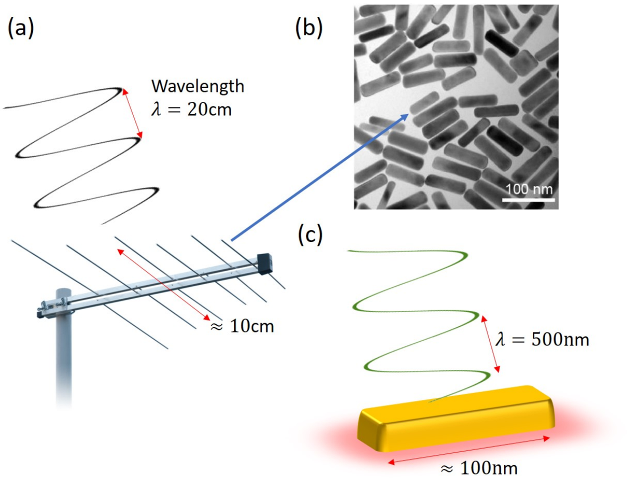

Fig. 1.1 The scaling down of rod antennas from macro- to nanoscale. A nanorod antenna is effectively a radio antenna (a), which is grown as a crystal in solution and thus shrunk down to the scale of 50-200 nm in length (b). Since they operate via plasmon propagation, nanoantennas are able to interact with light of wavelength in the range 400-1500 nm (c) and an ultra-confined near-field surrounds the nanoantenna upon illumination (red-shading).

Field confinement is demonstrated via two different physical mechanisms which both rely on the combination of spherical gold (Au) nanoparticles (diameter 60-80 nm) with the layered van der Waals dielectric, hexagonal-Boron Nitride (hBN). The Au nanoparticles act as optical nanoantennas because the light they emit via scattering transmits information about the properties and behaviour of the nanoscale field beneath. For both situations, confinement is achieved using high-angle dark field illumination techniques with an optical microscope and broadband illumination.

The basis of the examined structure consists of nanoparticles sitting atop a crystal of hBN transferred onto a flat gold (Au) substrate. Individual nanoparticles are illuminated at high-angle and via coupling between the nanoparticle and substrate the optical field is enhanced in the gap, inside the hBN crystal. Feedback between scattering and the enhanced field near the nanoparticles gives information about interactions with hBN in the gap.

Depending on the thickness of hBN the nature of interactions change completely. This is because as the distances between nanoparticle and gold substrate decrease, the mechanism of coupling between the nanoparticle and substrate changes from far-field (normal antenna behaviour) to near-field [1]. For this reason two distinct architectures are defined. For samples in which hBN crystals of 80-700 nm in thickness are used and far-field coupling dominates, the system is called the nanoparticle-on-microcavity (NPoMC) geometry. For samples in

---

[1] See the next chapter for description of these terms

which hBN crystals are of thickness 0.2-10 nm and near-field dominates, the system is called the nanoparticle-on-mirror (NPoM) geometry.

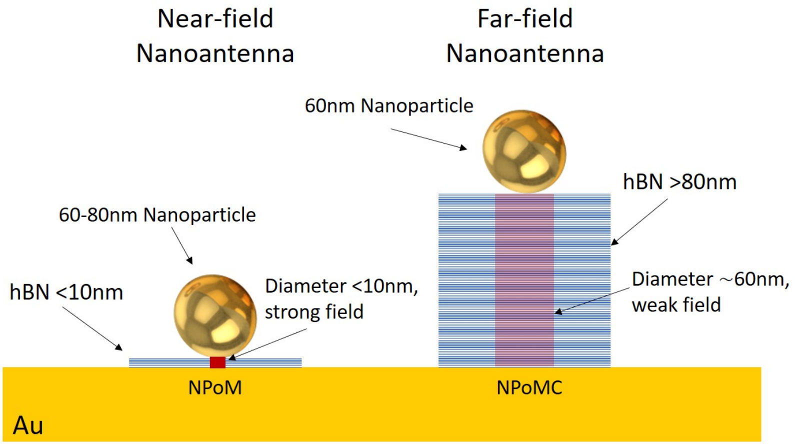

Fig. 1.2 How field interactions inside hBN on gold substrates change depending on hBN thickness during illumination of nanoparticles at high angle. For thin layers of hBN the field inside is strongly enhanced and tightly confined, whilst on thicker layers (>80 nm) there is reduced enhancement and the field is weakly confined. The coupling processes which cause field confinement operate via entirely different near- of far-field mechanisms.

## 1.1 Outline

**Chapter 2** aims to give the reader an understanding of the physics behind the experiments presented in this thesis. Optical scattering due to localised surface plasmons will be summarised with a short historical record of the use of plasmonic metals in art and the experiments of Michael Faraday. The physics behind scattering from sub-wavelength-scale particles is overviewed next, arriving at the theories of Lord Rayleigh for particles much smaller than the wavelength of incident light. This approach requires modification to understand scattering from noble metal nanoparticles, and so the Drude-Lorentz model of a bulk material interface is covered, leading to the dielectric function for conductive metals. This is followed by the basic theory behind plasmon formation at a flat interface and by shrinking this surface area the resultant discretisation enables understanding of localised surface plasmon (LSP) resonances. Chapter 3 uses a generalised Mie method in order to calculate mode positions for an hBN nanoparticle-on-microcavity (NPoMC) system, so there is a basic background to the theory added with more significant information found in the appendix. Electromagnetic cavities are then introduced leading to the required background for microcavities and plasmonic nanocavities, arriving finally at a description of the nanoparticle on mirror geometry (NPoM).

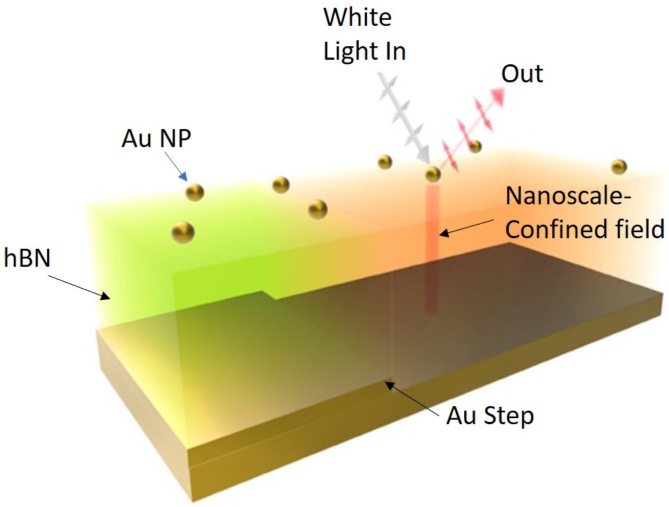

Fig. 1.3 Depiction of hBN optical cavity-coupled plasmonic nanoparticles studied in chapter 4, with the nano-confined field (red beam) propagating perpendicular to the substrate surface trapped between Au nanoparticle and flat Au mirror. The hBN slabs (>80 nm) are different colours in bright-field due to thin-film interference.

**Chapter 3** outlines the key experimental methods used for experiments in this thesis. This begins with a description of the single particle dark-field scattering microscopy setup used in the experiments in chapter 4 and 5. The chemical vapour deposition (CVD) of monolayer hBN on iron (Fe) allowed the statistical studies on large-area hBN crystals in this thesis, so growth and transfer of this material is covered. This is followed by an overview of nanoparticle growth and deposition, which should give the reader a solid understanding of the possible gap constituents. Chapter 4 and 5 use a simple method I developed called template exfoliation to embed 2D materials in metallic substrates, thereby minimising substrate-spacer separation. This method is described in this chapter, in addition to another more conventional transfer method which can be used for heterostructure fabrication.

**Chapter 4** covers an experiment studying the interaction of 60 nm Au nanoparticles coupled to an hBN optical microcavity. Fabrication and geometry, which consists nanoparticles atop of a few-100 nm thick crystal over flat gold (see Fig.1.3) is described first, followed by the experimental results. The basic theory behind expectations is covered and scattering is found not to correspond to expectations, with the appearance of anomalous modes and blue-shifts. Generalised Mie method calculations are used to calculate expected scattering with changing angle and polarisation which reveals these anomalies to be due to the presence of a new set of modes, which tightly confine vertically propagating light between nanoparticle and gold substrate (red beam Fig.1.1).

**Chapter 5** is the chapter in which I describe three separate studies of the nanoparticle-on-mirror (NPoM) geometry with hBN. The first uses exfoliated hBN with thickness ranging from 2-5 nm. By using atomic force microscopy (AFM), the height and morphology of the hBN can be determined and used to calculate interactions using the models described in chapter 2. This model is found not to accurately predict interactions and so measurements surrounding the crystal are taken, revealing the presence of surface contaminants which are invisible using other imaging techniques. By making corrections to account for this, interactions are correctly predicted along with an explanation for the wide variations due to morphological changes. Large-area trilayer hBN enables statistical analysis of over 400 nanoparticles, revealing differences in behaviour for nanoparticles on hBN compared to without hBN. Once again the original model fails, but the new model is able to explain disparities. Finally the chapter concludes with the experiment on monolayer hBN, for which all of the knowledge gained from exfoliated and trilayer hBN is used. Using the new model explanations are found for antenna enhancements on hBN with contaminants included.

**Chapter 6** overviews and discusses two other experiments which study the influence of tightly confined fields from nanoscale defects with as-grown monolayer $WS_2$ on Au, and from nanoparticle-on-mirror (NPoM) with perovskite nanoplatelets.

**Chapter 7** will round up all of the work presented as part of this thesis and suggest directions for future work as a result of my research.

# Chapter 2

# Foundations

This chapter looks back at the scientific foundations required to support and enable the work presented in this thesis. The opening section 2.1 provides an historical overview of the use and scientific study of micro- or nano-scale particles as optical scatterers. In section 2.2, scattering from sub-wavelength-scale particles is investigated, highlighting the dramatic enhancements to scattering observed from noble metal particles. An explanation of this phenomenon will require an understanding of plasmons, the subject of section 2.3. Section 2.4 will then cover the background for Mie theory, which is important for Chapter 4 and is covered in more depth in the Appendix. This theory is able to describe scattering from particles while including the effects of surface plasmons. When plasmonic particles are close to one another they interact and couple, producing new resonances at specific energies depending on a number of system parameters. This coupling process can be considered similar to coupling in optical microcavity systems, and section 2.5 covers simple optical microcavities and plasmonic nanocavities. Finally, the near-field enhancements close to metal surfaces led to the field of plasmonics and allows the discussion of a specific architecture used in this work, the nanoparticle on mirror (NPoM) geometry. The generalised Mie method described in the Appendix outlines a new approach developed by my collaborator Dr. Xuezhi Zheng which allows the rapid and accurate calculation of fields from microcavity-coupled plasmonic nanoparticles. This theory is used for the calculations found in Chapter 4 and so the reader may find this useful.

## 2.1 A Short History of Colloidal Nanometals

Either with or without their knowledge, artists, alchemists and blacksmiths have been using the unique optical properties of colloidal nanometals for well over 1000 years.

Fig. 2.1 (a) An example wall painting by a member of the Mayan empire during the classic period between 200-900AD, © 2000-2020 Salem Media [1]. The "Maya blue" pigment used contains nanoscale iron and chromium particles. (b) An example of Islamic lustreware from 800AD, which eventually made its way into Europe through Spain © 2012 Philippe Sciau, Licensee IntechOpen[2]. Following firing of the outside with metal salts, nanometals are embedded in the glass, ceramic or metal which gives the lustre. (c) A photo taken by Paul Wilkinson of, © The Royal institution. This is one of Faraday's original Au colloid solutions, which remains optically active to this day.

The earliest known examples of this include chemically resistant blue pigments used by painters during the Mayan empire (Fig.2.1(a)) and 4th century Romans who infused glass with gold nanoparticles to create the deep red of the Lycergus cup, only revealed upon illumination from the interior [16]. Stained glass, used extensively by pre- to early-modern Europeans, was developed even earlier in ancient China and involved the mixing of metallic salts at high temperature. Similar techniques lent a beautiful lustre to battle garments and pottery during the middle ages [16, 17] (Fig.2.1(b)). Throughout history, various peoples have found that the mixing of metal particles or metallic salts at high temperature can lead to unusual colouration. This year, the angle dependent colouration observed in daguerreotypes, one of the first photography techniques and the first to succeed in photographing people in 1834, was found to be due to embedded metal nanocrystals (Fig.2.2).

The first person to use a truly scientific approach to try and answer questions regarding the source of this colouration was Michael Faraday from 1854 [18]. For an entirely different experiment, he was attempting to form semi-transparent films of Au on microscope slides via chemical means and found that, following the washing of the slides, liquid waste products adopted a strange pink hue. He correctly determined that the mixture's behaviour must be due to the unknown optical properties of invisible particles of Au in the solution. By heating a metal salt precursor, $KAu(CN)_4$, he was able to perform a reduction with phosphorous to produce Au in solution [19]. He then took his "ruby fluid" and observed the way in

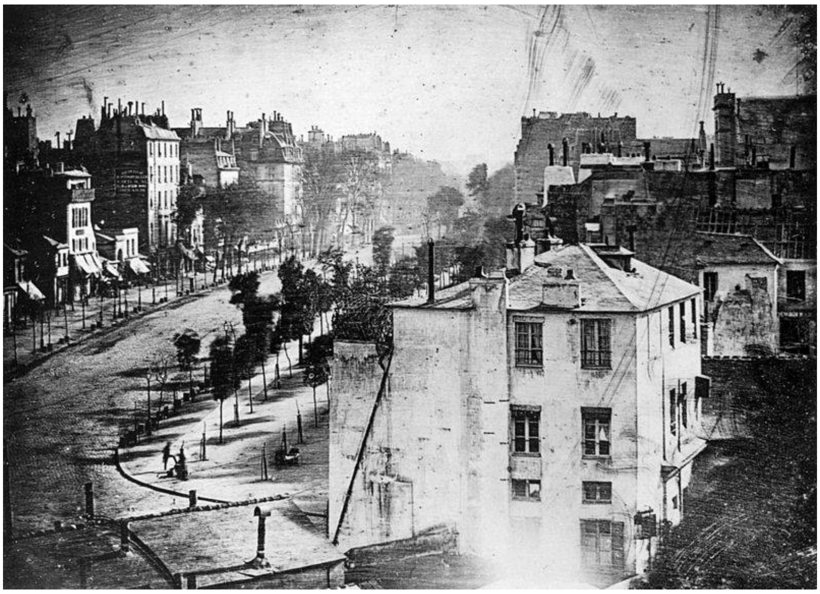

Fig. 2.2 This photograph, from 1834, is the first to contain people ever taken. It is an example of a dageurreotype, taken by Louis Dagguere himself. The exposure length required to take the image is so long (3-15 minutes) that only the man getting his shoes shined remained stationary long enough to end up in the image - this is actually the busy Boulevard du Temple in Paris. It was discovered earlier this year that Dageurrotypes are also the first example of plasmonic colour printing. Daguerrotypes form on silver plates and subtly change colour depending on viewing angle. These unusual properties arise due to the presence of metallic nanostructures on the surface.

which the light was scattered through the solution [20] (Fig.2.1(c)). His notes were the first detailed account of the preparation and optical properties of colloidal Au, and his samples have remained stable for well over 150 years in the basement of the Royal Institution in London [18]. We now know that the size of these Au particles was likely a few to many 10s of nanometres, so in some ways this is one of the first deliberate attempts to explain nanotechnology in action.

Illumination of Faraday's colloidal Au yielded an unusual optical response due to the presence of Au particles, but this could not yet be fully explained. In contrast to the pink hue lent by Au, it was found by John Tyndall a few years after Faraday that light scattered by nanoscale particulates in vials of air lent a blue rather than red colour to the transmitted light. These particles were of a similar size to colloidal Au, so small that they could not be observed individually, but collectively they preferentially interacted with certain wavelengths of light. It was clear that there was a dependence on the material properties of the interacting particles as well as the size.

The first thorough and mathematical approach used to quantify the influence of a particle on the propagation of light, was to consider particles which behave predominantly as radiative dipoles (i.e. like a micro- or nano-antenna)[21–23]. This dipole approximation was the approach taken by John William Strutt (Lord Rayleigh), in 1871 when he published papers on the colour and polarization of light scattered from water droplets[18]. Following mostly a combination of Rayleigh and Lorentz scattering the next section begins with a calculation of the radiated field for a single nanoparticle dipole in the quasistatic regime. Then, the classical frequency dependent dielectric permittivity for a given material will be derived. This will explain the scattering behaviour of very small nanoparticles with great success, however, it will be seen that this approach only goes so far and is inadequate for larger nanoparticles, many 10s of nanometres in diameter.

While it is useful as an appropriate introduction, in this thesis the focus is on the results of experiments requiring the interpretation of scattering from metallic nanoparticles of 60-80 nm in size illuminated by light of wavelength 400-900 nm. In the configurations seen here, scattering cannot be fully explained using the theories of Rayleigh and Lorentz. Therefore, to fully explain the size dependence of interaction with nanoparticles, the theory of Gustav Mie and an understanding of plasmonics is required, which will follow in section 2.3 and 2.4.

## 2.2 Optical Scattering from Sub-Wavelength-Scale Particles

The total influence of a single particle on incident light can be deduced from its extinction cross-section, which is proportional to the probability of an optical interaction occurring. A full treatment for the theory discussed here can be found from page 70, and then from page 139 of reference [22].

For a nanoparticle, the two most probable interactions are scattering or absorption, thus the extinction cross-section is the addition of its scattering $C_{sca}$ and absorption $C_{abs}$ cross-sections[22, 24]

$$C_{ext} = C_{sca} + C_{abs}. \tag{2.1}$$

The Lorentz-Lorenz equation (which is equivalent to the earlier Clausius-Mossotti relation) indicates that for a spherical particle of radius $R$, the ease with which charges are separated by a planar incident electric field to form a dipole is described in terms of the polarizability $\alpha$ using,

$$\alpha = 4\pi\varepsilon_m R^3 \left(\frac{\varepsilon - 1}{\varepsilon + 2}\right), \tag{2.2}$$

with the relative dielectric permittivity being the ratio between the dielectric constant of the particle and surrounding medium $\varepsilon = \varepsilon_p/\varepsilon_m$. Remembering Eq. 2.2, one can calculate the field radiated from an ideal dipole which oscillates at a frequency equal to that of the incident electric field.

Consider the geometry shown in Fig. 2.3. Here, a vertically polarised ($\hat{x}$) electric field $\vec{E}$, travelling in $z$ such that [22, 24],

$$\vec{E} = E_0 exp(i\vec{k}z - i\omega t)\hat{x}, \tag{2.3}$$

with angular frequency $\omega$, amplitude $E_0$ and wavevector $\vec{k}$. This field will induce a dipole moment $\vec{p}$ in the nanoparticle

$$\vec{p} = \varepsilon\alpha\vec{E}_o = \varepsilon\alpha E_0 e^{-i\omega_{di}t}\hat{x} \tag{2.4}$$

where this time $\omega_{di}$ is the angular frequency of dipole oscillations. The electric field radiated as a consequence of this excitation $\vec{E}_s$ is found by calculating the retarded potential at a distance $r$ from the dipole[22].

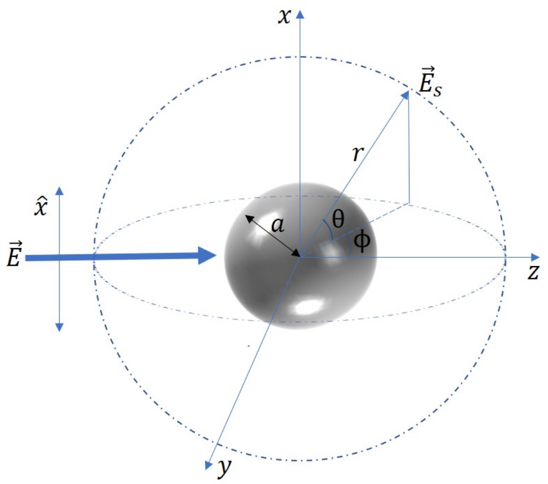

Fig. 2.3 The geometry used for the discussions in this section. A spherical nanoparticle of radius $R$ much less than the incident wavelength of light. A linearly polarised ($\hat{x}$) electric field $\vec{E}$ represents the incident light. The particle scatters the field at an angle, $\theta, \phi$, resulting in the detected field $\vec{E}_s$

Considering the quasistatic regime $\omega = \omega_{di}$ and the time dependent parts of both the field and dipole with $e^{i\omega t} = 1$ can be ignored. Additionally, since the dipole is being observed at a distance $r$ significantly greater than the excitation wavelength, we can ignore extra terms with $r^2, r^3, \ldots$.

Based on these assumptions and substituting in $q = kR$, where $R$ is the radius of the particle and the polarizability from Eq. 2.2

$$C_{sca} = \frac{k^4}{6\pi}|\alpha|^2 = \pi a^2 \frac{8}{3} q^4 \left| \frac{\varepsilon - 1}{\varepsilon + 2} \right| \tag{2.5}$$

and since absorption dominates the extinction for the nanoparticle

$$C_{ext} \approx C_{abs} = k\, Im\{\alpha\} = \pi a^2 4q\, Im\left\{ \frac{\varepsilon - 1}{\varepsilon + 2} \right\}. \tag{2.6}$$

Eq. 2.6 is equivalent to the famous Rayleigh scattering cross section, valid only when absorption dominates over scattering. This is true when $q << 1$, or in other words when particle size is significantly less than the wavelength of incident light. This is clearly the case for visible light of wavelength >400 nm incident upon particles such as molecules or those with radii on the order of a few-nanometres. Since the dipoles must oscillate at the same frequency as the incident light it is only possible to take this approach for very small particles such that there is negligible field gradient across the particle at any given time - this is the assumption of the quasistatic regime. The scattering cross section can be found by summing over all of the possible scattering angles gained from an angular intensity distribution. Eq.

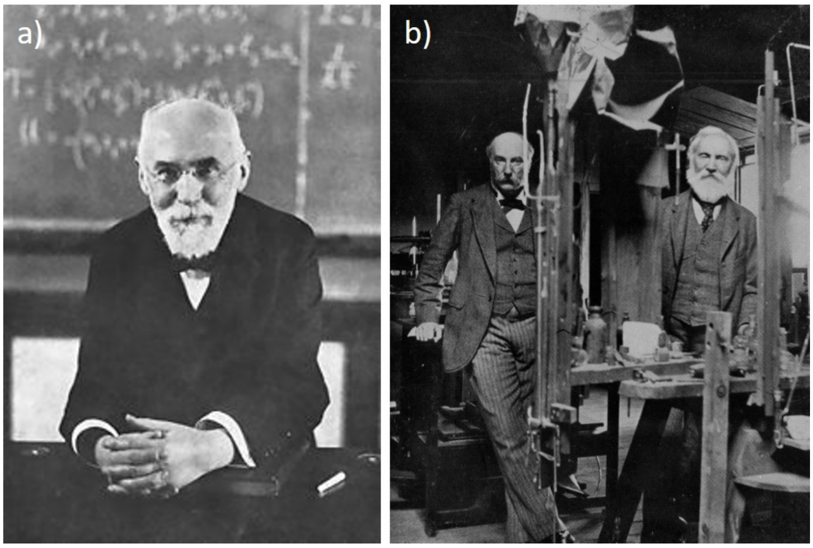

Fig. 2.4 (a) A classic photo of Lorentz in a lecture theatre. (b) Rayleigh (right) and Kelvin (left) looking proud of themselves in the lab [3]

2.6 comes from the fact that the relative dielectric permittivity $\varepsilon$ has both real and imaginary components. Thus the imaginary part of the extinction describes absorption or losses, while the real part describes other factors such as scattering.

Note in particular that as $\varepsilon \Rightarrow -2$ in equations 2.5 and 2.6, both scattering and absorption can approach a singularity. This is known as the Fröhlich condition, met only for materials which display negative dielectric permittivity within certain wavelength ranges. To explain this unusual condition and the mechanism behind it, the behaviour of different materials under illumination must be addressed. By understanding their behaviour under illumination, the dielectric function of a given material e.g. Au is arrived at [25, 26]. This will enable the calculation of extinction cross-sections, which can then be used to relate back to the polarisability of a nanoparticle with $q << 1$.

### 2.2.1 The Drude-Lorentz Model of a Flat Interface

The separation within a bulk material of charge carriers of mass $m$ driven by a local field $\vec{E}_{loc}$ can be described classically by

$$m\frac{d^2\vec{r}}{dt^2} + m\delta\frac{d\vec{r}}{dt} + m\omega_0^2\vec{r} = -e\vec{E}_{loc} \tag{2.7}$$

Here it is important to understand that $\vec{E}_{loc}$ is a generalised local field, which could theoretically be created by a number of sources i.e. not just by light. The separation force on the charge carriers is imparted parallel to the direction of electric field vector. The charges separated by the field form dipoles, which behave as a damped harmonic oscillator with damping factor $\delta$ and resonant frequency $\omega_0$. The dipole generates a restoring force $m\omega_0^2\vec{r}$ with resonance frequency $\omega_0$. The solution of Eq. 2.7 gives the displacement $\vec{r}$ as a function of photon energy of frequency

$$\vec{r}(\omega) = \frac{1}{m}\frac{-e\vec{E}}{(\omega_0^2 - \omega^2) + i\gamma\omega}. \tag{2.8}$$

The dipole moment is $\mu = e\vec{r}(\omega)$, but can also be described in terms of the polarizability using $\mu = \alpha\vec{E}$, thus along with Eq. 2.2 we also have,

$$\alpha(\omega) = \frac{e^2}{m}\frac{1}{(\omega_0^2 - \omega^2) + i\gamma\omega}. \tag{2.9}$$

Since $P(\omega) = N\alpha(\omega)E(\omega) = \varepsilon_0(1 - \varepsilon(\omega))E(\omega)$ one arrives at,

$$\varepsilon(\omega) = 1 + \frac{Ne^2}{\varepsilon_0 m}\frac{1}{(\omega_0^2 - \omega^2) + i\gamma\omega}. \tag{2.10}$$

Here $N$, $m$ and $e$ are the charge carrier density, mass and unit charge respectively, with $\varepsilon_0$ the permittivity of free space. To translate this to a real world material, we assume that the dielectric function is the same as summing the contribution from many dipoles. We then arrive at [27, 21],

$$\varepsilon(\omega) = 1 + \omega_p^2 \sum_j^n \frac{f_j}{\omega_{0,j}^2 - \omega^2 + i\gamma_j\omega}. \tag{2.11}$$

where $f_j$ is the oscillator strength of a given transition, $\omega_{0,j}^2$ is the spectral frequency and $\delta_j$ is the bandwidth of the $j$th transition [27]. The factor $Ne^2/\varepsilon_0 m$ is substituted by the square of the plasma frequency $\omega_p$, which is a useful factor related to the rate of collective motion for charge in the material. Metals display negative refractive indices below the plasma frequency.

In ellipsometry, the above classical equation for the dielectric dispersion has been extremely successful at calculating the permittivities for a wide range of bulk materials and is still used today.

### 2.2.2 Dielectric functions of bulk metals

In a bulk metal, electrons are generally free to move with a continuum of possible energies, there are contributions from both discrete interband and intraband transitions. Metals also require an additional offset $\varepsilon_\infty$ to account for the dielectric response of bound valence electrons in the metal[28]. In this classical interpretation, it's valid to write the frequency of oscillation in terms of a restoring force constant $\omega_{0,j}^2 = K/m_e$. Then for a material containing truly free electrons $K = 0$, thus we know the first term in the sum, leading us to the complex dielectric function

$$\varepsilon(\omega) = \varepsilon_\infty + \omega_p^2 \sum_j^{n-1} \frac{f_j}{\omega_{0,j}^2 - \omega^2 - i\delta_j\omega} - \frac{\omega_p^2}{\omega(\omega + i\delta_F)}. \tag{2.12}$$

The final term in this equation is identical to the Drude model for free electrons, and so this equation is commonly referred to as the Drude-Lorentz model. Over the years the precise interband transitions of bulk Au have become well understood and so this function describes the shape of the dielectric function of metals very well. Eq. 2.12 reveals that the real part of the relative dielectric permittivity function becomes negative for certain frequencies of light.

## 2.3 Plasmons

In the previous section was the first mention of the plasma frequency, a quantity used to describe the collective behaviour of charge carriers within a material. Plasmons are quasiparticles which represent the quanta, or energy states, of charge carrier plasma oscillations within a material [21, 23]. Each plasmon has an energy corresponding to a particular resonance condition, the frequency and amplitude of which depends on the specific coupling conditions between the plasma in the material and incident light.

The volume plasmon (i.e. within the volume of a metal), can be excited only for energies greater than or equal to the plasma frequency $\omega_p$ and is continuous as shown in Fig. 2.5. Both the plasma frequency and volume plasmons result naturally for charges separated along the k-vector component of the incident field. It can also be deduced then that the volume plasmon cannot couple to light, because the electric field radiated from the excited dipole plasmon is transverse rather than parallel to the direction of incidence. To excite the volume plasmon researchers can instead fire charged ions at the metal. Ballistic ions displace charge carriers along the direction of incidence, and thus the volume plasmon can be excited.

In contrast to the volume plasmon, which cannot be excited by light, a second type of plasmon called the surface plasmon, can be excited under certain conditions. These plasmons exist solely at an interface and the consequences of their excitation, such as field confinement, enable the work presented in this thesis.

The simplest way to understand a surface plasmon is to consider a flat interface between two materials in the presence of an optical field with a transverse magnetic (TM) polarisation component. This disregards any contribution due to $E_{x,y}$ along the plane of the interface, as it can be shown that transverse electric (TE) fields are unable to excite surface plasmons in this

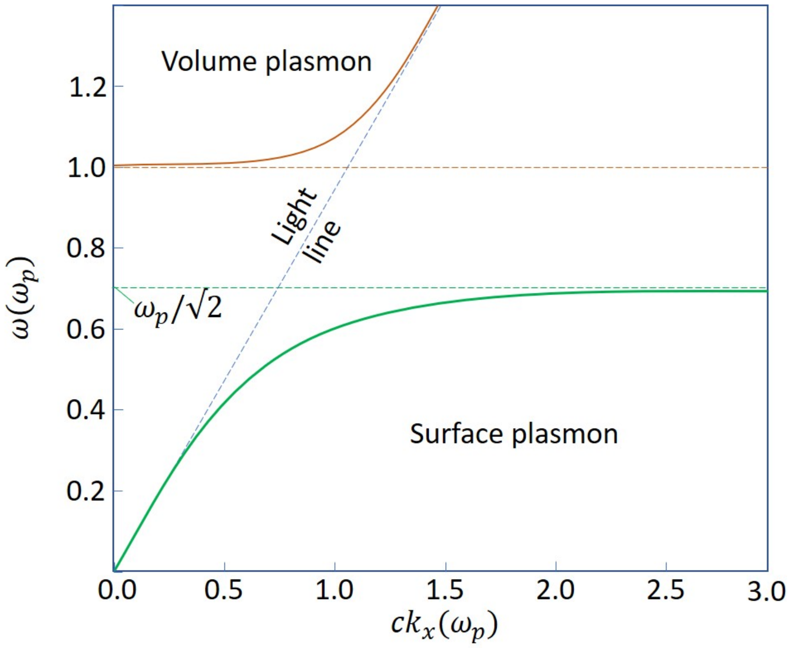

Fig. 2.5 Dispersion for a surface plasmon for a material which obeys the Drude equation with zero losses, i.e. $\varepsilon_2(\omega) = 1 - \frac{\omega_p^2}{\omega^2}$, and $\omega = 1$.

situation. This is depicted in Fig. 2.6. The area of the flat interface is significantly larger than the wavelength of incident light and is therefore significantly removed from the quasistatic regime discussed previously.

Using Ampere's law, for a wave propagating at the interface of two non-magnetic media, as depicted in Fig. 2.6, it is found that for continuity of tangential electric fields [28, 29],

$$\frac{k_{1z}}{k_{2z}} = -\frac{\varepsilon_1}{\varepsilon_2}. \tag{2.13}$$

For real and positive $k$, this means that the refractive indices for the two interfaces must have opposite sign in order for a surface plasmon to propagate,

$$\varepsilon_1 \varepsilon_2 < 0. \tag{2.14}$$

This is the first surface plasmon condition. Since metals are able to have a negative refractive index at certain frequencies of incident radiation, the metal-dielectric interface satisfies this condition at these frequencies. Au, for example has a negative dielectric permittivity within the visible region.

Using the example of a metal the dispersion relation is,

$$k_x^2 + k_{2z}^2 = \varepsilon_2 \mu_0 \omega^2. \tag{2.15}$$

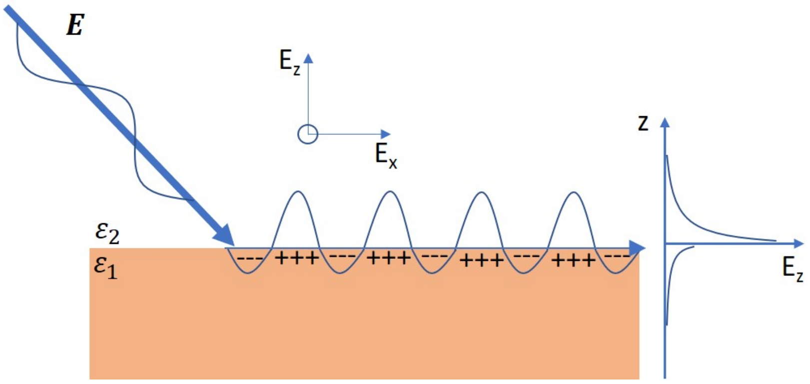

Fig. 2.6 The excitation, propagation and decay behaviour of a surface plasmon at a flat metal-dielectric interface.

Assuming no losses, squaring both sides of Eq. 2.15 and then solving for $k_x$ gives,

$$k_x = k_0\sqrt{\frac{\varepsilon_1\varepsilon_2}{\varepsilon_1+\varepsilon_2}} \tag{2.16}$$

with $k_0 = \sqrt{\varepsilon_0\mu_0}\omega$ being the free space wavenumber. In order to have a real $k_x$ the second surface plasmon condition must be satisfied,

$$-\varepsilon_2(\omega) > \varepsilon_1(\omega) \tag{2.17}$$

These two conditions mean that surface plasmons have the following key features[1]:

1. **Surface charges**: The surface plasmon induces coherent charge density oscillations at the metal surface as shown in Fig. 2.6. In this way the collective motion of charge can be visualised as a "ripple" travelling across the interface.
2. **Evanescent fields**: In z, these confined excitations are evanescent, decaying exponentially away from the interface. They decay more rapidly into the metal as shown in Fig. 2.6.
3. **Polarisation**: Surface plasmons have elliptical polarisation. They are polarised partially into and along the plane of the interface.
4. **Energy transport**: With their evanescent character, surface plasmons do not transport energy in the $z$ direction, only along the interface plane.
5. **Losses**: Losses are found through the imaginary part of the permittivity $\varepsilon_2$. Substituting a complex permittivity into Eq. 2.16 leads to damping of the plasmon. The

---

[1] This approach for describing the properties of a surface plasmon are inspired by reference [28]

substitution leads to imaginary parts for both $k_x$ representing damping of the plasmon as it propagates along the interface, and $k_{2z}$ representing energy dissipation in the form of heat into the metal.

6. **Dispersion**: Using the Drude dielectric function $\omega_2(\omega) = 1 - \omega_p^2/\omega^2$ with $\varepsilon_1 = 1$, Eq. 2.16 can be rearranged in terms of the frequency of incident light leading to the plasmon dispersion shown in Fig. 2.5. From this is can be seen that plasmon propagation is always slower than that of the incident light. Additionally, the surface plasmon dispersion never crosses the light line, which means that surface plasmons cannot be via excited direct optical illumination only.
7. **Light confinement**: The wavelength of surface plasmons can be far less than the wavelength of incident light - this enables confinement of light into sub-wavelength volumes and overcoming of the diffraction limit.
8. **Propagation length**: Using $Im(k_x)^{-1}$ is it possible to approximate the propagation length of the plasmon. This allows the identification of useful materials and devices i.e. Au is only a good material for light confinement below around 3.7eV, since above this energy the propagation length of the plasmon is extremely short due to large energy losses.

From plasmon property 6 and Fig. 2.5, it is seen that plasmons cannot be excited via direct illumination in air/vaccuum alone. Initially, a good idea might be to place a higher refractive index layer directly onto the metal surface (e.g. glass onto Au) which would reduce the speed of light so that the gradient of the light line is also reduced. However, plotting the new surface plasmon dispersion with higher $\varepsilon_1$ simultaneously decreases the initial gradient so that there is no crossing of the light line and thus, no excitation of the surface plasmon. However, by instead slightly raising the glass from the surface by a few nanometres, it is possible to excite surface plasmons along a flat interface using evanescent fields.

The two most common methods to achieve this include the Otto and Kretschmann geometries as depicted in Fig. 2.7 [28, 29]. If the angle of incidence [2] is greater than the critical angle $\theta_c$, total internal reflection occurs at the interior base of the prism, meaning that all of the incident light is reflected at the boundary. Within a few nanometres of the position of incidence for the internally reflected field, an evanescent field is projected into the other medium beneath the prism which maintains the properties of the field as they were inside the prism (with the reduced gradient light-line). If a metal surface is brought very close to this region, the evanescent field is able to reach across the air gap and excite the plasmon since

---

[2] A prism rather than just glass has to be used so that the angle into the glass is less than the critical angle.

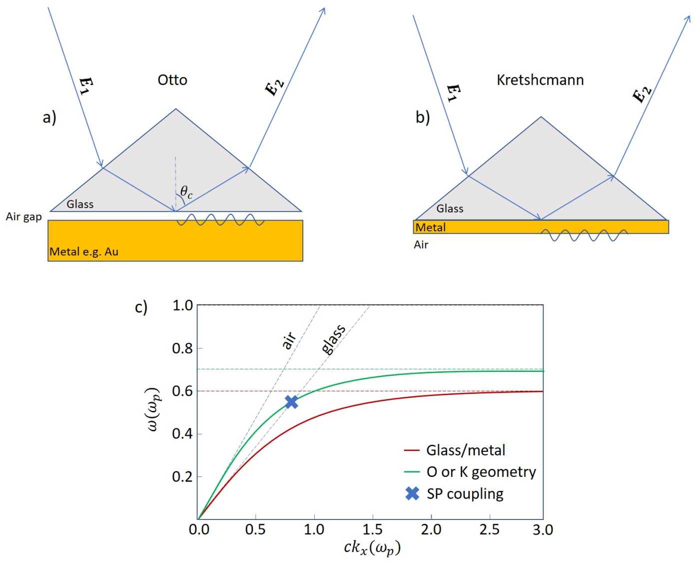

Fig. 2.7 In the Otto geometry (a) the evanescent field beneath the point of total internal reflection for light at angle $> \theta_c$ is able to launch a plasmon in a flat surface since the field maintains the properties as if it were in glass. The Kretschmann geometry (b) is very similar to the Otto, except the evanescent field passes through a very thin metal surface. This is significantly easier to fabricate, but not as efficient. c) Same as Fig. 2.5, but showing how a plasmon with a dispersion in air is able to cross with a light line in glass.

it's dispersion is as if it were in air but the light line is as it were in glass. The crossing of the light line in glass with the plasmon dispersion in air can be seen in Fig. 2.7(c).

The launching of a surface plasmon can be detected via the difference between incident field $\vec{E}_1$ and reflected $\vec{E}_2$. By changing the angle of incidence for either geometry the momentum into the interface plane can be varied and thus the entire plasmon dispersion can be mapped out. These methods are both highly sensitive to changes of refractive index near the interface, so similar architectures can for example be used to detect low levels of attached analytes.

In this thesis, the field a few nanometres from a propagating surface plasmon is defined as *near-field* because it decays in strength more rapidly from the interface than fields far ($> 2\lambda_{plasmon}$) from the plasmon, which are considered *far-field*. This far-field behaves as usual for any antenna, with $\vec{E}$ decaying as $1/r^2$ and $\vec{B}$ as $1/r$ from the source. Conversely, all components of the near-field decay with a multipole field dependence. This ensures that near-field effects never extend more than a few wavelengths from the source. Additionally, while receiving far-field light has no influence on the field at the source, near-field light can influence the radiation at the source. We will see the result of this in the section on plasmonic coupling. This unique behaviour allows, for example, secure phone payments using NFC technology[30].

### 2.3.1 Localised surface plasmons

The localisation of a surface plasmon to a nanoscale area significantly alters its excitation requirements and properties. To understand this, consider a wave propagating at an interface which now has geometrical boundary conditions on the order of a wavelengths or less. These boundaries lead to the formation of standing wave nodes which discretise excitation conditions and change required incident energies. Changing the area, morphology or two-dimensional shape (square, circle etc.) of the interface will change the propagation of the no localised surface plasmon and in turn it's excitation requirements. Optical scattering, rather than reflection, dominates interactions with nanoscale surfaces and so evanescent fields are not required in order to excite localised surface plasmons. Similarly, plasmons propagating along a closed three dimensional surface such as a spherical particle, interfere with one another constructively and destructively forming standing wave modes requiring specific frequencies of excitation (see Fig. 2.8).

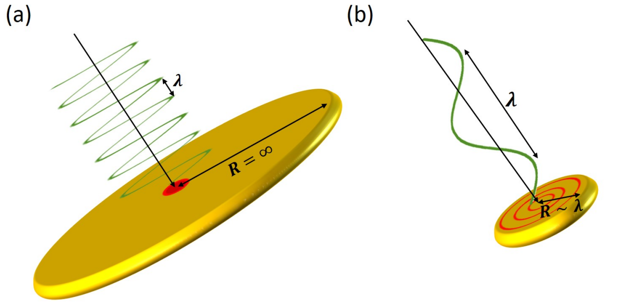

No localised surface plasmon    Localised surface plasmon (LSP)

Fig. 2.8 For an infinite gold plane (disc radius $R = \infty$) surface plasmons cannot be excited under normal illumination conditions (a). However, when the dimensions of the plane are reduced such that $R \sim \lambda$, surface plasmons are reflected at the boundaries and localised depending on the nanostructure geometry (b). Specific resonances are setup on the nanostructure, leading to a set of discrete resonances (red-rings in b). These modes are seen as peaks in scattering intensity.

Localised surface plasmons (LSPs) arise without the requirement for special architectures when the Frölich condition contained within Eq. 2.6 is met for a spherical metallic nanoparticle much smaller than the wavelength of light [21]. Below the plasma frequency $\omega_p$, the permittivity of Au becomes negative and relative permittivity approaches -2. The polarisability for the nanoparticle (Eq.2.2) therefore approaches a maximum as does the scattering cross-section $C_{scat}$. By separating complex from real terms and then substituting Eq. 2.11 into Eq. 2.5 for a nanoparticle with $q << 1$, another form of the scattering cross-section is arrived at,

$$C_{sca} = \frac{8}{3}\pi a^2 \frac{(\omega_p/\sqrt{3})^4}{(\omega^2 - (\omega_p/\sqrt{3})^2)^2 + \omega^2\gamma^2} q^4. \tag{2.18}$$

This equation shows that the relationship between scattering and incident frequency for a particle much smaller than the incident wavelength can be described by a Lorentzian curve. If damping is ignored, this Eq. 2.18 shows that at the Frölich condition scattering approaches a singularity at $\omega = \omega_p/\sqrt{3}$. This is physically unrealistic, hence the requirement for the inclusion of the damping term $\omega^2\gamma^2$ which prevents this situation and forms the Lorentzian peak. Apart from their differing excitation requirements, SPs and LSPs are fundamentally identical, so damping occurs for exactly the same physical reasons as discussed in the previous section.

LSPs also influence the direction of scattering, since there is a strong relationship between the geometry of the localised near-field and the measured far field scattering. Light will scatter preferentially in the same direction as the localised field vector, leading to characteristic scattering patterns which change with nanostructure geometry. In the following section on the Mie method, the damping term will be appear again with additional angle dependent terms.

Maximal polarisability is achieved for the dipolar localised surface plasmon resonance (LSPR), corresponding to charges separated over the spherical nanoparticle surface along a single axis. Since they still follow the rest of the rules followed by surface plasmons, localised plasmons depend on the dimensions and shape of the nanostructure, as well as the optical properties (e.g. refractive index) of both materials at the interface. As the size of a nanostructure increases, the quasistatic regime is left behind and therefore the assumptions made to reach equation 2.18 are no longer fully valid. An increasing number of possible resonances arise with increasingly time-dependent local fields and losses. To describe these additional resonances requires a more thorough treatment called the Mie method[31]. Au nanoparticles considered in this thesis range in diameter between 60 nm and 100 nm, being illuminated by light of wavelength 400 nm-100 nm and scattering cannot be understood within the framework of the quasistatic regime.

In the same way as has been seen for SPs along a planar interface, during propagation of an LSP an intense near-field decays exponentially into the surrounding medium away from the nanoscale region. This near-field is highly sensitive to the local (<few nanometres away) medium, (which may consist of molecules etc.), and LSP changes can be detected via changes in scattering rather than reflection. Also, although the plasmon is unable to impart energy away from the excited nano-object, losses in the metal lead to strongly localised heating under illumination. Depending on the size, local refractive index and choice of

material for the nano-object, the resonance can be tuned in order to maximise these effects at certain wavelengths of light [32–34]. LSPs also differ in that, due to nanscale morphological changes in a surface, near-fields from the propagating plasmon can be concentrated into even smaller volumes called hot-spots [35, 9, 36]. The field is localised most strongly at the position of a discontinuity, such as at structural edges and corners (see Fig. 2.9). This gives another degree of freedom for researchers to control or determine the exact point of interaction with the near-field, since optical scattering will be strongest at these position with resolution of a few nanometres.

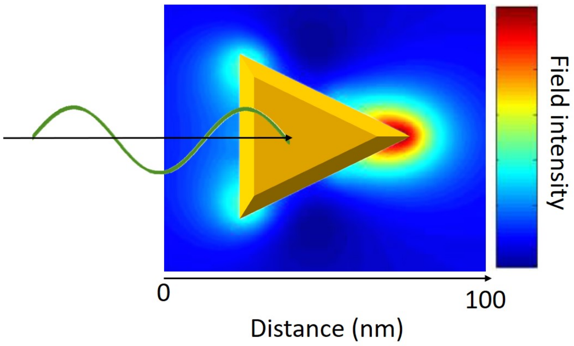

Fig. 2.9 Near field intensity surrounding a 50 nm nanotriangle calculated using Lumerical during illumination at resonance wavelength of 700 nm. The LSP resonances on the trangle surface mean that peak field intensity is maximised at the corners in regions called plasmonic hot-spots.

To summarise this chapter before introducing the Mie method, the dielectric function of metals has been described classically and using a combination of this with the polarisability for nanoparticles according to Eq. 2.9, it’s possible to explain optical interactions with metal nanoparticles much smaller than the wavelength of incident light. This leads to the discovery of a resonance at a specific frequency of light in a process attributed to the formation of a LSP. However, the fundamental assumption that the nanoparticle diameter is significantly less than the wavelength of incident light continues to restrict. Experimentally there appear clear differences between the results of Eq. 2.18, and those observed for larger particles such as red-shifting LSPRs and increasing linewidths (full-width half-maxima (FWHM)). Via the derivation for a flat plane it has been seen that when surface plasmons are not localised the dispersion becomes more complex. The locally time dependent nature of surface plasmons leads to a far greater number of possible resonance conditions. It was not until after the turn of the 20th century that Gustav Mie was able to derive equations to describe scattering from larger nanoparticles as a consequence of complex surface plasmon resonances. The Mie method is a convenient way to continue with the introduction of the localised surface

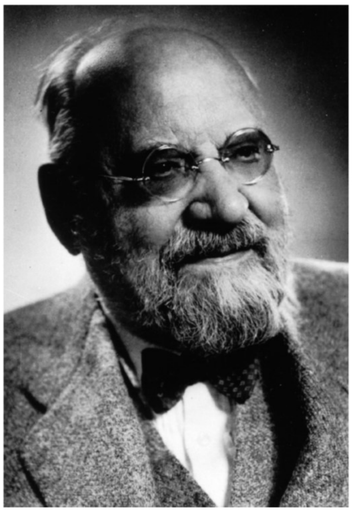

Fig. 2.10 A picture of Gustav Mie. When it comes to scattering from spherical particles it's always Mie Mie Mie

plasmon since, as shall be seen in the following, its existence is contained within the results of the method.

### 2.3.2 Mie theory overview

Despite all of the progress made through Rayleigh and the theories of Maxwell and Lorentz (and Lorenz!), up until the start of the 20th century there remained no thorough explanation for the large differences between theory and experiment for the scattering of metallic nanoparticles of larger radii i.e. which do not satisfy $q << 1$. In particular, the unusual interactions with nanoparticles of noble metals, deviated significantly from expectations. This was fundamentally due to the assumptions of the quasistatic regime made in previous sections, which were invalid as nanoparticle diameters increased and did not take into account the changes in scattering due to the presence of LSPs. It was not until 1908, that Gustav Mie[3] stepped into the fray to provide a more general solution for scattering from spherical nanoparticles of arbitrary radius and refractive index[31].

In the fourth chapter of this thesis there is a discussion of work which relies on the use of a new generalised Mie method. It is therefore useful to develop a basic understanding of the method. The Mie theory is a mathematical approach used to solve Maxwell's equations for radiation from a sphere of arbitrary size analytically. The theory attempts to isolate the possible resonant configurations of charge across a spherical surface and then to calculate the resultant near and far-fields as a function of radial distance from the nanoparticle. This is

---

[3] Although both Debye and Lorenz came to similar, but less substantial solutions earlier than Mie

significantly more thorough than a simple dipole approximation. As was briefly mentioned in the previous section, the distribution and k-vector of the near-field influences the strength and angle of scattering. There are many different radiative modes beyond the simple assumptions in the previous section and these resonances are due predominantly to LSPs. As nanoparticle size and refractive index changes, the number and specific form of the modes across the nanoparticle surface changes and consequently the measured scattered light is changed.

In the Mie theory, the absorption and scattering cross sections for any nanoparticle can be written as a multiplication of particle cross-sectional area and an interaction efficiency $Q$, thus $C = \pi a^2 Q$. This efficiency with, $Q_{ext} = Q_{abs} + Q_{sca}$, can be written in the form [22, 21]

$$Q_{sca} = \frac{2}{q^2} \sum_{l=1}^{\infty} (2l+1)\{|a_l| + |b_l|\} \tag{2.19}$$

$$Q_{ext} = \frac{2}{q^2} \sum_{l=1}^{\infty} (2l+1) Re(a_l + b_l) \tag{2.20}$$

with the electric scattering amplitude,

$$a_l = \frac{F_a^e(l)}{F_a^e(l) + iG_a^e(l)}, \tag{2.21}$$

and magnetic scattering amplitude,

$$b_l = \frac{F_b^m(l)}{F_b^m(l) + iG_b^m(l)}. \tag{2.22}$$

Here, $F_a^e(l)$, $G_a^e(l)$, $F_b^m(l)$ and $G_b^m(l)$ are related to the spherical Bessel and Neumann functions. To aid somewhat in visualising what this means, Bessel functions represent the radial component of vibrational modes on a circular film (e.g. on a drum). Neumann functions are also often referred to as Bessel functions of the second kind, because they are Bessel functions which are equal to unity at the origin instead of zero. Changing basis to spherical polar coordinates leads to the spherical Bessel and Neumann functions[37]. These functions contain both the amplitudes and angular dependence of the field. Equations 2.19 to 2.22 form the basis of Mie theory, from which it is theoretically possible to find the scattering cross-sections for particles of few to many hundreds of nanometres in diameter.

Eq. 2.18 contains the damping or dissipation parameter $\gamma$, but gives no information on what dictates the magnitude of this parameter. It is important to understand this because it will tell us the source of losses. As an example of the power of Mie theory, by expanding once again for small $q$ (things are always easier in the quasistatic regime) it is possible to find the dependence of the dissipation parameter. If the Bessel and Neumann functions are

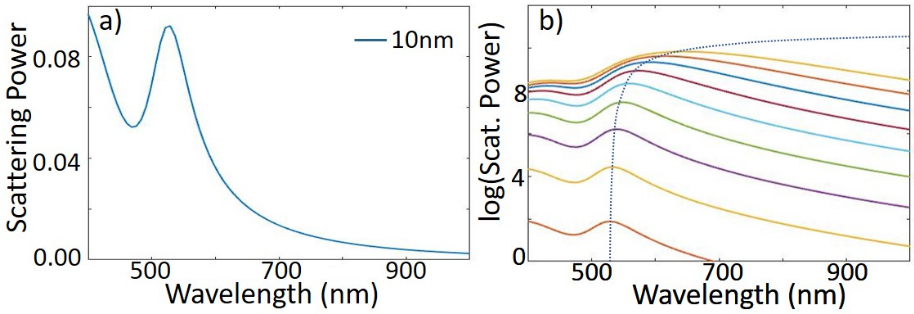

Fig. 2.11 Calculated normalised resonance using the generalised Mie method (see Appendix) for a 10 nm-diameter Au nanoparticle on Si (a) and a range of nanoparticles from 10-100 nm in diameter (log(scattering power)) (b) plotted as a function of wavelength $\lambda$.

expanded for small $q$, the magnetic part of the scattering parameter can be neglected leading to

$$F_a^e(l) \approx q^{2l+1} \frac{(l+1)}{[(2l+1)!!]^2} n^l (n^2-1) \tag{2.23}$$

$$G_a^e(l) \approx n^l \frac{l}{2l+1} \left\{ n^2 + \frac{l+1}{l} - \frac{q^2}{2}(n^2-1)\left[\frac{n^2}{2l+3}. + \frac{l+1}{l(2l-1)}\right]\right\} \tag{2.24}$$

Now for $q << 1$ only the dipole term $l = 1$ needs to be considered, and using Eq. 2.19 the scattering efficiency is just $Q_{sc}^{Mie} = 6|a_1|^2/q$. Substituting in Eq. 2.21 and doing an awful lot of algebra leads to,

$$Q_{sca}^{dip-Mie} \approx \frac{8}{3} \frac{\omega_{sp}^4}{(\omega^2-\omega_{sp}^2)^2 + \frac{4}{9}q^6\omega_{sp}^4} q^4. \tag{2.25}$$

This equation can be compared directly to equation 2.18, which gives the dependence of the dissipation parameter as

$$\gamma_{eff} = \frac{2}{3}\omega_{sp} q^3. \tag{2.26}$$

Damping alters the width of the Lorentzian peak with red-shifting mode position as seen in Fig. 2.11(b). This dissipation removes the singularity from the Frölich condition. The red-shift of the scattering peak with increased nanoparticle size is a result of the weakened restoring forces between charges as distance increases and the above treatment acts as an initial explanation for this. Eq. 2.26 says that as nanoparticle diameter decreases dissipative losses due to the surface plasmon increase. This makes intuitive sense, since for the dipole mode, the plasmon must travel further to complete one oscillation.

As has now been said a few times, for larger nanoparticles the assumption of small $q$ and therefore solely dipole resonance is inadequate. For higher order resonances further resonant modes l=1,2,3... are required. These are all however now contained within the Mie theory and so, although it becomes increasingly challenging computationally, there is now a model which can explain scattering for these higher order resonances too while including dissipation.

In the modern era, the Mie method remains a standard way to calculate the scattered far field from any spherical nanoparticle. It correctly predicts red-shifts and changes in mode linewidth seen with increasing particle diameter for metallic nanoparticles, something not achievable using approaches discussed in previous sections. As can be seen in the Appendix, the Mie method can even be generalised and used in combination with a transfer matrix approach in order to calculate particle scattering from considerably more complex coupled systems [38].

## 2.4 Electromagnetic cavities

Electromagnetic cavities are fabricated structures which confine electromagnetic fields at specific frequencies to a region of space, often well below the optical diffraction limit [39, 40]. The volume and optical properties of the entire structure dictate the wavelength of the confined field. The resultant confinement of the wavefunction, leads to discretisation of the field into a number of allowed resonant energy states and the intensity of the field can be significantly greater compared to fields outside of the cavity.

In this thesis, electromagnetic cavities are divided into two types, microcavities and nanocavities. Put simply, microcavities are electromagnetic cavities within which fields are confined to micrometer-scale volumes, while in nanocavities fields are confined to nanoscale volumes. The strongly altered properties of the field when compared to the incident light allow unique interactions with optically active materials placed inside or within the vicinity of the cavity.

Both micro- and nanocavities can be used to achieve similar aims (e.g. strong coupling [9, 36, 41]), but both have their upsides and downsides. In general, while microcavities are able to achieve exceedingly high field intensities with low losses (high $Q$ factors), they are not able to confine light to anywhere near as small volumes when compared to nanocavities. For nanocavities the opposite is true where dissipative losses reduce the achievable Q-factor significantly, but this is compensated by extremely small mode volumes. Additionally they both operate due to different mechanisms, with microcavities involving coupling of the far-field and nanocavities the near-field via coupling of plasmons. These differing mechanisms can quite drastically change the resultant behaviour of the cavity as will be seen in this chapter.

### 2.4.1 Optical microcavities

Due to the enhanced intensities and field confinement provided by microcavities, they are used regularly to observe novel optical phenomena[41, 42]. The simplest form of optical microcavity, and the one most relevant to this thesis, consists simply of three layers of differing refractive index material. Referring to Fig. 2.12(a), the cavity length $L$, which corresponds in this case to the thickness of medium 2, is on the order of the incident wavelength of light or greater. In many cases cavities, whether micro- or nanoscale, can initially be broken down into this simple three layer arrangement. There may be variations in scale, morphology, incident field properties, angle of incidence etc., but very often the starting point is the same.

Light travelling initially in medium 1 with $\varepsilon_1$, reaches the boundary with medium 2, $\varepsilon_2$, which is called the cavity medium, at which point one of three interactions occur at the interface; reflection, transmission or scattering. Each of these interactions alter the properties of the field depending on the refractive indices of both media. Ignoring scattering, the simplest process is then that light is transmitted into medium 2, with the rest reflected and lost. Transmitted light continues to propagate through medium 2, at which point it reaches the interface with medium 3, $\varepsilon_3$. Again, depending on the refractive index of each medium, some light is reflected back toward medium 1 and some transmitted into medium 3. From here on, each reflection at either interface reflects some of the light back into medium 2, and the optical field is therefore confined, with cavity losses at each bounce due to transmission out of medium 2 and back toward the source.

Now, the field confined within medium 2 has fundamentally different properties to the field in 1 and 3. Due to multiple back reflections, the optical field in medium 2 interferes both constructively and destructively leading to field superposition at specific frequencies called the cavity resonances, $\omega_c$. The resonances can be changed by changing the thickness of medium 2, or phase shifted by $\pi$ depending on, for example, $\varepsilon_2 > \varepsilon_3$ or $\varepsilon_3 > \varepsilon_2$. This interference effect is responsible for the discretisation of energies for fields inside a cavity. Assuming the incident field is resonant with one of these superimposed states, if the initial illumination was a pulse, the field would continue to propagate within the cavity of medium 2 for an extended period of time following the end of the pulsed excitation. This describes the lifetime of the mode in the microcavity, which depends on the rate of energy loss. For normal incidence into the cavity, this form of microcavity is called a planar standing wave microcavity and for any resonator, the losses are described by the cavity $Q$-factor.

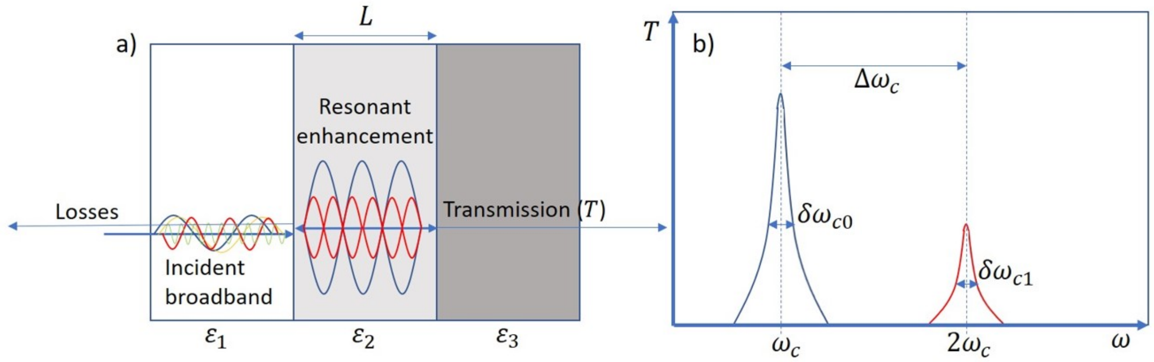

Fig. 2.12 A pictorial representation of a planar microcavity consisting of three layers of material with dielectric functions, $\varepsilon_1, \varepsilon_2$ and $\varepsilon_3$ and cavity length $L$ (a), broadband illuminated at normal incidence (a). The transmitted light is concentrated at specific frequencies depending on the microcavity parameters, leading to distinct modes with bandwidths $\delta\omega_{c0,c1}$ separated in frequency by an amount $\Delta\omega_c$

The Q factor can be broadly defined as,

$$Q = \frac{\omega_c}{\delta\omega_c} \tag{2.27}$$

where $\omega_c$ and $\delta\omega_c$ are the resonant cavity frequency and linewidth of the cavity mode respectively. In the same vein as the previous section on plasmons, the losses are contained within the linewidth of the cavity modes - a broader resonance typically means greater losses. If a significant amount of light is scattered or radiated away from the cavity, reflected on the way in, or transmitted straight through, this will increase the linewidth of the cavity resonance. The Q-factor is the first figure of merit (FOM), used to describe the level of energy loss from an electromagnetic cavity.

The second FOM is the cavity finesse, $F$, defined as,

$$F = \frac{\Delta\omega}{\delta\omega} = \frac{\pi\sqrt{R}}{1-R}, \tag{2.28}$$

where the $R$ is the power reflectivity and $\Delta\omega$ is the mode frequency separation $2\pi R/L$. The finesse is a measure of the spectral resolution of the microcavity i.e. how sharp the cavity modes are compared to their separation.

Once the finesse is known, it is possible to calculate the intensity enhancement within the cavity, which is the ratio between the intensity inside ($I_{cavity}$) and entering the cavity ($I_{incident}$),

$$\frac{I_{cavity}}{I_{incident}} \approx \frac{1}{1-R} = \frac{F}{\pi\sqrt{R}}. \tag{2.29}$$

As can be seen in Fig. 2.14(a), this maximal enhancement only occurs at particular positions within the microcavity. This means that planar optical microcavities must be very carefully designed so that for example, an emitter, is placed at the precisely correct position. Slight changes in temperature can change the cavity length $L$[43] so experiments aiming to observe the interaction of an emitter with an optical microcavity are usually done with highly controlled temperature conditions and require nanometre-precision growth techniques[44].

If instead of normal incidence into medium 2 the electric field enters at an angle, the resonance conditions for the above situation can be described by Fabry-Perot interference. Thus, this form of microcavity is called a planar Fabry-Perot microcavity. All of the above equtions still stand, but the modes for this type of microcavity shift with incident angle. The condition for constructive interference is dictated by the wave-vector component into the plane of the microcavity $k_{\perp} = kcos(\theta)$,

$$2Lkcos\theta = 2m\pi, \tag{2.30}$$

where $m$ is an integer. Rearranging this equation leads to the relation which reveals the cavity resonance frequencies $\omega_{cm}$,

$$\omega_{cm} = \frac{m\pi c/L}{\sqrt{n^2 - sin^2\theta}}. \tag{2.31}$$

A commonly used form of microcavity is a Bragg microcavity. It differs only in that medium 1 and 3 in Fig. 2.14 are Bragg mirrors, consisting of many dielectric layers which use interference effects to give extremely high reflectivity. Since they use interference effects, Bragg mirrors only operate effectively for specific frequencies of light [40]. Two different dielectric materials, with contrasting refractive indices are deposited alternately. The dielectric layers must have maximal contrast in refractive index between them, and the optical path length inside each material must be one quarter of the desired wavelength [44]. The cavity Q-factor can be improved by increasing the number of alternating layers, but the deposition process inevitably introduces interfacial scattering which eventually counteracts Q factor gains. Bragg microcavities can have mirror transmissivities less than one part in $10^6$ and microcavity Q-factors of $> 10^4$[40].

Although it is extremely challenging in terms of fabrication, the morphology of the Bragg mirrors can be tailored to reduce sideways losses by making them concave. Spherical mirror microcavities use the same idea but with highly polished mirrors, and pillar microcavities instead use total internal reflection to prevent lateral leakage [40].

In chapter 4 of this thesis, work is presented on the coupling of far-field between a nanoparticle and a Fabry-Perot cavity. This leads to the formation of a hybrid resonance between plasmonic LSPR and Fabry-Perot optical modes in addition to a new polarisation and angle dependent mode.

## 2.4.2 Plasmonic Nanocavities

Nanocavities are formed when near-fields generated by plasmons separated by a few nanometres couple to one another, trapping light tightly between them. On a nanometre scale they can often be broken down into the same three layer system shown in 2.14, but trapped fields operate via near- rather than far-field mechanisms (see end of section 2.3) which fundamentally alter the cavity behaviour. It will be seen in this section that near-field interactions change the dispersion for each plasmon such that new resonances occur at specific frequencies of incident light, highly sensitive to the nanoscale morphology of the nanocavity and interpretable via optical scattering [45, 46, 8, 47] as for LSPs on single nanoparticles (see section 2.3.1 and 2.3.2).

### The Plasmonic Dimer Optical Nanoantenna

A plasmonic dimer forms during coupling between LSPs on two spherical nanoparticles when separated by a gap of less than $\sim$ 10 nm forming a near-field coupled nanoantenna. With the right illumination conditions (see below) a nanocavity is formed in the region between the nanoparticles with width $w \sim \sqrt{Rd}$, where $R$ is the particle radius and $d$ is the inter-particle separation or nanocavity length.This means that for two nanoparticles of diameter 80 nm separated by 4 nm, the mode width is $\sim$ 13 nm [4][**?** ], well below the diffraction limit. The field enhancement in these nanocavities is significantly greater than with particle LSPs alone and can be used to detect changes in refractive index with significantly higher sensitivity [48, 49].

Starting in the quasistatic regime, as usual the two nanoparticles are described as interacting dipoles. Assuming that these two dipoles are dominated by Mie resonances for which $l = 1$, the interaction of two LSPs is dictated by the Coulomb interaction of the surface charges. When in close enough proximity (<10 nm for plasmons), modes hybridise and a number of possible energy states become available depending on resonance combinations [50, 51].

This hybridisation model for the nanoparticle dimer is analogous in many respects to the description of molecular energy level formation due to interacting atomic orbitals, in this case represented by the energy levels of the single nanoparticle plasmon [47, 51]. In

---

[4] An overview of coupling between nanoparticles calculated using the generalised Mie method can be found in the Appendix.

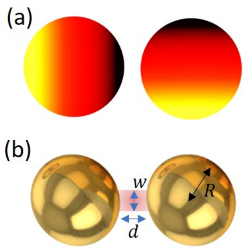

Fig. 2.13 (a) The two possible orthogonal surface charge configurations produced by the generalised Mie method with $l = 1$ for a non-interacting Au nanoparticle. (b) The problem definition for a coupled nanoparticle dimer (nanoantenna), consisting of two nanoparticles of radius $R$ separated by distance $d$, leading to a confined field of width $w$ in the gap.[4].

this model, electrons are treated as an incompressible, irrotational fluid of uniform density and the electron density is confined to a fixed positive background. Plasmon modes are self-sustained deformations of the electron liquid and, since this liquid is incompressible, the result is the resonant motion of surface charges across a sphere (as is the case for the Mie method).

Dimer formation is sensitive to incident polarisation. If the polarisation is parallel to the axis passing through the centre of both spheres, LSPs interact strongly due to the surface charge configuration. On the other hand, if polarisation is orthogonal to this axis individual LSPs interact weakly. For the same reasons hybridisation is dependent on incident angle, since magnitudes of the polarisation vector parallel or perpendicular to the inter-particle axis depends on angle. In Fig. 2.13(a) the charge configurations are orthogonal to one another, and therefore the coupling between these two particles would be very weak regardless of distance.

For the case of polarisation parallel to the inter-particle axis, LSPs on both nanoparticles ($l = 1$) oscillate in phase such that the positive and negative charges on each side face one another at gap. This forms a low energy state. Conversely with LSPs in anti-phase, surface charges with the same sign face one another at the gap, leading to a higher energy state. Since the probability of the lower energy state is greater, the in-phase mode is bright, meaning that it dominates contributions to far-field scattering. Correspondingly the anti-phase higher energy state is a dark mode, lending a negligible contribution to far-field scattering. The in-phase and anti-phase situations are correspondingly referred to as the bonding bright mode and anti-bonding dark mode respectively. The only optically detected resonance in scattering originates from the in-phase LSPs, forming what is referred to as the coupled mode for the plasmonic dimer[5]. A pictorial representation of hybridisation is shown in Fig.

---

[5] It is possible to detect the contribution from the anti-bonding dark mode using electron energy loss spectroscopy (EELS) [52]

2.14(a). In the figure the lower nanoparticle (semi-transparent) is replaced by an image quasi-particle. This is to demonstrate the similarities between a dimer and the nanoparticle-on-mirror (NPoM geometry), which is discussed in more depth below. This system replaces one of the nanoparticles with a flat gold mirror, over which surface charges emulate the motion of charges as if a second adjacent nanoparticle were present. For the discussions here, this picture is identical to the hybridisation model for two coupled nanoparticles.

As nanoparticle separation decreases, increased near-field interactions lead to changes in mode hybridisation. For separations greater than a few nanometres only the interaction between the individual $l = 1$ dipole modes in both nanoparticles are significant. In this case, the strength of the interaction can be approximated to decay according to the usual $1/d^3$ for two interacting dipoles. Higher order hybridised modes which rely on coupling between higher order LSP resonances (e.g. $l = 2, 3, 4...$) display interactions that decay more rapidly with distance and are therefore negligible for larger separations.

For the case of polarisation orthogonal to the inter-particle axis, the weakly interacting LSPs lead to two possible states, but here the dark mode is now the lower energy state (Fig. 2.14(b)). The higher energy bright mode has a similar resonance frequency to the single nanoparticle LSP, and is commonly referred to as the transverse mode of the plasmonic dimer[53]. Since the difference in energy between the bright and dark mode is relatively small and the bright mode is a higher energy state, its far-field intensity is almost always lower than for the coupled mode.

The LSPs on each nanoparticle remain highly sensitive to the refractive index of the surrounding environment and thus the position of the coupled mode can be tuned by altering this (e.g. via growth of a high-$n$ layer around the particles). In addition, since coupling is related to charges separated across a gap, the coupling strength is strongly influenced by the refractive index in the gap between nanoparticles. The gap therefore appears to bear a strong resemblance to a capacitor and, as will be seen for NPoMs next, a model which works on this basis is able to accurately predict the position of coupled modes with changing gap distance, $d$, and refractive index, $n_g$. Such models which enable the prediction of gap distance (or refractive index is $d$ is known), have led to many treating the plasmonic dimer as a ‘nanoscale ruler’, able to rapidly measure sub-nanometre geometrical changes optically [54–56, 8].

Along with the dependence of hybridisation on angle of illumination, the corresponding emission of the dimer modes are strongly angle dependent[57]. The transverse mode shows maximal emission parallel to the inter-particle axis, while the coupled mode shows maximal emission orthogonal to this axis.

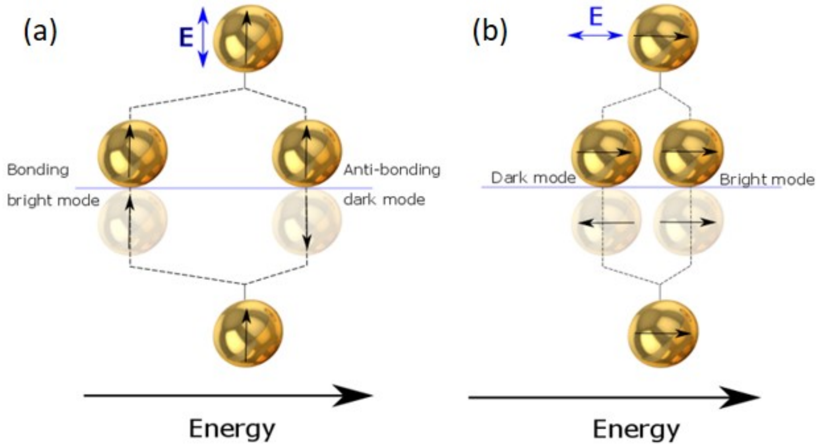

Fig. 2.14 The hybridisation model for a nanoparticle dimer formed using NPoM, with semi-transarent nanoparticles representing image quasi-particles on the other side of the Au interface (blue line). With polarisation along the inter-particle axis (a) exciting the $l = 1$ mode, the state with both nanoparticle LSPs in-phase is the bonding bright mode, visible in far-field as the coupled mode. With polarisation orthogonal to the inter-particle axis the inter-particle coupling is weak and the bright mode exists in at the higher energy state (b), visible in far-field as the transverse mode for the dimer.

### NanoParticle on Mirror (NPoM)

The nanocavities formed in such dimers appear extremely useful for nano-optics, but their use either as a measurement technique or as a plasmonic cavity (e.g. to achieve enhancement, coupling with molecules or materials) is severely limited due to a number of factors.

Firstly, the production of a high yield of plasmonic dimers with controllable, size, shape and separation in solution is a significant challenge in terms of chemistry [58–60]. Such a process must either grow and form dimers with the correct diameter simultaneously, or controllably aggregate single nanoparticles, usually via ligand substitution. In both situations, the processes are highly stochastic and time consuming, leading to low yields [6]. Additionally, dimers cannot be formed at the sacrifice of nanoparticle shape, they must remain of the desired shape (e.g. sphere, cube, triangle, etc.) regardless of the production method or else lose their accuracy as a plasmonic ruler (see above).

Secondly, it is very difficult to reliably position materials of interest into the gap between nanoparticles. If the process is solution based, either the encapsulating ligand must be the material of study or another substance in solution must be introduced. The presence of this material in the gap will once again be stochastic with very low yield, low control of the amount and of material orientation in the gap.

---

[6] The best seen in literature was 26% from reference [58]

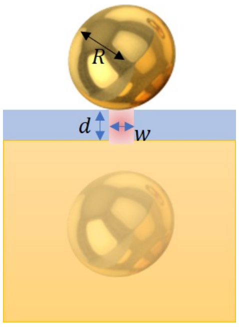

Fig. 2.15 The NPoM dimer, with a nanocavity formed inside a material of thickness $d$

Finally, taking all of the above into account, if dimers in solution are deposited onto a substrate to be analysed (e.g. via dark field scattering) it is very difficult to determine optically what system is being analysed. For example, frequently during aggregation, trimers as well as dimers form. These are often difficult to distinguish based on spectral analysis alone leading to outliers in the data. Also, the measured spectrum depends on the geometries of both nanoparticles, increasing the variation in gap distances and morphology. This directly increases the variance in the spectral data from dimer to dimer.

The NanoParticle on Mirror (NPoM) overcomes these significant problems by replacing one of the nanoparticles in the dimer with a flat noble metal substrate, separated by a spacer material of some kind (e.g. molecules, crystals). To achieve this, highly uniform nominally spherical metal nanoparticles [61] are deposited onto the substrate overlaid with material. Upon illumination, LSPs excited in the nanoparticle couple to image SPs propagating on the planar surface beneath. The behaviour of these surface charges mimics the behaviour of charges as if they were moving across a neighbouring particle, meaning that the system can be modelled as a real particle coupled to an image quasi-particle inside the metal surface (Fig. 2.15). The hybridisation model for the NPoM dimer is close in analogy to the real nanoparticle dimer [50, 62] (Fig. 2.14).

Crystals or molecules such as vdW materials and self-assembled-monolayers deposited onto gold substrates act as spacers between nanoparticle and mirror. Post-deposition of nanoparticles onto these materials the nanocavity field is concentrated inside the material, between nanoparticle and mirror. A 3D depiction of this system with a thin crystalline layer as gap spacer between nanoparticle and Au mirror is shown in Fig. 2.16(a). In the same way as seen for a dimer (see above), the spacer increases the distance between the nanoparticle and its mirror image, blue shifting the coupled mode. Simultaneously, the presence of the crystal increases the refractive index in the gap, red-shifting the coupled mode. The NPoM maintains the field orientation in the gap seen for the dimer nanoantenna, which is parallel to the inter-quasi-particle axis for thin gaps.

These plasmonic nanoantenna modes span the entire NPoM system and their resonance wavelengths can be predicted as suggested previously, by considering the NPoM as an LCR [7] circuit with a capacitance across the nano-gap in the quasi-static regime. Taking this approach, valid for the $l = 1$ (coupled) mode [46][8], leads to

$$\lambda_1^l = \lambda_p \sqrt{\varepsilon_\infty + 2\varepsilon_d + 2\varepsilon_d C_g / C_{NP}}, \tag{2.32}$$

where $\lambda_1^l$ is the resonance wavelength of the coupled mode, $\lambda_p$ the plasma wavelength, $\varepsilon_d$ the deielectric constant of material in the gap and $C_g$,$C_{NP}$ are the gap and nanoparticle capacitances respectively. $\varepsilon_\infty$ is the dielectric background and is related to the Drude metal permittivity, $\varepsilon_m$, and optical wavelength, $\lambda$, via

$$\varepsilon_\infty = \varepsilon_m + \left(\frac{\lambda}{\lambda_p}\right). \tag{2.33}$$

Both this parameter and the gap capacitance vary weakly with nanoparticle size for NPoM. The gap capacitance varies due to subtle differences in the field localision in the gap, since it is localised between a sphere and a flat surface rather than two spheres. $\varepsilon_\infty$ also varies for reasons of geometry and is found by measuring $\varepsilon_m$ using extinction spectroscopy and making calculations from Eq. 2.33.

The influence on coupling due to nanoparticle size and gap refractive index is encapsulated in the capacitance of the nanoparticle and gap respectively. For spherical dimers or NPoMs the overall nanoparticle capacitance is simply $C_{NP} = 2\pi R \varepsilon_0$, and the capacitance at the gap is related to the solid angle covering a surface area over which the nanocavity (of width $w$) spans [46, 45]. It can therefore be shown that $C_g = C_{NP} \varepsilon_g^\chi ln[1 + \beta R/d]$, leading to the key equation,

$$(\lambda_1^l / \lambda_p)^2 = \varepsilon_\infty + 2\varepsilon_d + 4\varepsilon_d \varepsilon_g^\chi ln[1 + \beta R/d]. \tag{2.34}$$

with characteristic values of $\chi = 0.5$ and $\beta = 0.15$ for spherical NPoMs. $\beta$ is found from the angle made from the centre of the sphere to the edge of the mode width in the gap[46]. The second order (quadrupole) antenna mode is found to have a resonance at $\lambda_2^l \sim \lambda_1^l / 1.25$ and as usual the coupling strength to far-field is proportional to $R^3$.

For the transverse mode the far-field emission pattern is similar to the dimer in that the maximal emission is orthogonal to the substrate, so along the inter-particle axis. However, the coupled mode for NPoM radiates at high angles with maximum emission at ~ 60° with a full width half maximum (FWHM) of 10°. This means that efficient excitation and collection

---

[7] L=inductance, C = capacitance, R=resistance

[8] This approach can be followed in significant depth in the original paper by F. Benz et. al. [46]

of NPoM requires a high numerical aperture (NA) objective, with $NA = n.sin(\theta_c)$, where $\theta_c$ is the collection angle from the sample. In this thesis a dark field microscope is used with $NA = 0.8$ which means that the maximum collection angle is 53°, therefore around 30% of light from a single NPoM is collected. These far-field radiation patterns can be directly interpreted in the dark field image of the NPoM. If an NPoM appears as a spot then the collected angular emission pattern is both low- and high-angle, thus both transverse and coupled mode are being excited within the visible spectrum. Conversely, if the NPoM appears as a ring, then the coupled mode is being predominantly excited. In chapter 4 this understanding of far-field emission patterns for a Au nanoparticle coupled to an optical cavity is used to show the existence of an independent high-angle mode.

To demonstrate NPoMs and use of this circuit model, consider the case of a 15 nm flake of $In_2Se_3$ in its $\alpha$ crystalline phase inside an NPoM (Fig. 2.16(b,c)) [63]. The of NPoM (Fig. 2.16(a)) is very closely replicated experimentally, with a single 100 nm nanoparticle sitting over the $In_2Se_3$, the edges of which are clearly visible in the dark field microscope setup discussed in section 3.1 (NA0.8) at 100× magnification (Fig. 2.16(b)). Using atomic force microscopy (AFM) on this flake shows that it has uniform thickness of around 15 nm (Fig. 2.16(c)). Like most van der Waals materials $In_2Se_3$ displays a highly anisotropic refractive index, but since the field for the coupled mode is predominantly orthogonal to the $In_2Se_3$/Au substrate the out-of-plane refractive index can be used. A 15 nm gap with a low refractive index would lead to a weak coupled mode, blue-shifted to the position of the transverse mode. However, the out-of-plane (vertical) refractive index $n_g$ of $In_2Se_3$-$\alpha$ is extremely high with a wavelength dependent value of $n_g \approx 3.8$ at the peak scattering of $\approx$665 nm [64]. This factor in addition to the use of large 100 nm nanoparticles, strongly red-shifts the coupled mode so that it is clearly distinguished from the transverse mode at 520 nm. Using the above equation with $\varepsilon_\infty$ corrected for nanoparticle radius and plasma wavelength $\lambda_p = 140$ nm, leads to a resonance wavelength for the bonding bright mode (coupled mode, $l = 1$) of 675 nm[9]. This is very close to the experimentally measured peak value and it will be seen that it is possible to get even closer by making a small correction to the model[10].

In addition to the brightest mode, corresponding to the coupled mode of the $In_2Se_3$ NPoM, there is an additional blue shifted mode labelled as a "hybrid" mode. These modes frequently occur in NPoM samples and are a result of nanoparticle faceting. Upon deposition onto a surface, nanoparticles preferentially bond via facets, which maximises surface interactions with the flat sample surface (in this case $In_2Se_3$). The LSPs which propagate over the flat facet couple to the antenna modes ($l = 1, 2, 3...$) of the entire system and these sets of modes

---

[9] There is some variation in reported plasma wavelengths for Au nanoparticles in the literature. The plasma wavelength is calculated from the average values of references[65–71]gathered from [25]

[10] Refer to the appendix for the values used in Eq. 2.34

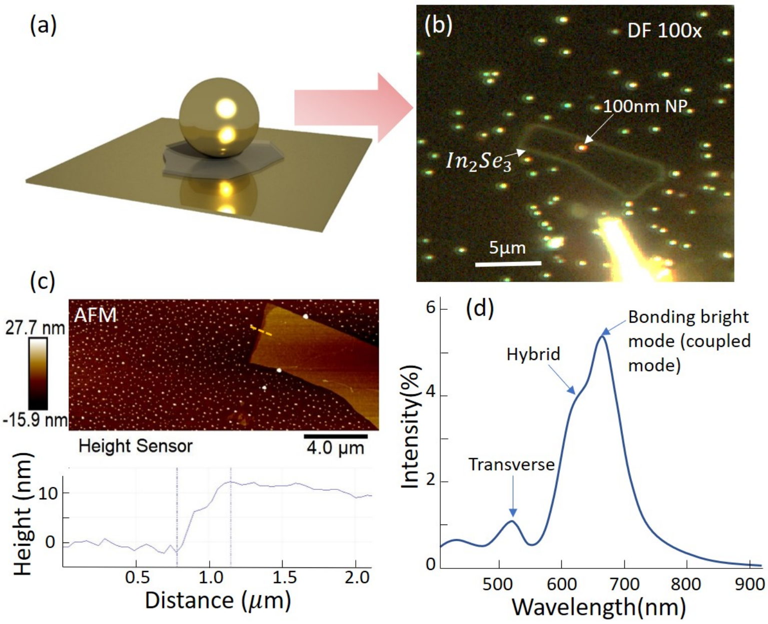

Fig. 2.16 A 3D representation of an NPoM adapted from [5] (a) and a dark field image of a 100 nm NPoMs on Au and on a $In_2Se_3$ gap spacer (b). The nanoparticle on $In_2Se_3$ (white arrow) is clearly orange in colour, compared to surrounding green NPs on Au. The height of the crystalline spacer is measured in AFM with the measurement taken along the orange dashed line(c), and compared to dark field scattering spectrum from the nanoparticle (d).

hybridise, forming polarisation dependent hybrid modes which are highly dependent on gap morphology[47, 72]. Whilst in this thesis the focus will be on the use of NPoM as a plasmonic ruler, i.e. monitoring changes in the coupled mode to determine gap distance or refractive index, these modes appear very frequently in spectra and so will be discussed in more depth below. While faceting can lead to a number of interesting physical phenomena, it complicates spectral analysis and depending on coupling strength can influence the position of the coupled mode [45, 47]. Faceting as a fraction of total particle surface area increases as a function of nanoparticle radius, and thus is particularly strong for 100 nm nanoparticles. Therefore such large particles are not commonly used for the NPoM experiments in this work despite their relative brightness. All of the work in on thin hBN in chapter 5 is completed using either 80 nm or 60 nm and in particular for 60 nm NPs, faceting plays a very weak role in NPoM behaviour.

An enormous advantage of the NPoM geometry is the very high number of NPoMs which can be deposited over large areas in a single step. This immediately establishes thousands of nanocavities encapsulating the material of interest and their density can be easily varied by changing the deposition time (see section 3.2.2). Through statistical analysis of hundreds (or thousands if automation is used) of dark field spectra, a broad dataset containing every possible variation to the NPoM system is gathered enabling rigorous testing of our models such as the one above.

In chapter 5, equation 2.34 will be used in order to calculate the $l = 1$ resonance wavelengths for NPoMs on hexagonal-Boron Nitride (hBN) of varying thickness. By taking a statistical approach it will be seen that this equation is invalid for non-molecular spacers which do not bind onto the nanoparticle surface and thus cannot displace ligands surrounding the nanoparticles. However, with a modification to the spacer properties within the circuit the model it is possible to correct for this and accurately predict resonance positions for $\lambda_1^l$ on hBN to within one standard deviation. This small modification to the model has a profound influence on the usual behaviour of the model, particularly at small gap sizes.

### LSPs on flat nanoparticle facets

As briefly discussed above, in addition to the transverse and coupled modes of NPoM other hybrid modes can appear which result from the outcoupling of modes propagating at facets. To understand this, the NPoM is broken down into the vertical dipole antenna and a metal-insulator-metal waveguide structure representing the facet-spacer-substrate.

To visualise the facet-spacer-substrate system consider the planar infinite structure seen in the section 2.4.1, Fig. 2.12, but now with a cavity length $L$ ranging from 0.5 - 10 nm. Optical far-fields in the visible range cannot be trapped in such a structure using the same approach, since the cavity length is significantly less than the incident wavelength of light. However, by substituting both encapsulating layers ($\varepsilon_1$ and $\varepsilon_2$ in Fig. 2.12) with a metal it is possible to excite plasmons on both metal surfaces and trap near-fields in the volume between the metal layers. This is an example of a metal-insulator-metal (MIM) patch-antenna structure in which two conductive metals are separated by a dielectric with permittivities $\varepsilon_m$ and $\varepsilon_g$ respectively.

The dispersion relation for a plasmon propagating along a facet in such a structure is described analytically in terms of the total wavevector $k_0^2 = k_\parallel^2 + k_\perp^2$ (i.e. parallel and perpendicular to plasmon propagation) by [73–75],

$$\left(\frac{k_\parallel}{k_0}\right)^2 = n_{eff}^2 = \varepsilon_g + 2\zeta[1 + \sqrt{1 + (\varepsilon_g - \varepsilon_m)/\zeta}], \tag{2.35}$$

with

$$\zeta = \left(\frac{k_0 d \varepsilon_m}{\varepsilon_g}\right)^{-2}. \tag{2.36}$$

This equation is equivalent to an effective dielectric permittivity $\varepsilon_{eff} = n_{eff}^2$, since the refractive index difference between the metal facet and gap dielectric dictates the propagation of the plasmon in terms of $k_0$. It is found that typical NPoM gaps ($\sim$ 10-20 nm Au facets) display high in-plane wavevectors and, since $k_0 = 2\pi/\lambda$, short effective wavelengths.

Compared to an open surface, this coupled plasmon patch-antenna system can control dissipative loss because the in-plane wavevector ($k_{||}$)) increases as gap size decreases causing a corresponding increase in $k_\perp$. The field penetration depth is

$$\sigma_\perp = \frac{1}{\Im\{k_\perp\}} = \frac{d}{2\varepsilon_g \Re\{1/\varepsilon_m\}}, \tag{2.37}$$

which means that as $k_\perp$ increases the penetration depth drops, thus the loss per unit length for MIM plasmons remains unchanged as the gap decreases[75].

The modes in this gap are discretised when the MIM junction becomes finite in scale, just as SPs become discretised into LSPs (see previous section). This is the case for example when a faceted nanoparticle is deposited onto a few-nm thick dielectric spacer such as hBN or $In_2Se_3$. Hence, the facet makes a finite MIM junction with the top metal surface area equal to the surface area of the facet. A 2D Fabry-Perot resonator model in which plasmons propagating along the facet are partially reflected at the edges leads to maxima and minima at specific positions depending on the frequency of the LSP. If the facet is assumed to be circular with a width equal to the mode width $w$, the discrete wavelengths are [8, 47],

$$\lambda_l^s = w\frac{\pi}{\alpha_l} n_{eff}(\lambda) \approx \lambda_p \sqrt{\frac{w\varepsilon_g}{d\alpha_l} + \varepsilon_\infty} \tag{2.38}$$

where $\alpha_l$ are zeroes of the Bessel function. $s$ indicates that these are facet modes and these modes are described using the notation $s_{mn}$ where the indices $m$,$n$, indicate the number of nodes in radial and azimuthal directions.

Since the required effective wavelengths are much shorter than the incident wavelength of light, on their own the coupling of these gap plasmons to free space is very poor ($\sim 10^{-4}$). However, as alluded to earlier, the antenna modes of entire NPoM structure are able to couple to these modes which dramatically increases their coupling to free-space and resultant intensity in far-field. The coupling between the sets of modes leads to anticrossing and hybrid modes denoted as $l + s_{mn} = j_n$, such as the hybrid mode highlighted in Fig. 2.16(d). Specific antenna modes ($l = 1, 2, 3...$) only couple to certain cavity modes ($s_{mn}$) depending on relative field orientation. Gap modes with odd $m$ support in-plane (horizontal) fields and are potentially visible for larger gap distances (>5 nm) since at these distances the antenna modes have a weak in-plane component. However, as gap distances decrease the field orientation in-gap due to the antenna modes becomes almost entirely vertical, thus odd cavity modes

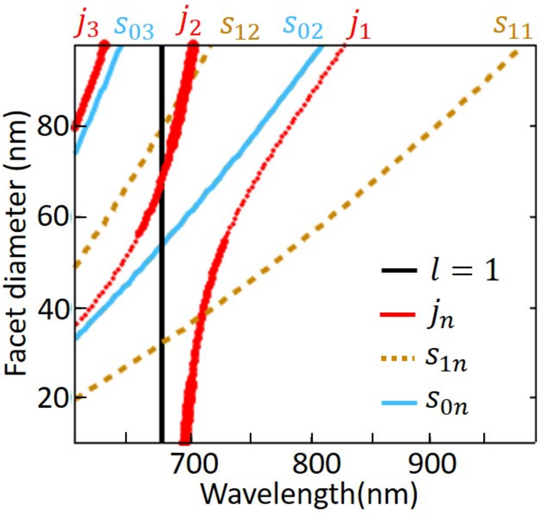

Fig. 2.17 The predicted wavelengths of dipole antenna ($l = 1$), gap ($s_{mn}$) and hybrid ($j_n$) modes with changing facet diameter for a 100 nm gold NP on 15 nm of $In_2Se_3 - \alpha$, with $n_g = 3.8$. This is calculated using NPoM v2 code, author J.J. Baumberg.

rapidly red-shift into the IR and are not efficiently outcoupled via hybridisation with the vertical antenna modes. Conversely, even $m$ gap modes support vertical fields and remain in the visible-NIR even for sub-nanometre gaps.

The expected wavelengths of these gap modes for our 15nm-thick $In_2Se_3$ flake with changing facet diameter is shown in Fig. 2.17. In addition the dipole antenna mode ($l = 1$) and hybridised antenna-gap modes ($j = 1,2,3$) are shown. From this figure it can be seen that at larger facet diameters ($\sim 20-40$ nm is reasonable for a 100 nm Au NP) the $j_2$ hybrid mode red-shifts to be $\approx 80$ nm from the $j_1$ mode. Additionally, the $s_{11}$ mode is very close in wavelength to the coupled mode above a facet diamter of 20 nm. In contrast, using the usual dipole antenna model with $\lambda_2^l = \lambda_1^l/1.25$, no modes would be visible except the dipole mode, with the quadrupolar ($l = 2$) mode at $\approx 530$ nm. Thus this model offers an explanation for why two modes appear in Fig. 2.16(d) [11].

In this case (Fig. 2.17 compared to Fig. 2.16(d)) the mode positions for $j_1, j_2$ do not appear to correspond precisely to the experimentally measured positions. This is because the modes depend sensitively on the nanoparticle morphology. For example, the coupling between antenna and gap modes depends very strongly on the morphology of the facet edges and a sharp facet edge will couple differently to a smooth edge [47]. This means that while the facet model discussed here is useful to explain the presence of extra modes in addition to the coupled mode, it is often hard to directly attribute or match resonance wavelengths with experiments. In part due to this difficulty, calculations in chapter 5 for hBN focus on the

---

[11] Calculated using NPoM v2 Igor code, author J.J. Baumberg

position of the antenna modes. Other modes are sometimes present in the datasets for those experiments, however their positions are found to vary significantly between nanoparticle due to this very subtle morphological dependence. It is found in chapter 5 that positions of the observed antenna modes can be well matched using a modified Eq. 2.34 and that the red-shift due to hybridisation (e.g. for $l = 1$ to $j_1$) is not a clear requirement for experiments with hBN.

### 2.4.3 The Thinnest Possible Dielectric Material: hBN

hBN is a type of van der Waals (vdW) material, meaning that it is a crystal comprised of stacked atomic layers held together by weak vdW forces. These weak inter-layer forces allow them to be separated using mechanical processes while keeping the individual layers intact [9].

Despite previous knowledge of their existence, it wasn't until the discovery of graphene in 2003 that the true potential of vdW materials became clear [76]. Novoselov and Geim's Nobel prize winning isolation of a single atomic layer of carbon from graphite using simple scotch tape [12], led to an explosion in research on these incredible materials. vdW materials revealed a whole new world for nanotechnology, a world in which two-dimensional quantum mechanical phenomena were easily accessible for experimentation.

Monolayer graphite was actually first produced in 1994, followed rapidly by hexagonal-Boron Nitride (hBN) the year after, however both of these samples were adsorbed to metallic surfaces. It's perhaps unsurprising then that following the isolation of graphene using the scotch tape method, it was quickly found that the same could be done with hBN[77].

While hBN does display it's own interesting optical properties (e.g. NIR-IR hyperbolicity [78]), within the context of this thesis it is most notable for its inertness. Indeed, the 1995 monolayer hBN paper highlights the fact that hBN retains it's electronic properties despite its adsorption to a range of metallic substrates [79]. Graphene on the other hand loses the vast majority of it's electronic properties when in contact which these substrates. In this thesis I take advantage of this inertness in order to study the baseline models for the NPoM and NPoMC.

#### General properties

Depending on what you read, hBN is defined as either a dielectric or as a wide band-gap semiconductor, with a band-gap of 5.9eV [80]. The highest energy samples are exposed to in this thesis is 3.1eV, so here hBN is treated as a dielectric. Its crystal structure including

---

[12] discovered at the university of Manchester, my previous university.

Fig. 2.18 The crystal structure of hBN is identical to graphite, but with carbon atoms replaced by boron (blue spheres) and nitrogen (red spheres). Individual layers can be easily separated via mechanical means such as the scotch tape method due to weak interlayer forces. Adapted Materials World magazine, "Why Boron Nitride Could Be the New Carbon", copyright Institute of Materials, London, UK.

it's interlayer spacing is identical to graphite, but with alternating boron and nitrogen atoms in place of carbon[81]. Due to higher impurity concentrations which weaken the intra-layer structure, hBN cannot be exfoliated down to its monolayer form as successfully as graphene. Monolayer hBN samples of greater than $20\mu m^2$ are extremely rare even with the highest quality materials, whilst exfoliated graphene samples of $>100\mu m^2$ are regularly achievable. To make NPoMC's, I use exfoliated hBN many 100s of monolayers in thickness, yielding significantly larger area samples. The crystals used in chapter 4 are also far from normal, as they are produced in Japan by K.Watanabe and T.Taniguchi, who are able to produce samples which are vastly superior in quality to any other hBN crystal in the world. The majority of groundbreaking experiments using exfoliated hBN also use crystals produced by this Japanese group. In my experiments on mono- and few-layer hBN, I avoid exfoliation completely and V. Babenko uses chemical vapour deposition (see next chapter) to produce samples of many milimetres in area.

### Optical properties

Due to its crystal symmetry, bulk hBN is birefringent. Perpendicular to the plane formed by each atomic layer, the real component of the refractive index is $n_z$=2.13 and parallel to the plane it drops to $n_{xy}$=1.65 [82]. It has been suggested that the refractive index of hBN may have a slight dependence on wavelength within the range 600 nm-650 nm, but the maximum possible decrease of <5% in $n_z$ has a negligible impact on the work presented in this thesis [83]. The imaginary component of the refractive index, which is responsible for the absorption of light by the crystal, is close to zero within the wavelength ranges used in this thesis. For this reason hBN less than 10 layers thick is extremely challenging to resolve using an optical microscope, meaning many researchers resort to using specially designed high-contrast substrates, dark-field, or scanning electron microscopy (SEM) to find hBN samples.

# Chapter 3

# Experimental Methods

In this chapter I will introduce the experimental methods used throughout the results chapters of this thesis. I will first introduce the experimental setup used for collecting optical measurements, before detailing the fabrication methods used and developed.

## 3.1 Dark-Field Scattering Microscopy

The microscope used for single particle dark-field spectroscopy is a modified Olympus BX-51 upright microscope which illuminates the sample in a reflective Köhler configuration. In bright field, incident and reflected light travel along the same paths through the centre of an high numerical aperture (NA) objective [1].

Referring to the lower left of Fig. 3.1 and looking at the path from the halogen lamp to the source from left to right, light is at first focussed toward an aperture stop (AS). At the aperture stop the black arrow indicates the direction of the conjugate image of the source (halogen lamp). Closing the iris at the aperture stop enables selective blocking of light in the k-space [2] of the sample plane which gives control over the range of incident angles reaching the sample. For experiments in this work the maximum range of incident angles is usually required, so this often remains untouched. A second iris is placed at the focal stop (FS) which controls illumination of the sample, i.e. increasing iris diameter increases the area of illumination and vice versa. This aperture lies in a field plane which is conjugate to the sample plane, thus if light is focussed onto the aperture edges it is automatically focussed onto the sample. A third lens is then used to focus the light onto the back focal plane of the objective via a 50:50 beam splitter (BS1). Additional optics (e.g. polarising filters) can be placed between this third lens and the beam-splitter in order to modify the light reaching the

---

[1] Olympus LMPLFLN-BD, 100x, NA=0.8

[2] Every point in the plane represents the direction of propagating rays

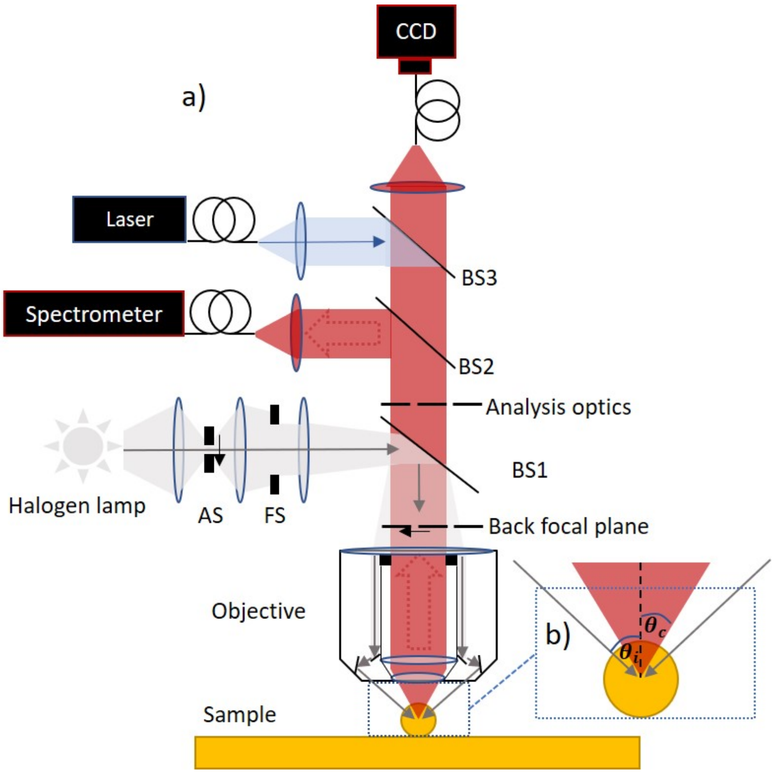

Fig. 3.1 The dark field spectroscopy configuration for experiments shown in this thesis. Arrows indicate whether light is travelling toward (grey, blue) or away from (red dashed) the sample.

sample. The light arriving at the sample is fully defocussed to achieve uniform illumination. Upon switching to dark field from bright field imaging mode, the majority of incident light is prevented from travelling down the centre of the objective allowing only the outermost fraction of light to enter into the objective (bottom Fig. 3.1(a)). A series of mirrors inside the objective then direct this outermost component of the incident light such that it leaves the objective at high angle ($\sim 56^o - 58^o$) while scattered light is collected for approximately all remaining angles ($\sim 0^o - 56^o$).

Upon scattering from an object on the sample (Au nanoparticle in Fig. 3.1), light returns back through the objective such that a k-space image of the sample can be viewed at the back focal plane of the objective. From the objective to spectrometer or CCD light rays propagate parallel to one another. This light is redirected to the spectrometer via a 50:50 beam splitter (BS2) and coupling into a multimode optical fibre. The beam splitters for coupling into the spectrometer or laser (BS2, BS3) can be removed and replaced in order to increase in-coupling of light to the CCD and improve imaging. Additional analysis optics can be inserted into the beam path in order to examine specific properties of the light from the sample.

### 3.1.1 Taking Optical Measurements

The numerical aperture of the objective is calculated using $NA = nsin(\theta)$, where $n$ is the refractive index of the surrounding medium and $\theta$ is the angle of the ray from the centre of the objective (Fig.3.1(b)). The NA for the objective used this this experiment is 0.8, leading to a maximum illumination and collection angle in bright field of $53^o$. In dark field, the maximum illumination angle is increased by $\sim 10\%$ meaning that the maximum illumination angle is $\sim 58^o$. For dark field illumination $\theta_i$ ranges from $56^o - 58^o$ and $\theta_c = 53^o$ (Fig.3.1(b)). This difference ensures that no reflected light is collected from the sample and only scattering objects (e.g. nanoparticles) are observed.

The spectral range of the entire system including spectrometer [3] extends from a wavelength of 400 nm to 1000 nm, although beyond $\sim$ 850 nm the collected signal weakens considerably due to a drop in detection efficiency for Si based detectors. This restriction at longer wavelengths is due to a combination of factors including the low intensity of the halogen source in NIR and the combined inefficiency of the optics and the spectrometer itself beyond this wavelength.

Due to differences in angular emission patterns for different modes in NPoM (see section 2.4.2), collection from the sample depends slightly on focal position. This makes sense by considering the transverse and dipole antenna modes, as seen in Fig. 2.16(d) at 520 nm and ~650 nm respectively. As previously discussed, the transverse mode scatters uniformly from the nanoparticle whereas the dipole antenna mode scatters light at high angles only (>$55^o$). This means collection of light from the transverse mode is independent of objective position within the focal range of the objective. In contrast, collection of high-angle light changes with position of the objective as the fraction high-angle emission from the dipole mode changes. Collection from the coupled mode can be enhanced by moving $\sim 1\mu m$ closer to the sample and therefore collecting more of the high-angle light.

Before collection of dark field scattering spectra from a sample, the contribution to scattering from the defocussed halogen source is referenced out and the background is subtracted. Since all of the setup shown in Fig. 3.1 excluding the sample is enclosed and all measurements are taken after minimising extraneous light, the background is due almost solely to shot-noise in the spectrometer's detector. Referencing is done in order to isolate the contribution of plasmonic scattering from other sample scattering by showing it as a fraction of the total scattered light arriving at the spectrometer. The referencing is done by focussing the light onto a uniform white-light scatterer, giving the full scattered spectrum of the light source. This 'perfect scatterer', leads to a reading in the spectrometer which represents the

---

[3] OceanOptics QE65000 operated at -20C

maximum possible count at each wavelength for a particular halogen source in this setup. Then the equation in order to arrive at a final dark-field spectrum is,

$$Scattering(\%) = \left( \frac{C_{sample} - C_{back}}{C_{ref} - C_{back}} \right) \times 100, \tag{3.1}$$

where $C_{sample}$ is the total, $C_{back}$ background and $C_{ref}$ the scattering spectrum of the light source. These are detected as number of counts as a function of wavelength received at the spectrometer. Thus, a scattering value of $1\%$ at a given wavelength can be interpreted as the nanoparticle scattering $1\%$ of the maximum possible amount of light at that wavelength. In other words, its efficiency at scattering light is $1\%$. All of the dark-field results shown in this thesis use this referencing technique. A new background and reference measurement must be taken before every set of measurements to take into account changes in the spectrometer temperature (increasing shot-noise), lamp degradation (changing the reference spectrum) and extraneous light.

## 3.2 Fabrication

### 3.2.1 Chemical Vapour Deposition and Transfer of Monolayer hBN

In this thesis I take advantage of significant advances in the growth on iron (Fe) and subsequent transfer of monolayer hexagonal boron nitride, achieved by Dr. Vitaliy Babenko (V.B.) of the University of Cambridge. The improvement in growth compared to other hBN on Fe samples is able to increase monolayer domain areas to $\sim 1\text{mm}^2$ and significantly decrease multilayer regions as a fraction of total hBN area. Even more importantly, the novel transfer process is clean and results in monolayer samples which adhere very closely to the Au substrate surface beneath after transfer.

Chemical vapour deposition is the growth of a thin (<10 nm) layer of solid material onto a catalytic substrate via the chemical reaction of vapour-phase precursors [84]. Reactions occur both while in the gas-phase and also at the substrate surface and can be promoted or initiated by heat, as is the case here. CVD processes are complex and involve a number of different, but interrelated steps leading to growth. In general however, CVD involves the injection of reactant gases into a heated chamber leading to partly pyrolised (decomposed at high $T$) reactants a few-nm from the substrate. Closer to the substrate a stagnant boundary layer forms within which reactions with the substrate and deposition occur. By varying the pressure, temperature, and chemical mixture in the CVD chamber the composition and concentration of the layers can be changed and consequently the deposition material quality

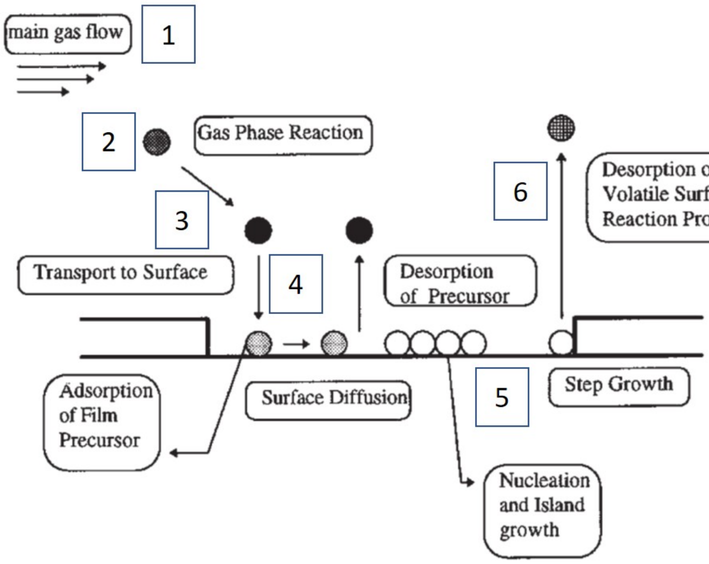

Fig. 3.2 Description of the CVD method and the general processes resulting in deposition of the solid layer. Modified from [6]

or rate changed. The general steps to achieve this are summarised in Fig. 3.2 and described as [84, 6] :

1. Evaporation and transport of reagents (i.e. precursors) in the bulk gas flow region into the reactor
2. Gas-phase reactions of precursors in the reaction zone to produce reactive intermediates and gaseous by-products
3. Mass transport of reactants to the substrate surface
4. Adsorption of reactants to the substrate surface
5. Surface diffusion to growth sites, nucleation and surface chemical reactions leading to film growth
6. Desorption and mass transport of remaining decompsed material away from the reaction zone

For the samples shown here, Fe foils of 0.1mm in thickness and 99.8% purity are cleaned in acetone and IPA and oxidised at 350°C for 5 minutes until the foil surface changes to brown in colour due to oxidation. The foil is then loaded into a custom cold-wall CVD system with a SiC-coated ($\sim 40\mu$ m) graphite heater. The use of uncoated graphite heaters

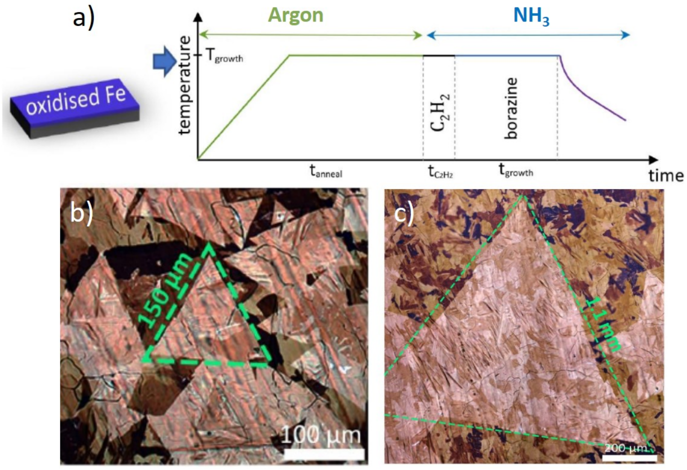

Fig. 3.3 Overview of the growth methodology for CVD hBN on *Fe* foil (a) and resultant monolayer hBN samples at $980^oC$ for 10 minutes and $950^oC$ for 4.5 hours at borazine flow rates of $0.08sccm$ and $0.01sccm$ respectively. Modified with permission from V.B.

leads to contamination of the sample with carbon, which must be prevented. The system is then pumped down to $\sim 1 \times 10^{-5}$ mbar and filled with Ar at $1 \times 10^{-2}$ mbar partial pressure. Ar is used to adjust the pressure in the chamber and because it is inert additional unwanted reactions are avoided. The temperature is then ramped up to $980^oC$ ($T_{growth}$) at $50^o$ C/min, followed by annealing in the Ar atmosphere for 20 minutes ($t_{anneal}$). After 20 minutes, the flow of Ar is stopped and the growth stage begun by introducing a flow of $NH_3$ to the chamber in addition to acetylene ($C_2H_2$) at a partial pressure of $3 \times 10^{-3}$ mbar for 5 minutes ($t_{C2H2}$). This step carburises the surface of the Fe foil, which controls seed concentration and nucleation for the next stage of growth. $NH_3$ was found to specifically reduce hBN damage from oxidative gas impurities (compared to Ar) and to mitigate excessive Fe evaporation. The flow of acetylene is then stopped and borazine introduced as the hBN precursor for 5 minutes ($t_{growth}$). Flow of the precursor is controlled with a mass flow controller connected between the borazine bottle and the chamber at a flow rate $0.08sccm$. The borazine is introduced in order to nucleate and grow hBN from the carbon seeds leading to step growth (step 5 Fig. 3.2.). After the growth stage, the sample is rapidly cooled (initial cooling rate of 200°C/min). It is found that the presence of oxygen and carbon in the bulk Fe suppresses multilayer growth leading to monolayer only growth and suppressed nucleation density.

Transfer of hBN (and all other layered materials) from good catalytic growth substrates such as Fe is a significant challenge due to a very strong interlayer interaction [85]. The usual transfer procedure is the full wet-etching of the substrate, with a polycarbonate layer over the hBN which leads to significant contamination of the final sample. The source of the

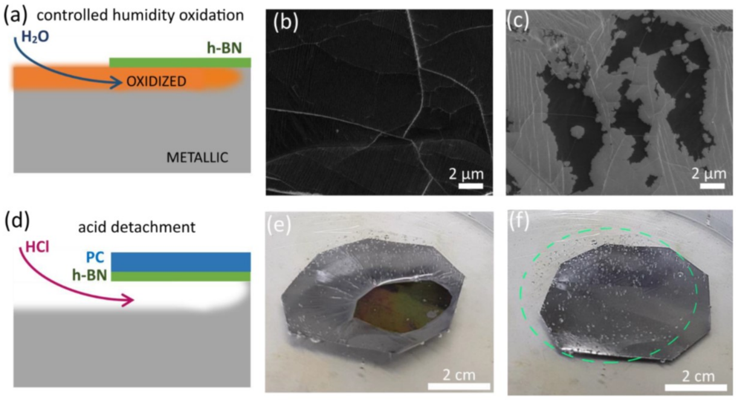

Fig. 3.4 Steps directly before cleaning and transfer to a Au substrate. Initially, the sample is oxidised further by being placed in a humidity chamber (a). The increased level of oxidation can clearly be seen with an InLens detector as a colour change from black to grey (b,c). The sample is then spincoated with PC at $1000 rpm$. The, the sample is placed in an HCl bath (d) and over a period of time de-adhesion from the bulk $Fe$ is clearly observed (e). Finally, afer full desorption the bulk $Fe$ sinks to the bottom of the $HCl$ bath (f) and the PC/hBN is ready to removed for cleaning and transfer to Au substrate. Used with permission of V.B.

contamination is not only from the etchant, but also from any impurities in the foil [4][86, 87]. This extra contamination from the substrate is often ignored in the literature, but plays a significant role even in high purity foils. Other transfer techniques include bubbling transfer [87] and dry peeling [88], but these usually lead to macroscopic damage and tearing. Such large scale damage must be minimised for NPoM measurements on monolayer hBN.

Instead of these techniques V.B. uses a high humidity environment in order to penetrate into the oxidised region and weaken the interaction with hBN Fig. 3.4(a). When placed into a heated humidity chamber the continued propagation of the oxide layer is enabled by the intercalation of $H_2O$ and a clear colour change is observed Fig. 3.4(b-c). The sample can then be spin-coated in polycarbonate at 1000 rpm (PC) and etched by floating on an HCl bath, which removes only the oxidised layer directly beneath the hBN. After some time the Fe substrate detaches from the hBN and sinks to the bottom of the bath. This significantly reduces the contamination from the etchant and foil impurities. The PC/hBN can is then transferred to three sequential deionised water baths picked up with a Au, or any other choice of substrate. The sample is then placed in a chloroform bath overnight to remove the PC and then heated to 350°C in an oven for 30 minutes. This burns off remaining PC and any liquid residue beneath the hBN, bringing it into contact with the substrate beneath via capillary forces. To decrease the hBN-Au separation even further, the sample is $O_2$ plasma etched for

---

[4] This author attempted etching of Fe in the usual manner and a clearly visible brown layer of porous carbon was left on the hBN surface

15 seconds at 30W, further removing contaminants. This $O_2$ etching step is shown not to damage the hBN.

Resultant Raman spectra and further analysis on samples transferred to 300 nm $SiO_2/Si$ substrates using this method is shown in chapter 5. To summarize, characteristic hBN peaks have linewidths for this CVD hBN comparable with the highest quality exfoliated hBN monolayer samples [89].

### 3.2.2 Nanoparticle Growth and Deposition

It will be seen in chapter 5 that knowledge of growth mechanisms and resultant nanoparticle properties is useful when working with 2D materials in NPoMs in particular. In this work 80 nm and 60 nm citrate capped nanoparticles (BBI solutions) are used with their exact production method a well-guarded secret, but the necessary framework behind the methodology is described here. In the appendix the behaviour of BBI nanoparticles in NPoM is compared to nanoparticles prepared using the method described here, with no significant difference observed except a fractional increase in variance of the dipole antenna mode wavelength due to the improved uniformity of the BBI nanoparticles.

Au nanoparticles can be grown via a few different methods[90, 91], but the most common method is via the reduction of $HAuCl_4$ with sodium citrate[92]. This results in nanoparticles which are citrate capped, meaning that they are surrounded by an electric double layer of citrate molecules (Fig. 5.3). This electric double layer leads to mutual repulsion between individual nanoparticles, preventing their aggregation in solution.

The first step for nanoparticle production is the synthesis of seeds, pioneered by Frens and Turkevich [93, 94]. These seeds are small ($\sim$ 10 nm) particles of Au which form the basis for construction of larger particles. To produce much larger ($>$ 50 nm) particles the aim is to reconstructions of these smaller nanoparticles in a controlled manner up to a well defined diameter and then stop the construction at the desired stage. In reference [92], a solution of 2.2mM of sodium citrate is added to 150mL of milli-Q (MQ) water and heated with vigorous stirring up to boiling point. After boiling commences 1mL of $HAuCl_4$ (25mM) is injected, which triggers the reduction process. The reaction is self-limiting and results in $\sim$ 10 nm particles at a density of $\sim 3 \times 10^{12}$ NPs/mL which are passivated with negatively charged citrate ions and suspended in $H_20$. The solution changes colour due to the presence of the Au seed particles, resulting in a modern day ‘ruby fluid’ (see chapter 2).

Once seeds are formed, the solution is immediately cooled to 90°C and a further 1mL of $HAuCl_4$ is injected. This new reaction stops after 30 minutes and is repeated twice. The reaction is then diluted by extracting 55mL of sample and adding 53 mL of MQ water with 2 mL of sodium citrate. This solution is then used as a new seed solution and the

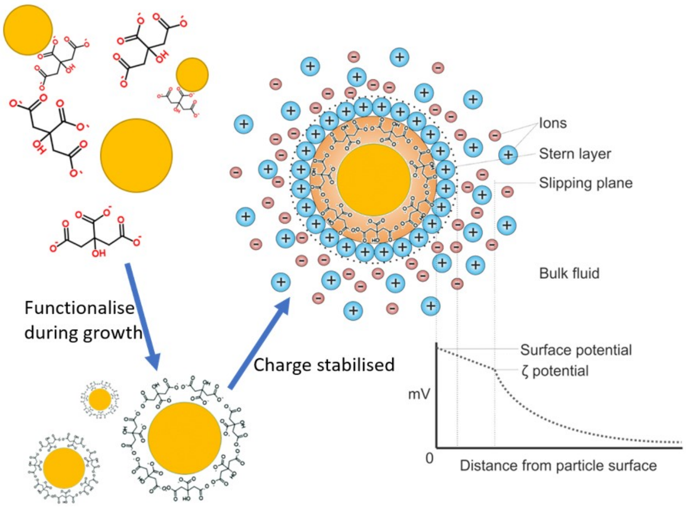

Fig. 3.5 A very basic outline of the passivation process during Au nanoparticle production with a description of how the field potential decays away from the nanoparticle with distance. Smaller nanoparticles represent nanoparticles of the same diameter but further away (into the page). This image is adapted from [7].

process repeated again until the desired size is achieved. To produce $\sim$ 60 nm nanoparticles takes 7 repeats and $\sim$ 80 nm nanoparticles require 9 repeats. With each step, at a high enough concentration passivating ligands surround the newly formed nanoparticle preventing continuation of the reaction. It is the presence of these ligands which is important to consider in analysing NPoM spectra in later chapters.

As a final note the faceting of a nanoparticle, which influences dark field spectra from individual NPoM in a number of ways (see chapter 2), is ultimately dictated by the production process. This has been studied at length in many papers [95–98] and there are a number of ways to reduce faceting which often involves etching in solution [99]. Highly spherical nanoparticles have been produced which would reduce variation in the dipole antenna mode for our samples, however this was attempted by my group in the past and it was seen that the facet reforms on contact.

The salt (NaCl) deposition method used in this thesis equilibrates charges surrounding the nanoparticles, causing them to crash out of solution over a period of seconds. It is prepared by adding 1mg of high-purity NaCl to 1mL of citrate capped BBI nanoparticles (1:1 ratio, salt:water). 200$\mu$L of this mixture is then added to a glass container and then shaken for 2 seconds followed by immediate pipetting of 50$\mu$L of the solution onto the Au substrate for 10s. After 10s the sample is rinsed with DI-water and blow-dried with a nitrogen gun. On average, this achieves nanoparticle densities of approximately 1 nanoparticle per 5$\mu$m$^2$ on the gold substrate. The key advantage to the process is that it leads to nanoparticle densities which are independent of the substrate adhesion. VdW materials for example, display very weak interactions with the substrate and therefore require 24 hour deposition times during which various other contaminants also adhere to the substrate. In the appendix different deposition methods are compared and contrasted, for example by changing the salt type and with no salt used. It is found that the position of the coupled mode wavelengths is largely independent of deposition technique.

### 3.2.3 The Template Exfoliation Method

It will be seen in chapter 5 that one of the significant issues with the transfer of layered materials onto Au is something that will be referred to as the 'bedsheet effect'. This refers to the tendency of a thin layered material to fluctuate in height above the surface of a flat substrate underneath. An image of this effect is shown in chapter 5. The influence of this can be significant for thin spacers in NPoM due to sub-nanometre sensitivity of the technique. Additionally, the adhesion of hBN (and many other layered materials e.g. transitional metal dichalcogenides) onto the surface of Au is extremely poor using the usual transfer methods making thin samples extremely time-consuming to fabricate.

To overcome these problems I have developed a new [5] template-exfoliation technique (Fig. 3.1.) which uses the ideas behind template stripping. Firstly, a Si wafer is bathed in acetone followed by sonication in IPA for 1 minute and hBN is then exfoliated onto the Si using the usual scotch tape method. 100 nm of Au (purity 99.9%) is then thermally evaporated directly onto the hBN/Si at a rate of 0.1 nm/s, which minimises the hBN-Au substrate separation and enhances adhesion. A small amount of epoxy is then applied, to which a second Si substrate is adhered. When using a razor blade to separate the attached substrates, Au preferentially detaches from the Si rather than epoxy, exfoliating the hBN crystals in the process and leaving them embedded in the Au/epoxy substrate surface. If the sample is monolayer, the single layer sticks to the evaporated Au surface and is 'embedded'[6]. This highly robust and versatile transfer method is applicable to a wide range of layered materials with low adhesion to unreactive metals. By tuning the thickness of evaporated Au, it is possible to change the amount of epoxy in contact with the edges of the layered crystal, thus influencing the exfoliated thickness. This method is particularly useful for situations in which minimising the metal/layered material separation is of prime importance, such as in plasmonics. This method is applicable to any 2D material, but is applied in this thesis to the transfer of exfoliated (chapter 4) and CVD grown hBN (chapter 5).

---

[5] To this authors knowledge this technique has not been published elsewhere

[6] Although it is difficult to visualise an embedded monolayer!

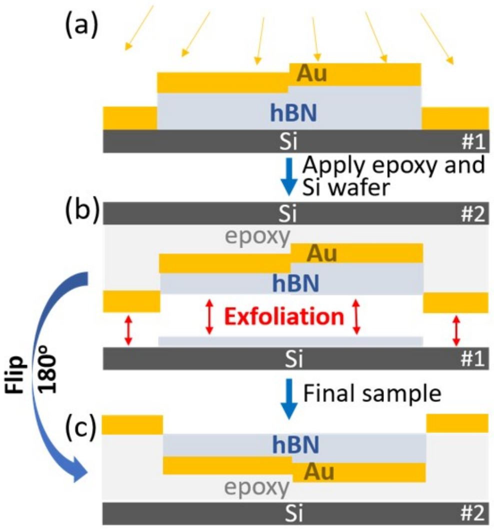

Fig. 3.6 Evaporation-exfoliation fabrication technique with (a) exfoliation of hBN crystal onto Si wafer followed by thermal evaporation of high-purity Au, (b) epoxying of second Si substrate onto Au/hBN/Si and subsequent template stripping from the surface, leading to (c) exfoliation and embedding of hBN crystals with atomically sharp Au steps beneath.

For monolayer samples confirmation of successful transfer is simple. All measurements on the hBN to establish quality, including Raman, are done while it lies on Si as usual. If after template exfoliation there is no longer any Raman signal from monolayer hBN on the discarded Si, then the transfer is successful. One limitation to this technique is that it is not as controllable as stacking of CVD monolayers to form few-layer samples. If used on a trilayer sample, for example, the method has a chance of separating all the stacked layers and undoing all of the hard work. It is also not well known how the evaporated Au assembles itself on the layered material, which may roughen the Au/hBN interface. No measurable influence of this was detected in the experiments presented in this thesis, but this may be due to the screening influence of adsorbants as shown later in chapter 5.

### 3.2.4 Transfer of exfoliated layered materials

In chapter 5 of this thesis there is a study of NPoM with exfoliated hBN crystals. The following method was used in order to produce this type of sample.

The starting point of transfer techniques for layered materials is the very simple and well known scotch tape method, involving the random exfoliation of thin crystals from the bulk crystal using some form of adhesive tape. Once an appreciable amount of the bulk crystal has come away and adhered to the tape, it can be folded over multiple times in order to exfoliate the crystals further. Additional exfoliations make individual pieces of crystal simultaneously thinner and smaller in surface area. In general the flakes need to be made as thin and with as large a surface area as possible, so the balance set by the number of exfoliations needs to be right for every 2D crystal since they each cleave differently. Even different batches of the same type of bulk crystal can behave differently, so it's important to be consistent with the supplier. With a region of tape covered in exfoliated few-nm thick crystals, a substrate is then stuck once onto that region leaving a number of exfoliated flakes behind on the substrate surface. The exfoliated flakes stick to the substrate because the electrostatic attraction between the top layers of the crystal and the substrate is greater than the van der Waals interaction between the layers at the cleavage thickness. The ubiquitous substrate used for transfer is Si/$\mathrm{SiO_2}$, and for this reason experts in transfer techniques have usually tailored their method specifically these substrates.

Likely in part due to the innate randomness of the technique, there appears to be a 'dark magic' which goes into transfer techniques for exfoliated 2D materials and frequently when experts are asked for the reasons why their specific transfer methodology works, they are unsure of the complete answer. As an example, the $O_2$ plasma etching of a $SiO_2$ transfer substrate is well known to charge the surface, aiding significantly in the transfer of thin and large area graphene flakes. Conversely, the same technique has no effect for the transfer of hBN flakes. In addition, both the cleaning process for the substrate and ambient conditions have a significant influence on transfer success while also varying depending on the specific layered material being used.

It was found early on in this project that the exfoliation of hBN onto Au using the usual scotch tape method has an extremely low probability of producing thin flakes. Additionally, the bright field contrast of thin hBN is very low on Au making identification of these layers exceedingly challenging and time consuming. For NPoMs, hBN flakes of area exceeding $10\mu\mathrm{m}^2$ within the thickness range <10 nm are required. This is because plasmonic coupling is only a significant factor below 10 nm, and multiple individual nanoparticles on any given thickness are required to demonstrate reproducibility.

To get around this problem the following method developed by David Purdie [100], a colleague at the Cambridge Graphene Centre, was adopted in order to produce few-nm flakes with large (10s $\mu m$) surface area. This process is partially described by Fig. 3.7, and can be summarised by the following steps:

1. A $1 \times 1cm^2$ $Si/SiO_2$ substrate was placed into in acetone bath for 2 minutes and subsequently sonicated in IPA for 5 mins.
2. The bulk hBN crystal was exfoliated using scotch tape as usual and transferred onto the substrate.

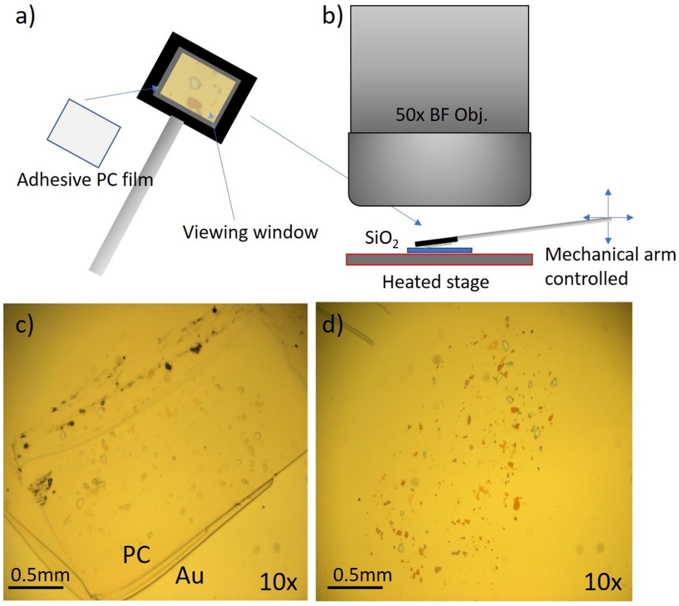

Fig. 3.7 The transfer technique for deposition of few-nm flakes of hBN onto flat Au. An approximately $5 \times 5mm^2$ piece of polycarbonate is placed over a hole attached to a thin metal rod (a) forming an adhesive transparent viewing window. This is placed under a 50× microscope objective (b) and a mechanical arm used to remove a region of exfoliated hBN flakes from $Si/SiO_2$, specified by the user and assisted by heating via a stage beneath the sample. The polycarbonate viewing window is then partially melted using the stage onto the prepared Au substrate leading to (c). The polycarbonate is then removed by placing in a bath of chloroform for 24 hours leading to (d).

3. The $SiO_2$ thickness on the substrate was 130 nm which, due to interference effects, provides the maximal bright field contrast for hBN.
4. An approximately $5 \times 5mm^2$ piece of polycarbonate (PC) is cut using a scalpel from the bottom of an adhesive sample box.
5. This square of PC is placed over a hole attached to a metal rod as depicted in Fig. 3.7(a). This PC acts both as a viewing window and an adhesive layer.
6. This rod is attached to a mechanical arm, enabling the positioning of the rod with micrometre precision beween the microscope objective and the sample (Fig. 3.7(b)).
7. The silicon substrate with hBN flakes is placed onto a heated microscope stage. Using a bright field microscope at 50× magnification the substrate is scanned and thin flakes are identified by eye.
8. Using the mechanical arm, the PC viewing window is positioned above the target thin flakes and lowered at an angle until contact is made with the flakes.
9. The temperature of the heated stage is increased to $80^oC$ which reduces the adhesive properties of the PC, increasing the chance of successful removal. The mechanical arm is gradually raised in micrometre increments until the entire region of PC removes the hBN from the Si. If the arm is raised by $\sim 5\mu m$ and the PC does not detach from the substrate, the temperature can be raised further until this is achieved.
10. A cleaned Au substrate replaces the Si/SiO2 substrate and the PC piece is now lowered in the same way onto the Au substrate surface
11. The temperature is now raised to around $130^oC$ such that the PC viewing window partially melts and is detached from the rod leaving hBN flakes with a few um thick layer of PC above (Fig. 3.7(c)).
12. The substrate is then placed in a bath of chloroform overnight in order to remove the PC
13. The sample can be checked using AFM/SEM in order to determine whether the cleaning has been successful and further cleaning completed if not (Fig. 3.7(d)).

## 3.3 Final Comments

Although not clearly evident in its relative length, a significant proportion of the time spent during my studies was spent looking for and developing the methods described in this chapter. The relatively simple steps described belie what is actually a subtle and complex problem, the production of clean and understandable samples of two-dimensional materials.

My hope is that this chapter has provided the reader with a good enough understanding of both the measurement and fabrication techniques required in order to conduct the experiments presented in this thesis. This understanding was vital in my analysis of both NPoMC and NPoM structures with hBN, in which sub-nanometre morphological changes and refractive index fluctuations strongly impact final results.

# Chapter 4

# Localised Nanoresonator Mode in hBN Plasmonic sub-Microcavities

## 4.1 Introduction

Many vdW heterostructure devices use hBN layers as an ideal dielectric substrate [101–104, 81] or dividing layer [105]. It is used due to its flatness and closely related crystallographic structure to other vdW materials (see section 3.2.4). It has been used for graphene heterostructures leading to vastly improved carrier mobilities [100] and has been shown to be a good barrier for tunnel heterostructures using vdW materials[106, 103]. When it is combined with transition metal dichalcogenides (TMDs) the resulting heterostructures show fascinating properties such as interlayer electron-phonon coupling[101] and tuneable strong interlayer exciton coupling [102]. Monolayer to bulk hBN has been found to exhibit quantum emission within the visible region at room temperature [107]. The use of hBN in such heterostructures can enable strong light-matter coupling in materials [108, 105], although so far this has only been achieved at low temperatures (e.g. 4.2K). The enormous potential for ultralow energy optical switching motivate exploring resonator enhancements in coupling to other 2D materials such as TMDs [35, 81, 105, 108–110]. As has been discussed, utilising plasmonic metals introduces rich nano-optics [9, 36, 46, 8, 47, 72, 5, 111–118] and there have been a number of high profile publications studying the combination of optical cavities with plasmonics, hence the study here of an Au/hBN microcavity system [1].

In this chapter it will be seen that despite its simplicity and in clear contrast to results from related structures [120–123], plasmonic scattering processes from Au nanoparticles on sub-micron thick hBN crystals are non-trivial, resulting in two distinct possible sets

---

[1] There is a thorough review of microcavity plasmonics available in reference [119]

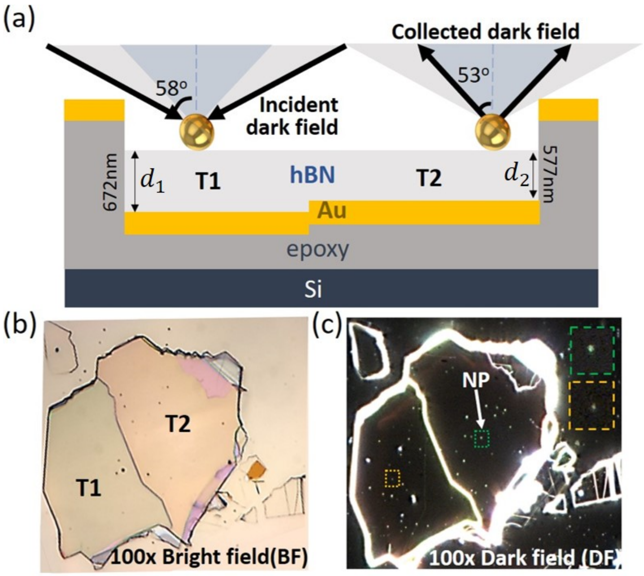

Fig. 4.1 Embedded hBN sample $60\mu m$ wide, with two crystal terraces (T1,T2). (a) Cross-section after nanoparticle deposition, showing in-/out-coupling angles for illumination with a 0.8NA objective. (b) Bright-field and (c) dark-field images at 100x magnification showing individual nanoparticles on each terrace.

of nanocavity-nanoparticle modes depending on polarisation and incidence angle. I have uncovered a new mode which, rather than resulting from coupling of Fabry-Perot modes with localised plasmon resonances [120, 121], requires angled TM illumination and operates via a different mechanism, related to the a surface mode called the Brewster mode [124]. The new mode is likely difficult to observe at greater thicknesses ($> 1\mu$m) because as the number of modes within a given wavelength range increases, brighter Fabry-Perot modes would screen out other modes. However, for sub-micron thickness hBN this mode is clearly identifiable and can be stronger than previously identified plasmon-coupled Fabry-Perot modes. The mode is characterised by a nanoscale-confined field which propagates beneath the nanoparticle. It is of highest intensity within a few nanometres from the particle, with field vector into the plane of the hBN, an unusual trait for microcavities [40].

## 4.2 Imaging of hBN microcavities

Planar microcavities of monolayer thickness uniformity employing high-quality hBN crystals embedded into gold, are formed by using the template-exfoliation method with a Au evaporation rate of 0.1Å/s as described in section 3.2.3. Each atomically-flat terrace corresponds to a micro- or nanocavity of different thickness with simple fabrication giving hundreds of these planar cavities distributed over cm-scale areas (Fig. 4.2). The colours of each embedded hBN crystal change with Fabry-Perot mode wavelength for bright-field light reflected back to the CCD. Crystals which appear brown-grey in Fig. 4.2 are those with thickness $< 80$ nm for which interfacial absorption dominates, meanwhile coloured crystals have thicknesses between $\sim 80$ nm and 1000 nm (Fig. 4.2(a,b)). Monodisperse and highly-spherical colloidal Au nanoparticles of 60 nm average diameter (produced by BBI Solutions) are deposited from solution onto the hBN using the NaCl method (section 3.2.2). Since the model used for simulations in this work assumes spherical nanoparticles, 60 nm particles were selected because they display a lower degree of faceting as a fraction of total surface area than nanoparticles of greater diameter (e.g. 80 nm nanoparticles) [97]. While the following observations are likely to apply to all vdW material microcavities fabricated in this manner, hBN is helpfully inert, insulating, chemically robust and lacks exciton resonances that complicate these observations.

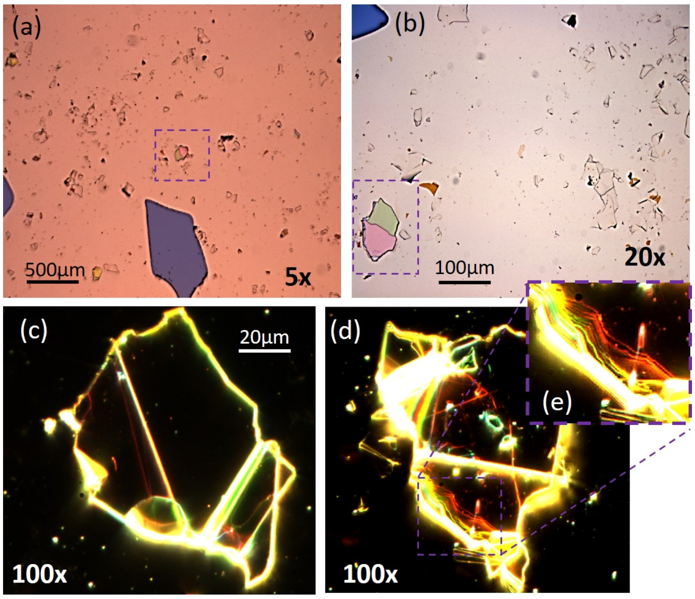

Fig. 4.2 Overview of samples formed using the template exfoliation method. 5× BF image (a) shows many hundreds of micro- and nanocavities embedded in a Au surface which are $\sim 1-10\mu$m across. Purple boxes highlight the sample used in this experiment. Two more representative sub-microcavities are shown in 100× DF (c,d), this time displaying clear steps and features beneath the hBN with colours dependent on hBN thickness. (e) Nanoscale Au steps beneath the hBN are clearly seen to change colour as scattered Fabry-Perot modes shift with increasing cavity length.

Using the setup as discussed in section 3.1, samples are broadband illuminated through an objective with numerical aperture NA0.8, so that light is collected for both dark-field (DF) and bright-field (BF) illumination in the angular range 0-53° (Fig. 4.1(a)). In BF, the angles of incidence and reflection are equal whilst the average DF illumination angle is 58°. Microscope 100× images of a nanoparticle-on-microcavity (NPoMC) sample in BF (Fig. 4.1(b)) and DF (Fig. 4.1(c)) resolve individual Au nanoparticles in DF as orange spots on terrace 1 (T1) and green spots on terrace 2 (T2). 22 and 16 NPs on T1 and T2 respectively are analysed on each terrace displaying consistent spectra, while brighter (by $> 3\sigma$) Au NP clusters are excluded, as are NPs near terrace edges. Au nanoparticle clusters are easily identified due to their significantly greater intensity and additional resonances due to plasmonic coupling with neighbouring particles. The scattering from nanoparticles near terrace edges was not included in the analysis as they were significantly influenced by additional scattering from the these edges. Other large contaminants appear in the bright field image as dark spots and are significantly more intense while displaying broad and irregular dark-field spectra.

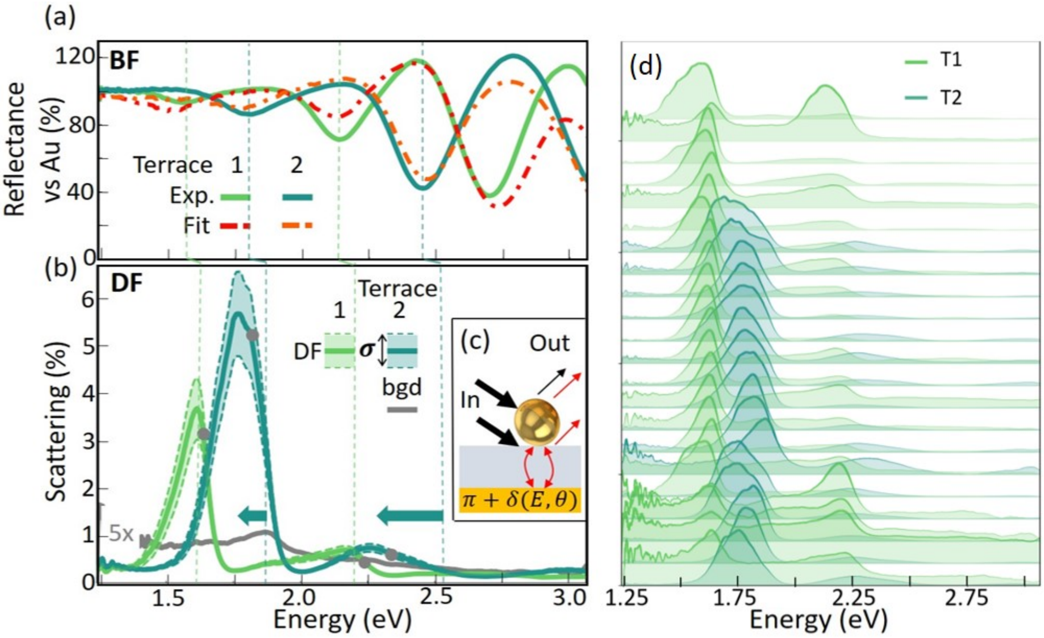

Fig. 4.3 (a) Bright-field reflectance, and (b) dark-field scattering from 22 (T1) and 16 (T2) nanoparticles. Dashed lines show one standard error bound, grey line is scattering background (×5) from lower hBN/Au interface away from NPs, grey dots mark peak positions of Fano resonances from resulting interference. Vertical lines show expected TE-polarised wavelengths for $d_{(1,2)}$. (c) Schematic interference in scattering and (d) all spectra taken in this experiment normalised to 1, demonstrating both the high uniformity of mode positions and the presence of additional modes.

As previously mentioned, observed BF colours (Fig. 4.1(b), 4.2(a,b)) result from thin-film interference which is used to calibrate each terrace thickness from the characteristic Fabry-Perot fringes (Fig. 4.3(a)), using uniaxial refractive indices $n_{x,y}$=1.65, $n_z$=2.13 (parallel to the $c$-axis) [82]. Fitted spectra (dashed) generated by the same generalised Mie solver used to calculate DF scattering (see next section), use reflectivities measured from the evaporated

Au outside each hBN flake, and give thicknesses $d_1 = 672 \pm 10$ nm for T1 and $d_2 = 577 \pm 8$ nm for T2. Minor deviations in the fringes are likely due to differences in the Au interface under and beside each hBN flake [125] as are variations between experimental and calculated values. This is due to differences in the assembly of thermally evaporated Au onto different surfaces, which alters the reflectivity between Au evaporated onto hBN compared to the surrounding Si substrate. This is largely because the exfoliation yields ultraclean hBN surfaces at crystal cleavage planes, whereas tape adhesive can be left on the surrounding Si substrate. There are expected to be slight differences in the evaporated Au/hBN interface (e.g. in terms of roughness) as a result of Au evapoaration. For example, work on graphene using an evaporation rate of 1.2Å/s has shown that nanocrystals of Au can form of up to 8 nm in diameter and 2 nm in height due to the high mobility of Au atoms on van der Waals material surfaces [125]. The significantly lower evaporation rate of 0.1Å/s was used for template exfoliation in order to minimise these effects.

Dark-field scattering spectra collected from each terrace show intense peaks which are similar for each nanoparticle (Fig. 4.3(b,c)). Solid lines show the average over 22 (T1) and 16 (T2) nanoparticles (dashed lines show standard error). While the scattering efficiency of coupled 60 nm Au NPs on bare Si is $< 0.2\%$, resonant enhancement here increases the scattered intensity by 1800% (T1) and 2800% (T2) (Fig. 4.3(b)). Often, the use of 60 nm nanoparticles in similar plasmonics experiments (e.g. NPoM) is limited by their low scattering efficiency which reduces the visibility of individual modes. However, here the combination of high intensity due to microcavity enhancement and low variability due to nanoparticle uniformity, enables reliable identification of features in the spectra such as asymmetric lineshapes and overlapping modes.

Within the wavelength range considered for this experiment the magnitude of the refractive index of gold is greater than that of bulk hBN. Overall, this leads to a $\pi$ phase-shift for dark field scattering when compared to bright field from both air/hBN and hBN/Au interface (Fig. 4.4). This is because for all scattering processes there is a $\pi$ phase shift for light which reflects before scattering, which then undergoes interference with light experiencing negligible phase shift upon direct scattering (Fig. 4.4(b,c)). This simple analysis therefore suggests that the peaks of nanoparticle dark field scattering should coincide with the minima of bright field reflectance for the same illumination angle.

In addition to this phase shift, there is a blue-shift expected due to the increase in illumination angle for dark field compared to bright field illumination[40, 126]. Correspondingly, vertical dashed lines shown in Fig. 4.3(b) represent the expected position of the bright field minima or dark field maxima if illumination angle increased from 53° to 58°. The blue

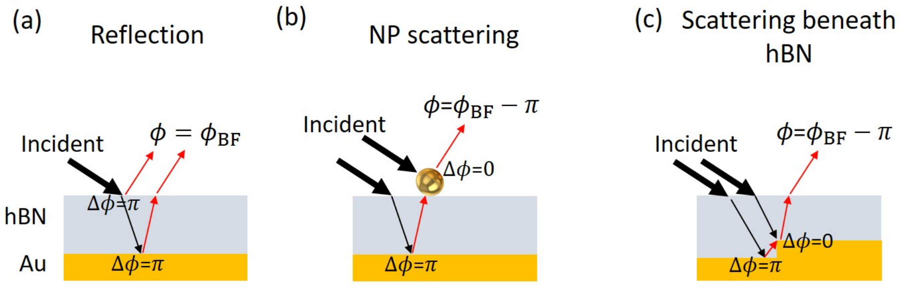

Fig. 4.4 Expected phase shifts at a given wavelength for out-coupling of Fabry-Perot modes compared to bright-field phase ($\phi_{BF}$)) for (a) BF reflection, (b) scattering from nanoparticles atop hBN and (c) steps or roughness beneath hBN.

shift can be explained by looking at the phase thickness equations for both TE and TM polarisations, $\beta_{TE}$ and $\beta_{TM}$,

$$\beta_{TE} = 2\pi \left(\tfrac{d}{\lambda}\right) \left(\frac{n_{xy}}{n_z}\right) \left({n_z}^2 - {n_a}^2 sin^2\left(\theta_i\right)\right)^{\frac{1}{2}} \tag{4.1}$$

$$\beta_{TM} = 2\pi \left(\tfrac{d}{\lambda}\right) \left({n_{xy}}^2 - {n_a}^2 sin^2\left(\theta_i\right)\right)^{\frac{1}{2}} \tag{4.2}$$

where $n_{xy}$, $n_z$ are the in and out of plane refractive indices of hBN respectively, $d$ is the hBN thickness, $\lambda$ is the wavelength and $n_a$ is the refractive index of the ambient. From this equation it is seen that the frequency which fulfils the Bragg interference condition $\beta_{TM} = \beta_{TE} = \pi/2$ is higher than for normal incidence. The magnitude of the shift can be seen in the calculated shifts shown later, in Fig. 4.6. Referring to the vertical dashed lines in Fig. 4.3(b), all dark-field peaks from both terraces are red-shifted by varying degrees from the expected positions based on the above analysis. In particular, there is a significant red-shift of $\approx 0.3\ eV$ for the higher energy mode for nanoparticles on T2. This suggests that the simple analysis presented in Fig. 4.4, is not enough to explain the behaviour of scattering from the nanoparticles. This indicates that shifts seen for nanoparticles are influenced by other mechanisms alongside the Fabry-Perot coupling for the planar cavity.

Scattering in regions surrounding the nanoparticles showed a weak background spectrum, a result of Au roughness at the hBN/Au interface. The weak background spectrum for T2 (grey Fig. 4.3(b)) has a maximum intensity at the value expected for the microcavity mode. This is supported by scattering from steps beneath hBN for T2 which shows a maximum at the same wavelength (Fig. 4.5(d)). As suggested by the above discussion, the phase shift for scattering from roughness and steps beneath the hBN is the same as the phase shift for scattering from nanoparticles (Fig. 4.4(c)) since scattered light (very small phase contribution) interferes with light experiencing a $\pi$ phase shift at the air/hBN or hBN/Au interface (see below).

### 4.2.1 Dark-field Scattering from Au Nanosteps

Bright steps of Au can be clearly seen beneath the hBN flakes (Fig. 4.4(c)) and occur as a natural result of the Au evaporation onto the multi-terraced crystal topology. Despite having step heights on the order of 0.4 nm to 10 nm , the collective plasmonic properties of many steps in combination with Fabry-Perot enhancements lead to sharp dark-field scattering peaks which can be treated as approximately a single step [2]. This is most clearly seen in Fig. 4.2(e), in which steps beneath hBN change colour from green to red as they get closer to the bottom of the cavity. These steps are expected to scatter light in such a way that dark-field peaks exactly coincide with BF minima for the terrace since there is no $\pi$ phase shift on reflection as for BF and therefore scattering maxima are exactly out of phase with BF maxima (Fig4.4a).

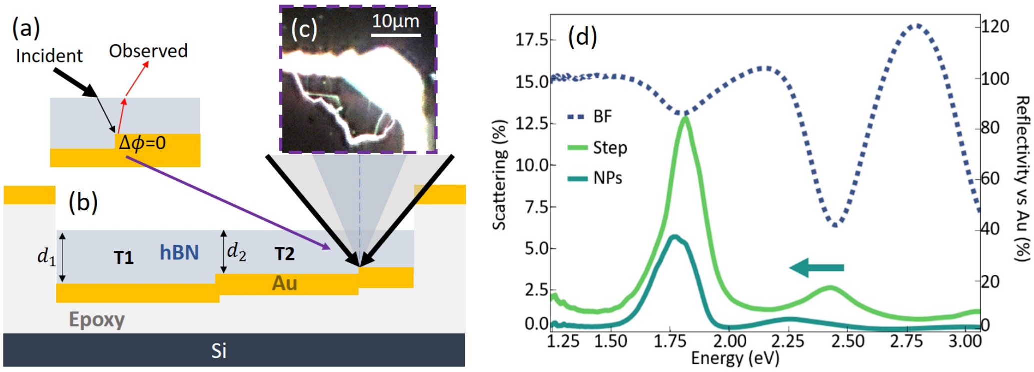

Fig. 4.5 Analysing scattering from the steps in this experiment. Since scattering replaces reflection there is no phase change $\Delta\phi$ when compared to observed light (a). If the pink terrace is included there is a third set of steps beneath the hBN between T2 and the pink terrace (b) as shown in the zoomed upper-left of Fig. 4.1c (c). (d) Comparison between experimental bright field (BF) reflectivity, dark field scattering from step, and DF from nanoparticles (NPs) on terrace 2. The sharp scattering from the step between two terraces shows the expected Fabry-Perot modes. The blue arrow shows shift due to NRM mechanism for nanoparticles which does not occur for steps.

Spectra were taken from the steps surrounding the pink terrace (top right of Fig. 4.1(b,c) and Fig. 4.5(b,c) adjacent to T2. The dark-field scattering measurements show a maxima at the same position as BF minima, as predicted with only Fabry-Perot coupling (Fig. 4.5(c)). There is no clear blue-shift for any of the modes at this high angle, in particular for the high

---

[2] According to my AFM studies (see section 5.1) cleavage of hBN never leads to single terrace steps of many 10*s* of nanometres, instead there are many smaller steps which are closely spaced

energy mode at 2.45 eV. This in clear contrast to the scattered light from the nanoparticles above which show clear blue-shifts from the BF minima.

To summarize this section, I note that the scattering peaks are not at the expected positions (dashed lines) from the scattering interference paths depicted in Fig. 4.4 and that the shifts differ significantly between the two terraces. In addition, the mode structure is not simple, as lineshapes appear asymmetric and frequently appear to consist of two, rather than a single resonance (Fig. 4.3(d)). A key observation is that the blue-shift is different for each mode and is significantly greater for higher energy modes than lower energy modes. This is in contrast to other work which shows red-shifts which are larger at lower energies and predictable using the Bethe-Schwinger cavity perturbation formula [120]. I will now show that the shifts are not a consequence of enhanced plasmonic phase shifts alone and are instead due to the existence of a new mode, independent of the Fabry-Perot mechanism.

## 4.3 Comparisons with Mie method calculations

To explain these observations, novel Mie method calculations were developed by Dr. Xuezhi Zheng of K.U. Leuven, with simulations designed and presented by myself. A description of this method composed by Dr. Zheng can be found in the Appendix. In the designs I used based on these Mie calculations, two optical pathways are initially considered, interfering the direct back-scattering from the NP with the forward-scattered light after it has propagated multiple times through the underlying microcavity. The phase shift on reflection at the lower hBN/Au interface is $\pi + \delta(E,\theta)$, where $\delta$ describes the phase shift due to changes in Au reflectivity with wavelength and angle. Dips in BF reflectivity correspond to Fabry-Perot resonances, where the resonant optical field inside the hBN increases light absorption in the Au mirror. In this situation the optical field at the top surface is also maximised, so forward scattering from the NP is expected to be strongest at these reflectivity dips (for the same illumination angle). Since DF illumination is recorded at higher incident angles than the BF reflectivity, the cavity resonances blue shift [40, 126] and for 58° are shown by the vertical dashed lines (Fig. 4.3(b)). However, this model cannot account for the shifted DF scattering peaks (blue-green arrows, Fig. 4.3(b)). All scattering peaks from both terraces are found to be red-shifted by different energies from the expected positions based on the simple model above, up to 300 meV for the higher energy T2 mode. This suggests that scattering resonances of nanoparticles on micro-cavities are influenced by extra mechanisms besides the outcoupling of planar Fabry-Perot modes.

To better understand the resonant modes in this system, extinction spectra with and without the NP were calculated. These are evaluated using a generalized Mie theory (see

Appendix) [38] considering a perfectly spherical Au nano-particle on top of a uniform hBN layer on flat Au (Fig. 4.3(c) and appendix Fig. A.2), with the $z$-axis parallel to the optic axis of the hBN crystal.

While the situation with the nanoparticle is more complex, it is instructive to break down the case without the nanoparticle to help with understanding the calculations shown in Fig. 4.6(a,b). Initially, the fraction of light entering the hBN is calculated as the incident angle increases. Without the nanoparticle, the interface reflection matrix $R$, which relates the reflected electric field $E_r$ to the incident field $E_i$ with incident s- ($E_{is}$) and p-polarisation ($E_{ip}$) via [127],

$$E_r = R\,E_i = \begin{bmatrix} E_{rp} \\ E_{rs} \end{bmatrix} = \begin{bmatrix} R_{pp} & R_{ps} \\ R_{sp} & R_{ss} \end{bmatrix} \begin{bmatrix} E_{ip} \\ E_{is} \end{bmatrix} \tag{4.3}$$

is diagonal in this symmetrical situation ($R_{ps}$=$R_{sp}$=0), leaving only $R_{pp} = R_{TM}$ and $R_{ss} = R_{TE}$. Beginning with the simpler TE situation, incident and reflected electric fields are defined in terms of polarisation-dependent refractive indices and incident angle $\theta_i$ by,

$$r_{TE01} = \frac{n_a cos(\theta_i) - (n_{xy}^2 - n_a^2 sin^2(\theta_i))^{1/2}}{n_a cos(\theta_i) + (n_{xy}^2 - n_a^2 sin^2(\theta_i))^{1/2}} \tag{4.4}$$

where $n_a$ is the refractive index of the ambient medium above hBN (here air) and $n_{xy}$, $n_z$, are the respective refractive indices for hBN in the x-y and z planes. Air, hBN and Au are labelled as medium *0,1* and *2* respectively meaning that $r_{TE01}$ corresponds to the reflectivity for s-polarised light at the air/hBN interface. Referring to this equation, the TE reflection resonances are equally-spaced at normal incidence and blue shift together with angle (Fig. 4.6(a)). The reflection coefficient at the hBN/Au interface is then,

$$r_{TE12} = \frac{(n_{xy}^2 - n_{Au}^2 sin^2(\theta_2))^{1/2} - n_{Au} cos(\theta_2)}{(n_{xy}^2 - n_{Au}^2 sin^2(\theta_2))^{1/2} + n_{Au} cos(\theta_2)}, \tag{4.5}$$

where $n_A u$ is the refractive index of Au as a function of wavelength and $\theta_2$ is the angle of light transmitted into Au. It can then be shown that the total reflectivity for the structure is,

$$R_{TE} = \frac{r_{TE01} + r_{TE12} e^{-i2\beta_{TE}}}{1 + r_{TE01} r_{TE12} e^{-i2\beta_{TE}}}. \tag{4.6}$$

The TM reflection coefficient at the air/hBN interface $r_{TM01}$ is described by [40, 126, 127]

$$r_{TM01} = \frac{n_{xy} n_z \cos(\theta_i) - n_a \left(n_z{}^2 - n_a{}^2 sin^2(\theta_i)\right)^{\frac{1}{2}}}{n_{xy} n_z \cos(\theta_i) + \ n_a \left(n_z{}^2 - n_a{}^2 sin^2(\theta_i)\right)^{\frac{1}{2}}}, \tag{4.7}$$

For TM reflectivity (Fig. 4.6(b)), this picture is complicated by effects at Brewster's angle (white dashed Fig. 4.6(a-d)) where the reflection at the air-hBN surface vanishes, eliminating multiple interference. Beyond this angle,

$$\theta_B = \operatorname{asin}\left(\left[\frac{{n_{xy}}^2 - 1}{{n_{xy}}^2 - {n_z}^{-2}}\right]^{1/2}\right) \simeq 56^\circ \tag{4.8}$$

the phase on reflection reverses, shifting the resonances by half their spacing. At this angle the intensity of reflected light at the air/hBN interface is zero, however the total TM reflectance never goes to zero due to the reflectance of Au as described by,

$$R_{TM} = \frac{r_{TM01} - r_{TM12}e^{-i2\beta_{TM}}}{1 + r_{TM01}r_{TM12}e^{-i2\beta_{TM}}}. \tag{4.9}$$

Here, when $r_{TM01} = 0$ the simple equation $R_{TM} = -r_{TM12}e^{-i2\beta_{TM}}$ describes the reflectance at the Brewsters angle.

The generalised Mie model shows scattering from the NP atop the microcavity is indeed enhanced at each extinction maxima (Fig. 4.6(c)). TE scattering peaks blue-shift with angles matching the reflectivity dips, weakening slightly at $\theta_B$ when polarisation-flipped NP scattering disappears. The predicted TE scattering peaks at 58° match the observed peaks at 2.25 eV and 1.55 eV (Fig. 4.6(c)) to within 0.1 eV. The larger extinctions at higher energy come from the stronger interband Au absorption above 2.5 eV.

By contrast, a completely different predicted behaviour is seen for TM polarised scattering (Fig. 4.6(d-f)) for both terrace thicknesses. Although blue-shifts are initially seen, a set of new modes appears around $\theta_B$, which dominate the total (TE+TM) scattering at 58° (Dashed white circles, Fig .4.6(d)). Since scattering measurements are typically taken at high angles $\sim \theta_B$, it is vital to understand the origin of these NPoMC modes.

## 4.4 Probing TM Scattering Modes

Comparing TM extinction (Fig. 4.6(b)) to scattering (Fig. 4.6(d)) highlights these peculiarities. At $\theta_B$, the extinction shows no microcavity modes, however the scattering spectrum gives new sharp modes. In simulations of the thinner microcavity T2 (Fig. 4.6(e,f)), the new peak at 1.9 eV becomes the dominant cavity mode, with a 200 meV red-shift from the expected position of the TE scattering peak (Fig. 4.6(e), blue-green arrow). This combination of nanoresonator and Fabry-Perot modes accounts well for the bright mode near 1.8 eV in Fig. 4.3(b).

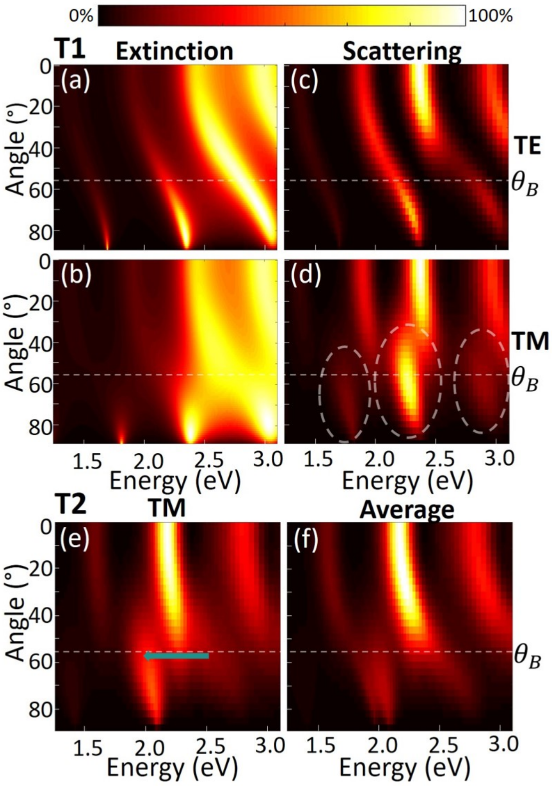

Fig. 4.6 Generalised Mie calculations for T1 (a-d) and T2 (e,f). For T1, extinction without NP (a,b) and scattering spectra for NP on microcavity (c,d) are shown as angle increases. Brewster angle $\theta_B$ is dashed. Extinction is from 0% (black) to 100% (white), scattering from 0% (black) to 5% (white). For T2, calculations are for (e) TM scattering and (f) average of TE and TM scattering. Blue-green arrow is comparison with Fig 4.3(b).

The generalised Mie theory shows these modes are produced by back-scattering from the NP, creating transverse localised cavity modes underneath it which are spatially confined in-plane to the nanoscale geometry of the NP (Fig. 4.7). Even for illumination angles significantly less than $\theta_B$ these surface modes can be excited and out-coupled. This new nanoresonator mode (NRM) is only seen at energies that can excite the microcavity-coupled vertical dipole antenna, forming a new scattering resonance at 2.25 eV.

To explore the nanoresonator modes, we track how they vary with increasing microcavity thickness (Fig. 4.7(a)) [40, 126]. The NRMs (white dashed line over first order NRM) redshift with increasing hBN thickness for constant illumination angle of 58°. Above $d = 300$ nm, several modes are seen, with energy spacings which decrease as expected for Fabry-Perot-type modes. Between the strongly-excited NRMs are weaker resonances matching the normal TE Fabry-Perot modes (yellow dashed line over second order FP mode). Plotting the thickness-dependent Q-factor of the dispersive NRMs shows a periodic modulation under an increasing envelope (Fig. 4.7(b)).

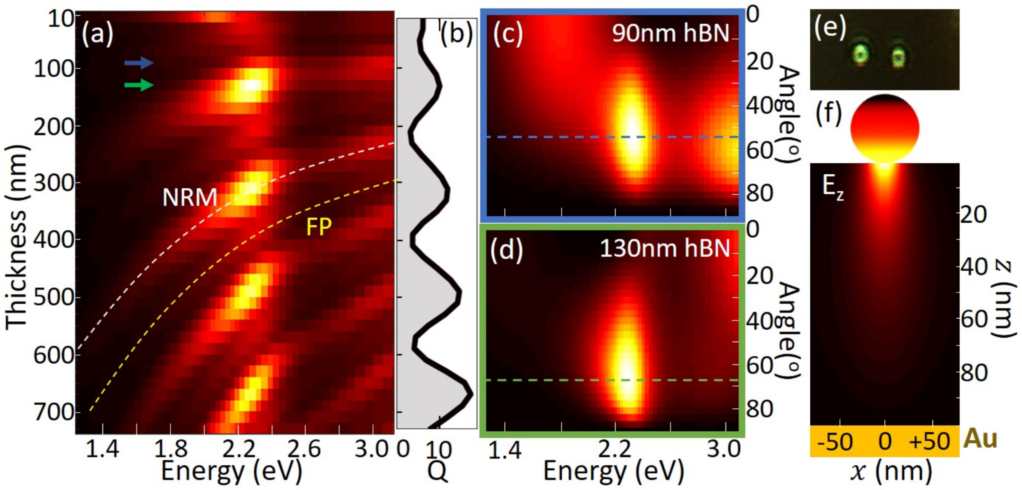

Fig. 4.7 (a) Thickness dependence of TM scattering of nano-resonator modes (NRMs, white dashed) at $\theta_i = \theta_B = 58°$, with faint Fabry-Perot modes (FP, yellow dashed) also seen and (b) calculated Q-factors. Arrows mark d=90,130 nm for angle-dependences in (c,d) where dashed lines mark angle of maximum scattering. (e) Typical experimental DF scattering images of 80-130 nm thick hBN nano-resonators at 100x magnification. (f) Field map of surface charges on 60 nm nanoparticle and scattered electric field ($E_z$) for nano-resonator mode with $L$=110 nm, $\theta_i = 58$ deg. All scatter intensity (a-d) and field plots (e) are normalised between 0% (black) and 100% (white).

These resonant modes can be excited at incident angles from 40-80° with energies from 1.4-2.4 eV. The high-angle resonant lowest mode is clearly visible for hBN $L$>90 nm (Fig. 4.7(c,d)). They appear strongest when near-resonant with the nanoparticle transverse plasmon mode around $\lambda = 550$ nm (2.25 eV). The angle of maximum scattering intensity (blue and green lines, Fig. 4.7(c,d)) shifts from 52° to 68° when the hBN thickness increases from 90 nm to 130 nm, showing their coupling is not precisely tied to $\theta_B$.

At thicknesses of 80-170nm the lowest order NRM has the least extra contributions from the FP-coupled modes (Fig. 4.7(a)). Experimentally, nanoparticles on hBN flakes within this range display ring-shaped dark-field scattering images due to the high-angle outcoupling of light from the NRMs (Fig. 4.7(e) and depicted in Fig. 4.8). This confirms their dominant out-of-plane $E_z$ resonant fields, completely different from Fabry-Perot microcavities. These TM nano-resonator modes seen in the NPoMC geometry are thus attributed to multiple scattering and reflection underneath the NP (Fig. 4.7(f)). This is because at $\theta_B$ all other cavity feedback disappears at the hBN/air interface. Treating scattering from the nanoparticle as a microcavity end mirror with low reflectivity (following Fabry-Perot behaviour), we indeed expect the Q-factor to increase with thickness. This is because such nano-resonators approach the limiting case when the lateral dimensions of a cavity back-reflector approach a point. As expected, the Q-factor per unit length decreases with increasing thickness since diffraction from NP causes lateral spreading of the retro-reflecting light beyond the optical cross-section of the resonant NP. The NRM field distribution (Fig. 4.7(f)) is similar to that from individual Au NPs, but resonant at 58° and nearly 10-fold stronger than without the underlying Au mirror.

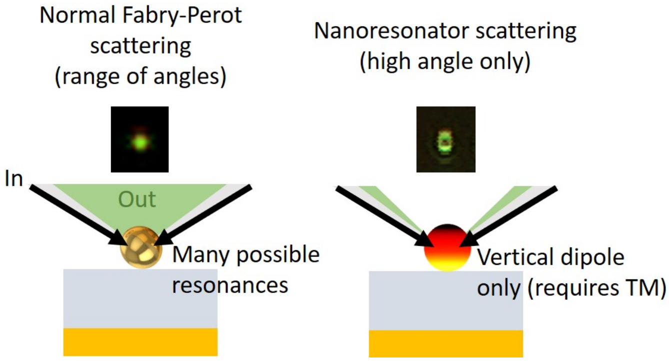

Fig. 4.8 The NPoMC which scatters Fabry-Perot modes (a) appears as a spot because out-coupling to far-field is at a wide range of angles, and strongest perpendicular to the substrate plane. The NPoMC which scatters NRMs (b) is only accessible via TM polarised light when nanoparticle-cavity coupling leads to formation of a vertical dipole which emits only at high-angles. This appears as a ring in far-field.

The NRMs depend on cavity thickness as for conventional Fabry-Perot modes, but experience far stronger plasmonic phase shifts due to multiple scattering, which needs to be taken into account. Plasmonically enhanced cross-sections mean that although dielectric nanoparticles also show NRMs, they are more than fifty-fold weaker and there is no maximum close to the excited transverse or antenna modes of the nanoparticle around 2.25-2.30 eV (Fig.4.9(a)). To support further the observation of NRM modes and explore the differences between plasmonic metal nanoparticles and dielectric nanoparticles, I calculate the Q factor and FOM (defined as Q/thickness) as a function of thickness (Fig.4.9(b)). Both Au nanoparticles and Si nanoparticles of 60 nm in diameter can support NRMs, but the Q-factor and FOM is higher for plasmonic nanoparticles.

I find that the field inside the hBN is nearly 10-fold weaker without the Au mirror underneath (compare Fig. 4.10(a,b)), and does not possess a resonance at the specific high angle of the NRM mode (comparing Fig. 4.10(c,d)). As expected for a mode with field vector into the hBN crystal plane the NRMs depend most strongly on the in-plane refractive index of hBN as shown in Fig. 4.11.

These nano-resonator modes resemble previously observed Brewster modes, but with the both mirrors replaced by flat Au and a NP [124, 128, 129]. To compare with previous observations, a similar mode was previously identified by in a multilayer structure in 1974 [124]. Additionally, observation of the strong coupling regime between the quantum well

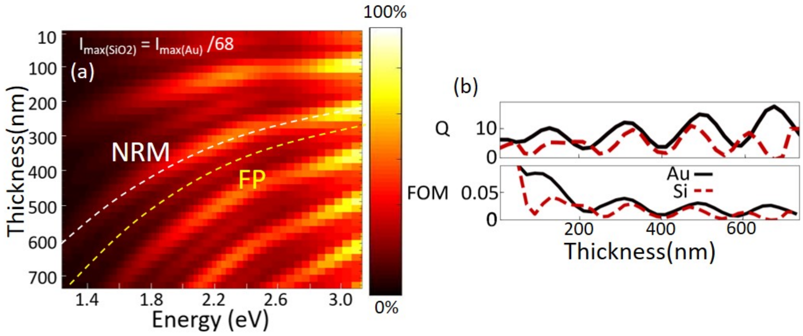

Fig. 4.9 TM scattering modes from silica nanoparticle of 60 nm in diameter (a) and corresponding Q-factors (b). The brighter modes are due to the NRM mechanism with fainter modes due to the usual TE Fabry-Perot mechanism. Calculation comparing Q-factor and FOM for Au and silica nanoparticles (n = 1.5). These are extracted from the calculated spectral peaks in the mode spectrum.

excitons and a high incidence ‘Brewster cavity mode’ was reported in 2019 [128]. In these other works the Brewster mode appears in the cavity formed by two different mirror types (Fig.4.12). The first one is a multilayer DBR (DBR without top layer), which replaces the Au mirror in this experiment. The second one is called the total internal reflection mirror, which is the interface between the top layer and the air and replaces the nanoparticle here. The angle of illumination into these structures is therefore dependent on the refractive index of the top layer, which defines the conditions for total internal reflection. The top layer of the multilayer structure is an intra-cavity gap (media between the mirrors, in our case this replaces hBN). The Brewster mode in these works differs from the usual Fabry-Perot modes by condition for the standing wave formation. For the usual Fabry-Perot cavity mode, the standing wave satifies the condition that the width of intra-cavity gap should be equal to the integer number of half wavelength, $\lambda_c = 2nL/(Ncos(\theta))$, where $n$ is the refractive index, $d$ is the width of intra-cavity gap and $N$ is an integer. The standing wave condition for the Brewster cavity mode differs from the Fabry-Perot cavity mode condition. The difference comes from the phase jump by $\pi$ for the wave reflected from the total internal reflection mirror. So, the Brewster cavity mode standing wave condition is instead,

$$E = \frac{hc^2}{2nL}\left(p + \frac{1}{2}\right)\cos(\theta), \tag{4.10}$$

where $p$ is an integer, arising from additional $\pi$ phase jumps compared to Fabry-Perot modes. The jump appears only in TM polarization therefore the Brewster mode appears only in the TM polarization.

The modes I have presented here are similar to the Brewster modes presented in this other work but do not require a DBR, operate via scattering from a plasmonic nanoparticle instead

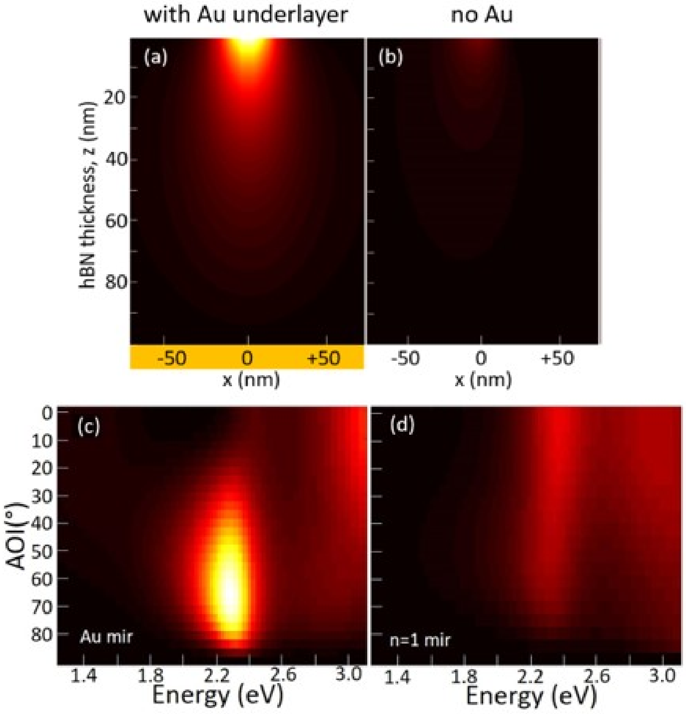

Fig. 4.10 (a,b) Optical field $E_z$ (a) with, and (b) without gold mirror beneath hBN plotted on same intensity scale which is normalised for the case with a Au underlayer between 0% (black) and 100%. (c,d) Angle dependence of 130 nm hBN sub-microcavity system (c) with, and (d) without gold mirror beneath.

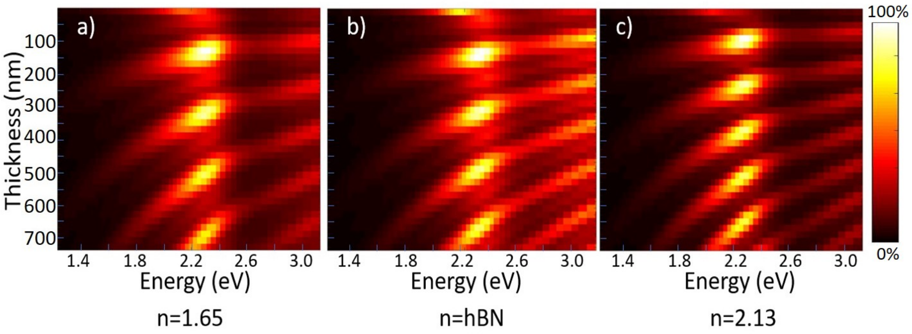

Fig. 4.11 The thickness dependence of TM NRM modes with 60 nm Au NPs at 58 degrees incidence with constant $n = 1.65$ (a), uniaxial $n = n_{hBN}$ (b) and constant $n = 2.13$ (c)

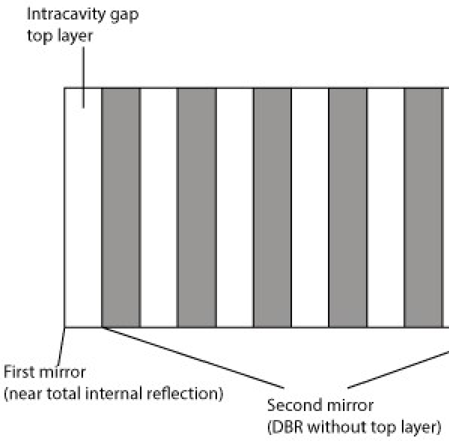

Fig. 4.12 Visual description of previous types of optical microcavities used in other works in order to observe Brewster modes. For my experiment the near total internal reflection mirror is replaced by a 60 nm Au nanoparticle, DBR mirror by flat Au and top layer by single-crystalline hBN.

of total internal reflection and replace one cavity mirror with Au. The complex refractive index of Au means that while the overall behaviour is similar to as described in equation 4.10, an exact analytic function cannot be written to define the modes position in wavelength. To be more precise, nanoresonator modes experience additional shifts of $\delta(E,\theta)$ dependent on the mirror, cavity and nanoparticle compositions. This has some analogy to Goos-Hänchen effects, in which the overlap of incident and reflected wavefronts leads to a slight phase shift of the reflected light after internal reflection [130]. In this work, the combination of effects shifts the peaks considerably away from equation 4.10. As a result of the nature of this mode, these NRMs are tightly confined to the geometry of the Au nanoparticle and therefore critically probe the morphology and scattering at the top interface.

Although the calculations yield good agreement with the mode energies, they do not account well for measured scattering intensities. The model predicts modes at energies close to the transverse plasmon mode should have greatest scattering intensity, but experimentally the modes at lower energies are much stronger. I suggest this may be due to additional Fano resonance [109, 131] from the continuum scattering background (due to the slightly rough lower Au surface, grey line Fig. 4.3(b)), which is stronger at lower energies. Such Fano effects produce the asymmetric-lineshape low-energy peaks and also the small (50 meV) extra blue-shifts of the calculated modes (grey points, Fig. 4.3(b)) compared to those experimentally observed. It is also possible that the morphology of the nanoparticle favours outcoupling of cavity modes at lower energies.

## 4.5 Conclusion

In conclusion, exfoliated hBN crystals were embedded in Au forming uniform planar half-microcavities. By depositing Au nanoparticles on top of these crystals to form NP-on-microcavity (NPoMC) structures and using single nanoparticle spectroscopy, the plasmonic and Fabry-Perot enhancements were identified which control interfacial scattering mechanisms and corresponding red-shifts in the mode positions. I identify a new microcavity nano-resonator mode (NRM) which can be excited only for TM polarisation at angles $\theta_B \pm 20^\circ$ and which depends on microcavity thickness and refractive index. It is shown that this mode arises from multiple reflections between scatterer and Au mirror. Subtle phase shifts and Fano coupling within this microcavity control its exact spectral position.

These NRM modes are vital to understand when exploring the coupling of nanoparticles with the new materials landscape of TMDs. The same fabrication techniques can be used to produce NPoMC structures with other TMDs instead of hBN and it is expected that the same modes should be observed for these materials. Because of the extreme sensitivity of these modes, this work is valuable in studying architectures which take advantage of enhancements at nanostructure or NPoMC interfaces.

# Chapter 5

# Few-layer to Monolayer hBN NPoM

In the chapter 2 of this thesis, there was a discussion of the nanoparticle on mirror (NPoM) geometry and an overview of what we have discovered thus far about this useful architecture. All of these previous works focussed on the use of optically active spacer layers in order to demonstrate novel nano-optics.

In previous work on graphene Fig. 5.1(1), dark field scattering from graphene NPoMs was collected for monolayer graphene up to 5 layers thick[5]. Whilst NPoMs on thicker graphene showed red-shifting coupled modes with decreasing number of layers as expected, monolayer graphene NPoMs showed split peaks (see Fig. 5.1(1)). Since the majority of the field in the NPoM was calculated to be perpendicular to the graphene plane, the spacer was treated as a dielectric. This splitting was attributed to virtual dipoles forming within the highly laterally conductive graphene layer. However, graphene's conductivity and atomic thickness, which approaches the quantum regime for plasmonics [132, 133], makes it difficult to determine the underlying mechanism behind any given mode behaviour.

In 2015, further work with $MoS_2$ Fig. 5.1(2) enabled much deeper analysis of the NPoM system, with the spacer treated as an inert dielectric of thickness $\sim 0.8$ nm in the gap [8]. The ruling out of explanations relating to spacer behaviour enabled significant further study into the base NPoM system, including its use as a plasmonic ruler and identification of new hybrid facet modes, antenna modes and a discussion of their relative outcoupling to far-field (Fig. 5.1(2)). Most recently in 2017, the consequences of this improved understanding were brought to fruition in the study of NPoM with $WSe_2$ multilayer spacers Fig. 5.1(3) [9]. In this work strong coupling was observed in around 12 layers of $WS_2$ at room temperature, a big advance for the plasmonics community (Fig. 5.1(3)).

One of the main projects worked on throughout my PhD work has been the study of monolayer hBN as a spacer layer in NPoM (see chapter 2), with an estimated thickness of $\sim 0.3 - 0.4$ nm depending on the fabrication method [134]. Unlike $MoS_2$ and graphene, this

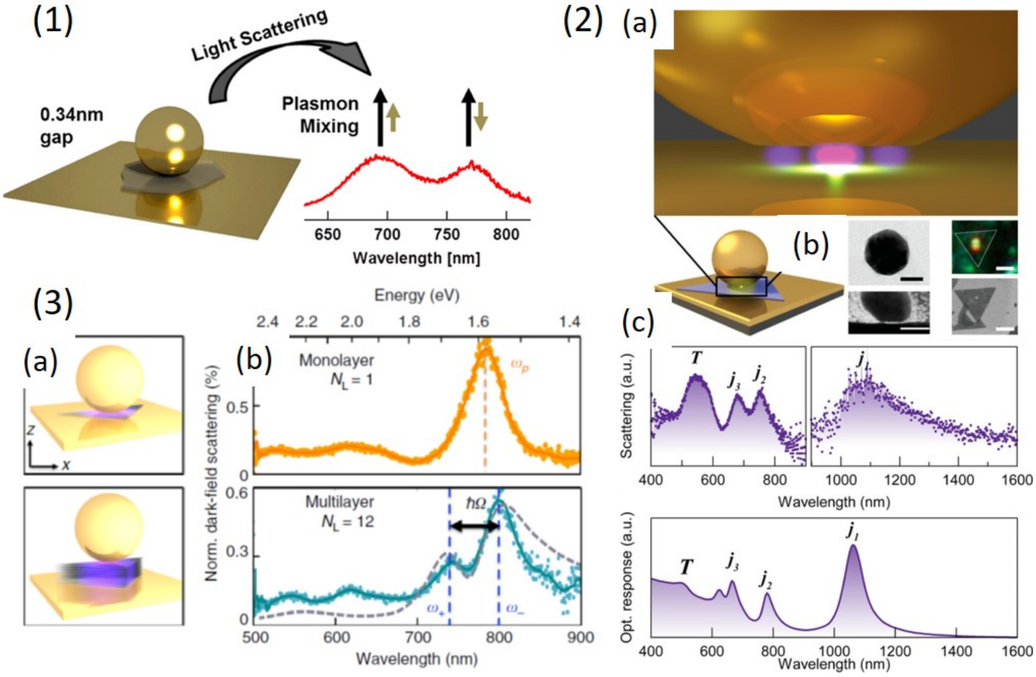

Fig. 5.1 Overview of the principle results of the three publications from within my research group which utilise the properties of vdW materials to observe novel nano-optics. These works can be found at the corresponding references. (1) The graphene virtual dipole paper [5]. (2) the $MoS_2$ morphology paper, in which the ultra-confined gap enabled probing of nanoscale changes (b) and measurement of IR modes(c) with new theory to support the observations[8]. (3) The most recent work on strong-coupling to multilayer $WSe_2$(a), on monolayer the usual coupled modes were observed, but on multilayer Rabi splitting was observed [9].

material can be considered as an inert dielectric throughout the visible range of wavelengths most useful for NPoM, as it has a bandgap beyond $\sim 5.9$eV[80]. There were a number of key aims for this work:

1. To further the understanding of NPoM for an atomically thin spacer and attempt to reach the quantum regime for plasmonics using this system (achievable below $\sim$1 nm with high-n gaps)[56, 133].
2. By multilayer stacking this atomic thickness spacer, to enhance the resolution in gap change and corresponding tuning rate of the coupled mode, thereby testing our current models for NPoM to their absolute limit.
3. Use our understanding of hBN in NPoM from single to multilayer as the fundamental groundwork for further studies on van der Waals heterostructures based on hBN in plasmonics.
4. Identify changes in refractive index with thickness. The behaviour of this property with decreasing thickness and for single crystal compared to thin films has been questioned and would be highly valuable information[82, 135] [1]. Additionally, it is not well understood how the screening due to substrate and environment influences the measured index for mono- or few-layer hBN.

In this work, initially the case of exfoliated few-layer hBN is discussed. Deep insights into the exact morphology of the interface can be gained from this system in the same way as achieved for $MoS_2$[8]. However, rather than focus on the influence of nanoparticle faceting, which was one of the focal points of the work on $MoS_2$, there will be an in-depth look at the exact constituents of the gap and the resulting influence on the spectral position of the antenna modes. The key change in approach is the direct comparison between otherwise identical NPoMs with and without hBN present in the gap, which enables the identification of new influencing factors. This study reveals a number of very important features which are potentially unique to layered materials as gap layers and henceforth lays the required groundwork for development of thin 2D materials in NPoM. In addition, it should apply to dielectric spacers including molecules if they do not bind directly with the Au nanoparticle surface.

With the knowledge gained from the exfoliated case, trilayer hBN will be studied, which consists of three millimetre-scale monolayer hBN layers which are grown via chemical

---

[1] References [82, 135] both take anisotropy into account correctly but arrive at different values for a single crystal compared to a thin film [135]

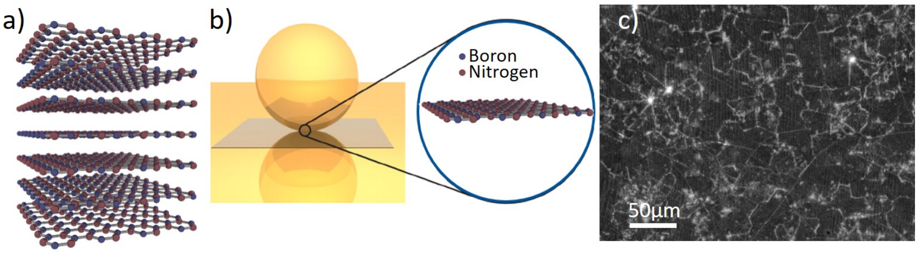

Fig. 5.2 The layered structure of hexagonal boron nitride (a) shows that it is one of the rare materials for which a single layer is an atom thick. This atom thick layer can be placed in NPoM (b), with the ultimate aim to have NPoM's distributed over large area CVD hBN on Au (c).

vapour deposition (CVD, see chapter 3 for growth details) and iteratively stacked above one another. This is the first large-area few-layered material studied using NPoM in our group [136]. The principle advantage of this system is the ability to gather many hundreds of individual spectra distributed over large areas and undertake more thorough statistical analysis [137]. Work on the monolayer CVD hBN system will be presented which displays highly unusual results based on our current models[46, 47, 8, 45]. However, using the knowledge gained from exfoliated and trilayer CVD samples it is possible to explain these results in an intuitive way. The chapter will close on ways in which to improve NPoM with layered materials and some suggestions for future routes.

## 5.1 Exfoliated few-layer hBN in NPoM

The simplest way to begin gathering data on hBN NPoM is by using layers exfoliated from a bulk crystal onto Au. This acts as a starting point to check the thickness dependence for the hBN NPoM system, since exfoliated crystals inherently display a distribution of different thickness crystals and terraces (as seen in the previous chapter). The growth and transfer of multiple monolayers of CVD hBN is more challenging, time consuming and is unable to give as broad a distribution of gap thicknesses.

Typically the method presented in section 3.2.4 is used for the fabrication of heterostructures, since the same steps can be used to precisely rotate and position flakes on top of one another. This is likely the method which would be used for any future NPoM heterostructure experiments over the next few years.

The sample to be discussed here is the same as depicted in Fig 3.7(c,d), which shows hBN flakes successfully transferred onto Au before and after polycarbonate removal. This sample serves as an introduction to the experimental methodology which will be used throughout the rest of this chapter, and also as an introduction to the behaviour of the hBN-NPoM system.

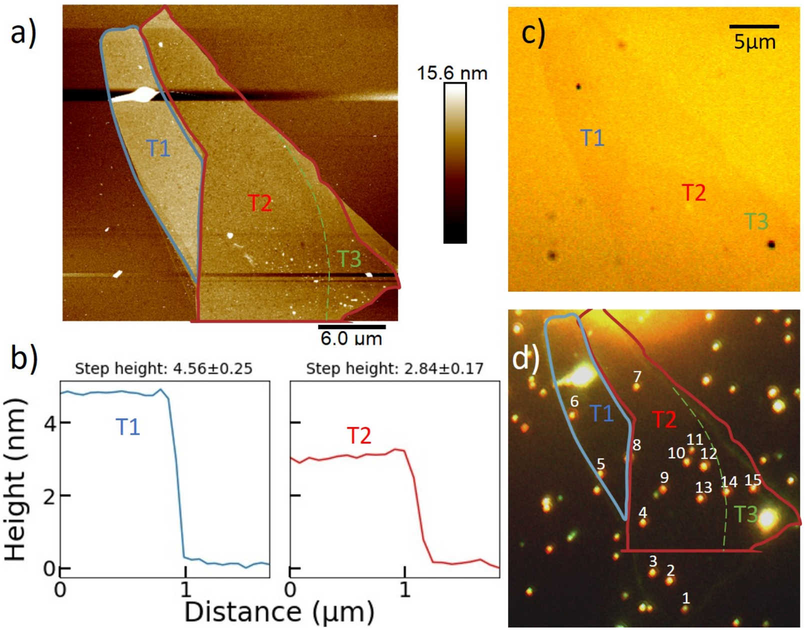

Fig. 5.3 The exfoliated hBN flake on Au, fabricated using the methodology outlined in section 3.2.4. AFM analysis (a,b) allows measurement of two distinct terraces of heights 4.56 ± 0.25 nm and 2.84 ± 0.17 nm from the Au substrate surface. Post nanoparticle deposition according to section 3.2.2, bright-field (c) demonstrates the low optical contrast of thin hBN and dark field shows the position of 80 nm Au nanoparticles on each terrace.

In this chapter, AFM is used to confirm the removal of polycarbonate (PC), and determine the thickness of hBN flakes before nanoparticle deposition. The ability to reliably measure spacer thickness by finding a well-defined crystalline edge is a useful advantage for vdW materials compared to self-assembled monolayers (SAMs) [98, 56, 117]. The individual hBN flake to be analysed here is shown in the AFM height image for the sample (Fig. 5.2(a)), displaying a clean surface with only small amounts of residue PC which appear as specks of white (i.e. spikes in height). The sample was selected due to its few-nm thickness and two relatively large area terraces at differing heights. These terraces are bordered with blue for the thicker terrace (T1) and in red for the thinner (T2). Corresponding step heights shown in Fig. 5.2(b) were measured at multiple points along the hBN flake edge to confirm that they were the same thickness across the whole terrace. These measurements were then averaged before and after each step, leading to a height of 4.56 ± 0.25 nm and 2.84 ± 0.17 nm for T1 and T2 respectively. The errors for these values were calculated by addition of the standard deviation of the values before and after the step. It will be seen later that these are minimum possible errors, the real errors are larger than these values. In addition to the two terraces of clearly different height, there is a small region of the flake within the thin red region which is separated by dashed green. This region is greater in height than T2 by between 1 and

2 monolayers. The very frequent presence of slightly thicker layers on any given flake is one of the key issues with using exfoliated hBN in comparison to CVD. Due to the growth parameters used here (see section 3.2.1) it is not possible to grow more than one monolayer of hBN with CVD except in multilayer seed regions, which are clearly visible as small areas of significantly thicker defective material and are thus easily excluded[136].

A 100× bright-field (BF) image of the flake can be seen in Fig. 5.2(c), the low contrast of which highlights the difficulty of identifying thin hBN on Au. hBN does not absorb visible light and contrast only occurs due to changes in optical path due to differences between the optical interface at hBN/Au and air/Au [77, 80, 134]. The optical path difference increases with greater hBN thickness leading to higher contrast. The interlayer spacing for hBN has been shown to be the same as graphite [138], $\sim 0.4$ nm, and considering that the spacing between a substrate and a monolayer transferred via this method is usually $\sim 2$ layers [2], the terraces consist of $\sim 9$ and $\sim 5$ layers of hBN. By exfoliating first onto Si/SiO2 for enhanced contrast and then transferring regions with many flakes, it is possible to deduce the position of very thin flakes using the relative position of other thicker crystals with higher contrast.

Nanoparticles deposited is as described in the section 3.2.2, by adding NaCl to a solution of 80 nm citrate capped BBI Au nanoparticles. This charge destabilises the solution causing individual nanoparticles to crash out onto the hBN sample. The resultant sample is shown at 100× dark field illumination in Fig. 5.2(d), and it can clearly be seen that there is not a significant difference in the density of nanoparticles on or off the hBN. This lack of dependence on hydrophobicity, along with the reduced deposition time is a big advantage of this deposition method compared to others (e.g. full immersion for long periods). At the end of this chapter it will be shown that the choice of deposition method from solution makes no significant difference to the NPoM spectra. Each nanoparticle on the hBN flake has been numbered for individual analysis, with their corresponding dark field spectrum shown in Fig. 5.4.

In Fig. 5.4, red spectra correspond to spectra collected from nanoparticles on the T2 of thickness 2.84 nm, blue from T1 of 4.56 nm and green T3 with thickness range 2.84-3.50 nm. Nanoparticle 9 displays two sharp peaks, but since no other particles display this feature, this is likely due to the close proximity of a second nanoparticle which can also be seen in the image. As they are in the same region, it is likely either that the two nanoparticles are plasmonically coupled or that the far-field light from both individual NPoMs is superimposed at the detector. Disregarding this nanoparticle, all of the other spectra display prominent peaks above 600 nm which are significantly brighter than the transverse mode at $\approx 530$ nm. The modes with resonances above 600 nm are the important modes related to plasmonic

---

[2] It will be seen for CVD transferred flakes later that this spacing can be reduced by annealing the sample

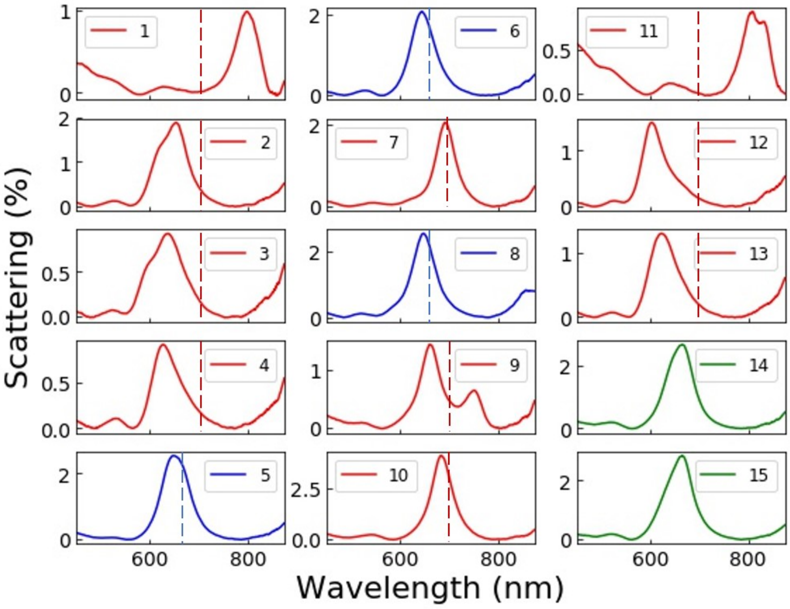

Fig. 5.4 Figure showing all of the spectra from 80nm nanoparticles deposited on the sample shown in figure 3. The numbers in each legend correspond the numbering shown in 3(d). Red spectra represent those which sit on the thick terrace, T1, of 4.56 nm, blue on the thin terrace, T2, of 2.84 nm, and green T3, of range 2.84-3.50 nm. Dashed lines represent the calculated expected position of the coupled mode for each spectrum.

coupling between the nanoparticle and Au beneath, thus we have formed an NPoM with exfoliated hBN of two distinct thicknesses as the gap spacer.

As a reminder, the generalised circuit model described in chapter 2 can be used to predict wavelength of the dipole antenna mode $\lambda_1^l$, using the equation

$$(\lambda_1^l/\lambda_p)^2 = \varepsilon_\infty + 2\varepsilon_d + 4\varepsilon_d\varepsilon_g^\chi ln[1+\beta R/d]. \tag{5.1}$$

Here, $\lambda_p$ is the plasma wavelength, $\varepsilon_d$, $\varepsilon_g$, are the permittivity of the surrounding medium and the gap respectively, with $\varepsilon_\infty = \varepsilon_m + \lambda/\lambda_p$. $R$ is the radius of the particle and $d$ the gap distance and $\chi$ and $\beta$ have characteristic values $\chi = 0.5$ and $\beta = 0.15$ for NPoM assuming spherical particles. Although it does not take into account faceting, it has been shown that this is a good model for non-conductive NPoM with gaps not approaching the quantum regime in thickness [46, 47].

For modelling of the experiments in this chapter the same coordinate basis is used as in the previous chapter, with the $z$ axis orthogonal to the substrate surface and $x-y$ in-plane. Since for the dipole antenna mode the near-field in the gap is almost entirely vertical (out-of-plane), the refractive index $n_z = 2.13$ is appropriate for the refractive index of hBN. The in-plane refractive index only becomes relevant for gap modes $s_{mn}$ with odd $m$, and for gap

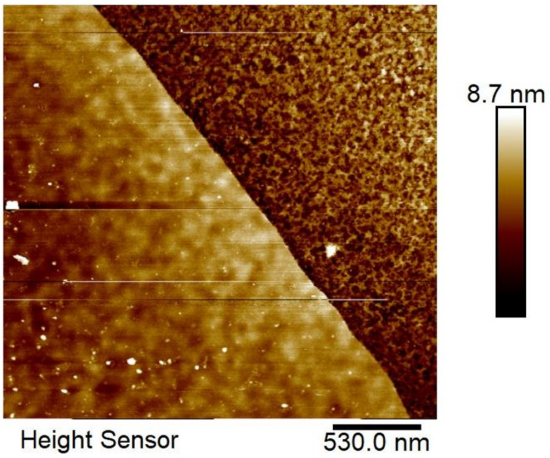

Fig. 5.5 A closer look in AFM at the hBN flake shown in figure 5.3(d), in the region of nanoparticle 7 on T2. The step between T2 (left) and the Au surface (left) of 2.8 nm is clearly seen. It can also be seen that there are fluctuations in height of ±0.5 nm of the hBN layer approximately every $20-60nm^2$. The Au appears rough due to the small scan area, but the rms is 0.8 nm which is good for evaporated Au. Small white spots of average size $\sim 5$ nm are remnant polycarbonate or other residues.

distances at least >5 nm. The surrounding medium is air with $n = 1$, Au permittivity is taken from reference [139][3].

By substituting in these values in addition to others which can be found in the appendix, the expected position of the dipole antenna mode $\lambda_1^l$ is 657 nm and 701 nm for the 4.56 nm (T1) and 2.84 nm (T2) terrace respectively. Dashed lines have been added to Fig. 5.4 in order to show these expected positions and it is clearly seen that this does not square well with the experimental data, since there are only two nanoparticles on T2 with a coupled mode above 700 nm. Hence, it is found that it is not enough to draw directly from the initial AFM step height measurement in Fig. 5.3(b) and assume that only hBN is present in the gap.

### 5.1.1 Inclusion of hBN Height Variation

A higher resolution image is shown in Fig. 5.5, which displays fluctuations in height above the Au surface of ±0.5 nm around the average for the thinner hBN terrace. Since these fluctuations in height vary over a surface area on the order of the area of a nanoparticle facet, the variation in the average spacer thickness needs to be evaluated to include these height changes. This leads to a new gap thickness of $d = 2.8 \pm 0.7$ nm based on the AFM height data, where the value here is the same but with increased in order to encapsulate the influence of variations. Additionally, since the hBN is only in direct contact with the Au

---

[3] Johnson and Christy, 1972

underneath when the fluctuation in height is at a minimum, it is possible to conclude that the hBN thickness is $2.8-0.5nm = 2.3 \pm 0.3$ nm This is clearly less than the average measured step height from the lower resolution AFM measurement.

Based on this analysis, now consider the spacer as a hybrid material consisting of air, with thickness $d_{air}$, refractive index $n_{air} \approx 1$ and hBN with thickness $d_{hBN}$, refractive index $n_{hBN}$, such that $d = d_{hBN} + d_{air}$ (Fig. 5.6). When the height of the spacer is $d = 2.3$ nm there is only hBN in the gap and the refractive index is $n_z = n_{hBN} = 2.13$ as initially expected. However, when it is 3.3 nm the spacer consists of 1 nm ($d_{air}$) of air and 2.3 nm ($d_{hBN}$) hBN. Assuming that the relative thicknesses in 2D are directly translatable to the 3D gap volume, if a weighted average is used the effective refractive index in the gap drops to $n_g = (1 \times 1nm + 2.13 \times 2.3nm)/3.3nm = 1.79$. Using this information it is possible to extract maximum and minimum values for $d$ and $n_g$ and thus establish the acceptable range of values for the dipole antenna mode on our thin terrace of hBN. The results of this analysis are shown in table 5.1.

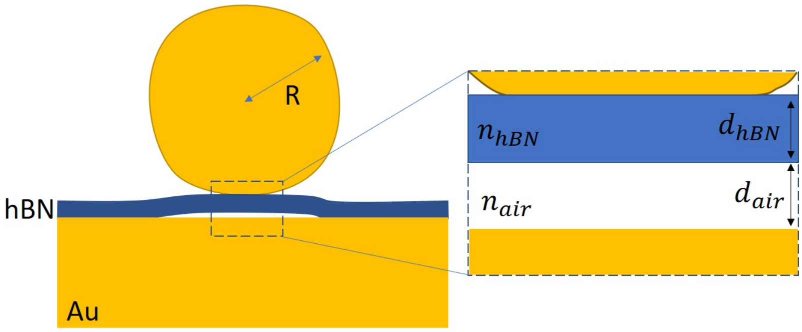

Fig. 5.6 The hybrid model of the gap for a nanoparticle of radius $R$ atop a layer of hBN of thickness $d_{hBN}$ with refractive $n_{hBN}$ which fluctuates in height above a Au substrate. Fluctuations in height mean that an air gap of thickness $d_{air}$ must be included with refractive index $n_{air} = 1$.

In contrast, such spacer fluctuations are undetectable on the thicker hBN terrace and the AFM height image reveals that this region is highly uniform. This is because the increased number of hBN layers increases the rigidity of the crystal, preventing this ‘bedsheet effect’. For this reason the original expected value for the peak position can be used of $657 \pm 5$ nm, using the error from the AFM measurement.

With knowledge of these spacer fluctuations and an initial approach to deal with them, it is now appropriate to move onto analysis of the dataset shown in Fig. 5.4. As would be expected based on the above AFM analysis, the three nanoparticles on the thicker terrace (blue in Fig. 5.4) are highly consistent both in peak position and intensity, displaying scattering efficiencies between $2.1-2.4\%$ and an average peak position for the dipole antenna mode of 646 nm (Fig. 5.7(a)). This average peak value is within 3 standard deviations of the expected

Table 5.1 Table showing the peak positions for the dipole antenna mode calculated using the circuit model and taking into account both the change in spacer thickness and refractive index as a result of height fluctuations.

| **Circuit model positions for $l = 1$ on thinner hBN terrace (nm)** | | |
|---|---|---|
| $n_g = 2.13, d = 2.34$nm | $n_g = 1.96, d = 2.84$nm | $n_g = 1.79, d = 3.34$nm |
| 720 | 684 | 654 |

value for this terrace of $657 \pm 5$ nm and it will be seen later that the remaining blue-shift from the expectation value of 11 nm can be readily explained. According to Eq. 5.1, greater spacer thickness leads to smaller changes in spectral position for the same change in thickness, and it is the combination of this factor with the enhanced crystal rigidity which leads to the reproducible spectra.

In contrast to nanoparticles on the thick terrace, there are 9 nanoparticles with a much greater degree of spectral variation on the thinner terrace. All spectra consist of two peaks, with a persistent peak which appears around 610 nm in addition to the coupled mode which shifts considerably in the range $620 - 820$ nm. The mode at 610 nm can be attributed to the $s_{11}$ mode since it does not appear to correlate strongly with the position of the coupled mode (see section 2.4.2). It is to be expected that the variation in peak position for the coupled mode increase with thinner layers as NPoM becomes more sensitive to changes in nanoparticle morphology and thickness, however the magnitude of variation cannot be explained by this aspect alone. As was discussed earlier, the additional effect of decreased rigidity in the hBN crystal leads to height fluctuations in thinner layers which contribute directly to this variation. The averaged dark field spectra from this terrace show a centre red-shifted by only 7 nm, to 653 nm, from the average for the thick terrace, while the expected (average) wavelength now including hBN height changes is 684 nm (centre column Table.5.1). The majority of spectra display peaks varying between 620 nm and 700 nm, indicating that nanoparticles are more likely to sit over a region with spacer thickness at values closer to 3.3 nm and with corresponding lower refractive indices due to the presence of air in the gap (Table 5.1). This is likely because the hBN height changes occur over surface areas similar in scale to the facet area, hence a nanoparticle deposited over an hBN surface valley will most probably be raised up at the facet edges. Using this logic, nanoparticles sitting on a region in which the spacer is solely hBN are unlikely to occur. Based on the above analysis it can be concluded that the more red-shifted spectra are the most representative case for a purely hBN spacer. Indeed, note that the inclusion of spectra 1 and 11 in the average shown in Fig 5.5a, which display coupled modes around 800 nm, shifts this peak position closer to the new expected average wavelength of 684 nm taking into account the influence of the air gap. However, such a large red-shift cannot be explained within the framework so far since even if it were over a height minima such that $d_{gap} = 2.34$ nm, a much higher refractive index of $n_g \approx 2.8$ would be required.

To explain the remaining differences between expected and measured coupled mode positions, a final modification to the model is required.

### 5.1.2 Inclusion of Passivating Ligands

All of the averaged experimentally measured spectra are blue-shifted relative to expectations based on the above analysis. Fig. 5.7(a), includes an average of spectra from 30 nanoparticles of 80 nm in diameter without hBN in the gap, taken from other particles in the vicinity of the hBN flake. With no passivating ligand surrounding the 80 nm nanoparticle, these nanoparticles would display only a single mode at $\approx$ 530 nm corresponding to the transverse mode of the nanoparticle. This would indicate direct contact between the nanoparticle and Au underneath which prevents the plasmonic coupling leading to the $l = 1$ dipole antenna mode. The fact that a dipole antenna mode is present for all nanoparticles around hBN, indicates that passivating ligands act as a robust spacer layer. Although passivating ligands are expected to be disordered over the nanoparticle surface, here I show that new calculations to estimate their contribution to this hBN NPoM system match well with experimental values.

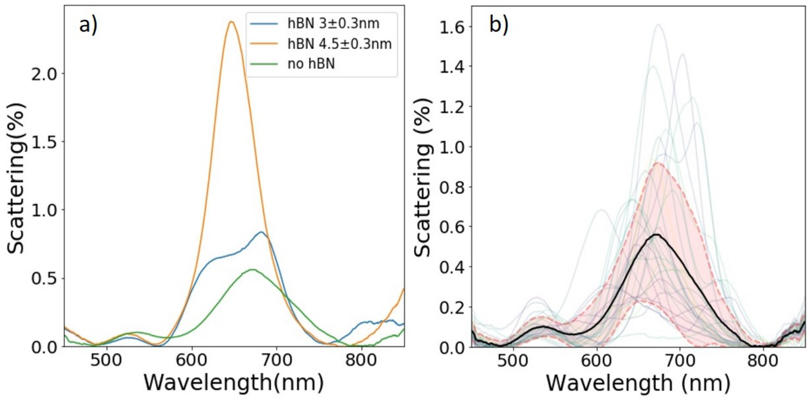

Fig. 5.7 Analysis of data on and off the hBN flake shown in figure 5.3. The average DF spectra (a) for nanoparticles on both thick and thin region, in comparison to spectra for nanoparticles around the flake (i.e. on Au). (b) shows a more in depth look at the spectra for 29 nanoparticles around the flake including standard deviation. (c) Shows the distribution of Q factors for the 29 spectra around the flake.

As discussed in chapter 3, the passivating ligands for the Au nanoparticles used in this thesis are citrate molecules, the refractive index of which is expected to have a maximum value of 1.5 at room temperature [140]. The average peak position for 29 nanoparticles of 80 nm diameter on Au surrounding the hBN flake is 659 nm. Using the same methodology as before while assuming that all of the spacer region is filled with citrate molecules suggests a citrate thickness of $\approx 2.1$ nm based on the experimental data. In actuality, it is likely that only a fraction of the total gap volume contains citrate, so this is a maximum thickness.

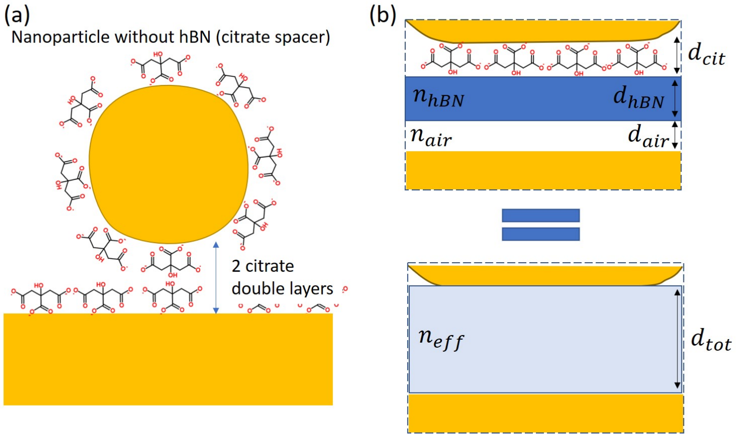

Fig. 5.8 A visualisation of the NPoMs without hBN (a). In this case the predicted thickness of $\approx$ 2.1 nm consists of 2 citrate layers. The pictures of molecules correspond to the physical molecule thickness plus the electric double-layer. The final adapted model includes the presence of these ligands enabling the calculation of wavelengths shown in Table 5.2 (b). In my model, this three stage system is assumed equivalent to a uniform slab of dielectric with $d_{tot} = d_{cit} + d_{hBN} + d_{air}$ and the effective $n_{eff}$ equal to the average of all layer refractive indices weighted by their thicknesses.

Based on previous studies on citrate binding mechanisms to Au nanoparticles [141], the thickness of this citrate layer in solution has a value of $0.8 - 1$ nm. With a gap refractive index of 1, the spacer thickness for dipole antenna mode at 657 nm would be $\approx 0.8$ nm, i.e. 1 citrate layer. Since our spacer thickness estimation using a refractive index of 1.5 is more than double this value and the refractive index lies between 1-1.5 regardless of gap volume fill fraction, it is reasonable to conclude that the spacer consists of between 1 and 2 double layers of citrate [141]. Referring to Fig. 5.7(b), the rare spectrum with a peak above 700 nm may have spacer thicknesses of 1 citrate layer, but the majority appear to have 2. The most likely explanation for this is that an extra residue layer is lying on the Au surface despite the cleaning measures taken, and this is supported by data and calculations from section 5.2 onward. The variation of the coupled mode is directly proportional to the variation in the number of citrate layers, and changes in its structure on the nanoparticle surface. It is well known that ligand structure and surface density can change at facet edges which may influence the number of layers or refractive index in a complex way and this will also be seen later in this chapter[141]. In the appendix I present a number of ways to remove these ligands, the most promising of which is $O_2$ plasma etching, however the process introduces its own problems in the form of damage to the sample.

Table 5.2 Table showing the peak positions for the dipole antenna mode calculated using the circuit model taking into account both the change in hBN height, citrate layer and consequent change in gap refractive index.

| Thin terrace | | | |
|---|---|---|---|
| 1 citrate layer | $n_g = 1.94$<br>$d = 3.34$nm | $n_g = 1.84$<br>$d = 3.84$nm | $n_g = 1.72$<br>$d = 4.34$nm |
| $\lambda_l^1$ (nm) | 668 | 647 | 628 |
| 2 citrate layers | $n_g = 1.84$<br>$d = 4.34$nm | $n_g = 1.77$<br>$d = 4.84$nm | $n_g = 1.68$<br>$d = 5.34$nm |
| $\lambda_l^1$ (nm) | 637 | 624 | 617 |

| Thick terrace | |
|---|---|
| 1 citrate layer | $n_g = 2.02$<br>$d = 5.56$nm |
| $\lambda_l^1$ (nm) | 631 |
| 2 citrate layers | $n_g = 1.94$<br>$d = 6.56$nm |
| $\lambda_l^1$ (nm) | 618 |

To estimate the influence of citrate on the mode positions, the resultant increase in height and change in gap refractive index needs to be taken into account once again. The thickness of 1 citrate layer will be taken as 0.9 nm with refractive index as 1.5. Taking this into account in addition to the bedsheet effect, the peak values shown in table 5.2 for the thin terrace are blue-shifted by the citrate and match the experimental data significantly better. The median value for one citrate layer now lies within one standard error of the experimental value. The calculations suggest that the presence of 1 citrate layer on hBN can explain the typical experimental peak positions, as 2 would blue-shift the spectra further from the average.

Based on the above analysis of an exfoliated hBN flake, there are a number of factors which increase variation in spectra and decrease data quality. In order of significance, these factors are:

1. Fluctuations in hBN height (bedsheet effect) and corresponding variation in $n_g$ and $d$
2. Presence of citrate passivating ligands and corresponding variation in $n_g$ and $d$
3. Limited area of hBN reduces possible number of nanoparticles for data collection, reducing statistical confidence
4. Changes in facet shape/size influencing outcoupling from gap
5. Fluctuations in nanoparticle size

6. Fluctuations/roughness in Au surface

All of these factors increase in significance with decreasing gap size. Points 4 and 5 are set by the nanoparticle production method and are controlled by the manufacturer[61]. The roughness of the Au surface is improved by using template-stripping or by very slow thermal evaporation rates. The other points in this list can be addressed as follows:

1. Use large area CVD hBN to collect spectra from many hundreds of nanoparticles, thereby improving statistical confidence in results
2. Transfer the hBN in such a way as to minimise the influence of the bedsheet effect
3. Remove adsorbents from the gap, either by depositing ligand-free nanoparticles or by removing the citrate post-deposition

Since they have such a large and clearly detectable influence on the experimental data, these points must be addressed for thinner hBN layers. In following sections on trilayer and monolayer hBN, various methods will be discussed and implemented to reduce the influence of these factors. Removing adsorbents will prove to be more challenging to overcome, with various methods to achieve this discussed toward the end of this chapter.

## 5.2 Trilayer hBN

The growth and transfer of monolayer CVD hBN is described in section 2.3.2. The transfer of 3 layers of hBN is achieved via repetition of the same steps and cleaning processes described for monolayer three times.

### 5.2.1 Analysis of hBN Trilayer on Au

The first challenge when working with very thin hBN is proving it exists on the substrate. Thankfully, trilayer hBN is simpler to work with than monolayer, because it is easier to observe in bright field illumination as it has three times better optical contrast. While it still has very low contrast on Au under a bright field microscope objective, the trilayer can be observed by eye at an angle with bright illumination from above (Fig. 5.9(a)). Since three monolayers of hBN are stacked above one another, the number of multilayer regions per unit area (seen clearly as white regions in SEM (Fig. 5.9(b)) triples compared to monolayer (Fig 5.19(b)). The fact that multilayer density increases by approximately three times is one indication that three monolayers have been successfully transferred. It can be clearly

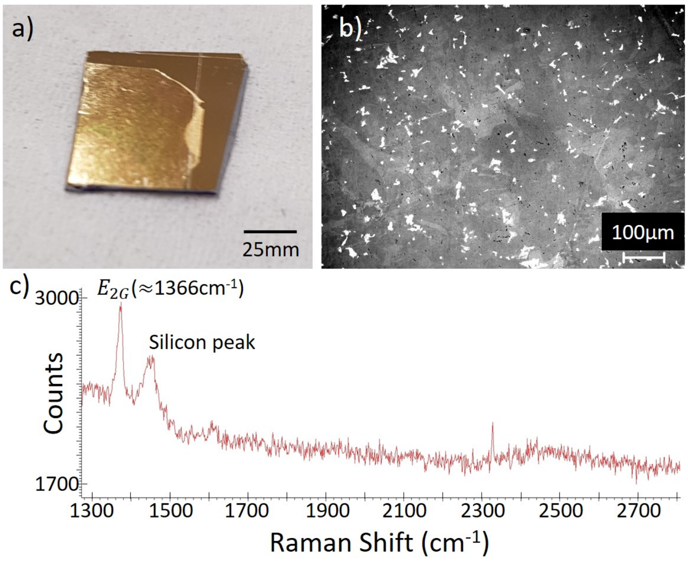

Fig. 5.9 Qualitative and quantitative observation and measurement of the hBN trilayers used in this experiment. The contrast due to the trilayer is clearly seen by eye when viewed at an angle under bright illumination (a). The density of multilayers, seen as white regions in (b), is extremely low despite the stacking of multiple layers of hBN. Raman scattering of the material on a Si substrate with 552 nm wavelength incident (c) fully confirms the presence and high quality of the hBN monolayers transferred to form the trilayer.

seen in Fig. 5.9(b) that the multilayer density remains low despite the stacking ($< 3$ defects per $100\mu m^2$), with all areas between consisting of trilayer hBN. SEM reveals no tears in the layers apart from at the edges, and there are very few folds in the layers, a success resulting from the transfer procedures reviewed in chapter 3.2.1. As previously stated, Raman scattering by hBN cannot be detected on Au for monolayers using our systems and the same is found to be true for trilayer. Transferring monolayers from the same Fe foil growth substrate onto Si rather than Au enables further confirmation of the presence of hBN (Fig. 5.9(c)). The strong Raman scattering of the $E_{2G}$ peak clearly shows the presence of monolayer hBN. It's linewidth and relative intensity is on the order of Raman measurements on exfoliated samples [77].

Another method to measure the number of hBN layers, or at least to confirm it is greater than 1 layer, is by using bright field reflectivity referenced to Au. Based on previous bright field measurements on exfoliated hBN, the reflectivity drops by $\approx 1\%$ for every 0.5 nm of hBN. Therefore $\sim 1.5$ nm of hBN is predicted to show a reflectivity of 97% of the bare gold at 400 nm when placed on Au, which matches closely with experimental measurements for this sample[77].

While these measurements confirm the presence and quality of the hBN trilayer, they do not give information on the precise thickness. The previous section demonstrated the extreme

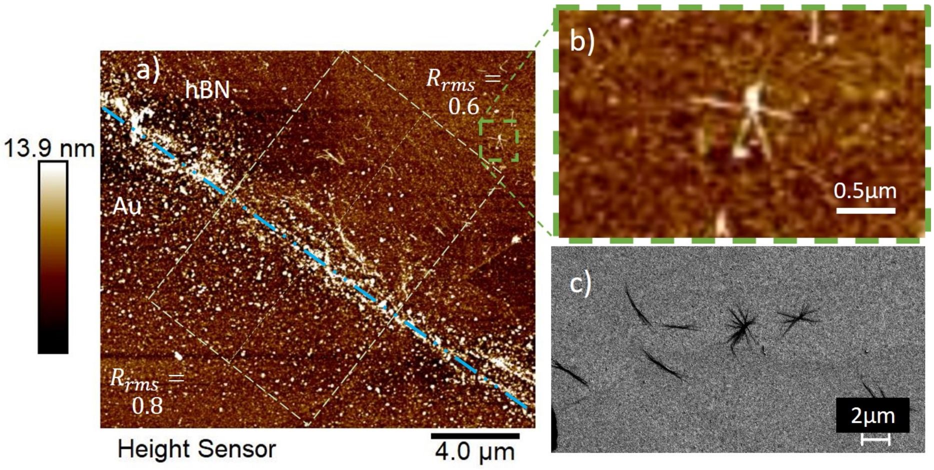

Fig. 5.10 Using AFM analysis to determine trilayer thickness and confirm presence of the material by comparing with features observed in SEM. Two edges of the trilayer sample (a,b) shown in Fig 5.7 with blue lines indicating the trilayer edge with text indicating a Au or hBN region. White boxes enclose the region over which values were flattened and averaged to reduce the influence of noise, with the RMS roughness shown in Au and hBN regions for comparison. One clear identifier of the presence of trilayer are the star like multilayer growth regions shown in AFM (c) and SEM (d).

sensitivity of the NPoM system, highlighting the importance of knowing this value accurately and thus AFM is required. AFM analysis of different edges on the trilayer sample from Fig. 5.9(a,b) is shown in Fig. 5.10(a,b). In the images, the edges of the transferred trilayer are highlighted by blue dashed lines. Used to improve accuracy of the step height measurement at the trilayer edge, white dashed boxes represent the area over which the height data is averaged, with the angle of the box representing the orientation such that it is perpendicular to the step edge. As shown in Fig. 5.10, whilst the sample is very clean $\pm 10\mu m$ from the edges, folds and defects appear which trap impurities during the cleaning process, increasing spikes in the data in these areas.

This sample had to be prepared using an evaporated rather than template stripped Au substrate, which has the undesirable effect of increasing the root mean squared (RMS) roughness. This is required because to burn off residues from the hBN surface, the substrate must be annealed at $350°C$ which breaks down the epoxy beneath the Au, subsequently deforming the Au surface above. The use of certain solutions can also damage the epoxy if the substrate is immersed in a bath, as is the case here. This increase in RMS roughness makes it more challenging to measure the height of the hBN trilayer accurately. Since the spacing between each layer is 0.4 nm with the separation between hBN-Au $0.4 - 0.8$ nm e.g.(1-2L), the thickness of the AFM trilayer is expected to be between $1.2 - 1.6$ nm. The RMS of the evaporated Au is 0.8 nm, so averaging over a large area is very important otherwise the trilayer is difficult to distinguish above the noise.

Using the method of averaging either side of the trilayer edge as described and levelling the image to account for substrate tilt, the thickness of the trilayer was found to be $1.5 \pm 0.5$ nm. The error in this value takes into account the standard deviation in height values on Au and on hBN, which are 0.3 nm and 0.16 nm respectively. The thickness value was taken at a distance of $10\mu m$ from the trilayer edge, beyond which the thickness remained within error. This is because at the edge of the trilayer there are significant variations in height due to folds and tears in the layers. Since the production of this trilayer sample involves multiple monolayer transfers, it might be expected that the height fluctuations as a consquence of the bedsheet effect would be more prominent for this sample. However, the measured thickness values match well the expectations for trilayer hBN and thus the problem of height variation in the spacer appear to have been, for the most part, addressed. The transfer process, and in particular the strong heating step, removes other residues trapped between Au, hBN and between the hBN layers bringing them together via capillary forces as liquid migrates toward the edges. Nonetheless, across the entire area of the sample fluctuations in height within the error measurable using AFM are to be expected and will be attributed predominantly to air pockets between layers during the following calculations.

The change in the RMS roughness from Au to hBN reveals the way in which the hBN lies over the Au surface, very important for a technique as sensitive as NPoM. If the RMS roughness on Au and hBN was the same, this would mean that the hBN exactly fits the morphology of the Au surface. In this experiment the measured RMS roughness drops from 0.8 nm to 0.7 nm, which indicates that the hBN matches the morphology of the Au well, but still implies that it lies on the surface like a sheet thereby slightly smoothing out the surface. This change in the way the hBN lies across the Au surface is not expected to have a significant effect on the data, but may make a small measurable contribution to blue-shifting of the dipole antenna mode.

### 5.2.2 80 nm Nanoparticles on Trilayer hBN

With accurate knowledge of the height of the hBN trilayer spacer and it's thickness, 80 nm nanoparticles were deposited onto the sample surface using the usual technique. The sample at 100× DF clearly shows that the nanoparticles change colour, from majority green off-hBN to red on-hBN (Fig. 5.11(a)). This indicates that the coupled mode off-hBN is red-shifted beyond the visible range, while on-hBN the coupled mode lies in the red region of the visible spectrum. Due to the large area of hBN material, 256 nanoparticles could be measured both on trilayer hBN and 184 on Au (Fig. 5.11(b,c)). This meant that far more rigorous statistical analysis could be completed on the sample compared to for exfoliated hBN. The dark field scattering measurements for 80 nm NPoMs both on and off hBN are shown in Fig. 5.11 with

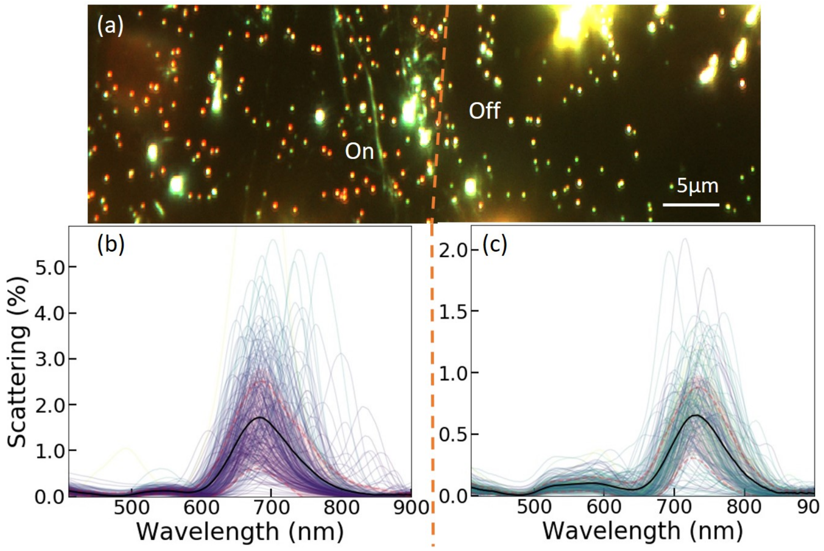

Fig. 5.11 Averaged dark field spectra off-(a) and on-hBN (b) with standard deviations in intensity indicated by red-dashed lines and all spectra behind. The two averages are also shown in the same graph for intensity comparison.

additional statistical analysis of peak data continued from Fig. 5.12 onwards. Due to the growth method, multilayer regions are always significantly thicker than trilayer and are easily observed in dark field as bright and amorphous regions $\sim 1\mu m$ in diameter. Since these regions were clearly identifiable, assuming no tears in the hBN layer (none were identified in SEM) it is reasonable to conclude that spectra from all nanoparticles were taken on trilayer hBN regions only.

Based on the results of the thicker exfoliated sample, citrate is expected to play a clear role, so the first task is to quantify the influence of citrate in terms of dark field scattering. Comparing the average scattering spectra for 80 nm on Au (Fig. 5.12(a)) to the measurements off exfoliated hBN (Fig. 5.7), the peak position is clearly red-shifted from 657 nm to 727 nm due to a change in the adsorbents on the surface. This indicates that this sample is significantly cleaner, and therefore the thickness of adsorbents in the gap has decreased compared to the exfoliated sample, from 2.1 nm to 0.9 nm, e.g. a single layer of citrate assuming $n_g = 1.5$. This shows why one layer of citrate on hBN was required to explain the experimental data for the exfoliated sample, while two was required on Au surrounding the flake. Only 29 nanoparticles were measured around the exfoliated hBN, thus it is possible (but improbable) that were more spectra taken, the average would have tended to the same wavelength. This highlights the importance of taking a larger number of spectral measurements.

As previously mentioned, these results highlight the importance of reducing the influence of citrate and a number of potential methods for achieving this are presented in the appendix. It also shows how gap adsorbents can vary between otherwise similar samples and therefore measurements both with and without the spacer material, but with the same deposition parameters, should be taken for each experiment as a reference.

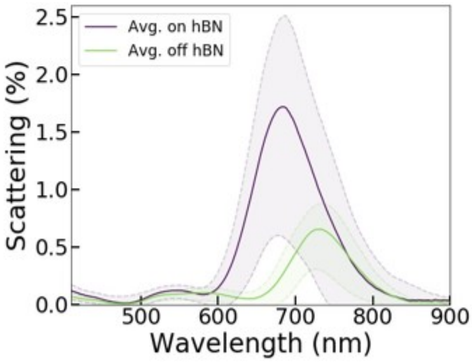

Fig. 5.12 Averaged dark field spectra off- (green) and on-hBN (purple) with standard deviations in intensity indicated by dashed lines.

Comparing the data off-hBN (Fig. 5.11(c)) to on-hBN (Fig. 5.11(b)) shows that the average spectrum is blue-shifted by the presence of trilayer hBN and that the spectral distribution displays greater spread, with a number of dipole antenna mode peaks at values greater than 800 nm. The standard deviation in intensity is also larger with trilayer hBN, showing that the spread of intensity values is greater (Fig. 5.12) and, just as was found for the exfoliated sample, the scattering intensity from NPoMs on hBN is considerably greater (2.7× ) despite the significantly larger gap which weakens coupling and blue-shifts modes.

While plots of the average spectrum as shown in Fig 5.12 are extremely useful as an initial tool to distinguish clear differences between datasets, they are less helpful for identifying and analysing individual modes. This was seen clearly for nanoparticles on the exfoliated hBN sample, where an analysis of all spectra (Fig. 5.4) was required for a good understanding of the system. A simple mean such as this can lead to unrepresentative asymmetric modes which blur additional modes, increase apparent linewidth, and provide little clear information on the spread in wavelength of the peak positions for each mode. Additionally, even for samples which display only a single mode in addition to the transverse mode, depending on the skew of mode distributions the mean value can be an unrepresentative measure of the expected peak position.

Fig. 5.13 demonstrates the clear advantage of large-area CVD hBN compared to exfoliated, where spectra from many hundreds of NPoM structures on an identical thickness of hBN can be taken and the resultant distribution analysed. Here the spectra are sorted from bottom of the graph to top according to the position of the coupled mode[4]. This new representation of the data allows identification of more subtle differences between the NPoM responses. While the averages (Fig. 5.12) show single asymmetric modes, upon close inspection of Fig. 5.13 individual spectra for both on and off hBN frequently show multiple modes in addition to the bright dipole antenna mode. This is to be expected based on the discussions from section 2.4.2.

---

[4] The data is sorted by the brightest mode, with the coupled mode assumed to dominate scattering intensity

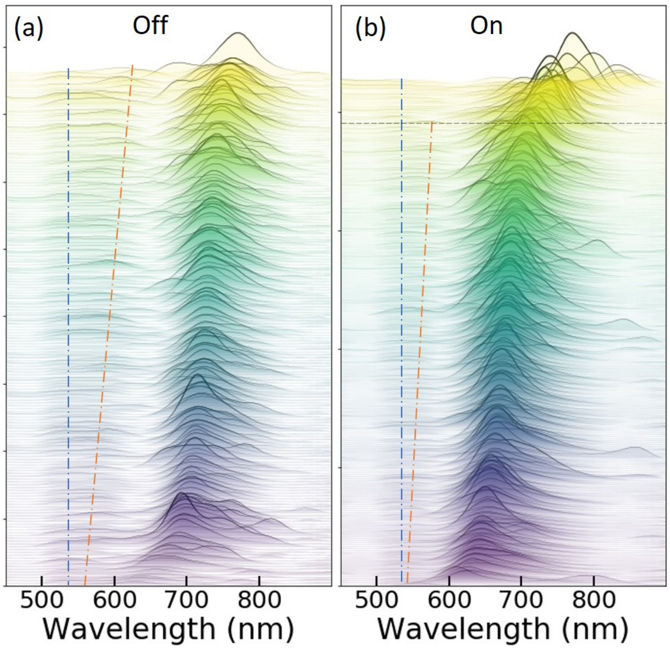

Fig. 5.13 All of the dark field spectra considered in this experiment, both off (a) and on (b) trilayer hBN NPoM, plotted from bottom to top in order of brightest mode peak wavelength. Blue dashed lines represent the constant position of the transverse mode for scattering from individial nanoparticles. Orange dashed lines track the average peak position of the $l = 2$ mode observed to move in sync with the coupled mode position.

Focussing on the brightest dipole antenna peaks first, both distributions display a characteristic tail for the most blue-shifted modes and then a range of more evenly distributed values around the mean. This region of even distribution spans a wavelength range of around 700-775 nm for off-hBN and 625-700 nm for on-hBN. In contrast to 80 nm NPs off-hBN, data for on-hBN shows a clear red-shifting tail above 720 nm (grey dashed line, $\approx 15\%$ of spectra with the largest red-shifts) which is not observed for data off-hBN.

In addition to the behaviour of the coupled mode, spectra for on-hBN more frequently display weaker modes strongly red-shifted from the bright dipole antenna mode. The position in wavelength of this additional mode fluctuates significantly, implying that its presence is due to hybrid modes which depend strongly on the variable geometry of the gap facet and its edges, the most likely candidate for which is $s_{11}$ (see section 2.4.2). The blue dashed lines indicate the constant position of the transverse mode, whilst orange tracks the progress of another mode identified for nanoparticles both on-hBN and off-hBN. This mode is very clearly proportional to the wavelength of the $l = 1$ mode and therefore is attributed to the $l = 2$ mode. The position of this mode matches very well with calculations discussed in chapter 2, from which the mode is expected to sit around $\sim \lambda_l^l/1.25$ below the dipole antenna mode and vary around this wavelength due to changes in facet and edge geometry as the $j_2$

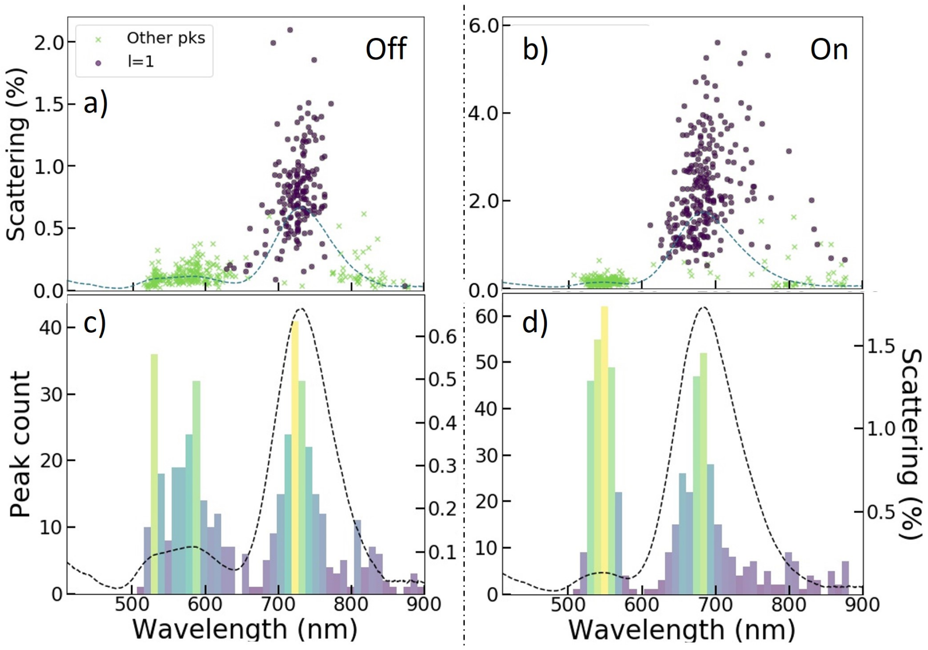

Fig. 5.14 Peak positions for dark field scattering from 80 nm nanoparticles on (a) and off (b) trilayer hBN. Beneath each spectrum is a histogram for on (c) and off (d) trilayer hBN to add clarity and aid in peak identification with yellow bars representing the maximum count and blue-black the minimum. The dashed lines represent the average scattering spectra as shown in Fig. 5.12.

hybrid mode. For on-hBN NPoMs this mode can be tracked up to the final 15% of the most red-shifted spectra, at which point it also rapidly red-shifts.

### 5.2.3 Mode Distributions

A peak finding algorithm is applied to the data shown in Fig. 5.13 to create scatter plots as shown in Fig5.14(a,b). In these scatter plots the points are divided into two groups which are defined in the plots by their colour. Dark purple points originate from peaks of maximal scattering intensity, corresponding to the dipole antenna modes. Light green crosses represent other mode positions including additional red-shifted modes such as the transverse, $l = 2$ and facet modes. Each identified cluster within these peak distribution plots, corresponds to the distribution in wavelength and intensity of an individual mode, containing a great deal of information about the behaviour of that mode. In particular, the distribution of a mode cluster in wavelength and intensity can be used to extract clues about the behaviour of NPoM with hBN. In assigning these modes it is assumed that the coupled mode never sits above 900 nm.

The data for Fig. 5.14(a,b) is used to create peak position histograms (Fig. 5.14(c,d)). Use of histograms in this way helps to identify individual modes with spikes corresponding to modal peak positions, giving a clearer indication of their distribution in wavelength. For example, comparing the average spectra off-hBN to Fig. 5.13 there is identification of a mode which most frequently appears just above 800 nm and is not identifiable in the averaged spectrum. This mode gives the averaged spectrum off-hBN (Fig. 5.11(c)) an asymmetry with a tail toward longer wavelengths, not a true reflection of the data. Meanwhile, the histogram for nanoparticles on trilayer hBN (Fig5.14(d)) shows a distribution of peak wavelengths which is positively skewed (i.e. tailing off at longer wavelengths, see below).

The randomness of an individual cluster can be described in part by its skew, the magnitude of which is proportional to the fraction of values beyond a given wavelength and their distance from the mean value. If the number of points either side of the mean wavelength value are equal and their distances are randomly distributed, the distribution is a Gaussian. This would indicate no clear trend in wavelength, i.e. the dependence on refractive index and gap distance is linear. A negative or positive skew means that values tend to lie below and further from the average or above and further from the average respectively. Generally, a skew magnitude of $> 0.5$ implies that there is a slight non-gaussian trend to the distribution and a magnitude $> 1$ means than the trend is clearly non-gaussian. The skew for a mode distribution can give a clue toward the relationship between peak wavelength or scattering intensity in the nanogap.

Assuming a constant refractive index with gap distance, it is expected that the distribution for the coupled mode display a positive skew, since as gap distance decreases with constant refractive index, modes are red-shifted by a larger degree. However, as seen for the exfoliated hBN experiment the presence of lower refractive index contaminants in the gap along with hBN causes the effective refractive index to drop with increasing gap distance. The influence of this effect on mode distributions is seen in the following analysis. [5]

This analysis is extended to try and identify the exact characteristic behaviour of NPoM with hBN despite the presence of citrate, and used to show comparative trends with wavelength and intensity. Modes which depend on facet geometry vary significantly depending on a number of different morphological influences and thus are not particularly useful for gaining an initial insight into the influence of hBN in NPoM. For this reason, the distribution of the well-understood coupled modes (dark purple points in Fig. 5.14(a,b)) is focussed upon for analysis.

Comparing therefore the distribution of the dipole antenna mode on and off-hBN (blue points, Fig. 5.15), there is a clear difference between the distributions. Here, blue dashed lines represent standard deviations in intensity, wavelength and red dots lie at the mean values.

---

[5] It is assumed in this analysis that fluctuations in nanoparticle size and morphology play a negligible role in the coupled mode position compared to changes in gap properties. This assumption is supported by the experimental results from here onward.

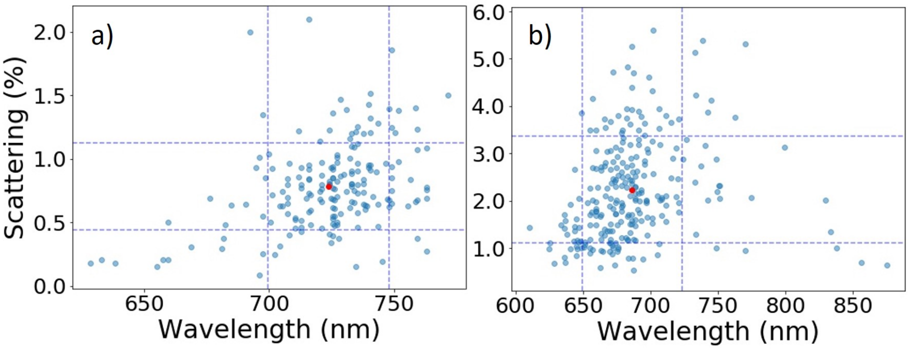

Fig. 5.15 Comparing the wavelength and intensity distributions for 80 nm nanoparticles off (a) and on (b) trilayer hBN. Blue dashed lines correspond to the standard deviation values in intensity and wavelength, while red-dots correspond to the mean.

Nanoparticles off-hBN (Fig. 5.15(a)) show a distribution with an average $l = 1$ mode at $\lambda_1^l = 724 \pm 19$ nm and scattering of $0.8 \pm 0.3\%$. The skew of the distribution in wavelength is -0.68, indicating a slight non-gaussian trend due to the blue-shifting tail observed for shorter wavelengths in Fig. 5.13(a). This is opposite to expectations based on equation 5.1, where as spacer thickness is decreased with constant gap refractive index dipole modes should show increasingly red-shifted modes. The skew in intensity is 1.13, indicating a clear tail toward higher intensities due to the fact that scattering is not able to take negative values.

The mean dipole mode on trilayer hBN lies at $\lambda_l^1 = 684 \pm 27$ nm with a scattering of $2.3 \pm 1.1\%$, $2.7\times$ greater than off-hBN. This intensity enhancement is almost identical to observations made on thicker hBN, showing that it is the result of the addition of hBN material to the NPoM gap. The dipole antenna mode (Fig. 5.15(b)) displays a positive skew of $+0.80$, opposite to the trend off-hBN. It has been seen that spectra both on and off hBN initially display a blue-shifting tail (Fig. 5.13), however on hBN at longer wavelengths a more significant red-shifting tail counteracts this trend in the distribution leading to a positive skew overall. Based on equation 5.1 positively skewed data is to be expected, but the magnitude of the positive skew should increase with increasing average dipole antenna position. For an average mode wavelength of 684 nm, blue-shifted from the data off-hBN, the magnitude of the red-shift at longer wavelengths cannot be explained within the framework of equation 5.1 alone.

To explain this we require consideration of the hybrid nature of the spacer as for the previous section. Using equation 5.1 and assuming the entire measured thickness is hBN, the experimental position of the dipole antenna mode on the trilayer sample lies at more than three standard deviations from the expected value of 766 nm for $n_g = 2.13$ and $d_{hBN} = 1.5$ nm. Once again, this blue shift indicates that the real gap size is larger and refractive index lower. Including the known effect of citrate and assuming a single layer of thickness 0.9nm as calculated before, $n_{eff} = ((1.5nm \times 2.13) + (0.9nm \times 1.5))/(2.5nm) = 1.89$ with a total gap thickness of $d_{tot} = 2.4$ nm. This significantly blue-shifts the expected position down to 693 nm, still red-shifted from the experimental position, but well within one a standard deviation of ±27 nm. It is clearly possible to predict the average position of the dipole antenna mode well by changing the refractive index to account for citrate. The wider variation in peak position for trilayer hBN must therefore be due to either a difference in the behaviour of the spacer when citrate and/or air are included, or due to inherent properties of the hBN in the gap. We will explore these possibilities from here onward.

### 5.2.4 Modification of the Circuit Model

To explain the distribution in wavelength for 80 nm Au NPs on trilayer hBN an adapted model is required which takes the hybrid nature of the spacer into account. To do this a weighted average replaces the constant $\varepsilon_g$ in equation 5.1 and a full functional dependence is properly investigated. With the further confirmation of the accuracy of using the weighted average above, equation 5.1 is modified simply to,

$$\left(\frac{\lambda_1^l}{\lambda_p}\right)^2 = \varepsilon_\infty + 2\varepsilon_d + 4\varepsilon_d\varepsilon_g(d_{tot})^\chi ln[1 + \beta R/d_{tot}], \tag{5.2}$$

with $d_{tot} = d_{hBN} + d_{cit} + d_{air}$ and the new thickness dependent dielectric gap permittivity,

$$\varepsilon_g(d_{tot}) = \frac{d_{hBN}\varepsilon_{hBN} + d_{cit}\varepsilon_{cit} + d_{air}}{d_{tot}}. \tag{5.3}$$

Plotting this relationship (Fig. 5.16) sheds light more clearly on the behaviour of hybrid spacers in NPoM. In the figure, yellow dashed curves are to be used as a reference, representing calculations completed as usual using equation 5.1 with the spacer as pure hBN (no citrate or air) and thickness swept from 0 to 10 nm, thus $\Delta d_{tot} = \Delta d_{hBN}$. Red curves result from the same approach, but for citrate rather than hBN, thus $\Delta d_{tot} = \Delta d_{cit}$. Dark brown curves represent the adapted relationship described by equation 5.2 including the change in gap refractive index due to constant citrate and hBN layers $d_{cit} = 0.9$ nm, $d_{hBN} = 1.5$ nm, but with ‘air pocket’ thickness swept from 0 to 10 nm, thus $d_{tot} = \Delta d_{air} + d_{hBN} + d_{cit}$. For the dark brown curves, the minimum gap thickness is $d_{cit} + d_{hBN} = 2.4$ nm when $d_{air} = 0$. Horizontal dashed lines intersect at thicknesses of 2.4 nm and 0.9 nm, corresponding to the expected $\lambda_1^l$ on trilayer hBN (brown) and off-hBN (orange, citrate only).

Comparing the dark brown to other curves, the blue-shift due to the presence of lower index material in the gap is clearly present in the modified model (Fig. 5.13a). Above a

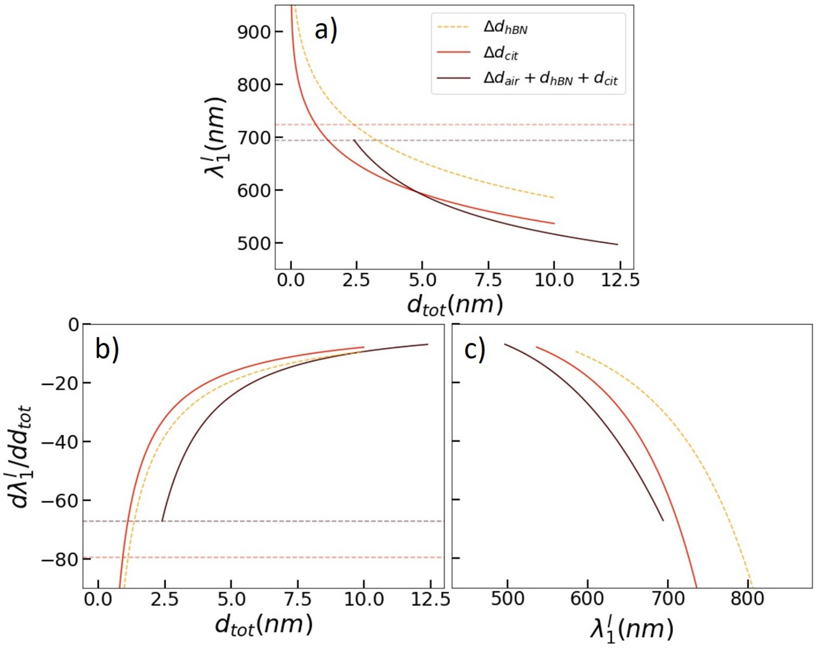

Fig. 5.16 Modifying the circuit model to include changing refractive index with gap distance $d_{tot}$. Compared to the usual circuit model with constant $n_g$ and changing $d_{cit}$(orange), $d_hBN$(yellow), the hybrid model shows a sharper red-shift for larger gaps (brown) (a). Brown and orange dashed horizontal lines, correspond to expected values on and off-hBN respectively. The gradient (tuning rate) is then explored as a function of gap distance $d_{tot}$(b) and coupled mode position (c).

thickness $d_{tot} = 7.5$ nm the trend observed is approximately the same as the original model, with a constant blue-shift for the same spacer thickness. However, as the air thickness decreases to small values ($d_{tot} = 2.4 - 5$ nm) the gradient rapidly increases (Fig. 5.13b), red-shifting $\lambda_1^l$ faster than described by equation 5.1. The modified relationship (dark brown) crosses the citrate curve (orange curve) so that for the same position of $\lambda_1^l$ the gradient is higher, and when there is no air present the red shift is comparatively small despite the significantly greater thickness (orange horizontal compared to dark brown). The inclusion of the hybrid refractive index leads to a gradient increase of ×1.7 for an equivalent thickness of pure hBN (Fig. 5.16(b)). The increase in magnitude of the spread for dipole antenna peaks seen in Fig. 5.15 is proportional to the gradient, because for the same change in spacer thickness the wavelength shift will be greater. Note that this gradient value is the same as to the ‘tuning rate’ for the couple mode often used in literature [56].

Based on the coupled mode wavelength off-hBN the thickness of citrate on Au is calculated to be 0.9 nm using equation 5.1. On Au the gradient is larger than on the much thicker trilayer spacer, but the difference is small, with a gradient increase of only ×1.2 (orange vertical line compared to dark brown Fig. 5.16(b)). Considering the gradient as a function of $\lambda_1^l$ (Fig.5.16(c)), usually when decreasing the thickness of two different pure spacers the difference between $\lambda_1^l$ for the same gradient value increases (orange compared to dashed yellow Fig. 5.13(c)). Conversely, for a hybrid spacer the difference initially increases, but then decreases (dark brown compared to other curves Fig. 5.16(c)).

This gradient increase for the same dipole antenna position goes some way to explaining why the distribution shows a wider range than expected using a constant refractive index for a given thickness. Intuitively, this behaviour is the result of the simultaneous increase in the overall refractive index of the spacer as the air thickness decreases. However, based solely on this analysis nanoparticles on Au should still display a larger spread and positive skew than on trilayer hBN, since the gradient is larger at 0.9 nm with $n_{gap} = 1.5$. Additionally, the significantly lower spread for the distribution off-hBN cannot be explained by fluctuations in the thickness of citrate with constant refractive index, since if the thickness is reduced the gradient on Au increases by a larger factor than when the same occurs while on trilayer hBN.

The most likely explanation for this difference is the behaviour of citrate in the gap. If the amount of citrate in the gap varies, it should also be possible to model it as a hybrid gap which depends on the fill-fraction. This will be addressed in further detail for the monolayer hBN case.

A dramatic increase in scattering intensity is clear for nanoparticles on trilayer hBN which increases from an average of 0.8% to 2.3%, very high compared to other 80 nm NPoMs (e.g. SAMs of the same thickness) [11, 8]. In this case, there is no reasonable situation in which the hybrid nature of the spacer alone (i.e. the presence of citrate and/or air) can explain the behaviour. The same gap contaminants are present for nanoparticles on Au and the gap is significantly smaller, but the scattering is far weaker. This means that the enhancement is due to the specific properties that the presence of hBN brings to the nanogap. This intensity should be related to the enhancement in the gap, e.g. if hBN increases the near-field gap enhancement despite the larger gap size, this may correlate with the enhancement in far-field.

### 5.2.5 Gap Enhancement and Coupled Mode Linewidths

To explore this, the Q-factor for each coupled mode is calculated to determine whether the presence of hBN improves in-coupling to the gap and boosts field enhancement. The field enhancement in the gap is proportional to the gap refractive index ($n_g$) and inversely proportional to the gap distance ($d$)[45]. For small gaps ($\lessapprox$ 5 nm) the lateral localisation of the field has an approximate spatial FWHM of $\Delta x = \sqrt{2Rd/\varepsilon_d}$, which matches simulations in previous literature [133]. Light of field amplitude $E_0$ is incident at high angle on this spherical nanoantenna with polarisability $\alpha = 4\pi R^3 \chi$ where,

$$\chi = \frac{\varepsilon_m - \varepsilon_s}{\varepsilon_m + 2\varepsilon_s} \approx 2 \tag{5.4}$$

for Au in air close to $\lambda_1^l$ in this case. Energy $\frac{1}{2}\varepsilon_0 \alpha E_0^2$ is concentrated into the nanogap mode of volume

$$V = \frac{d\pi \Delta x^2}{4ln2} = \frac{\pi R d^2}{2ln2n_g^2}. \tag{5.5}$$

This therefore contains energy of

$$\frac{1}{2}\varepsilon_0 \varepsilon_g V E_m a x^2 \tag{5.6}$$

which is boosted by the Q-factor, leading to,

$$\frac{E_{max}^2}{E_0^2} = (16ln2) Q n_g \frac{R^2}{d^2}. \tag{5.7}$$

Comparing the Q-factors on and off hBN (Fig. 5.17) reveals only a slight difference in the averages, with a value of $9.6 \pm 1.7$ off-hBN and $9.0 \pm 2.2$ on hBN. For 80 nm Au NPs on citrate (i.e. off trilayer hBN) $d_g = 0.9$ nm and $n_g = 1.5$ leading to $E_{max}^2/E_0^2 = 3.15 \times 10^5$.

Meanwhile, according to the new hybrid gap model, which has been shown to more accurately predict mode positions, now $d = d_{tot}$ and $n_g = n_{eff}$. For 80 nm Au NPs on trilayer hBN, $d_{tot} = 2.4$ nm and $n_{eff} = 1.89$. Substituting the remaining values leads to $E_{max}^2/E_0^2 = 5.24 \times 10^4$ which is $> 6\times$ reduced enhancement in the nanogap compared to off-hBN. This means that on average there is not an increase in $Q$-factor on trilayer hBN which is able to counteract the increase in gap size and lead to an enhancement of in-coupling to the gap.

Next, the relationship between the full width half maximum (FWHM) and intensity of the dipole mode is examined (Fig. 5.18(a)). Off-hBN, the scattering value shows no clear dependence on the FWHM of the dipole antenna mode, but on trilayer hBN there is a clear relationship whereby scattering is seen to increase as the FWHM of the mode drops.

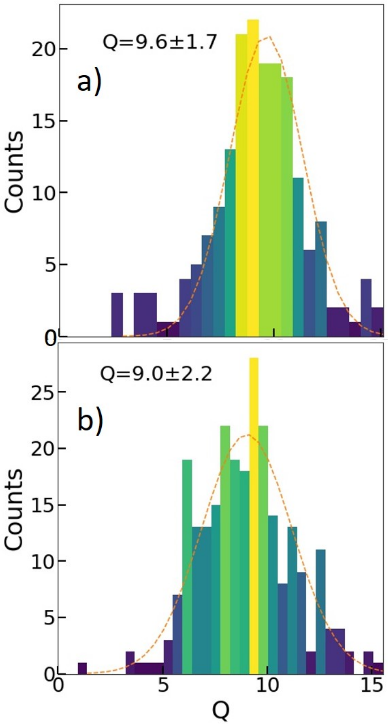

Fig. 5.17 The Q-factors calculated from coupled modes for 80 nm spherical Au nanoparticles off (a) and on (b) trilayer hBN.

In other words, the brightest individual modes most frequently display the lowest value of FWHM. To try and approximate this relationship, ln(scattering) vs FWHM is plotted (Fig. 5.18(b)). There is a close to linear relationship (purple dashed line), indicating an approximately exponential relationship of the coupled mode and its radiative coupling rate, decreasing at longer wavelengths on-hBN, compared with no clear trend off-hBN. Along with the scattering enhancement relative to off-hBN, this appears to be a feature of NPoM with hBN, but is likely a feature of all spacers which cannot be displaced in the gap such as other vdW materials.

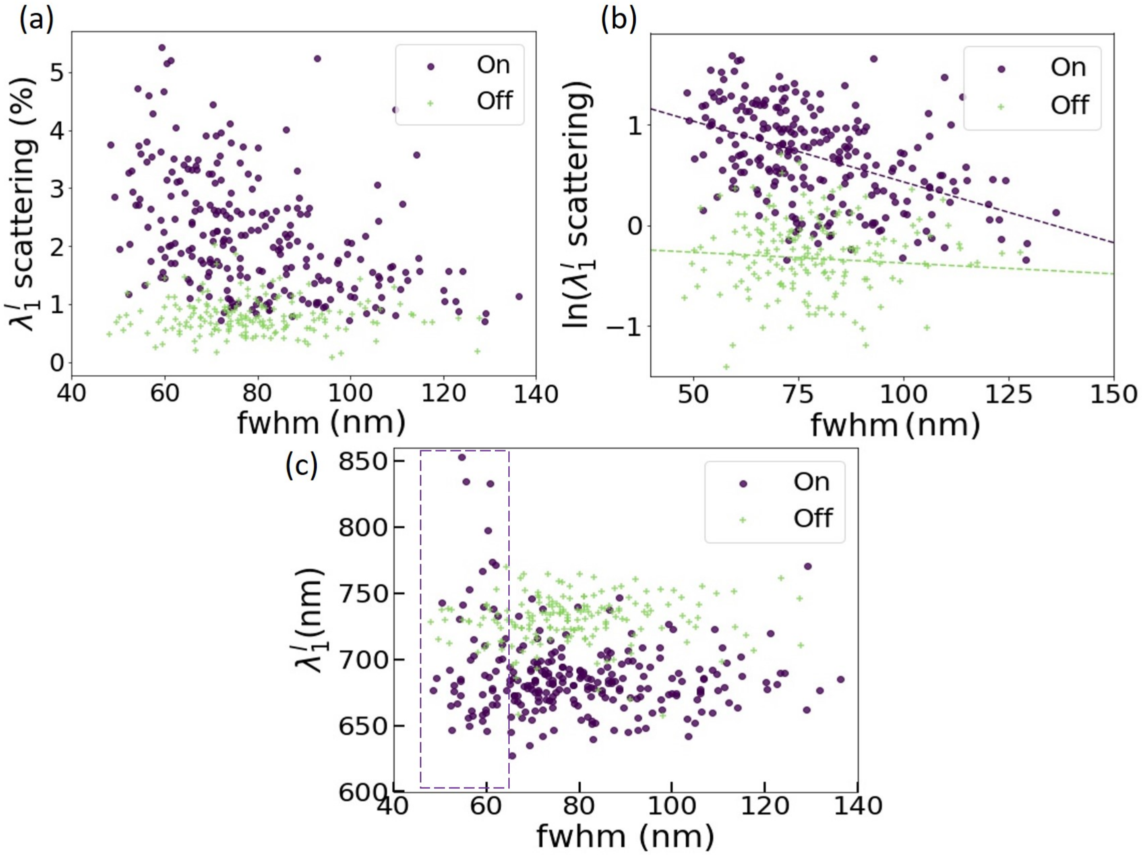

Fig. 5.18 (a) Comparing the FWHM to the intensity of the dipole antenna ($l = 1$) mode, with purple dots representing on-hBN, and green crosses off-hBN. While not perfectly matching the trend on-hBN ln(scattering) vs FWHM (b) shows a close to linear relationship with trend lines on (purple dashed) and off hBN (green lines) confirming this. (c) Shows the clear difference in peak position for the coupled mode on and off-hBN in addition to the broader spread of peak positions on-hBN.

Finally, the relationship between the FWHM and $\lambda_1^l$ is examined, showing no clear overall trend either on or off hBN. However, one feature of this graph is that almost all of the red-shifted peaks above 730 nm also have the lowest FWHM's, below 60 nm. Unfortunately, this is partially the result of peak-fitting errors which can sometimes lead to an overestimate of the FWHM if it is unable to resolve two individual modes. These peaks correspond mostly to the $\sim 15\%$ of NPoMs in the region of the red-shifting tail, which are clearly separated from other overlapping modes and therefore the measured FWHM is lower.

## 5.3 CVD Monolayer hBN

The ultimate aim of this chapter is to understand the behaviour of thin hBN in NPoM leading up to the thinnest possible spacer, an atomic monolayer. All of what has been learned so far will be vital for our understanding of this final situation.

### 5.3.1 Monolayer hBN on Au Analysis

The monolayer is transferred as before onto a surface of evaporated Au, with an RMS roughness of 0.8 nm. On measuring the monolayer edge with AFM, the roughness decreases to 0.7 nm, showing that the material still lies across the Au surface, but adheres more closely to the Au morphology than for trilayer, as expected.

Measuring the height of the hBN monolayer on Au using AFM is problematic due to its extremely low thickness. By flattening and averaging either side of the monolayer edge, the mean thickness of the monolayer was measured to be $0.3 \pm 0.2$ nm. Measurements on identical monolayer samples by collaborators with the Hofmann group (University of Cambridge) [134] on $SiO_2$ found the thickness of hBN to be $4.1 \pm 0.1$ nm before annealing and $2.4 \pm 0.1$ nm post-annealing, so the mean value matches up well with expectations. The large negative error is greater than the value of the mean and this is likely due to AFM tapping mode oscillations above the hBN surface, leading to a skew toward higher thickness values. Preferably, the measurement should have been taken in contact mode at an extremely low scan rate and this would be a recommendation for any future experiments.

Images of the sample (Fig. 5.19) show the monolayer on Au substrate observed using a range of imaging techniques. The Raman spectrum for monolayer hBN transferred from the same Fe growth substrate was shown previously in Fig. 5.9(c). The sample shows weaker optical contrast than trilayer, but can still be seen by eye when viewed at an angle with bright illumination above (Fig. 5.19(a)), is due to visibility of remaining PC and hBN folds. Seen as bright white areas in Fig. 5.19(d), these are easily excluded from the dark field collection. SEM (Fig. 5.19(b)) shows an image almost identical to the trilayer, but with $\approx 1/3$ of the number of multilayer (white) regions as expected. Multilayer regions, folds and tears are clearly seen in dark field (Fig. 5.19(c)) as is the edge of the hBN layer on Au. An advantage

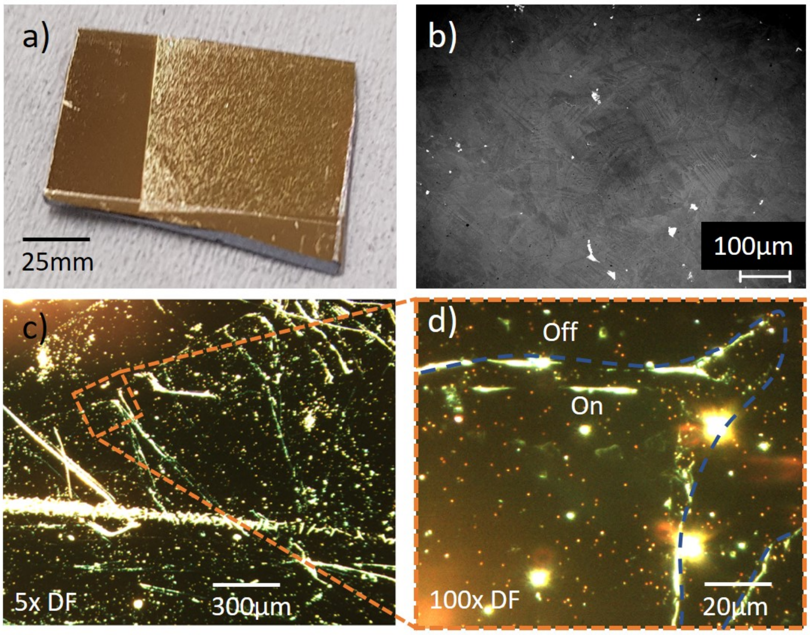

Fig. 5.19 Imaging of the monolayer on Au sample using (a) bright field (b) SEM, (c), 5× dark field and (d) 100× DF. The number of multilayers per unit area seen in the SEM image in (b) is a third of the number seen for the trilayer as expected. Regions on and off the monolayer are labelled, with red dots representing 60 nm Au nanoparticles. The edge of the tear enclosed by the orange box (c) is bordered by a blue dashed line (d) to indicated the boundary between on-hBN and off-hBN. Bright regions are due to multilayers, folds and polymer residues from the transfer.

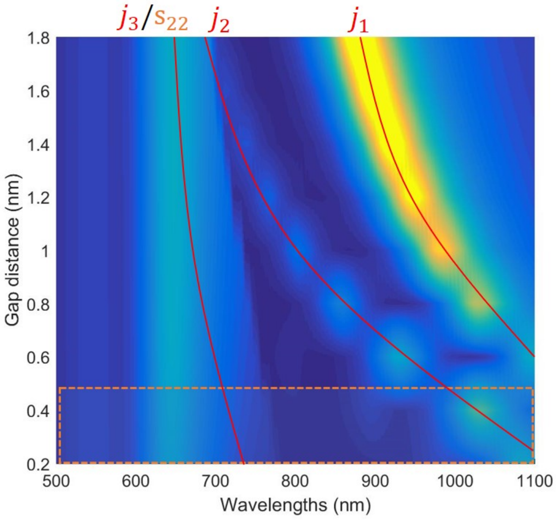

Fig. 5.20 Lumerical calculation for an 80 nm NPoM with gap refractive index of 2.13 and facet diameter 20 nm calculated at different gap distances. The dashed-orange box covers the expected values for the thickness of monolayer hBN, with both $j_1$ and $j_2$ beyond the detection range for this experiment.

of using layered materials in NPoM are the clearly identifiable regions of the sample such as the tear in the dashed orange box, Fig. 5.19(c). Using these regions as points of reference it is possible to return to the exact same set of nanoparticles for each set of measurements.

### 5.3.2 60 nm Nanoparticles on Monolayer hBN

For the main experiment, 60 nm nanoparticles were used instead of 80 nm for three important reasons. Firstly, assuming a constant refractive index hBN spacer with no contaminants present ($n_z = n_g = 2.13$, $d = 0.3$ nm), according finite-difference time-domain calculations[6] the position of the dipole antenna mode for an 80 nm nanoparticle would sit well above the detection limit of the dark-field system which is limited by the high NA of the objectives used (Fig. 5.20). If 80 nm nanoparticles were used higher order modes are more likely to be misattributed to the coupled ($l = 1$) mode. By using 60 nm nanoparticles the expected coupled mode wavelength is blue-shifted significantly and predictions lie within the detection limit of the spectrometer. Secondly, 60 nm nanoparticles display reduced faceting in comparison to 80 nm nanoparticles. This allows us to focus on the position of the dipole antenna mode without variation in facet sizes playing a major role. Finally, by changing nanoparticle diameter we are thoroughly testing the consistency of the classical model with changes in gap, facet and nanoparticle diameter.

---

[6] Required because Eq. 5.1 is invalid for such thin spacers

60 nm nanoparticles were deposited using the techniques described previously and are clearly observable at 100x DF as red dots (Fig. 5.19(d)). The edges of the monolayer are defined by dashed blue lines for clarity and regions on and off are labelled as such. Nanoparticle spectra on and off-hBN were taken 10's of microns from the edge positions, but the edge is shown here to demonstrate that there is not an immediately recognisable difference in the colours of the nanoparticles on or off monolayer hBN. This is in contrast to the trilayer hBN, where nanoparticles were red on and green off the region of the thicker hBN spacer (Fig. 5.11(a)). As usual nanoparticles close to these bright defects are not included in data collection.

The spectra gathered from 216 and 224 60 nm nanoparticles on and off monolayer hBN respectively are shown in Fig. 5.21 along with the average and standard deviation for both datasets. While the distribution of spectra on and off show differences which will be discussed below, the average spectra for both are highly similar both in intensity and coupled mode wavelength. Comparing scattering from 60 nm nanoparticles off-hBN to 80 nm NPs off-hBN, the average intensity has dropped significantly and coupled mode blue-shifted for all nanoparticles on citrate/Au as expected. On monolayer hBN the intensity has also dropped back to expectations for a 60 nm NPoM, the clear enhancement for 80 nm nanoparticles on trilayer hBN has vanished.

Next the entire dataset is peak-sorted from bottom to top in order of increasing $\lambda_1^l$ (Fig. 5.22). The data here is normalised to 1 because the lower intensity for 60 nm nanoparticles reduces the visibility of weaker peaks compared to 80 nm NPs. In terms of the distributions the similarity between Fig. 5.22 and Fig. 13 is striking. Both show an even distribution about their averages and again a blue-shifting tail is seen at shortest peak wavelengths. More importantly, above $\sim$ 700 nm the red-shifting tail seen for trilayer hBN NPoM at longer wavelengths appears once again (above the grey-dashed line). The NPoM system here is different in a number of important ways from the sample in the previous section with reduced nanoparticle faceting, diameter and spacer thickness. This suggests strongly that the red-shifting tail at longer wavelengths on-hBN is a result of the presence of hBN in the gap, as posited for 80 nm nanoparticles on trilayer hBN. This observation implies that the intensity enhancement seen for 80 nm nanoparticles on trilayer hBN is the result of an independent effect from that which causes the red-shifting tail of the distribution. This is because the red-shifting tail is due to the hybrid nature of the spacer, with mobile molecules in addition to a crystalline solid, not the properties of the hBN itself.

For both datasets there are a number of split peaks in addition to peaks which appear at wavelengths red-shifted from the dipole antenna mode. This demonstrates that despite the reduction in faceting, some measurable consequences of mode hybridisation remain.

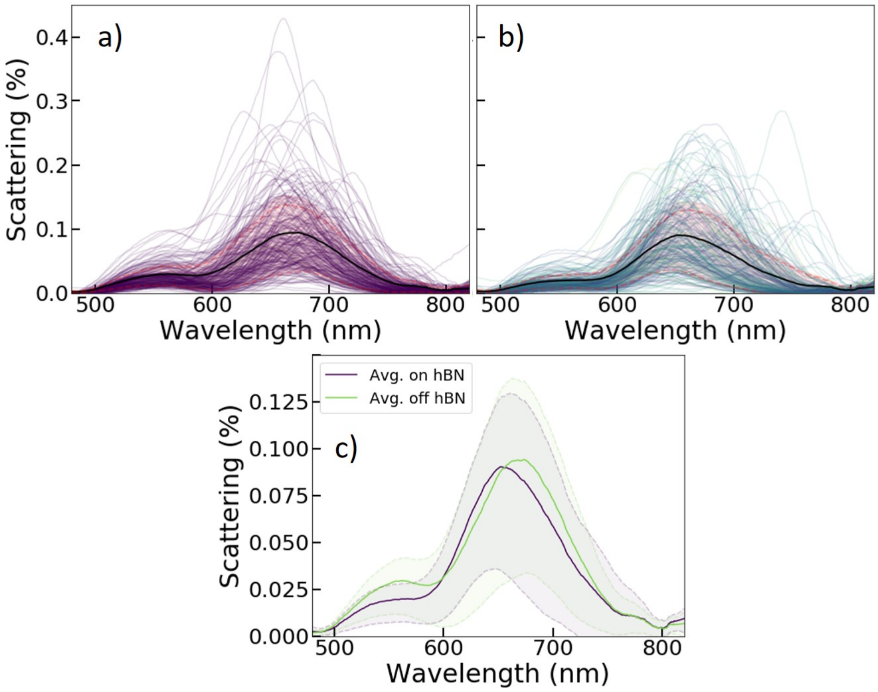

Fig. 5.21 All dark field spectra off (a) and on (b) a single monolayer of hBN on Au including the average (black curves) and standard deviation (red dashed curves). The averages with their standard deviations are shown (c) for direct comparison.

However, reassuringly the magnitude of the red-shift for these additional modes has dropped compared to 80 nm NPs due to the reduction in faceting. Also matching with Fig. 13(b), the red-shifting tail reveals a number of modes which are proportional to the coupled mode and blue-shifted by $\sim \times 1.25$ from the position of the dipole antenna mode, matching the previous assignment of these modes to the second order dipole antenna mode $l = 2$ for 80 nm NPs on trilayer hBN.

## 5.3.3 Mode Distributions

As for trilayer, plotting the intensity and wavelength for each detected peak on and off-hBN enables much more detailed analysis of mode distribution (Fig. 5.23). As before, purple points represent the dipole antenna peaks for each spectrum, while green crosses correspond to other peak positions (Fig. 23(a,b)). The corresponding histogram off-hBN (Fig. 5.23(c)), shows an approximately Gaussian cluster of peaks around 560 nm. This results from overlapping transverse and brighter $l = 2$ modes which partially obscure the weaker transverse mode at $\approx 530$ nm. The dipole antenna mode also shows an approximately Gaussian distribution about the average.

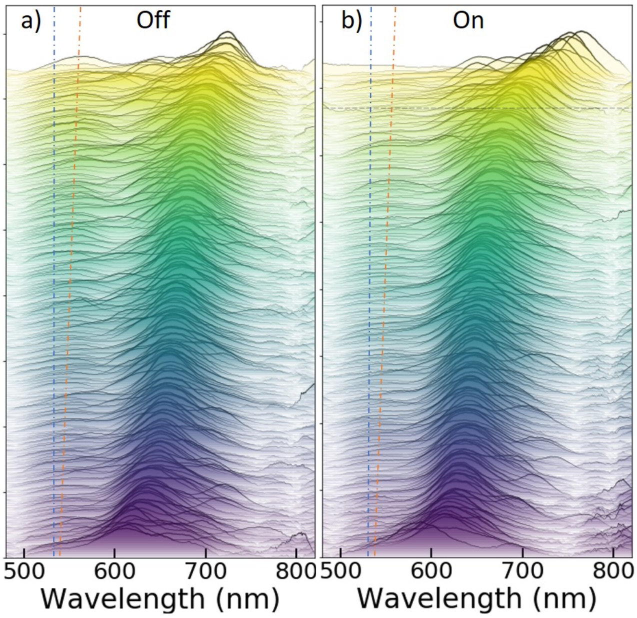

Fig. 5.22 All normalised spectra from 60 nm nanoparticles off (a) and on (b) monolayer hBN sorted from bottom to top in order of ascending maximum peak position. The orange and blue dashed lines track the wavelengths of the same modes seen both on-hBN and off-hBN.

On-hBN (Fig. 5.23(d)), the overlapping tranverse and $l = 2$ modes lead to a maximum scattering between 530 nm and 550 nm. This occurs because, in proportion with $l = 1$, the $l = 2$ mode is slightly blue shifted compared to off-hBN and the spread of $l = 2$ is larger. The peak count maximum for the coupled mode ($l = 1$) is slightly blue-shifted from the average peak scattering (Fig. 5.23(d), black dashed line) due to its skewed distribution, matching with the experiment on trilayer hBN. Thus, while the averaged spectra for on and off-hBN are very similar, the most commonly occurring (modal) peak position is more clearly blue-shifted compared to on Au. This implies that the increase in thickness due to hBN blue-shifts the antenna mode by a greater degree than the red-shift due to the gap refractive index increase. It will be seen later that this can only be explained by a hybrid refractive index, adding further support for the adjusted model leading to equation 5.2.

Moving to an in-depth analysis of the coupled mode as before, the average coupled mode wavelength for 60 nm nanoparticles on Au (off-hBN) lies at a wavelength of $669 \pm 23$ nm with an intensity of $0.11 \pm 0.06\%$ (Fig. 5.24(a)). Comparing this to expectations, so using equation 5.1 with a constant refractive index of $n_g$ =1.5, leads to a calculated thickness of 0.96 nm, very close to the hBN trilayer sample of 0.90 nm. This is once again in line with citrate thicknesses in the literature [141] and is reassuring since both samples were prepared using the same method. This demonstrates the consistency of citrate thickness given the same Au substrate surface and nanoparticle diameter. It also shows the reliability of the original

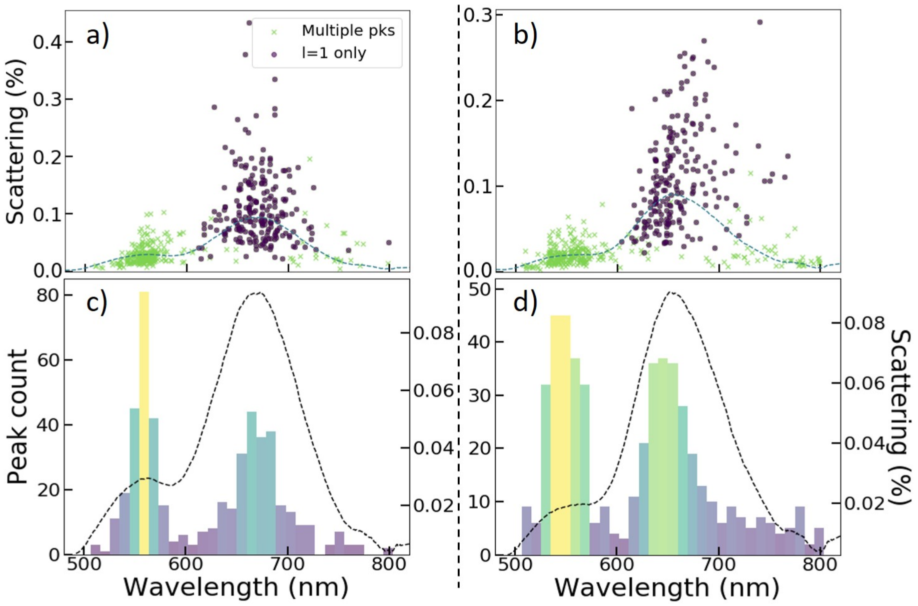

Fig. 5.23 All peaks detected for the dark field spectra shown in Fig. 5.22 for off (a) and on (b) monolayer hBN along with the average spectrum (blue dashed curve). Purple circles represent the brightest peak in a given spectrum and green crosses any other detected peak. Using these peak positions histograms for off (c) and on (d) monolayer hBN are plotted with colour corresponding to count.

model with a constant gap, able to explain the average change in spectra from 80 nm to 60 nm nanoparticles.

The wavelength distribution skew for the $l = 1$ mode off monolayer hBN is $-0.03$, which shows that the distribution is close to symmetric about the mean wavelength, i.e. it is a Gaussian distribution[7]. This is in slight contrast to a non-symmetric distribution with a negative skew of -0.68 for 80 nm nanoparticles on Au for the previous sample, however both appear to show a relatively weak dependence on the gap properties which should dictate the coupled mode position. In light of this, while it is able to predict the average wavelength of the $l = 1$ modes well, neither equation 5.1 or 5.2 in which $\varepsilon_{eff}$ is the key variable are able to explain the distribution for 60 nm or 80 nm nanoparticles on citrate/Au.

Based on the experimental data for 80 nm and 60 nm nanoparticles off-hBN, a more likely model for the gap is a variable refractive index between a maximum of $\sim 1.5$ and a minimum of 1 as the ratio of citrate (or another contaminant such as water, $n_{H_2O} = 1.33$) to air in the gap changes with an approximately constant gap distance. For a constant thickness with changing $n_g$ the variation in $\lambda_1^l$ is close to linear, which could explain the symmetrical distribution about the average value in some cases. The negative skew would result if there were a skew

---

[7] Two values were removed from this distribution since they were $> 3\sigma$ from the average wavelength value. This is a valid approach for a distribution with low skew such as this.

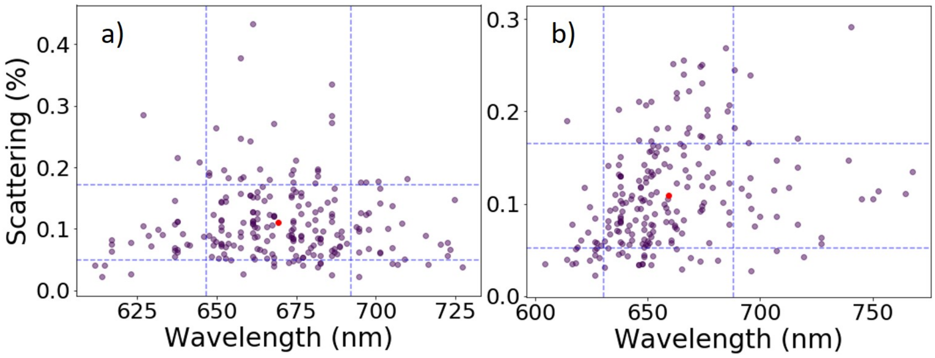

Fig. 5.24 Scattering and intensity distributions for dipole antenna modes on (a) and off (b) monolayer hBN. Blue dashed lines represent the standard deviations from the mean value (red dot), in both intensity and wavelength.

in the volume fill-fraction of citrate molecules in the gap, which may depend on nanoparticle radius or shape. The gradient of this linear relationship increases with nanoparticle diameter $R$, which will increase the distribution spread. Thus, it is expected that the magnitude of any negative skew will increase with nanoparticle radius as is found in the previous section for 80 nm nanoparticles. Small changes in gap distance are still to be expected, and the combined influence of a small increase in gap with a decrease in refractive index might explain the the blue-shifting tail at shorter wavelengths for all spectra. This would occur both on and off-hBN, since citrate is present in both cases. There are expected to be both variations in the thickness and refractive index of the gap for citrate, but based on these experimentally measured distributions on Au it appears that a linear change in wavelength with changing refractive index is the dominant mechanism. Along with this linear influence, small random fluctuations in nanoparticle size and shape will contribute to the spread, but they are not expected to dramatically influence the distribution skew.

On monolayer hBN the average coupled mode wavelength for 60 nm NPoM is blue-shifted by 10 nm compared to off-hBN at $659 \pm 29$ nm with an identical scattering of $0.11 \pm 0.06\%$. Recall, that the coupled mode for 80 nm nanoparticles on trilayer hBN was also blue-shifted compared to off-hBN. The coupled mode distribution for 60 nm Au nanoparticles on monolayer hBN shows a skew toward longer wavelengths of $+1.27$. This is in line with the value for 80 nm nanoparticles on trilayer hBN which was also positively skewed, with a value of $+0.80$. Thus, the influence of thin hBN in NPoM is to skew the data toward longer wavelengths. This is also matches the observations of a red-shifting tail made for monolayer (Fig. 5.22(b)) and for trilayer hBN (Fig. 5.13(b)). The most significant contributing factor to this skew is the red-shifting tail at longer wavelengths, which counteracts the linear influence of the variable volume fraction of citrate in the gap - as discussed above.

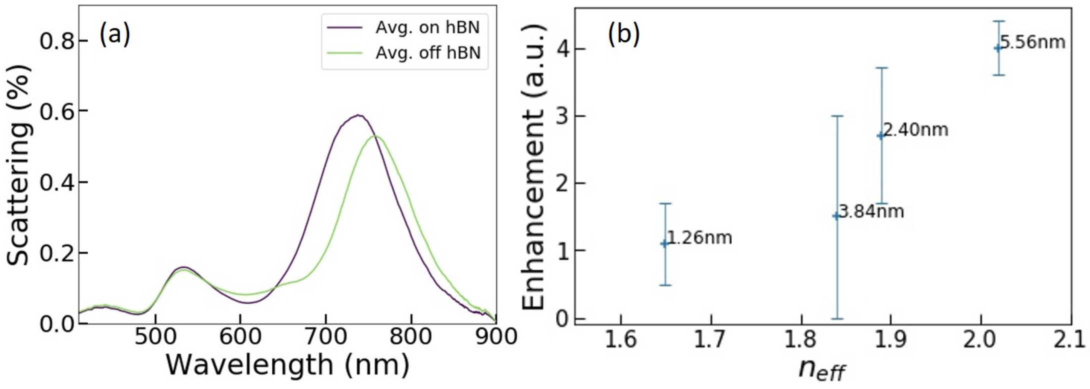

Fig. 5.25 Comparison of the average spectrum for 80 nm nanoparticles on and off monolayer hBN (a) and the intensity enhancement as a function of effective refractive index ($n_eff$) for 80 nm nanoparticles on hybrid spacers with total thicknesses ($d_{tot}$) corresponding to point labels (b). Error bars are calculated from the standard deviation in scattering at the coupled mode maxima thus, due to the strong positive intensity distribution skew, negative errors are over-exaggerated while positive errors are under-exaggerated i.e. there is a tendency toward higher enhancement values.

As previously mentioned, the significant intensity increase observed on both thicker hBN samples is no longer present which suggests that this is only observed when hBN material is thicker and/or with nanoparticles of greater size. To determine which of these is the case, 80 nm nanoparticles were deposited onto a separate monolayer hBN sample.

### 5.3.4 80nm Nanoparticles on Monolayer CVD hBN

The average spectra for fifty 80 nm nanoparticles on and off monolayer hBN are shown in Fig. 5.25. The relationship between on and off-hBN is almost identical to 60 nm NPoM on monolayer hBN with a slight blue-shift for nanoparticles on hBN. The experimental coupled mode wavelength off-hBN (on Au) lies at average of $735 \pm 47$ nm with an intensity of $0.6 \pm 0.4\%$ [8]. The value of coupled mode wavelength average closely matches the behaviour on Au for the trilayer sample which was at a wavelength of $724 \pm 19$ nm. Note that due to the lower number of spectra, the error on the wavelength and intensity values has not yet converged to its minimum value, hence its greater magnitude.

On monolayer hBN, the 80 nm nanoparticles show average peak wavelengths of $727 \pm 30$ nm and an intensity of $0.7 \pm 0.3\%$. The significantly smaller intensity increase indicates that the dominant determining factor for the enhancement is the thickness of the boron nitride, but that there may be a small contribution due to nanoparticle size.

Considering experiments from few-nm, trilayer and monolayer hBN together, there remain two possible explanations for the enhancement observed for thicker spacers. The

---

[8] The intensity appears higher than the average peak (Fig. 5.22) due to rounding

first relates to a correlation between the effective refractive index $n_{eff}$ and the magnitude of the enhancement (Fig. 5.22a). In the graph, point labels correspond to the total spacer thickness including contaminants, thus the 1.26 nm corresponds to the monolayer, 2.4 nm to trilayer, 3.84 nm to thin terrace (which includes hBN morphology) and 5.56 nm to thick terrace, displaying the largest enhancement of all the samples. Although more experiments are needed to show the full relationship, this demonstrates that the refractive index ($n_g = n_z$) is the dominant influence on far-field intensity of the coupled mode.

An in-plane facet mode, strongest at larger gaps, may preferentially outcouple to far-field due to the birefringence. Simulations would be required to verify this hypothesis and unfortunately they are not present in this work. However, it must be noted that if this were the case, then the observed scattering enhancement would not be unique to hBN, and should be observed for other layered crystalline spacers (e.g. TMDs). The other possibility is that the refractive index of hBN in its monolayer form is reduced by the presence the Au substrate and/or contaminants, weakening the coupling of NPoM. It would not be possible to detect this change for the reasons described below.

### 5.3.5 Screening of Monolayer hBN by Contaminants in the Gap

For 60 nm nanoparticles on pure monolayer hBN the expected position based on equation 5.1, which assumes the spacer is insulating, is 886 nm, which is significantly greater than $3\sigma$ from the mean experimental value of $659 \pm 29$ nm. It has been shown in previous well-known literature that this model clearly breaks down for such small gaps [133, 45] and the classical circuit model leading to equation 5.1 becomes invalid due to the presence of quantum tunneling across the gap. This tunneling process causes a blue-shift in the coupled mode away from expectations of the classical circuit model.

Using multiple different techniques, it has been clearly shown that I have succeeded in creating NPoM with monolayer hBN in the gap. Replacing equation 5.1 with 5.2, I will now show that no quantum mechanical treatment is required in this case to explain the coupled mode position on this material, since contaminants are not displaced and screen the presence of monolayer hBN.

Immediately, adding 0.96 nm of citrate to the gap and using equation 5.2 gives $n_{eff} = 1.65$ and $d_{tot} = 1.26$ nm. This leads to a coupled mode wavelength of 667 nm, very close to the position of the antenna mode for nanoparticles on monolayer hBN of 659 nm. Notably it is also almost precisely equal to the coupled mode wavelength of 669 nm for 60 nm nanoparticles off monolayer hBN.

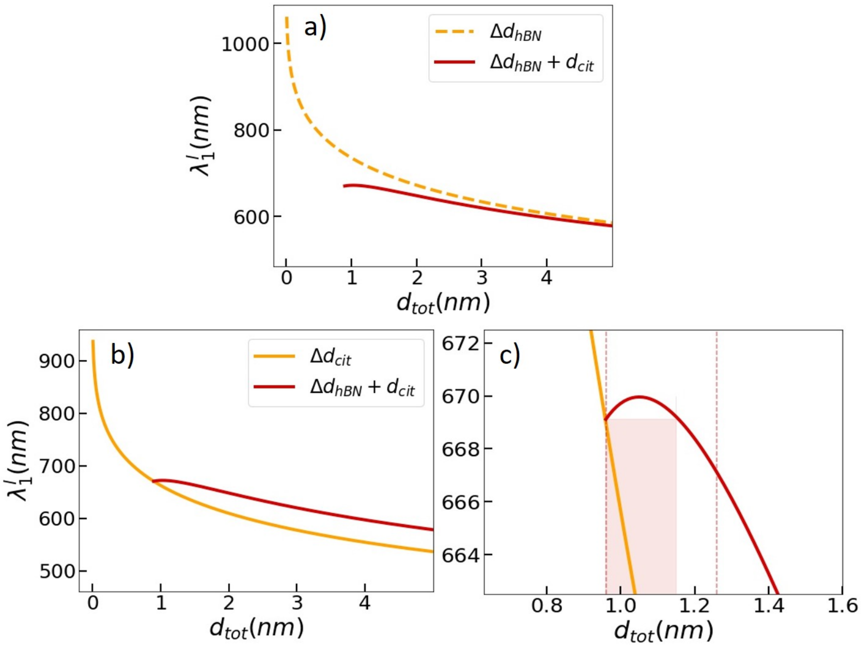

Fig. 5.26 Comparing the thickness dependence for NPoM with hBN spacer with and without a citrate layer of constant thickness 0.95 nm (a) calculated using equation 5.2. Comparing the thickness dependence of citrate to citrate with changing hBN (b) and a zoomed in figure showing the behaviour of the model for small thicknesses of hBN (0.1-0.5 nm) (c).

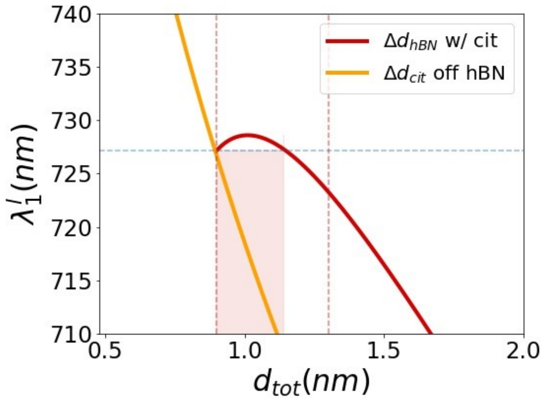

Fig. 5.27 Comparison of the calculated average spectrum for 80 nm nanoparticles on (red) and off (orange) a monolayer of hBN with citrate present.

To understand this, equation 5.2 is plotted for 60 nm nanoparticles with a changing thickness of hBN lying underneath [9] and a constant 0.96 nm of citrate ($\Delta d_{hBN} + d_{cit}$). This is then compared to the thickness dependence of pure hBN and citrate on Au (Fig. 5.26).

It can be seen that initially for and hBN thickness $>\sim 3$ nm the presence of citrate makes little difference to the model for hBN only (Fig. 5.26(a)), contributing only a very small blue-shift. Below 2 nm of hBN however, the curve reaches an inflexion point and the gradient begins to decrease. The gradient continues to decrease, becoming negative at around $d_{tot} = 1.05$ nm (or $d_{hBN} \sim 0.1$ nm) until the wavelength of the antenna mode equals the wavelength for citrate only at 669 nm (Fig. 5.26(b,c)). Therefore, for 60 nm nanoparticles at an hBN thickness of 0.19 nm the coupled mode wavelength lies at the same

---

[9] Although the order of the layers makes no difference to this simple calculation.

position as with no hBN present in the gap (red filled area, Fig. 5.26(c)). For a real physical thickness of hBN $0.26 - 0.41$ nm [134] the position of the antenna mode is similar, but slightly blue-shifted from when there is no hBN present and therefore it cannot be easily detected using the coupled mode position from NPoM.

The clear consequence of this is that as long as citrate is present and the thickness of hBN is larger than the screening distance of 0.19 nm there is a blue-shift of the mode for a monolayer ($d_{hBN} > 0.3$ nm) and this is seen for all of the hBN NPoM samples in this chapter. Matching with observations for 80 nm nanoparticles on and off monolayer hBN, $\lambda_1^l$ follows approximately the same relationship for thin hBN (Fig. 5.27), but red-shifted due to the greater nanoparticle diameter. The thickness at which $\lambda_l^l$ is equal to the coupled mode wavelength on and off-hBN (highlighted in red Fig. 5.26(c),5.27) is largely independent of the nanoparticle diameter increasing only slightly from 0.19 nm to 0.24 nm. Therefore, the coupled mode wavelength on citrate defines a threshold over which the coupled mode on-hBN cannot pass for any thickness of hBN in NPoM.

Consider the most red-shifted spectra for nanoparticles on Au (Fig. 5.20(a)) assuming that for these modes the refractive index is a maximum of 1.5. These peaks for nanoparticles off hBN lie at a wavelength of 730 nm, leading to a calculated thickness of 0.45 nm based on Eq.5.1. For a thickness of citrate of 0.45 nm on monolayer hBN, based on Eq.5.2 the antenna mode lies at 723 nm. This explains modes on monolayer hBN up to 95% of the maximum wavelength positions. As before, the red-shifting tail occurs because of the increase in tuning rate for a hybrid spacer (Fig. 5.16.) means than only a slight difference in citrate thickness on hBN compared to on Au is required for a large red-shift.

### 5.3.6 Gap Enhancement and Coupled Mode Linewidths

Due to the presence of passivating ligands the gap enhancement becomes quite unpredictable. Just as for trilayer hBN, comparing the Q-factors on and off monolayer hBN (Fig. 5.28) reveals only a slight difference in the averages, but this time with reduced values of $8.0 \pm 2.1$ off-hBN (Fig. 5.28(a)) and $8.2 \pm 1.7$ on hBN (Fig. 5.28(b)). This indicates that the Q-factor is proportional to the nanoparticle size. For 60 nm Au NPs on citrate (i.e. off monolayer hBN) the parameters $d_g = 0.96$ nm and $n_g = 1.5$ leading to $E_{max}^2/E_0^2 = 1.30 \times 10^5$, which is $\sim 2.7\times$ weaker confinement than for the trilayer sample.

According to the new hybrid gap model for 60 nm Au NPs on monolayer hBN, $d_{tot} = 1.26$ nm and $n_{eff} = 1.65$. Substituting the remaining values leads to $E_{max}^2/E_0^2 = 8.5 \times 10^4$ which is a $1.5\times$ reduced enhancement in the nanogap compared to off-hBN. In contrast to the above, on trilayer hBN sample the enhancement is $1.6\times$ weaker than for 60 nm nanoparticles on monolayer hBN, with the increase in nanoparticle size, gap index and Q-factor unable

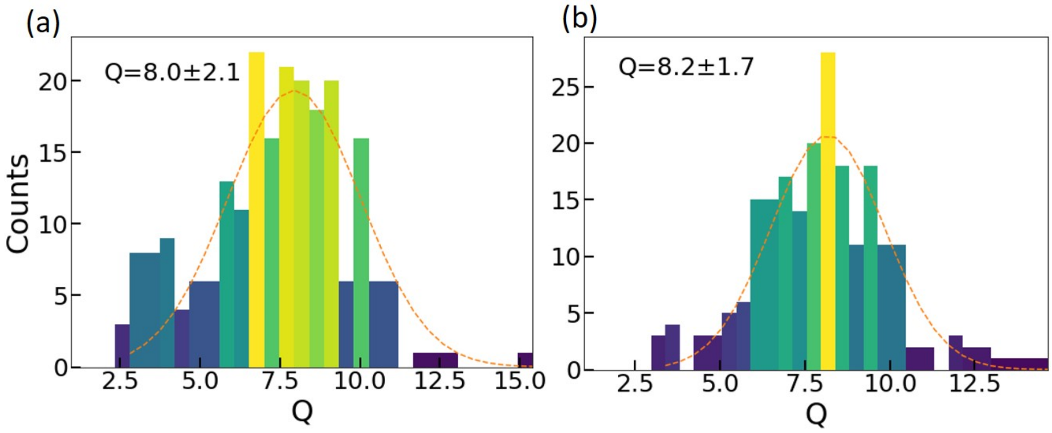

Fig. 5.28 Comparing Q-factors off (a) and on (b) monolayer hBN.

to counteract the strong dependence on gap distance. The fact that these calculations are consistent when comparing on-hBN to off across different gap sizes and nanoparticle sizes is highly reassuring.

The clear and approximately exponential increase in scattering as a function of FWHM for 80 nm nanoparticles on trilayer hBN, is not observed for 60 nm nanoparticles on monolayer hBN or for 80 nm NPs on monolayer hBN (Fig. 5.29). Instead the FWHM values both on and off hBN are clustered around 70 nm, showing no clear difference between datasets. The distribution has a reduced spread in FWHM values, but this is a comparatively weak behaviour. This suggests that the intensity enhancement and scattering as a function of FWHM observed for 80 nm nanoparticles on trilayer hBN are linked. It is therefore probable that the approximately exponential dependence will reappear when the effective refractive index is higher.

In a similar fashion to the data for trilayer hBN there is no clear trend between FWHM and $\lambda_1^l$, showing only the small average blue-shift on monolayer hBN as observed for trilayer hBN. Again there is the clear tail to the distribution at low FWHM for a small fraction of modes corresponding to the red-shifting tail, which was also seen for the data on trilayer hBN. Again, the reason for this is that many dipole antenna modes are split in wavelength such that they are not clearly resolvable as two individual modes, thus if the fit is not successful the linewidth is overestimated. More red-shifted values are more clearly separated from the rest of the distribution, so improvements to the fitting methods will be required for future experiments measuring linewidths.

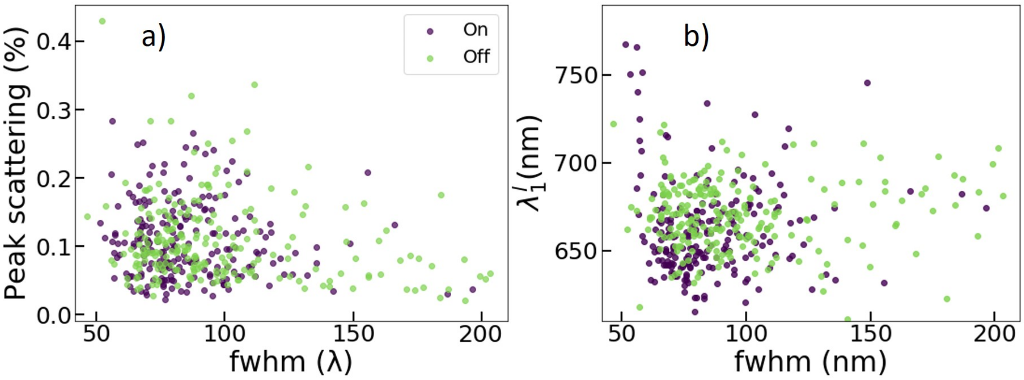

Fig. 5.29 Comparing full width half maxima (FWHM) of 60 nm nanoparticle dipole antenna modes to peak scattering (a) and wavelength of the dipole antenna mode $\lambda_1^l$ (b) both on(purple) and off(green) monolayer hBN.

## 5.4 Conclusions and Outlook

To summarise and discuss the key points learned about the influence of hBN of thickness 0.3-4.6 nm in NPoM using citrate-capped nanoparticles of diameter 60-80 nm:

**Red-shifting tail explained by hybrid gap**: For both 60 nm and 80 nm Au nanoparticles on monolayer and trilayer hBN respectively, the presence of hBN positively skews the peak distribution of the dipole antenna mode. A characteristic red-shifting tail at the longest wavelengths is observed which contributes to this positive distribution skew. I propose that the reason for this is the hybrid nature of the refractive index which increases the tuning rate (gradient) for a given spacer material. This is because the refractive index increases simultaneously with decreasing gap. The skew of the peak distribution and Q-factor are proportional to nanoparticle size as would be expected.

Other work using molecules with similar refractive indices have demonstrated coupled modes beyond 800 nm, suggesting that citrate is displaced in the gap. There is no mechanism for citrate displacement in the gap for inert spacers, due to the lack of a binding mechanism to the Au nanoparticle surface.

**Coupled mode positions on hBN are explained by hybrid gap**: Due to the hybrid gap, both 60nm and 80nm nanoparticles on monolayer hBN show blue shifts of $\sim$ 10 nm, and 80 nm nanoparticles on trilayer are also clearly blue-shifted. For monolayer hBN, this is a shift 20× lower in magnitude and in the opposite direction to expectations based on Eq.1 and assuming a constant hBN refractive index gap with $d = 0.3$ nm. By modifying the circuit model to include the hybrid gap, I show that reason for this is likely to be the screening of thin hBN layers by gap contaminants which severely limits the red-shift of the coupled mode on-hBN. Based on my analysis, the coupled mode on any thickness of hBN cannot shift significantly (> a few nm) beyond the wavelength of the mode off-hBN.

Based on this thorough analysis I do not consider quantum effects, damage or both to be the most likely explanation for my observations. They can be predominantly explained using this classical model, fundamentally because the spacer thicknesses are greater than initially anticipated.

**Large intensity enhancement is seen for trilayer or thicker**: For 80 nm nanoparticles on trilayer hBN there is a large intensity increase compared to on Au. Unusually, this appears to be related almost solely to the value of the gap refractive index and depends only weakly on the gap distance. Along with other measurements of enhancements, this suggests that the measured far-field is not a strong indicator of the field enhancement in the gap. There may also be contributions to this enhancement due to birefringence of hBN if this influences the facet modes, but this would require full simulations to confirm.

**Coupled mode distributions are explained by citrate fill-fraction** Off-hBN the distributions are display clearer symmetry than on-hBN for both 80 nm and 60 nm nanoparticles. This is explained by variable volume fractions of contaminant molecules in the gap with a constant gap distance. This changes the usual relationship to a closely linear one, which would explain a more symmetrical skew. Again the skew appears to be proportional to the nanoparticle radius, indicating that nanoparticle size strengthens the influence gap properties.

Looking to the future, a number of problems have been overcome through this work which should dramatically improve the NPoM system with layered materials. AFM images show a significant measured reduction in the influence of morphological changes using the novel transfer techniques developed by V.B., the influence of which is measured using both 60 nm and 80 nm nanoparticles. This work acts as a significant reference study for nanoparticles on Au with adsorbents in the gap, improving our understanding of the influence of mobile contaminants on the gap properties and resultant far-field scattering. My modification of the refractive index in the circuit model to account for these adsorbents appears to accurately reflect real data for the dipole antenna mode and highlights that their presence can be included in classical models with great success.

This work is the an example of large-scale analysis of NPoM with a 2D material and significantly improves confidence results compared to previous work on other 2D materials in NPoM. Successful detection, through intensity enhancements and distribution analysis allows hBN to be detected despite the influence of other materials in the gap. This should also remain valid for other vdW materials and thus novel nano-optics is still interpretable despite their presence.

The outlook for 2D materials in NPoM remains good, but I believe my work highlights the importance of considering contaminants. Effort needs to be focussed on minimising the removal of these contaminants before we can be confident that the gap constituents consist of the vdW material alone. This is a significant challenge, as cleaning needs to be completed with minimal damage to NPoMs. Throughout this project I attempted a wide range of different methods in order to achieve this aim with partial success, with some results of this shown in the appendix. In the short term, $O_2$ plasma etching in order to remove contaminants is a promising solution, but this must be carefully tuned in order to minimise damage. SEM studies will likely be required in order to establish the effect of this technique on individual NPoMs. In the medium term the gas-phase deposition of nanoparticles onto these materials is a promising method since it produces nanoparticles without capping ligands of high size uniformity.

# Chapter 6

# Nanocavities With $WS_2$ and Perovskite Nanoplatelets

## 6.1 Introduction

In chapter 4 and 5 dielectric hexagonal-Boron Nitride of sub-$\mu$m and sub-nm thickness was encapsulated between plasmonic nanoparticles and a Au mirror. Field confinement between nanoparticle and mirror led to measurable changes in high-angle optical scattering as a function of wavelength. Aided by the lack of optical activity for hBN, this work enabled an unprecedented examination of plasmonic-microcavity and nanocavity heterostructures with inert (i.e. non-binding) materials, while excluding other effects due to optical activity of the encapsulated material. This led to the discovery of the new nano-resonator mode and allowed the development of an analytic model which included the presence of contaminants in the nanogap.

Ultimately, the aim for both of these chapters was to use the results of these hBN case-studies as foundations from which to build useful NPoM-related devices in future. As was previously discussed, other optically active layered materials are frequently combined with hBN in order construct vdW heterostructures with enhanced properties at the nanoscale. The knowledge gained in previous chapters may allow researchers to unlock some of these unique properties via nanoscale field confinement.

Having therefore thoroughly examined the ‘bare-bones’ nanoparticle-on-mirror, this chapter now focusses on the use of optically active materials in the this geometry. The focus is on two different classes of material, the properties of which are enhanced inside nanocavities:

1. Monolayer transition-metal dichalcogenides, in this case CVD monolayer $WS_2$ grown directly onto a Au substrate
2. Layered metal-halide perovskite nanoplatelets, in this case methylammonium-lead-iode (known as MAPI) deposited from colloidal solution

These experiments each offer an exciting look into a potential future for these diverse material types in NPoM or other plasmonic heterostructures.

## 6.2 Light Emission from Plasmonic Nanostructures in As-Grown $WS_2$ on Au

Monolayer $WS_2$ is known to display a wide range of fascinating optical effects when combined with plasmonic arrays and particles such as room-temperature strong-coupling [142, 143] and enhanced photoluminescence [144–147]. Its strong interlayer coupling with $MoS_2$ [148] makes it very promising as a component of future vdW heterostructures.

The growth of monolayer $WS_2$ via chemical vapour deposition (CVD) onto Au foils is now a well-known method to produce large-area and high-quality films[149, 150]. The typical measures of material quality such as Raman or photoluminescence (PL) are strongly quenched on Au, so they are taken post-transfer. This is a slow, difficult and often unreliable process of bubble transfer which leads to damaged layers[149].

Gold is known to display photoluminescence as a result of the radiative recombination of holes in the d-band with electrons in the conduction (sp) band [151, 152]. This process has an extremely low quantum yield on flat gold surfaces of $\sim 10^{-10}$, but is enhanced significantly on roughened gold substrates. This enhancement is due to localised field enhancements on the nanoscale rough surface[152] and peaks at the maximum absorption for Au, around 500-530 nm. As researchers began working more frequently with plasmonic nanostructures (e.g. gold nanoparticles), it was noticed that photoluminescence was significantly greater than previous predictions[153]. This was found to be due to the influence of localised surface plasmons, which at resonance improves radiation coupling efficiency providing additional contributions to d-hole relaxation rate [154].

Here, I show that the scattering from defects in the Au foil, attributed to nanoscale plasmonic defects, almost always peak very close to the position of the A-exciton for $WS_2$ on Au at 618 nm. The emission is always blue-shifted from the position of the dark-field peak, which closely matches the absorption due to the A-exciton. This study highlights the importance of carefully distinguishing between phololuminescnece from Au and single electron semiconductor transitions. It raises questions about the relationship between nanostructure plasmon resonance and the direct transition of an adjacent semiconductor.

### 6.2.1 Dark-field and Light Emmision Measurements

$WS_2$ monolayers were grown onto Au foils according to methods described in reference [150] by Dr. Ye Fan of the Hofmann group. Optical images of the same region of foil at 100× magnification in bright-field (BF) and dark-field (DF) illumination are shown in Fig. 6.1(a,b). In bright-field, few features of interest are observed, with bright yellow regions corresponding to large clusters of multilayer regions, large foil defects and contamination (e.g. carbon). Dark-field imaging at 100× magnification reveals grain-boundaries in the $WS_2$ (white arrow, Fig. 6.1) in addition to red points of light which are in stark contrast with the surrounding regions. The highlighted red-points in this image all display sharp resonance frequencies ranging between 600-650 nm, in clear contrast to surrounding yellow regions which broadly scatter light in the range 450-800 nm. The red-points of light are distributed with a density of approximately 2 per $100\mu m^2$, and this density is used to match with features of a similar density in SEM. Note that this scattering wavelength corresponds closely to the wavelength of the A-exciton for $WS_2$.

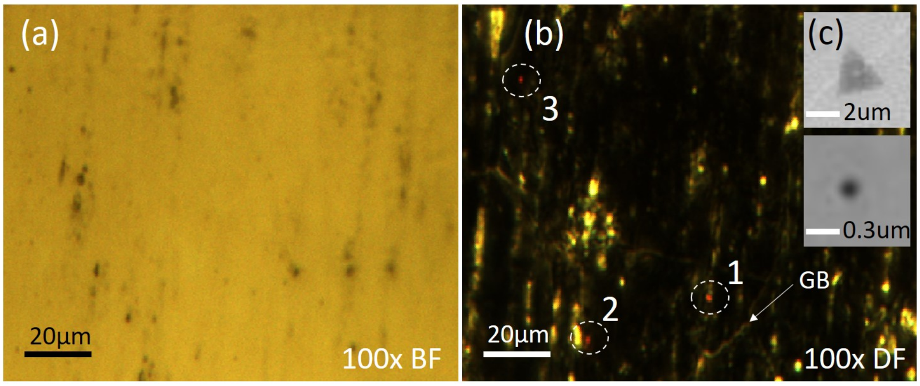

Fig. 6.1 Imaging the $WS_2$ sample grown onto gold foil using optical bright-field (a) and dark-field (b) microscopy at 100× magnification. The sample was also imaged in SEM in order to identify the origin of sparsely distributed red-points (circled with white in (b)), and two possible candidates were identified - triangular multilayers (top (c)) or metal defects (bottom (c)).

Referring to SEM data (Fig. 6.1(c)), two initial candidates were identified for the red-points by comparing the density of the observed objects with dark-field. The first are small $\sim 2\mu m$ triangular regions of multilayer $WS_2$ which occur as a result of the CVD growth process (upper image, Fig. 6.1(c)). If thick enough, the edges of these multilayer regions may be detectable in dark-field. Photoluminescence from multilayer $WS_2$ is expected to be weak since it is an indirect transition, and it red-shifts as a function of the number of layers [155]. The second candidates are black circular defects of around 200 nm to 400 nm in diameter which are initially attributed to pits in the Au surface, but might also be attributed to protrusions. Contaminants such as carbon of such a scale would not be detectable in dark-field above the very large background from the surrounding foil. Defects in Au surfaces are often observed in other substrates (e.g. template stripped gold), and are characterised by their sharp resonances at a wide range of wavelengths within the visible region. The wide range of possible wavelengths is due to the subtle dependence of the localised plasmon resonance on the morphology of the defect.

The dark field spectra for the three red points in Fig. 6.1(b) are shown in Fig. 6.2 as dark blue curves, with peaks at 608 nm for 1, 632 nm for 2 and 614 nm for 3. Thirty further defect measurements indicate that the consistency of the scattering signal for these red-regions is such that $> 85\%$ of all observed scattering peaks are in the wavelength range 600-650 nm. The brightness of these regions ($\sim 5-12\%$) means that they are clearly visible despite the large background from the gold foil. The magnitude of this scattering matches well with expectations for a nanostructure of 200-400 nm in size. Multilayer regions of $WS_2$in the size range 1-$3\mu m$ would not scatter so strongly and so are unlikely to be the source. Dark-field spectroscopy from the edges of deposited TMD layers has been shown to be a good approximation for the absorption spectrum of the material, and these consistent spectra suggest that scattering from the red-defects may be related to absorption of the A-exciton for $WS_2$ [156].

The sample was illuminated using a laser at 447 nm with power measured at the sample of $400\mu W$. Away from the red-regions there was a non-negligible emission count due to photoluminesence from the rough Au surface which had to be accounted for[157]. This luminescence appears in the form of a rising background which peaks at 520 nm and is as a result of radiative recombination of holes in the d-band with electrons in the sp-band of gold [151]. Ten measured counts were taken of this background PL and the average was subtracted from all of the emission measurements shown in this section. Taking this into account, illumination of red-defects led to clear light emission in the range of 400-3000 counts in brightness (bright green curves). To stress, no emission except from the rising background was observed unless illuminating red-defects with clear scattering peaks between 600 and 650 nm. A feature of light emission from these defects is that it always peaks at a blue-shifted wavelength from the DF peak. The blue-shift for defect 1 is 20 nm, 2 is 17 nm and 3 is 14 nm. The blue-shift does not appear to be strongly dependent on the dark-field resonance wavelength. This blue-shift of luminescence compared to absorption for photoluminescence from plasmonic nanostructures has been observed before in multiple

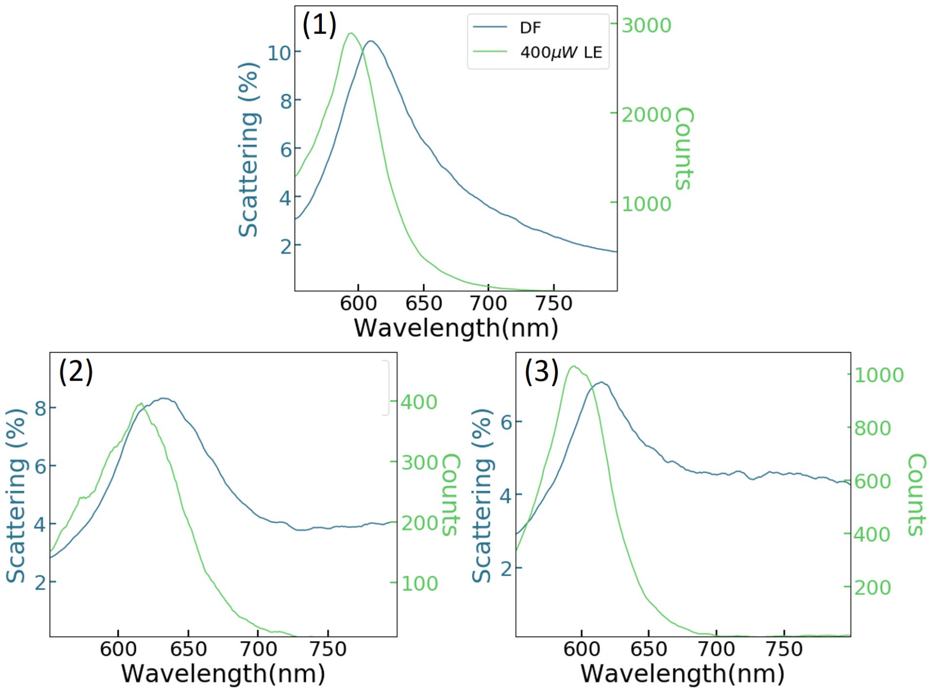

Fig. 6.2 Imaging the WS$_2$ sample grown onto gold foil using optical bright-field (a) and dark-field (b) microscopy at 100× magnification. The sample was also imaged in SEM (c) in order to identify the origin of sparsely distributed red-points (circled with white in (b)).

other works. It is believed to be due to the high population densities available at higher energies (closer to 500 nm)[153, 154].

Polarised dark-field scattering measurements are taken in order to further confirm the nature of the defects. A linear polariser is placed in the illumination path between the light source and the objective and rotated in 90° intervals. This linearly polarises the light reaching the objective, but subsequent illumination of the sample is from all directions. This means that all s-polarised light which does not cancel out is still only in the plane of the substrate as required, while p-polarised light has both transverse (parallel to the substrate plane) and vertical components (perpendicular to the substrate plane). By rotating the polariser by 90° the sum of polarisation changes by a maximal amount and gains or loses vertical polarisation, but this cannot be considered a switch between p and s-polarisation.

The surface of the Au foil displays very weak polarisation dependence and varies in intensity by $\sim 0.5\%$ when changing polariser angle by 90°. An average increase with changing polarisation was measured at 10 points away from the defects and this was used to correct polarisation measurements on the defects. These observations strongly resemble results using s- and p-polarised light from experiments on nano-disc arrays coupled to a Au mirror, separated by 20 nm of $SiO_2$ [158].

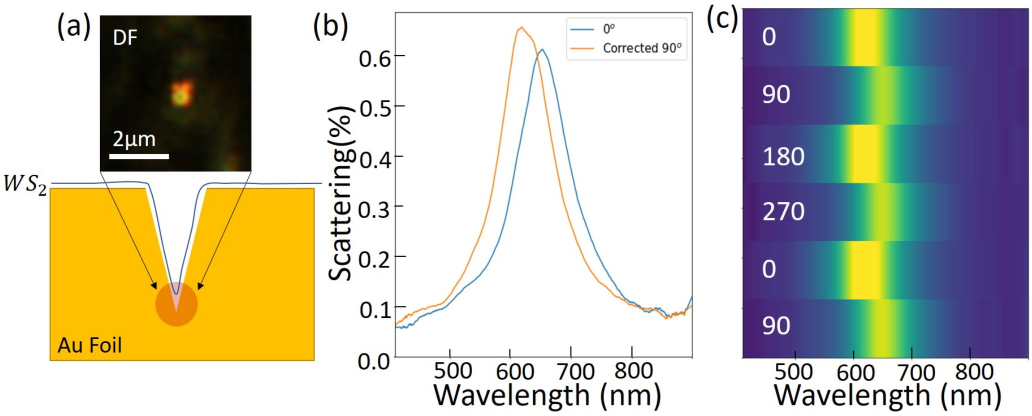

Fig. 6.3 (a) is a simple depiction of the proposed defect in Au foil and its appearance in dark field at 100× magnification, which forms a concentrated near-field much like a nanocavity. (b) shows dark field scattering from the defect shown in (a), and the way in which it shifts with changing polarisation. The changes are the same for full rotations of the polariser in 90° increments as shown in (c).

As seen in Fig. 6.3(b,c) rotating the polariser in 90° increments leads to a maximal change in the brightness of 9% and wavelength of 35 nm ($100meV$) for the dark-field scattering peak from the example defect. There is variation in the polarisation response for different defects, with the majority showing negligible wavelength shifts, but clear increases in intensity with changes in linear polarisation. This likely reflects the non-uniformity of defect geometries. These polarisation measurements suggest further that the nature of the defect is plasmonic, and is less likely to originate from multilayers or contaminants on the surface.

To discount influences from other collective behaviours (e.g. two photon emission), the power dependence of emission from defect 1 was examined. The results of this study are shown in Fig. 6.4, showing a clearly linear relationship between measured counts and power at the sample (Fig. 6.4(a)). The defects are highly robust against damage and the spectrum is not affected up to a power of 2mW (Fig. 6.4(b)). This implies that the emission is purely due to single electron transitions or emission from the metal and cannot be attributed to other effects such as trions (which would not be expected at RT)[159]. This robustness at high power suggests that the defects are likely to be nano-holes in the foil surface. Other work has shown that holes are more robust than nanoscale protrusions and particles [160]. Both holes and protrusions scatter at a similar magnitude for the same diameter.

### 6.2.2 Source of Emissive Defects in as-grown $WS_2$ on Au

Based on the above results and discussion, the source of the red defects appears to be plasmonic, indicating a defect in the Au foil which is attributed to a 200-400 nm hole in the

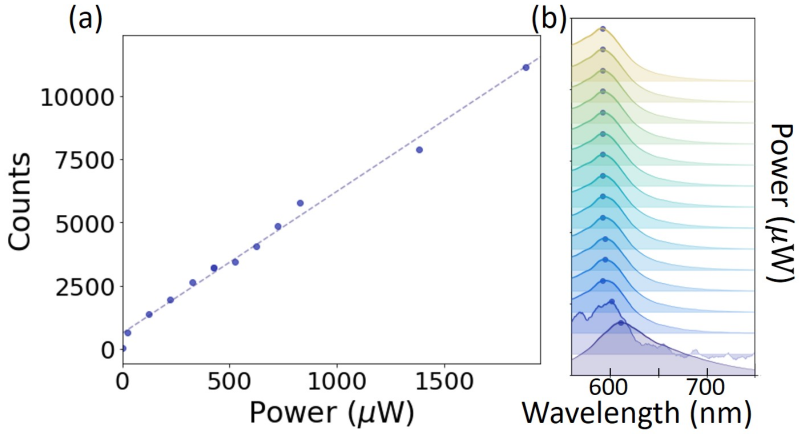

Fig. 6.4 The intensity of light emission from defects increases linearly with increasing power at the sample (a). The normalised emission spectrum (b) is stable as power is increased from 0 to 2mW. In (b), power increases from bottom to top and the bottom spectrum is the normalised dark field scattering spectrum.

foil surface. There is a clear change in dark-field scattering during changes in polarisation, which further supports attribution to a plasmonic effect. The observed light emission is most likely due to photoluminescence from gold, plasmonic enhancement of which dramatically increases the efficiency of light generation and shows a characteristic blue-shift from the scattering peak of the nanostructure. A power dependence experiment gives linear increases in emission, as expected for emission from Au nanostructures [153, 154]. Unfortunately, the overlapping of this emission with the emission from $WS_2$ means it is difficult to determine whether there is any contribution due to the direct transition. There is likely to negligible emission from the $WS_2$ as a result of plasmonic enhancement as the combination of both processes would lead to non-linear emission intensity with power.

The reproducibility of the scattering spectra for the defects likely misleading and not linked to the direct transition for monolayer $WS_2$. However, based on SEM images, the size, shape and morphology of these structures can vary significantly (they are produced randomly), so the uniformity of scattering is unexpected. A link between the emission from these defects and light emission from monolayer $WS_2$ would be extremely interesting, but I have not been able to find literature which discusses any form of coupling between LSPs and adjacent semiconductor absorption.

Uncertainty in the results of this experiment can be removed by completing the same experiment on Au foil without the presence of $WS_2$.

Despite this, the experiment demonstrates the importance of taking into account emission processes from metals during plasmonics experiments involving photo-active materials. This is particularly the case for those materials for which emission is strongly quenched by the presence of the plasmonic metal, and thus its emission signatures are strongly suppressed. Especially for large nanostructures (e.g. 100 nm NPs) and at higher powers, emission from Au can be non-negligible and in some cases dominant.

## 6.3 NPoM with Methylammonium Lead-Iodide

Alongside the great excitement surrounding opto-electronic properties of 2D materials such as TMDs, work on perovskites has continued to progress in leaps and bounds. The metal halides have attracted particular attention due to their unique properties, with the efficiency of photovoltaic devices made using these materials quickly increasing from 4% to 23% over a 6 year period [161, 162]. They are also extremely good light emitters, but are severely restricted in their bulk form due to a small exciton binding energy and mobile ionic defects[161]. Recently, researchers have therefore begun to focus on tuning of their size and shape to form structures such as nanocrystals and nanoplatelets (Fig. 6.5(b,c)). The pseudo-cubic structure of these crystals is shown in Fig. 6.5(a) and is described by the chemical formula $ABX_3$ [161, 10]. A is a metal or organic cation centre (+1 oxidation state), B is a metal ion (+2 oxidation state), and X is a halide ion (-1 oxidation state). By changing the chemical constituents of the crystal the band gap can be broadly tuned within the visible to near-infrared range[161].

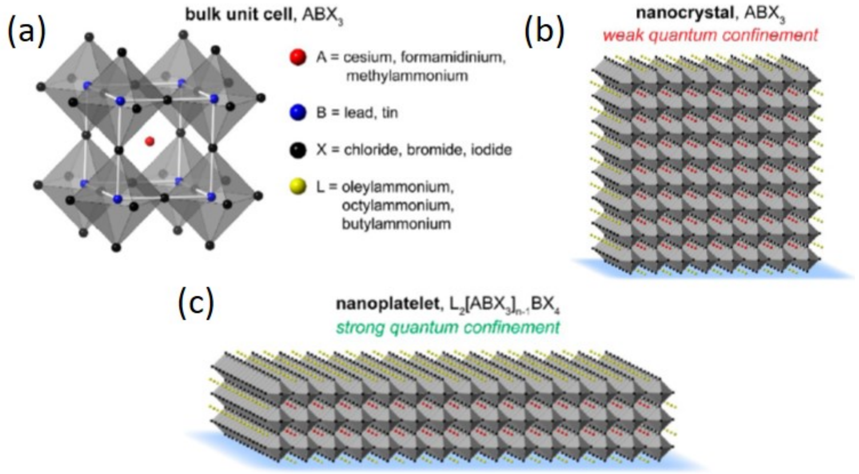

Fig. 6.5 The pseudo-cubic metal halide crystal structure (a) and its nanoscale forms, ranging from colloidal nanocrystals (b) and more recently to nanoplatelets (c). This figure is reprinted and adapted with permission from [10]. Copyright 2017 American Chemical Society.

The recently demonstrated ability of these materials to form nanoplatelets via a process called ligand-assisted exfoliation [162] gives yet another method of tuning the bandgap of metal halides via quantum confinement. The process of exfoliation changes the formula of the metal halide perovskite to $L_2[ABX_3]_{n-1}BX_4$, where $L$ represents the ligand species and $n-1$ the number of unit cells for the nanoplatelet [163]. The formation of perovskite nanoplatelets opens up the possibility of examining their behaviour when exposed to a nanoscale near-field by using the NPoM geometry. In this section we focus on NPoM with the metal halide perovskite methylammonium lead iodide ($CH_4NH_3PbI_3$, commonly referred to as MAPI) in the form of a trilayer nanoplatelet of $\approx$ 2 nm in thickness. As the structure changes from cubic nanocrystal (weak quantum confinement) to trilayer nanoplatelet (strong quantum confinement), the photoluminescence emission wavelength blue-shifts from 740 nm to 610 nm. The exciton binding energy increases significantly, enhancing emission on the monomolecular scale[162] and opening the door for novel nano-optics such as strong-coupling.

### 6.3.1 Sample Fabrication and Images

All colloidal MAPI solutions are synthesised by Dr. Javad Shamsi from the group of Sam Stranks at the University of Cambridge. There is a recent and very thorough review of the production methods and optical properties for MAPI (and other metal halides) written by Dr. Shamsi in reference [161]. Post-synthesis, all samples are fabricated by depositing 100 $\mu$L of MAPI solution onto template-stripped Au substrates and spin coating at 1000rpm for 10s[1]. This distributes the colloidal solution evenly over the substrate surface with nanoplatelets predominantly lying flat over the Au.

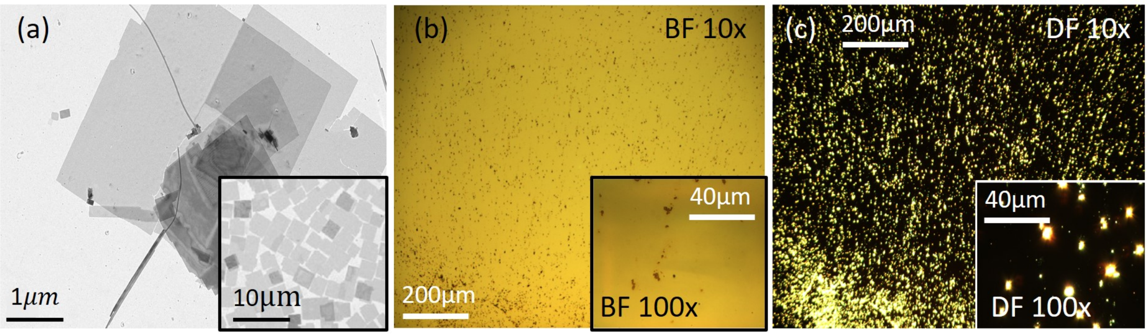

Fig. 6.6 Images of a fabricated MAPI on Au sample showing $\sim 3\mu$m wide flakes of unknown thickness in SEM (a) which arrange themselves on the substrate. Bright-field (BF) (b) and dark-field (c) images show that the density of aggregated material on the substrate is low enough to take effective measurements.

---

[1] It was also found that blow-drying the sample with nitrogen achieved similar results, but with marginally less reproducibility

Example SEM, BF and DF images of MAPI samples are shown for trilayer MAPI in Fig. 6.6, displaying nanoplatelets of $3\mu m$ in diameter which are closely packed and covering $\sim 80\%$ of the substrate surface. There are regions of stacked layers (Fig. 6.6a), but the vast majority are single nanoplatelets. In the optical images the density of aggregated regions is clearly low enough to be able to observe nanoparticles without significant extraneous scattering influencing the data. Single MAPI nanoplatelets are not visible in images except in SEM, where the flakes appear darker for thicker nanoplatelets. The way in which the platelets distributed themselves across the surface appears to be the same on both $SiO_2$ and Au substrates.

### 6.3.2 Multilayer MAPI Quenching

Nanoplatelets of thickness <10 nm are promising for the demonstration of novel nano-optics using NPoM since MAPI is a direct band-gap semiconductor for this entire range of thicknesses. We previously demonstrated strong coupling to the indirect A-exciton transition in multilayer $WSe_2$ in 2017 [9], but we have not succeeded in coupling to a direct transition in crystalline materials using NPoM [2]. We will begin by looking at thicker nanoplatelets (or more cubic nanocrystals) with a band gap at an energy of 1.67 eV, before moving to thinner layers.

Comparing Fig. 6.7(a) with the inset of Fig. 6.6(b), MAPI was found to distribute itself differently when compared to trilayer. The density of aggregates increased, and changed in shape, reflecting the difference in geometry of the thicker nanoplatelets. Initially, the light emission from aggregated multilayer material was recorded over a period of 5 minutes during irradiation of the MAPI with a 447 nm laser and 0.14 $\mu$W at the sample surface. The behaviour on Au is compared to $SiO_2$ substrates with the results (normalised to 1) shown in Fig. 6.7. This was done in in order to determine how the presence of Au influences the emission properties of MAPI.

There is a clear difference between the emission response for multilayer MAPI on $SiO_2$ compared to on Au substrates. For both samples the intensity of PL begins at 740 nm and decays over time due to a combination of quenching within the aggregate and oxidation of the MAPI upon exposure to air. Oxidation of MAPI occurs both in a dry ambient environment and as a result of illumination via a complex photo-oxidation process, reducing the photoluminescnce quantum yield as the material degrades [164, 165].

The multimodal nature of the responses (most clearly visible on Au, but also present on $SiO_2$) is a result of the aggregation of nanoplatelets with different thicknesses, which

---

[2] Although others have using other plasmonic structures

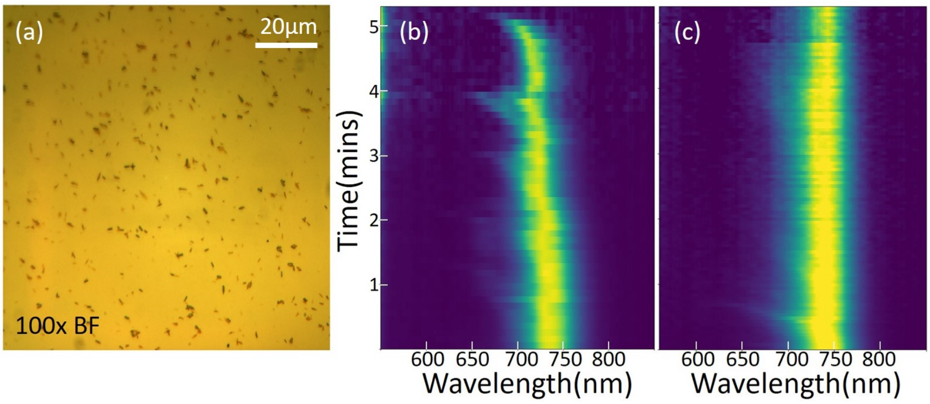

Fig. 6.7 Comparison between emission, normalised to 1, from aggregates of multilayer MAPI on a Au (a) and on $SiO_2$ (b) subsrate with illumination from a 447 nm laser with a power of $0.14\mu W$ at the surface.

emit at a range of wavelengths. This multimodal behaviour changes significantly with time, with individual modes lessening in intensity and blue-shifting in wavelength. The principle PL emission is approximately constant on $SiO_2$, but blue-shifts on Au, which indicates that quenching due to the presence of Au must play a role in the resonance position for this material.

The oxidation process should be the same on both substrates under the same illumination conditions, so the quenching properties of the Au must dominate the observed difference in behaviour. The presence of the Au substrate must lead to preferential emission from thinner layers in the aggregate, perhaps as charges are trapped and have a lower probability of transfer to the Au substrate. This unusual response indicates that the properties of the material are likely to be influenced by encapsulation in NPoM and this expectation is supported in literature [166].

### 6.3.3 Spectroscopy of Trilayer MAPI on Gold

The trilayer sample produced for this set of experiments was shown in Fig. 6.6. Initially the bright-field reflectance is referenced against a clean Au substrate and measured at five different points on the MAPI/Au sample (Fig. 6.8(a)). For three of the measurements (green, orange, blue) no material is visible by eye, whilst the other two measurements (red, purple) are taken on aggregated material (red-brown in colour Fig. 6.6(b)). This was done in order to determine the layer number for the nanoplatelets and to improve understanding of how nanoplatelets are distributed over the substrate surface.

Whilst the presence of individual-few MAPI nanoplatelets is not visible by eye, reflectance measurements at all points show clear absorption, therefore demonstrating good sample coverage post-spin-coating. The measurement on the thickest aggregate (purple curve, Fig. 6.8(a)) reveals the optical activity of the nanoplatelets, with clear reflectance minima at 605 nm and 560 nm. This matches very well with expectations for trilayer MAPI based on the literature, with the peak at 605 nm corresponding to the direct interband transition [161, 162]. In the literature, the unit cell of MAPI has been calculated to be 0.66 nm thick and correspondingly the thickness of trilayer MAPI has been measured at $\approx 2$ nm using AFM [162]. Based on this thickness value and using an in-plane refractive index of 2.5 [167], calculations show that the lowest measured reflectance of 6% (blue curve Fig. 6.8(a)) originates from single trilayer MAPI nanoplatelets on Au [3].

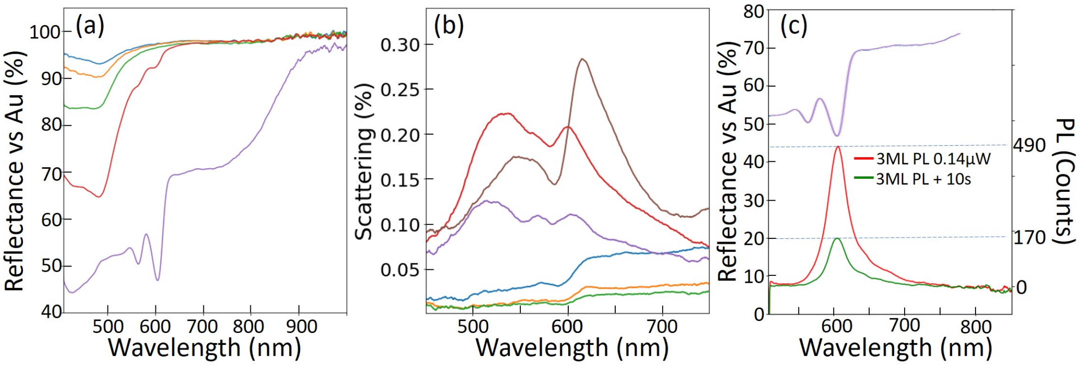

Fig. 6.8 Reflectance measurements referenced to Au for 5 difference regions on the sample (a), with visible aggregated regions showing clear minima at 605 nm and 560 nm corresponding to the direct and indirect transition for trilayer MAPI (purple curve). Dark field measurements(b) on 6 dark regions show clear peaks at the close to the direct transition, while illumination with $0.14\mu W$ at the sample, 447 nm, (c) shows strong emission (red curve) 2 nm below the reflectance minimum for the direct transition (purple curve).

Next, dark-field scattering measurements are taken from six different ‘dark-regions’ on the sample, i.e. points where no material is visible by eye, away from aggregated material (Fig. 6.8(b)). These measurements show a high variation in scattering but all show a clear peak or step at wavelengths ranging between 600-610 nm, matching well with reflectance measurements for the direct inter-band transition for trilayer MAPI. There is a fainter peak at the indirect transition of 560 nm as was also seen in the reflectance. The broader peak is close to the minimum reflectance value and is due to plasmonic scattering onto the Au substrate which peaks in the range 500-530 nm. Variations in peak position may be related due to changes in nanoplatelet layer number, which changes the absorption at the Au/MAPI interface, red-shifting the mode.

---

[3] This does not take into account potential differences between refractive indices for thin-films compared to nanoplatelets or the complex part of the refractive index.

Illumination of the aggregated nanoplatelets with a 447 nm laser at 0.14$\mu$ W leads to strong emission at a wavelength of 607 nm, 2 nm below the reflectance minima for the direct transition and in-line with expectations (Fig. 6.8(c)) [163, 10]. The emission is dominated by the trilayer direct transition with only weak emission from more red-shifted modes, suggesting a high yield of trilayer MAPI. The emission drops over time as quenching and oxidation occurs ($> 50\%$ in 10 s) and does not blue-shift, indicating that monolayer and trilayer MAPI were not present in high quantities. No emission was detectable from non-aggregated material, due to the combination of low optical absorption and quenching from the Au substrate beneath. This is to be expected for thin layers of semiconductor material, which are more strongly influenced by substrate properties than thicker layers[166, 168].

## 6.3.4 Trilayer MAPI in NPoM

Gold nanoparticles of 80 nm diameter are deposited from solution (see chapter 3) immediately after spin-coating MAPI onto template stripped Au as described above. This process must be immediate because the MAPI fully oxidises in air over a period of 10 hours, so experiments have a limited window of success. Dark-field scattering measurements were taken from 160 nanoparticles, with the average dark-field scattering spectrum and corresponding peak positions shown in Fig. 6.9.

Based on the average scattering spectrum, the presence of MAPI strongly influences dark-field scattering from 80 nm NPoMs. Most significantly, the scattering magnitude of all modes, apart from the transverse mode at 530 nm, is significantly less than the value on Au (see chapter 5). The average scattering for the coupled mode of 80 nm NPs on Au substrates is $\sim 0.6\%$, thus the 780 nm mode here is suppressed in intensity by $\sim 6\times$.

Using a citrate thickness of 0.9 nm over a MAPI thickness of 2 nm with a refractive index of 2.5, the average position of the coupled mode is expected to be $\sim 700$ nm based on the model presented in the previous chapter. However, the highly variable experimental data does not match this expectation, with two modes having average resonances at 610 nm and 780 nm. The observed mode fluctuates significantly in peak wavelength, a consequence of the variability of the spacer, with spacers ranging from many layers overlapping to areas with no material. The oxidation of the MAPI material with time also influences its refractive index, which in turn influences coupled mode position [4]. The larger red-shift of the mode might be explained by the close proximity of high-$n$ MAPI material.

Based on the model developed in the previous chapter, the peak position of the coupled mode should not shift beyond the position for the material with no spacer present (i.e. only

---

[4] I have not been able to determine the refractive index of oxidised MAPI

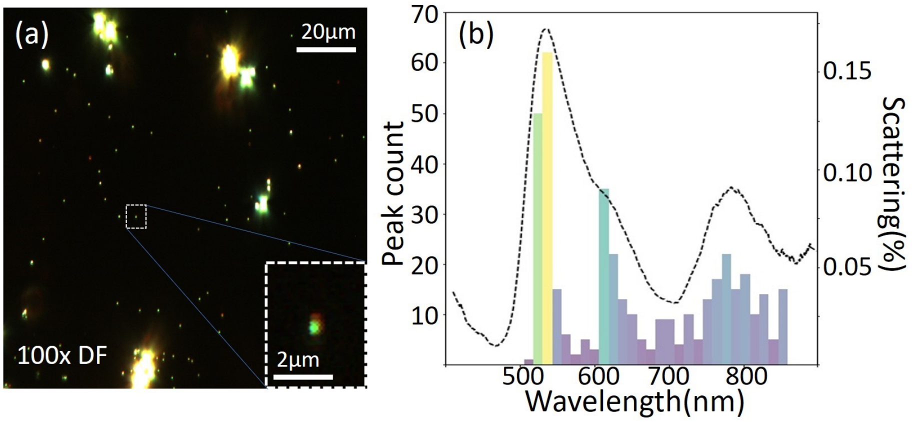

Fig. 6.9 Dark-field image (a) and average spectra (black dashed line, b) collected from 160 80 nm Au nanoparticles on trilayer MAPI. A peak count histogram (b) is used in order to identify resonances within the highly variable dataset with colours in proportion to count value (blue-yellow).

citrate capping ligand present in the gap). Thus, the model appears to break down for MAPI. A red-shifted coupled mode indicates stronger plasmonic coupling between nanoparticle and mirror than was observed for hBN. In addition, the experiments on hBN suggested a proportionality between spacer refractive index and scattering intensity, which is not observed here. The resonance wavelength is possibly explained by the high-$n$ material surrounding the MAPI NPoM's (i.e. stacked layers next to the structure) which red-shifts the coupled mode beyond the maximum value of 750 nm without a spacer. I am unable to explain the reduction in the scattering intensity unless the material beneath is oxidised and therefore has a significantly lower refractive index. The ligand used for the formation of nanoplatelets is oleic acid, with a refractive index of 1.38, which is not significantly less than citrate. If this was included the gap refractive index would be lowered further.

Overlapping MAPI layers would contribute to blue-shifting of the coupled modes, so this cannot be used to explain the highly red-shifted mode position.

### 6.3.5 Simultaneous Scattering and Emission Measurements on MAPI NPoM

Simultaneous dark-field and photoluminescence spectroscopy measurements are taken in order to correlate the dark-field scattering with light emission and to tune modes across the wavelength of the direct transition (see next). As power at the sample is increased to above a threshold (typically >150 $\mu$W), heating leads to partial melting and motion of mobile surface atoms to the base of the nanoparticle, growing the bottom facet [47, 157]. This is now known to lead to red-shifting of the coupled mode position over a time period of many seconds, until a physical link between nanoparticle and mirror (bridging) occurs. The technique was used in our previous work on strong coupling with multilayer $WSe_2$, to tune the coupled mode across the indirect transition [9]. Just before bridging, the coupled modes rapidly red-shift out to infra-red wavelengths, beyond the detection limit of our setup. Bridging, which links nanoparticle and mirror via a metallic nanowire, then rapidly blue-shifts the modes, continuing to do so as the bridge increases in diameter until a saturation point is reached. The observed resonances once a bridge is formed are the result of the charge transfer plasmon [169, 157].

In the experiment shown in Fig. 6.10, the power is ramped in intervals of approximately 25 $\mu$W every 30 seconds. Notably, for this nanoparticle the intensity of the coupled mode dominates scattering, and the progression of this mode specifically is tracked in this experiment. At low powers (<100 $\mu$W) modes initially red-shift with no detected light emission (Fig. 6.10). This is in-line with expectations since the facet grows due gold atom migration and the emission from single Au nanoparticle-on-mirror has been calculated to be extremely weak [157, 47]. However, at a power of 175 $\mu$W stable emission is observed and the coupled mode begins to blue-shift as opposed to the expected red-shift of the mode to IR before bridging. The blue-shifting behaviour of dark-field scattering continues at higher powers, showing stable light emission which tracks with the position of the dark-field modes (Fig. 6.10(b,c)). This in-sync progression continues until the emission reaches 610 nm, 300 $\mu$W, close to the emission from the direct transition for trilayer MAPI, at which point the process stops. As was also observed for defects in Au foils with $WS_2$, the emission is clearly blue-shifted from the position of dark-field, in this case by 30 nm.

Emission linewidth remained constant for all powers with intensity rising linearly (Fig. 6.11), meaning that emission related to non-linear processes can be discounted. Other such experiments were conducted on other nanoparticles and there were no clear signatures of strong coupling as modes tuned across the 605 nm direct transition for MAPI trilayer nanoplatelets. The high variability of results was a significant issue when looking for the signatures of strong-coupling.

Light emission from silver nanocubes on a silver mirror has been observed before, in a similar experiment from within my group [157]. Emission tuned in-sync with the progression of the dark-field modes, however the expected red-shifts to IR occurred and once bridging was completed, emission stopped. Also in this work, the efficiency of emission from gold nanoparticles on gold mirrors was calculated to be extremely low, below the detection limit of our setup. Conversely, in this case no clear bridging process was observed and emission continues for all incident powers.

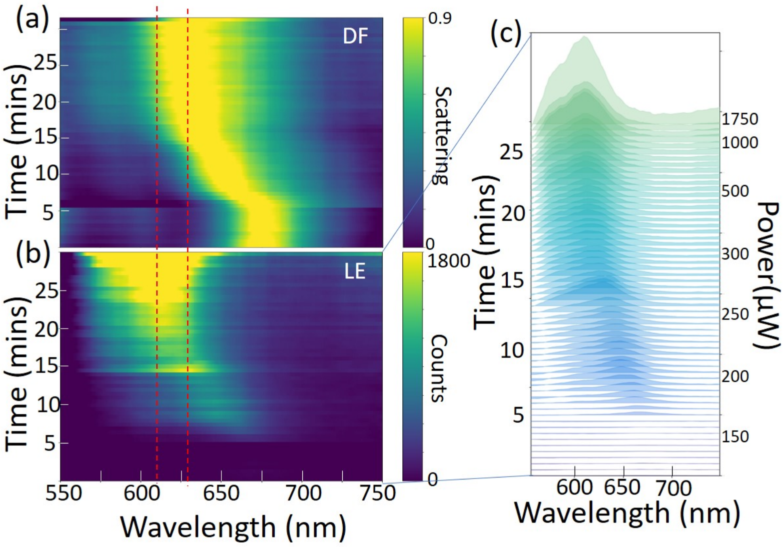

Fig. 6.10 Simultaneous dark-field scattering (a) and emission measurements (b,c) taken for a single 80 nm MAPI NPoM with red dashed lines drawn at the peak wavelengths for scattering and emission. The nanoparticle was illuminated with a 447 nm laser with power increased by approximately 25$\mu W$ every 30 seconds.

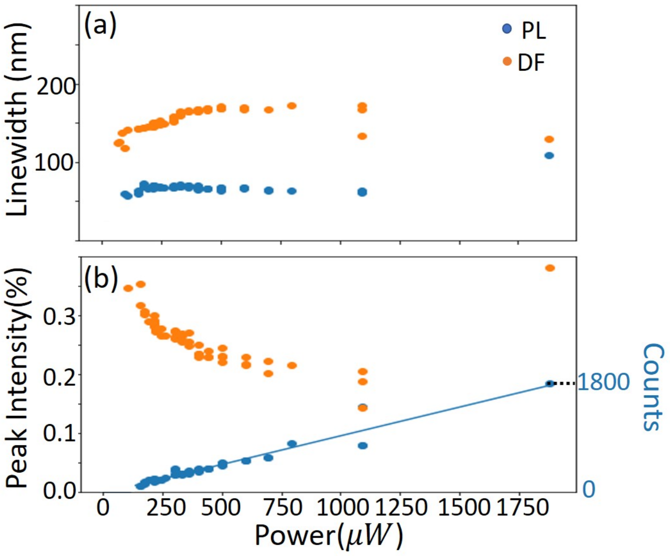

Fig. 6.11 Measurements of linewidth (a) and peak intensity (b) for both dark-field (orange) and light emission (blue) as a function of power at the sample.

The data indicates that a solid spacer of MAPI must exist between the nanoparticle and mirror beneath, which prevents bridging. Initially the facet grows at usual, leading to red-shifts of the coupled mode, but eventually this process is counteracted by a secondary process, most likely photo- and thermally assisted oxidation of the MAPI which is near-field enhanced. The oxidation process reduces the refractive index of both the material in the gap and the surrounding material, leading to blue-shifts of the dipole-antenna mode.

The linear power dependence and clear blue-shift from the dark-field, suggests once again that the light emission is from gold. However, these nanoparticles clearly behave differently from defects in Au foils as they change morphology with increasing incident power. Once again the tendency of the dark-field to peak at wavelengths close to the direct transition of an adjacent semiconductor is likely to be misleading.

## 6.4 Conclusion

A barrier to interpretation of these $WS_2$ and trilayer MAPI experiments is that the active semiconductors display approximately the same band-gap. This makes it extremely difficult to distinguish between emission from Au and emission from the direct semiconductor. To clarify these results, the same work should be completed on semiconductors with band-gaps at longer wavelengths. If dark-field peaks show a tendency to overlap with the direct transition at this new and longer wavelength, and emission is once again observed, then a novel process is occurring. Until this is done, the hypothesis that all light emission is from the metal, must remain as the explanation for the above results.

The oxidation of MAPI is a problem for all experiments using this material. Future experiments should look to protect the sample post deposition of nanoparticle, for example by spin-coating a transparent dielectric such as poly methyl methacrylate (PMMA).

Direct growth of $WS_2$ and other TMDs appears extremely promising for plasmonics applications. Nanoparticles of 100 nm diameter were clearly visible on the rough Au foil, but the use of single crystalline Au as a growth substrate would significantly reduce roughness and enable detection of more subtle nano-optical effects. Most significantly it would avoid the need for transfer of these materials, which currently leads to so many further problems. Patterned gold growth substrates are another potential route, onto which $WS_2$ could be grown and measurements taken directly. Seeding of multilayer $WS_2$ from nanostructures may limit this however.

# Chapter 7

# Conclusions and outlook

In this thesis an important type of optically active heterostructure was thoroughly interrogated using dark-field spectroscopy in combination with state of the art surface analysis and fabrication techniques. The basic architecture consisted of a nanoparticle atop a crystal of hexagonal-Boron Nitride deposited over a flat substrate of Au. The nanoparticle coupled via fields propagating across the gap to the Au mirror beneath and by changing the thickness of hBN the coupling mechanism changed dramatically. Such changes were interpreted via far-field high-angle scattering from the nanoparticle and strong knowledge of subtle fabrication features.

In the first experiment, Au nanoparticles coupled to hBN optical sub-microcavities (>80 nm) embedded in Au. The resultant scattering from these NPoMCs is found to be far more complex than was shown in the past [121, 120], resulting from a combination of Fabry-Perot enhancement processes and a new nanoresonator mode (NRM). Calculations showed that the NRMs were strongest at particular angles around the Brewster angle, at which there is only an influence for TM polarisation. The resonances were shown to result from light trapping between the nanoparticle and mirror underneath hBN, confined to the nanoscale geometry of the nanoparticle and dependent subtly on its morphology. In contrast to Fabry-Perot modes coupled to individual nanoparticle LSPs, which are well documented, these modes display field-vectors perpendicular to the plane of the sub-microcavity ($E_z$ in the model) which is unusual for microcavities. The addition of these modes to our previous knowledge of microcavity-coupled plasmonics, therefore enables access to new field orientations in the cavity in a simple way, controlled via incident angle and polarisation. Meanwhile, hBN has become a ubiquitous substrate or dividing layer for van der Waals heterostructures, able to enhance a number of optical properties and enable novel band structure engineering such as inter-layer excitons[80, 106, 102]. The observation of NRMs in hBN can therefore enable their integration into novel microcavity heterstructure systems which combine plasmonic and optical enhancements with the unique properties of van der Waals heterostructures.

The second set of experiments represent an unprecedented study of van der Waals materials in the nanoparticle-on-mirror geometry (NPoM). These systems have been shown to be extremely powerful for the demonstration of novel nano-optics and thus a full understanding of the system is of vital importance. hBN uniquely enables this full understanding because it is optically inert, meaning that it is possible to exclude a great number of other explanations for observations in NPoM. Three different samples were studied in which the classical circuit model [46] failed to accurately predict coupled mode positions based on the usual assumptions. The model therefore was adapted to take into account the change in refractive index as a result of the presence of passivating ligands, which correctly predicted the coupled mode wavelengths in every case. This adaptation changes the spacer to a hybrid material consisting of multiple different layers of differing refractive index.

The use of large-area, ultra-high-quality CVD hBN annealed at 350°C enabled the statistical analysis of over 400 nanoparticles both on trilayer and monolayer hBN varying in size from 60-80 nm. As a result it was seen that despite these contaminants, the presence of hBN in the gap could be clearly detected via intensity enhancements (also seen on exfoliated hBN) and the positive skew of the coupled mode distributions. It was posited that the intensity enhancement is dominated by increases in the effective (including citrate) refractive index in the gap, hence the contrasting negligible enhancement for monolayer hBN and very strong enhancement for few-layer hBN. The positive skew of the coupled mode distribution in wavelength on-hBN was a result of the hybrid variation of refractive index with gap distance, which increases the tuning rate at greater thicknesses of material. This appeared in clear contrast to the distribution for coupled mode wavelength on-Au despite the expected greater tuning rate for smaller gap sizes. To explain this difference the gap containing contaminants is considered as filled by variable quantities of molecules for the same gap distance. In this case the tuning rate is linear and greatly reduced. A final fundamental consequence of the presence of passivating ligands is that the maximum coupled mode wavelength on-hBN is set to within a few-nanometres by the maximum coupled mode wavelength off-hBN (i.e. with ligands alone on Au).

Finally, the plasmonic enhancement of the optically active layers $WS_2$ and MAPI was studied. For CVD $WS_2$ grown onto Au, defects in the foil surface showed emission which overlapped with scattering from the direct band-gap transition. This emission was clearly blue-shifted from the position of scattering and displayed spectral positions which shifted with changing polarisation. This led to the conclusion that the emission was in fact from the Au defect. 80 nm MAPI NPoMs showed an anomalous suppression of the coupled mode intensity and modes red-shifted beyond expectations based on the modified circuit model. The red-shifts were explained by the presence of stacked nanoplatelets in the vicinity of the nanoparticle facet. In addition, a similar blue-shifted light emission as was seen for $WS_2$ was observed which tracked with changing coupled mode wavelength and matched the direct transition for MAPI. This emission was attributed once again to emission from Au rather than the material emission due to the blue-shifted behaviour.

The wide range of results found using these otherwise similar structures reveals the enormous range of possibilities for NPoMC and NPoM systems. A such, a few ideas for future experiments and useful architectures based on my experiments are shown in Fig. 7.1.

In the NRM microcavity (Fig. 7.1(a)) deposition of an optically active layer (e.g. $WSe_2$, other TMDs, MAPI etc.) over thick (>80 nm) hBN before deposition of NPs will enable NRMs to excite vertical dipoles in optical layers. Insertion into a microcavity (which allows high angle illumination) would give researchers improved access to all field components by changing incident angle and polarisation. This may enable strong-coupling to materials which display vertical exciton moments (e.g. multilayer $WSe_2$ or molecules)[9].

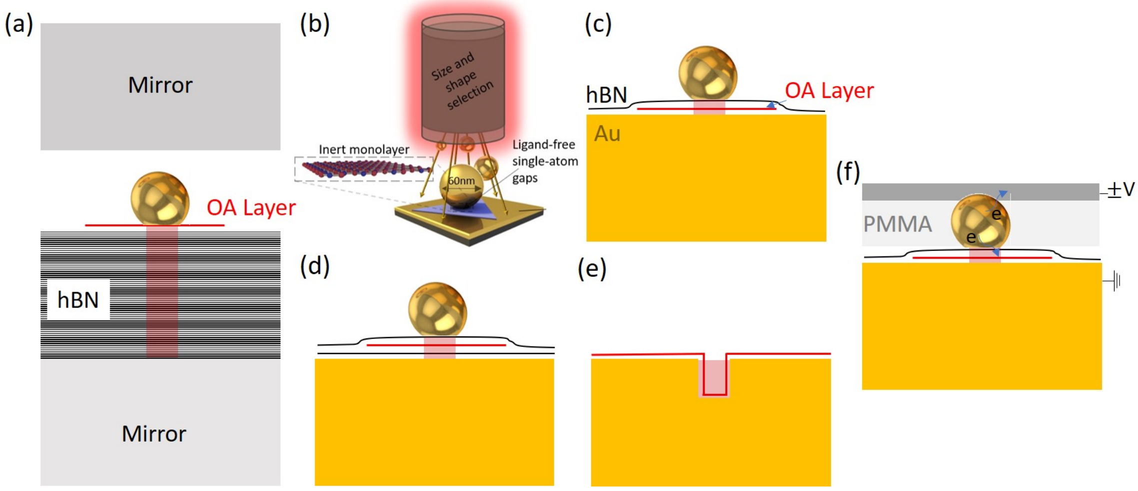

Fig. 7.1 Depictions of an NRM microcavity (a), gas-phase deposition (b), protection and encapsulaltion with hBN (c,d), nanostructured CVD Au substrates (e) and the biasing of NPoM tunnel heterostructures(f).

For the next few systems (Fig. 7.1(c-f)), the optimal situation is the deposition of nanoparticles without ligands, for example via gas-phase deposition (b). Progress toward this aim is shown in the appendix.

These ligand-free nanoparticles can be deposited onto optically active layers (OA layer in figure), which are protected by monolayer to few-layer CVD hBN (c). This would prevent oxidation of perovskite nanoplatelets (e.g. MAPI) and may enable novel nanooptics in hybrid systems. This is preferred to protection with PMMA which will have detrimental effects on the optical properties of the sample. In the same vein, the optically active layer can be fully encapsulated with few-monolayer hBN to reduce quenching by the Au substrate and provide further protection.

As-grown $WS_2$ on Au foils can be modified to be grown onto more ordered nanostructured Au. The patterning of nanoscale holes pre-growth would form nanocavities the optical properties of which could be measured before and after growth of $WS_2$. This may enable the enhancement of novel optical properties in $WS_2$ (and other semiconductors grown on Au), and knowledge of emission from Au from my work would help identify features.

# References

[1] Overview of Mayan Art, 2020, https://www.historyonthenet.com/overview-of-mayan-art, History on the Net, Salem Media.

[2] Philippe Sciau. Nanoparticles in ancient materials: The metallic lustre decorations of medieval ceramics. In Abbass A. Hashim, editor, *The Delivery of Nanoparticles*, chapter 25. IntechOpen, Rijeka, 2012.

[3] Rayleigh and lorentz. https://www.sciencephoto.com/media/222829/view/portrait-of-physicists-lord-rayleigh-and-kelvin. Accessed: 2019-09-30.

[4] Sperical harmonics example. https://docs.enthought.com/mayavi/mayavi/auto/example_spherical_harmonics.htmll. Accessed: 2019-11-21.

[5] Jan Mertens, Anna L. Eiden, Daniel O. Sigle, Fumin Huang, Antonio Lombardo, Zhipei Sun, Ravi S. Sundaram, Alan Colli, Christos Tserkezis, Javier Aizpurua, Silvia Milana, Andrea C. Ferrari, and Jeremy J. Baumberg. Controlling subnanometer gaps in plasmonic dimers using graphene. *Nano Letters*, 13(11):5033–5038, Nov 2013.

[6] A. Jones. *Basic Concepts*, chapter 1, pages 1–42. John Wiley and Sons, Ltd, 2008.

[7] Jay N. Meegoda, Shaini Aluthgun Hewage, and Janitha H. Batagoda. Application of the diffused double layer theory to nanobubbles. *Langmuir*, 35(37):12100–12112, 2019. PMID: 31433652.

[8] Daniel O. Sigle, Jan Mertens, Lars O. Herrmann, Richard W. Bowman, Sandrine Ithurria, Benoit Dubertret, Yumeng Shi, Hui Ying Yang, Christos Tserkezis, Javier Aizpurua, and Jeremy J. Baumberg. Monitoring morphological changes in 2D monolayer semiconductors using atom-thick plasmonic nanocavities. *ACS Nano*, 9(1):825–830, 2015.

[9] Marie-Elena Kleemann, Rohit Chikkaraddy, Evgeny M. Alexeev, Dean Kos, Cloudy Carnegie, Will Deacon, Alex Casalis de Pury, Christoph Grosse, Bart de Nijs, Jan Mertens, Alexander I. Tartakovskii, and Jeremy J. Baumberg. Strong-coupling of wse(2) in ultra-compact plasmonic nanocavities at room temperature. *Nature communications*, 8(1):1296–1296, Nov 2017. 29101317[pmid].

[10] Mark C. Weidman, Aaron J. Goodman, and William A. Tisdale. Colloidal halide perovskite nanoplatelets: An exciting new class of semiconductor nanomaterials. *Chemistry of Materials*, 29(12):5019–5030, 2017.

[11] Rohit Chikkaraddy, Bart de Nijs, Felix Benz, Steven J Barrow, Oren A Scherman, Edina Rosta, Angela Demetriadou, Peter Fox, Ortwin Hess, and Jeremy J Baumberg. Single-molecule strong coupling at room temperature in plasmonic nanocavities. *Nature*, 535(7610):127–130, 2016.

[12] M. Shahpari and D. V. Thiel. Fundamental limitations for antenna radiation efficiency. *IEEE Transactions on Antennas and Propagation*, 66(8):3894–3901, Aug 2018.

[13] Constantine A. Balanis. *Antenna Theory: Analysis and Design*. Wiley-Interscience, USA, 2005.

[14] Harry A. Atwater. The promise of plasmonics. *Scientific American*, 296(4):56–63, 2007.

[15] Oluwafemi S. Ojambati, Rohit Chikkaraddy, William D. Deacon, Matthew Horton, Dean Kos, Vladimir A. Turek, Ulrich F. Keyser, and Jeremy J. Baumberg. Quantum electrodynamics at room temperature coupling a single vibrating molecule with a plasmonic nanocavity. *Nature Communications*, 10(1):1049, 2019.

[16] Sneha Mohan Bhagyaraj and Oluwatobi Samuel Oluwafemi. *Nanotechnology: The Science of the Invisible*. Elsevier Ltd., 2018.

[17] P. (Victoria Ferguson and Albert Museum). Islamic Art and Material Culture Subject Specialist Network: Lustre across time, 2016.

[18] S.L. Croft. Colloidal gold. *Electron Microscopy Reviews*, 5(2):iii–iv, 2002.

[19] Xiaofeng Chen, Lin Zhu, Mengjiao Huang, and Chaoyong Yang. *Synthesis of Gold Nanoparticles and Functionalization With DNA for Bioanalytical Applications*. Elsevier Inc., 2019.

[20] Micheal Faraday. Faraday ' s notebooks : Gold colloids. page 146, 1856.

[21] Xiaofeng Fan, Weitao Zheng, and David J. Singh. Light scattering and surface plasmons on small spherical particles. *Light: Science & Applications*, 3(6):e179–e179, 2014.

[22] P J Dobson. Absorption and Scattering of Light by Small Particles. *Physics Bulletin*, 35(3):104–104, 1984.

[23] Boris Luk'yanchuk, Nikolay I Zheludev, Stefan A Maier, Naomi J Halas, Peter Nordlander, Harald Giessen, and Chong Tow Chong. The Fano resonance in plasmonic nanostructures and metamaterials. *Nature materials*, 9(9):707–15, 2010.

[24] *Particles Small Compared with the Wavelength*, chapter 5, pages 130–157. John Wiley and Sons, Ltd, 2007.

[25] Anastasiya Derkachova, Krystyna Kolwas, and Iraida Demchenko. Dielectric function for gold in plasmonics applications: Size dependence of plasmon resonance frequencies and damping rates for nanospheres. *Plasmonics*, 11(3):941–951, Jun 2016.

[26] Robert L. Olmon, Brian Slovick, Timothy W. Johnson, David Shelton, Sang-Hyun Oh, Glenn D. Boreman, and Markus B. Raschke. Optical dielectric function of gold. *Phys. Rev. B*, 86:235147, Dec 2012.

[27] Colby Foss and Daniel Feldheim. *Metal Nanoparticles*. CRC Press, Oct 2001.

[28] Ulrich Hohenester. *Nano and Quantum Optics: An Introduction to Basic Principles*. Springer International Publishing, 2019.

[29] Stefan Alexander Maier. *Plasmonics - Fundamentals and Applications*. Springer, 2007.

[30] R. Want. Near field communication. *IEEE Pervasive Computing*, 10(3):4–7, July 2011.

[31] Helmuth Horvath. Gustav mie and the scattering and absorption of light by particles: Historic developments and basics. *Journal of Quantitative Spectroscopy and Radiative Transfer*, 110(11):787 – 799, 2009. Light Scattering: Mie and More Commemorating 100 years of Mie's 1908 publication.

[32] Prashant K. Jain. Taking the heat off of plasmonic chemistry. *The Journal of Physical Chemistry C*, 123(40):24347–24351, Oct 2019.

[33] Liselotte Jauffred, Akbar Samadi, Henrik Klingberg, Poul Martin Bendix, and Lene B. Oddershede. Plasmonic heating of nanostructures. *Chemical Reviews*, 119(13):8087–8130, Jul 2019.

[34] Radwan M. Sarhan, Wouter Koopman, Roman Schuetz, Thomas Schmid, Ferenc Liebig, Joachim Koetz, and Matias Bargheer. The importance of plasmonic heating for the plasmon-driven photodimerization of 4-nitrothiophenol. *Scientific Reports*, 9(1):3060, 2019.

[35] L. C. Flatten, Z. He, D. M. Coles, A. A. P. Trichet, A. W. Powell, R. A. Taylor, J. H. Warner, and J. M. Smith. Room-temperature exciton-polaritons with two-dimensional ws2. *Scientific Reports*, 6(1):33134, 2016.

[36] Wenjing Liu, Bumsu Lee, Carl H. Naylor, Ho-Seok Ee, Joohee Park, A. T. Charlie Johnson, and Ritesh Agarwal. Strong exciton-plasmon coupling in mos2 coupled with plasmonic lattice. *Nano Letters*, 16(2):1262–1269, Feb 2016.

[37] The bessel function and the related neumann function. https://www.nbi.dk/~polesen/borel/node6.html. Accessed: 2019-09-30.

[38] R. Mittra J. J. Baumberg X. Zheng, A. Casalis de Pury and G. A. E. Vandenbosch. *IEEE Transactions on Antennas and Propagation (submitted)*, 2019.

[39] *Electromagnetic Cavities*, pages 207–226. Springer New York, New York, NY, 2007.

[40] Guillame Malpuech Fabrice P. Laussy J. Alexey Kavokin, J. Baumberg. *Microcavities*. Oxford University Press, 2017.

[41] Xiantong Yu, Yufeng Yuan, Jianhua Xu, Ken-Tye Yong, Junle Qu, and Jun Song. Strong coupling in microcavity structures: Principle, design, and practical application. *Laser & Photonics Reviews*, 13(1):1800219, 2019.

[42] Xiaoze Liu, Tal Galfsky, Zheng Sun, Fengnian Xia, Erh-chen Lin, Yi-Hsien Lee, Stéphane Kéna-Cohen, and Vinod M. Menon. Strong light-matter coupling in two-dimensional atomic crystals. *Nature Photonics*, 9(1):30–34, 2015.

[43] Richard W. Fox. Fabry-perot temperature dependence and surface-mounted optical cavities. *Photonics North 2008*, Jun 2008.

[44] C. Kruse, S. Figge, and D. Hommel. 14 - growth of ii–vi and iii-nitride quantum-dot microcavity systems. In Frank Jahnke, editor, *Quantum Optics with Semiconductor Nanostructures*, Woodhead Publishing Series in Electronic and Optical Materials, pages 447 – 484. Woodhead Publishing, 2012.

[45] Jeremy J. Baumberg, Javier Aizpurua, Maiken H. Mikkelsen, and David R. Smith. Extreme nanophotonics from ultrathin metallic gaps. *Nature Materials*, 18(7):668–678, 2019.

[46] Felix Benz, Bart de Nijs, Christos Tserkezis, Rohit Chikkaraddy, Daniel O. Sigle, Laurynas Pukenas, Stephen D. Evans, Javier Aizpurua, and Jeremy J. Baumberg. Generalized circuit model for coupled plasmonic systems. *Optics Express*, 23(26):33255, 2015.

[47] C. Tserkezis, R. Esteban, D. O. Sigle, J. Mertens, L. O. Herrmann, J. J. Baumberg, and J. Aizpurua. Hybridization of plasmonic antenna and cavity modes: Extreme optics of nanoparticle-on-mirror nanogaps. *Physical Review A - Atomic, Molecular, and Optical Physics*, 92(5):1–6, 2015.

[48] Yang Shen, Jianhua Zhou, Tianran Liu, Yuting Tao, Ruibin Jiang, Mingxuan Liu, Guohui Xiao, Jinhao Zhu, Zhang-Kai Zhou, Xuehua Wang, Chongjun Jin, and Jianfang Wang. Plasmonic gold mushroom arrays with refractive index sensing figures of merit approaching the theoretical limit. *Nature Communications*, 4(1):2381, 2013.

[49] Xiang Meng, Richard Grote, Jerry Dadap, Nicolae Panoiu, and Richard Osgood. Engineering metal-nanoantennae/dye complexes for maximum fluorescence enhancement. *Optics Express*, 22, Sep 2014.

[50] P. Nordlander and E. Prodan. Plasmon hybridization in nanoparticles near metallic surfaces. *Nano Letters*, 4(11):2209–2213, Nov 2004.

[51] E. Prodan and P. Nordlander. Plasmon hybridization in spherical nanoparticles. *The Journal of Chemical Physics*, 120(11):5444–5454, 2004.

[52] Ai Leen Koh, Kui Bao, Imran Khan, W. Ewen Smith, Gerald Kothleitner, Peter Nordlander, Stefan A. Maier, and David W. McComb. Electron energy-loss spectroscopy (eels) of surface plasmons in single silver nanoparticles and dimers: Influence of beam damage and mapping of dark modes. *ACS Nano*, 3(10):3015–3022, Oct 2009.

[53] Sammy W. Verbruggen, Maarten Keulemans, Johan A. Martens, and Silvia Lenaerts. Predicting the surface plasmon resonance wavelength of gold-silver alloy nanoparticles. *The Journal of Physical Chemistry C*, 117(37):19142–19145, Sep 2013.

[54] Ryan T. Hill, Jack J. Mock, Angus Hucknall, Scott D. Wolter, Nan M. Jokerst, David R. Smith, and Ashutosh Chilkoti. Plasmon ruler with angstrom length resolution. *ACS Nano*, 6(10):9237–9246, Oct 2012.

[55] Carsten Sönnichsen, Björn M. Reinhard, Jan Liphardt, and A. Paul Alivisatos. A molecular ruler based on plasmon coupling of single gold and silver nanoparticles. *Nature Biotechnology*, 23(6):741–745, 2005.

[56] Charlie Readman, Bart de Nijs, István Szabó, Angela Demetriadou, Ryan Greenhalgh, Colm Durkan, Edina Rosta, Oren A. Scherman, and Jeremy J. Baumberg. Anomalously large spectral shifts near the quantum tunnelling limit in plasmonic rulers with subatomic resolution. *Nano Letters*, 19(3):2051–2058, Mar 2019.

[57] W. Rechberger, A. Hohenau, A. Leitner, J. R. Krenn, B. Lamprecht, and F. R. Aussenegg. Optical properties of two interacting gold nanoparticles. *Opt. Commun*, page 137, 2003.

[58] Luca Piantanida, Denys Naumenko, and Marco Lazzarino. Highly efficient gold nanoparticle dimer formation via dna hybridization. *RSC Adv.*, 4:15281–15287, 2014.

[59] Lin Cheng, Jibin Song, Jun Yin, and Hongwei Duan. Self-assembled plasmonic dimers of amphiphilic gold nanocrystals. *The Journal of Physical Chemistry Letters*, 2(17):2258–2262, Sep 2011.

[60] Israa Haidar, Jean Aubard, Georges Lévi, Stéphanie Lau-Truong, Ludovic Mouton, Daniel R. Neuville, Nordin Félidj, and Leïla Boubekeur-Lecaque. Design of stable plasmonic dimers in solution: Importance of nanorods aging and acidic medium. *The Journal of Physical Chemistry C*, 119(40):23149–23158, Oct 2015.

[61] Aunpspecs. Accessed: 2019-11-24.

[62] Jack J. Mock, Ryan T. Hill, Aloyse Degiron, Stefan Zauscher, Ashutosh Chilkoti, and David R. Smith. Distance-dependent plasmon resonant coupling between a gold nanoparticle and gold film. *Nano Letters*, 8(8):2245–2252, Aug 2008.

[63] Xin Tao and Yi Gu. Crystalline-crystalline phase transformation in two-dimensional in2se3 thin layers. *Nano Letters*, 13(8):3501–3505, Aug 2013.

[64] C. Julien, M. Eddrief, K. Kambas, and M. Balkanski. Electrical and optical properties of in2se3 thin films. *Thin Solid Films*, 137(1):27 – 37, 1986.

[65] M. A. Ordal, Robert J. Bell, R. W. Alexander, L. L. Long, and M. R. Querry. Optical properties of fourteen metals in the infrared and far infrared: Al, co, cu, au, fe, pb, mo, ni, pd, pt, ag, ti, v, and w. *Appl. Opt.*, 24(24):4493–4499, Dec 1985.

[66] A. Derkachova and K. Kolwas. Size dependence of multipolar plasmon resonance frequenciesand damping rates in simple metal spherical nanoparticles. *The European Physical Journal Special Topics*, 144(1):93–99, 2007.

[67] Chris Oubre and Peter Nordlander. Optical properties of metallodielectric nanostructures calculated using the finite difference time domain method. *The Journal of Physical Chemistry B*, 108(46):17740–17747, Nov 2004.

[68] P. G. Etchegoin, E. C. Le Ru, and M. Meyer. An analytic model for the optical properties of gold. *The Journal of Chemical Physics*, 125(16):164705, 2006.

[69] Nathaniel Grady, Naomi Halas, and P. Nordlander. Influence of dielectric function properties on the optical response of plasmon resonant metallic nanoparticles. *Chemical Physics Letters*, 399:167–171, 11 2004.

[70] Martin G. Blaber, Matthew D. Arnold, and Michael J. Ford. Search for the ideal plasmonic nanoshell: The effects of surface scattering and alternatives to gold and silver. *The Journal of Physical Chemistry C*, 113(8):3041–3045, Feb 2009.

[71] Ellen J. Zeman and George C. Schatz. An accurate electromagnetic theory study of surface enhancement factors for silver, gold, copper, lithium, sodium, aluminum, gallium, indium, zinc, and cadmium. *The Journal of Physical Chemistry*, 91(3):634–643, Jan 1987.

[72] Marie-Elena Kleemann, Jan Mertens, Xuezhi Zheng, Sean Cormier, Vladimir Turek, Felix Benz, Rohit Chikkaraddy, William Deacon, Anna Lombardi, Victor V. Moshchalkov, Guy A. E. Vandenbosch, and Jeremy J. Baumberg. Revealing nanostructures through plasmon polarimetry. *ACS Nano*, 11(1):850–855, Jan 2017.

[73] Cai W. García de Abajo F. J. Kuttge, M. and A. Polman. Dispersion of metal-insulator-metal plasmon polaritons probed by cathodoluminescence imaging spectroscopy. *Phys. Rev. B*, 80:033409, 2009.

[74] Anatoly V. Zayats, Igor I. Smolyaninov, and Alexei A. Maradudin. Nano-optics of surface plasmon polaritons. *Physical Reports*, 408(3-4):131–314, Mar 2005.

[75] Ruoxi Yang and Zhaolin Lu. Subwavelength plasmonic waveguides and plasmonic materials. *International Journal of Optics*, 2012, 07 2012.

[76] K. S. Novoselov, A. K. Geim, S. V. Morozov, D. Jiang, M. I. Katsnelson, I. V. Grigorieva, S. V. Dubonos, and A. A. Firsov. Two-dimensional gas of massless dirac fermions in graphene. *Nature*, 438(7065):197–200, Nov 2005.

[77] Roman V. Gorbachev, Ibtsam Riaz, Rahul R. Nair, Rashid Jalil, Liam Britnell, Branson D. Belle, Ernie W. Hill, Kostya S. Novoselov, Kenji Watanabe, Takashi Taniguchi, Andre K. Geim, and Peter Blake. Hunting for monolayer boron nitride: Optical and raman signatures. *Small*, 7(4):465–468, 2011.

[78] Siyuan Dai, Jiamin Quan, Guangwei Hu, Cheng-Wei Qiu, Tiger H Tao, Xiaoqin Li, and Andrea Alù. Hyperbolic phonon polaritons in suspended hexagonal boron nitride. *Nano Letters*, 19(2):1009–1014, 2019.

[79] A. Nagashima, N. Tejima, Y. Gamou, T. Kawai, and C. Oshima. Electronic structure of monolayer hexagonal boron nitride physisorbed on metal surfaces. *Phys. Rev. Lett.*, 75:3918–3921, Nov 1995.

[80] G. Cassabois, P. Valvin, and B. Gil. Hexagonal boron nitride is an indirect bandgap semiconductor. *Nature Photonics*, 10(4):262–266, 2016.

[81] Jingang Wang, Fengcai Ma, and Mengtao Sun. Graphene, hexagonal boron nitride, and their heterostructures: properties and applications. *RSC Adv.*, 7:16801–16822, 2017.

[82] T. Ishii and T. Sato. Growth of single crystals of hexagonal boron nitride. *Journal of Crystal Growth*, 61(3):689–690, May 1983.

[83] Daniel Wintz, Kundan Chaudhary, Ke Wang, Luis A. Jauregui, Antonio Ambrosio, Michele Tamagnone, Alexander Y. Zhu, Robert C. Devlin, Jesse D. Crossno, Kateryna Pistunova, Kenji Watanabe, Takashi Taniguchi, Philip Kim, and Federico Capasso. Guided modes of anisotropic van der waals materials investigated by near-field scanning optical microscopy. *ACS Photonics*, 5(4):1196–1201, 2018.

[84] Mikko Ritala, Jaako Niinisto, Susan Krumdieck, Paul Chalker, H Aspinall, Martyn E Pemble, Wayne L Gladfelter, Barry Leese, Ronald A Fischer, Harish Parala, Ravi Kanjolia, Russell D Dupuis, S E Alexandrov, Stuart J C Irvine, Robert Palgrave, and Ivan P Parkin. *Chemical Vapour Deposition*. The Royal Society of Chemistry, 2009.

[85] Willi Auwärter. Hexagonal boron nitride monolayers on metal supports: Versatile templates for atoms, molecules and nanostructures. *Surface Science Reports*, 74(1):1 – 95, 2019.

[86] AT Murdock, CD van Engers, J Britton, V Babenko, SS Meysami, H Bishop, A Crossley, AA Koos, and N Grobert. Targeted removal of copper foil surface impurities for improved synthesis of cvd graphene. *Carbon*, 122:207–216, 2017.

[87] Soo Min Kim, Allen Hsu, Min Ho Park, Sang Hoon Chae, Seok Joon Yun, Joo Song Lee, Dae-Hyun Cho, Wenjing Fang, Changgu Lee, Tomas Palacios, Mildred Dresselhaus, Ki Kang Kim, Young Hee Lee, and Jing Kong. Synthesis of large-area multilayer hexagonal boron nitride for high material performance. *Nature communications*, 6:8662–8662, Oct 2015. ncomms9662[PII].

[88] Ruizhi Wang, David G. Purdie, Ye Fang, Fabien Massabuau, Philipp Braeuninger-Weimer, Oliver J. Burton, Raoul Blume, Robert Schloegl, Antonio Lombardo, Robert S. Weatherup, and Stephan Hofmann. A peeling approach for integrated manufacturing of large mono-layer h-bn crystals, 2018.

[89] Lu Hua Li, Jiri Cervenka, Kenji Watanabe, Takashi Taniguchi, and Ying Chen. Strong oxidation resistance of atomically thin boron nitride nanosheets. *ACS Nano*, 8(2):1457–1462, Feb 2014.

[90] Yi-Cheun Yeh, Brian Creran, and Vincent M. Rotello. Gold nanoparticles: preparation, properties, and applications in bionanotechnology. *Nanoscale*, 4:1871–1880, 2012.

[91] Neus G. Bastús, Joan Comenge, and Víctor Puntes. Kinetically controlled seeded growth synthesis of citrate-stabilized gold nanoparticles of up to 200 nm: Size focusing versus ostwald ripening. *Langmuir*, 27(17):11098–11105, 2011.

[92] Christoph Ziegler and Alexander Eychmüller. Seeded growth synthesis of uniform gold nanoparticles with diameters of 15 to 300 nm. *The Journal of Physical Chemistry C*, 115(11):4502–4506, 2011.

[93] G. FRENS. Controlled nucleation for the regulation of the particle size in monodisperse gold suspensions. *Nature Physical Science*, 241(105):20–22, 1973.

[94] John Turkevich, Peter Cooper Stevenson, and James Hillier. A study of the nucleation and growth processes in the synthesis of colloidal gold. *Discuss. Faraday Soc.*, 11:55–75, 1951.

[95] Zewei Quan, Yuxuan Wang, and Jiye Fang. High-index faceted noble metal nanocrystals. *Accounts of Chemical Research*, 46(2):191–202, Feb 2013.

[96] L D Marks and L Peng. Nanoparticle shape, thermodynamics and kinetics. *Journal of Physics: Condensed Matter*, 28(5):053001, Jan 2016.

[97] Matthew R. Hauwiller, Layne B. Frechette, Matthew R. Jones, Justin C. Ondry, Grant M. Rotskoff, Phillip Geissler, and A. Paul Alivisatos. Unraveling kinetically-driven mechanisms of gold nanocrystal shape transformations using graphene liquid cell electron microscopy. *Nano Letters*, 18(9):5731–5737, Sep 2018.

[98] Felix Benz, Rohit Chikkaraddy, Andrew Salmon, Hamid Ohadi, Bart de Nijs, Jan Mertens, Cloudy Carnegie, Richard W. Bowman, and Jeremy J. Baumberg. Sers of individual nanoparticles on a mirror: Size does matter, but so does shape. *The Journal of Physical Chemistry Letters*, 7(12):2264–2269, Jun 2016.

[99] You-Jin Lee, Nicholas B. Schade, Li Sun, Jonathan A. Fan, Doo Ri Bae, Marcelo M. Mariscal, Gaehang Lee, Federico Capasso, Stefano Sacanna, Vinothan N. Manoharan, and Gi-Ra Yi. Ultrasmooth, highly spherical monocrystalline gold particles for precision plasmonics. *ACS Nano*, 7(12):11064–11070, Dec 2013.

[100] D. G. Purdie, N. M. Pugno, T. Taniguchi, K. Watanabe, A. C. Ferrari, and A. Lombardo. Cleaning interfaces in layered materials heterostructures. *Nature Communications*, 9(1):5387, 2018.

[101] Chenhao Jin, Jonghwan Kim, Joonki Suh, Zhiwen Shi, Bin Chen, Xi Fan, Matthew Kam, Kenji Watanabe, Takashi Taniguchi, Sefaattin Tongay, Alex Zettl, Junqiao Wu, and Feng Wang. Interlayer electron phonon coupling in wse2hbn heterostructures. *Nature Physics*, 13(2):127–131, 2017.

[102] Simone Latini, Kirsten T. Winther, Thomas Olsen, and Kristian S. Thygesen. Interlayer excitons and band alignment in mos2/hbn/wse2 van der waals heterostructures. *Nano Letters*, 17(2):938–945, Feb 2017.

[103] Gwan-Hyoung Lee, Young-Jun Yu, Changgu Lee, Cory Dean, Kenneth L. Shepard, Philip Kim, and James Hone. Electron tunneling through atomically flat and ultrathin hexagonal boron nitride. *Applied Physics Letters*, 99(24):243114, 2011.

[104] S. Dai, Q. Ma, M. K. Liu, T. Andersen, Z. Fei, M. D. Goldflam, M. Wagner, K. Watanabe, T. Taniguchi, M. Thiemens, and et al. Graphene on hexagonal boron nitride as a tunable hyperbolic metamaterial. *Nature Nanotechnology*, 10(8):682–686, Jun 2015.

[105] S. Dufferwiel, S. Schwarz, F. Withers, A. A. P. Trichet, F. Li, M. Sich, O. Del Pozo-Zamudio, C. Clark, A. Nalitov, D. D. Solnyshkov, G. Malpuech, K. S. Novoselov, J. M. Smith, M. S. Skolnick, D. N. Krizhanovskii, and A. I. Tartakovskii. Exciton-polaritons in van der waals heterostructures embedded in tunable microcavities. *Nature Communications*, 6(1):8579, 2015.

[106] Markus Parzefall, Aron Szabo, Takashi Taniguchi, Kenji Watanabe, Mathieu Luisier, and Lukas Novotny. Light from van der waals quantum tunneling devices. *Nature Communications*, 10(1):292, 2019.

[107] Toan Trong Tran, Cameron Zachreson, Amanuel Michael Berhane, Kerem Bray, Russell Guy Sandstrom, Lu Hua Li, Takashi Taniguchi, Kenji Watanabe, Igor Aharonovich, and Milos Toth. Quantum emission from defects in single-crystalline hexagonal boron nitride. *Phys. Rev. Applied*, 5:034005, Mar 2016.

[108] Xiaoze Liu, Tal Galfsky, Zheng Sun, Fengnian Xia, Erh-chen Lin, Yi-Hsien Lee, Stéphane Kéna-Cohen, and Vinod M. Menon. Strong light–matter coupling in two-dimensional atomic crystals. *Nature Photonics*, 9(1):30–34, Dec 2014.

[109] Hye Yun Jeong, Un Jeong Kim, Hyun Kim, Gang Hee Han, Hyangsook Lee, Min Su Kim, Youngjo Jin, Thuc Hue Ly, Si Young Lee, Young-Geun Roh, Won-Jae Joo, Sung Woo Hwang, Yeonsang Park, and Young Hee Lee. Optical gain in mos2 via coupling with nanostructured substrate: Fabry-perot interference and plasmonic excitation. *ACS Nano*, 10(9):8192–8198, Sep 2016.

[110] Wenyi Wang, Andrey Klots, Yuanmu Yang, Wei Li, Ivan I. Kravchenko, Dayrl P. Briggs, Kirill I. Bolotin, and Jason Valentine. Enhanced absorption in two-dimensional materials via fano-resonant photonic crystals. *Applied Physics Letters*, 106(18):181104, 2015.

[111] Tony Low, Andrey Chaves, Joshua D. Caldwell, Anshuman Kumar, Nicholas X. Fang, Phaedon Avouris, Tony F. Heinz, Francisco Guinea, Luis Martin-Moreno, and Frank Koppens. Polaritons in layered two-dimensional materials. *Nature Materials*, 16(2):182–194, 2017.

[112] Di Zheng, Shunping Zhang, Qian Deng, Meng Kang, Peter Nordlander, and Hongxing Xu. Manipulating coherent plasmon-exciton interaction in a single silver nanorod on monolayer wse2. *Nano Letters*, 17(6):3809–3814, Jun 2017.

[113] Serkan Butun, Sefaattin Tongay, and Koray Aydin. Enhanced light emission from large-area monolayer mos2 using plasmonic nanodisc arrays. *Nano Letters*, 15(4):2700–2704, Apr 2015.

[114] Sina Najmaei, Adnen Mlayah, Arnaud Arbouet, Christian Girard, Jean Léotin, and Jun Lou. Plasmonic pumping of excitonic photoluminescence in hybrid mos2-au nanostructures. *ACS Nano*, 8(12):12682–12689, Dec 2014.

[115] Jinxiu Wen, Hao Wang, Weiliang Wang, Zexiang Deng, Chao Zhuang, Yu Zhang, Fei Liu, Juncong She, Jun Chen, Huanjun Chen, Shaozhi Deng, and Ningsheng Xu. Room-temperature strong light-matter interaction with active control in single plasmonic nanorod coupled with two-dimensional atomic crystals. *Nano Letters*, 17(8):4689–4697, Aug 2017.

[116] Nils Lundt, Sebastian Klembt, Evgeniia Cherotchenko, Simon Betzold, Oliver Iff, Anton V. Nalitov, Martin Klaas, Christof P. Dietrich, Alexey V. Kavokin, Sven Höfling, and Christian Schneider. Room-temperature tamm-plasmon exciton-polaritons with a wse2 monolayer. *Nature Communications*, 7(1):13328, 2016.

[117] Rohit Chikkaraddy, Xuezhi Zheng, Felix Benz, Laura J. Brooks, Bart de Nijs, Cloudy Carnegie, Marie-Elena Kleemann, Jan Mertens, Richard W. Bowman, Guy A. E. Vandenbosch, Victor V. Moshchalkov, and Jeremy J. Baumberg. How ultranarrow gap symmetries control plasmonic nanocavity modes: From cubes to spheres in the nanoparticle-on-mirror. *ACS Photonics*, 4(3):469–475, Mar 2017.

[118] Xuezhi Zheng, Niels Verellen, Vladimir Volskiy, Ventsislav K. Valev, Jeremy J. Baumberg, Guy A. E. Vandenbosch, and Victor V. Moshchalkov. Interacting plasmonic nanostructures beyond the quasi-static limit: a "circuit" model. *Optics Express*, 21(25):31105, 2013.

[119] Ralf Ameling and Harald Giessen. Microcavity plasmonics: of photonic cavities and plasmons. *Laser & Photonics Reviews*, 7(2):141–169, 2013.

[120] Anirban Mitra, Hayk Harutyunyan, Stefano Palomba, and Lukas Novotny. Tuning the cavity modes of a fabry–perot resonator using gold nanoparticles. *Opt. Lett.*, 35(7):953–955, Apr 2010.

[121] Markus A. Schmidt, Dang Yuan Lei, Lothar Wondraczek, Virginie Nazabal, and Stefan A. Maier. Hybrid nanoparticle-microcavity-based plasmonic nanosensors with improved detection resolution and extended remote-sensing ability. *Nature Communications*, 3(1):1108, 2012.

[122] Mohsen Bahramipanah, Shourya Dutta-Gupta, Banafsheh Abasahl, and Olivier J. F. Martin. Cavity-coupled plasmonic device with enhanced sensitivity and figure-of-merit. *ACS Nano*, 9(7):7621–7633, Jul 2015.

[123] Jui-Nung Liu, Qinglan Huang, Keng-Ku Liu, Srikanth Singamaneni, and Brian T. Cunningham. Nanoantenna-microcavity hybrids with highly cooperative plasmonic-photonic coupling. *Nano Letters*, 17(12):7569–7577, Dec 2017.

[124] H. F. Mahlein. Generalized brewster-angle conditions for quarter-wave multilayers at non-normal incidence$*$. *J. Opt. Soc. Am.*, 64(5):647–653, May 1974.

[125] Recep Zan, Ursel Bangert, Quentin Ramasse, and Konstantin S. Novoselov. Evolution of gold nanostructures on graphene. *Small*, 7(20):2868–2872, 2011.

[126] R.M.A. Azzam and N.M. Bashara. *Ellipsometry and polarized light*. North-Holland personal library. North-Holland Pub. Co., 1977.

[127] H Fujiwara. *Ellipsometry of Anisotropic Materials*, chapter 6, pages 209–248. John Wiley and Sons, Ltd, 2007.

[128] G. Christmann, A. V. Trifonov, A. Tzimis, Z. Hatzopoulos, I. V. Iorsh, J. J. Baumberg, and P. G. Savvidis. High-angle optically accessible brewster cavity exciton-polaritons. *Phys. Rev. B*, 99:241402, Jun 2019.

[129] Thierry Taliercio, Vilianne Ntsame Guilengui, Laurent Cerutti, Eric Tournié, and Jean-Jacques Greffet. Brewster "mode" in highly doped semiconductor layers: an all-optical technique to monitor doping concentration. *Opt. Express*, 22(20):24294–24303, Oct 2014.

[130] Allan W. Snyder and John D. Love. Goos-hänchen shift. *Appl. Opt.*, 15(1):236–238, Jan 1976.

[131] Xiaomu Wang and Fengnian Xia. Van der Waals heterostructures: Stacked 2D materials shed light. *Nature Materials*, 14(March):264–265, 2015.

[132] A Sanders, R W Bowman, and J J Baumberg. Tracking Optical and Electronic Behaviour of Quantum Contacts in Sub-Nanometre Plasmonic Cavities. *Scientific Reports*, 6(May):32988, 2016.

[133] Kevin J. Savage, Matthew M. Hawkeye, Rubén Esteban, Andrei G. Borisov, Javier Aizpurua, and Jeremy J. Baumberg. Revealing the quantum regime in tunnelling plasmonics. *Nature*, 491(7425):574–577, 2012.

[134] Andrea Crovetto, Patrick Rebsdorf Whelan, Ruizhi Wang, Miriam Galbiati, Stephan Hofmann, and Luca Camilli. Nondestructive thickness mapping of wafer-scale hexagonal boron nitride down to a monolayer. *ACS Applied Materials & Interfaces*, 10(30):25804–25810, Aug 2018.

[135] M. Schubert, B. Rheinländer, E. Franke, H. Neumann, J. Hahn, M. Röder, and F. Richter. Anisotropy of boron nitride thin-film reflectivity spectra by generalized ellipsometry. *Applied Physics Letters*, 70(14):1819–1821, 1997.

[136] Vlad-Petru Veigang-Radulescu Barry Brennan Andrew J. Pollard Oliver Burton Jack A. Alexander-Webber Robert S. Weatherup Barbara Canto Martin Otto Daniel Neumaier Stephan Hofmann Vitaliy Babenko, Ye Fan. *IOP publishing(submitted)*, 2020.

[137] Cloudy Carnegie, Jack Griffiths, Bart de Nijs, Charlie Readman, Rohit Chikkaraddy, William M. Deacon, Yao Zhang, István Szabó, Edina Rosta, Javier Aizpurua, and Jeremy J. Baumberg. Room-temperature optical picocavities below 1 nm3 accessing single-atom geometries. *The Journal of Physical Chemistry Letters*, 9(24):7146–7151, Dec 2018.

[138] Oded Hod. Graphite and hexagonal boron-nitride have the same interlayer distance. why? *Journal of Chemical Theory and Computation*, 8(4):1360–1369, Apr 2012.

[139] P. B. Johnson and R. W. Christy. Optical constants of the noble metals. *Phys. Rev. B*, 6:4370–4379, Dec 1972.

[140] Audrey Moores and Frédéric Goettmann. The plasmon band in noble metal nanoparticles: An introduction to theory and applications. *New Journal of Chemistry*, 30:1121–1132, 08 2006.

[141] Jong-Won Park and Jennifer S. Shumaker-Parry. Structural study of citrate layers on gold nanoparticles: Role of intermolecular interactions in stabilizing nanoparticles. *Journal of the American Chemical Society*, 136(5):1907–1921, Feb 2014.

[142] Zhuo Wang, Zhaogang Dong, Yinghong Gu, Yung Huang Chang, Lei Zhang, Lain Jong Li, Weijie Zhao, Goki Eda, Wenjing Zhang, Gustavo Grinblat, Stefan A. Maier, Joel K.W. Yang, Cheng Wei Qiu, and Andrew T.S. Wee. Giant photoluminescence enhancement in tungsten-diselenide-gold plasmonic hybrid structures. *Nature Communications*, 7(May):11283, 2016.

[143] Mathias Geisler, Ximin Cui, Jianfang Wang, Tomas Rindzevicius, Lene Gammelgaard, Bjarke S. Jessen, P. A. D. Gonçalves, Francesco Todisco, Peter Bøggild, Anja Boisen, Martijn Wubs, N. Asger Mortensen, Sanshui Xiao, and Nicolas Stenger. Single-crystalline gold nanodisks on ws2 mono- and multilayers for strong coupling at room temperature. *ACS Photonics*, 6(4):994–1001, Apr 2019.

[144] Sin Yuk Choi, Cho Tung Yip, Guang-Can Li, Dang Yuan Lei, Kin Hung Fung, Siu Fung Yu, and Jianhua Hao. Photoluminescence enhancement in few-layer ws2 films via au nanoparticles. *AIP Advances*, 5(6):067148, 2015.

[145] Johannes Kern, Andreas Trügler, Iris Niehues, Johannes Ewering, Robert Schmidt, Robert Schneider, Sina Najmaei, Antony George, Jing Zhang, Jun Lou, Ulrich Hohenester, Steffen Michaelis de Vasconcellos, and Rudolf Bratschitsch. Nanoantenna-enhanced light–matter interaction in atomically thin ws2. *ACS Photonics*, 2(9):1260–1265, 2015.

[146] Fei Cheng, Alex D. Johnson, Yutsung Tsai, Ping-Hsiang Su, Shen Hu, John G. Ekerdt, and Chih-Kang Shih. Enhanced photoluminescence of monolayer ws2 on ag films and nanowire–ws2–film composites. *ACS Photonics*, 4(6):1421–1430, 2017.

[147] Humberto R. Gutiérrez, Nestor Perea-López, Ana Laura Elías, Ayse Berkdemir, Bei Wang, Ruitao Lv, Florentino López-Urías, Vincent H. Crespi, Humberto Terrones, and Mauricio Terrones. Extraordinary room-temperature photoluminescence in triangular ws2 monolayers. *Nano Letters*, 13(8):3447–3454, 2013. PMID: 23194096.

[148] Sefaattin Tongay, Wen Fan, Jun Kang, Joonsuk Park, Unsal Koldemir, Joonki Suh, Deepa S. Narang, Kai Liu, Jie Ji, Jingbo Li, Robert Sinclair, and Junqiao Wu. Tuning interlayer coupling in large-area heterostructures with cvd-grown mos2 and ws2 monolayers. *Nano Letters*, 14(6):3185–3190, Jun 2014.

[149] Yang Gao, Zhibo Liu, Dong-Ming Sun, Le Huang, Lai-Peng Ma, Li-Chang Yin, Teng Ma, Zhiyong Zhang, Xiu-Liang Ma, Lian-Mao Peng, Hui-Ming Cheng, and Wencai Ren. Large-area synthesis of high-quality and uniform monolayer ws2 on reusable au foils. *Nature Communications*, 6(1):8569, 2015.

[150] Seok Joon Yun, Sang Hoon Chae, Hyun Kim, Jin Cheol Park, Ji-Hoon Park, Gang Hee Han, Joo Song Lee, Soo Min Kim, Hye Min Oh, Jinbong Seok, Mun Seok Jeong, Ki Kang Kim, and Young Hee Lee. Synthesis of centimeter-scale monolayer tungsten disulfide film on gold foils. *ACS Nano*, 9(5):5510–5519, May 2015.

[151] A. Mooradian. Photoluminescence of metals. *Phys. Rev. Lett.*, 22:185–187, Feb 1969.

[152] G. T. Boyd, Z. H. Yu, and Y. R. Shen. Photoinduced luminescence from the noble metals and its enhancement on roughened surfaces. *Phys. Rev. B*, 33:7923–7936, Jun 1986.

[153] Michael R. Beversluis, Alexandre Bouhelier, and Lukas Novotny. Continuum generation from single gold nanostructures through near-field mediated intraband transitions. *Phys. Rev. B*, 68:115433, Sep 2003.

[154] Dmitry Sivun, Cynthia Vidal, Battulga Munkhbat, Nikita Arnold, Thomas A. Klar, and Calin Hrelescu. Anticorrelation of photoluminescence from gold nanoparticle dimers with hot-spot intensity. *Nano Letters*, 16(11):7203–7209, 2016. PMID: 27700125.

[155] Weijie Zhao, Zohreh Ghorannevis, Leiqiang Chu, Minglin Toh, Christian Kloc, Ping-Heng Tan, and Goki Eda. Evolution of electronic structure in atomically thin sheets of ws2 and wse2. *ACS Nano*, 7(1):791–797, 2013. PMID: 23256505.

[156] Jan Mertens, Yumeng Shi, Alejandro Molina-Sánchez, Ludger Wirtz, Hui Ying Yang, and Jeremy J. Baumberg. Excitons in a mirror: Formation of "optical bilayers" using mos2 monolayers on gold substrates. *Applied Physics Letters*, 104(19):191105, 2014.

[157] Jan Mertens, Marie-Elena Kleemann, Rohit Chikkaraddy, Prineha Narang, and Jeremy J. Baumberg. How light is emitted by plasmonic metals. *Nano Letters*, 17(4):2568–2574, 2017. PMID: 28267346.

[158] Sebastian K. H. Andersen, Anders Pors, and Sergey I. Bozhevolnyi. Gold photoluminescence wavelength and polarization engineering. *ACS Photonics*, 2(3):432–438, 2015.

[159] Gerd Plechinger, Philipp Nagler, Julia Kraus, Nicola Paradiso, Christoph Strunk, Christian Schüller, and Tobias Korn. Identification of excitons, trions and biexcitons in single-layer ws2. *physica status solidi (RRL) – Rapid Research Letters*, 9(8):457–461, 2015.

[160] Pavel N. Melentiev, Anton E. Afanasiev, Arthur A. Kuzin, Alexey V. Zablotskiy, and Victor I. Balykin. Giant enhancement of two photon induced luminescence in metal nanostructure. *Opt. Express*, 23(9):11444–11452, May 2015.

[161] Javad Shamsi, Alexander S. Urban, Muhammad Imran, Luca De Trizio, and Liberato Manna. Metal halide perovskite nanocrystals: Synthesis, post-synthesis modifications, and their optical properties. *Chemical Reviews*, 119(5):3296–3348, 2019. PMID: 30758194.

[162] Verena A. Hintermayr, Alexander F. Richter, Florian Ehrat, Markus Döblinger, Willem Vanderlinden, Jasmina A. Sichert, Yu Tong, Lakshminarayana Polavarapu, Jochen Feldmann, and Alexander S. Urban. Tuning the optical properties of perovskite nanoplatelets through composition and thickness by ligand-assisted exfoliation. *Advanced Materials*, 28(43):9478–9485, 2016.

[163] Mark C. Weidman, Michael Seitz, Samuel D. Stranks, and William A. Tisdale. Highly tunable colloidal perovskite nanoplatelets through variable cation, metal, and halide composition. *ACS Nano*, 10(8):7830–7839, 2016. PMID: 27471862.

[164] Yixin Ouyang, Yajuan Li, Pengchen Zhu, Qiang Li, Yuan Gao, Jianyu Tong, Li Shi, Qionghua Zhou, Chongyi Ling, Qian Chen, Zhengtao Deng, Hairen Tan, Weiqiao Deng, and Jinlan Wang. Photo-oxidative degradation of methylammonium lead iodide perovskite: mechanism and protection. *J. Mater. Chem. A*, 7:2275–2282, 2019.

[165] Nicholas Aristidou, Irene Sanchez-Molina, Thana Chotchuangchutchaval, Michael Brown, Luis Martinez, Thomas Rath, and Saif A. Haque. The role of oxygen in the degradation of methylammonium lead trihalide perovskite photoactive layers. *Angewandte Chemie International Edition*, 54(28):8208–8212, 2015.

[166] Ma. De Lourdes Ruiz Peralta, U. Pal, and R. Sánchez Zeferino. Photoluminescence (pl) quenching and enhanced photocatalytic activity of au-decorated zno nanorods fabricated through microwave-assisted chemical synthesis. *ACS Applied Materials & Interfaces*, 4(9):4807–4816, 2012. PMID: 22939243.

[167] James M. Ball, Samuel D. Stranks, Maximilian T. Hörantner, Sven Hüttner, Wei Zhang, Edward J. W. Crossland, Ivan Ramirez, Moritz Riede, Michael B. Johnston, Richard H. Friend, and Henry J. Snaith. Optical properties and limiting photocurrent of thin-film perovskite solar cells. *Energy Environ. Sci.*, 8:602–609, 2015.

[168] Udai Bhanu, Muhammad R. Islam, Laurene Tetard, and Saiful I. Khondaker. Photoluminescence quenching in gold - mos2 hybrid nanoflakes. *Scientific Reports*, 4(1):5575, 2014.

[169] Fangfang Wen, Yue Zhang, Samuel Gottheim, Nicholas S. King, Yu Zhang, Peter Nordlander, and Naomi J. Halas. Charge transfer plasmons: Optical frequency conductances and tunable infrared resonances. *ACS Nano*, 9(6):6428–6435, 2015. PMID: 25986388.

[170] N. S. Tabrizi, M. Ullmann, V. A. Vons, U. Lafont, and A. Schmidt-Ott. Generation of nanoparticles by spark discharge. *Journal of Nanoparticle Research*, 11(2):315, May 2008.

[171] F. Tavakoli and J. S. Olfert. An instrument for the classification of aerosols by particle relaxation time: Theoretical models of the aerodynamic aerosol classifier. *Aerosol Science and Technology*, 47(8):916–926, 2013.

# Appendix A

# More on the calculations

## An overview of the generalised Mie method

The following description of the Generalised Mie method fundamentals are extracted from the supplementary material of my paper entitled 'Localised Nanoresonator Mode in Plasmonic Microcavities'. It is intended for those readers which wish to know more about the theory behind the calculations I used to isolate the NRMs. The majority of the work for this section was completed by my collaborator Xuezhi Zheng, at KU Leuven, Belgium.

### A.0.1 Main Equation

We first consider the scattering of a plane wave by a single sphere as shown in Fig.A.1. The classical Mie theory expands the incident plane wave in terms of the standing spherical wave functions, $\mathbf{M}_{nm}^{(1)}$, $\mathbf{N}_{nm}^{(1)}$, by

$$\mathbf{E}_{inc}\left(\mathbf{r}\right)=\sum_{nm}a_{nm}\mathbf{M}_{nm}^{(1)}\left(k\mathbf{r}\right)+b_{nm}\mathbf{N}_{nm}^{(1)}\left(k\mathbf{r}\right), \tag{A.1}$$

and the scattered field in terms of the radiating spherical wave functions, $\mathbf{M}_{nm}^{(3)}$, $\mathbf{N}_{nm}^{(3)}$,

$$\mathbf{E}_{scat}\left(\mathbf{r}\right)=\sum_{nm}c_{nm}\mathbf{M}_{nm}^{(3)}\left(k\mathbf{r}\right)+d_{nm}\mathbf{N}_{nm}^{(3)}\left(k\mathbf{r}\right), \tag{A.2}$$

The definitions for $\mathbf{M}_{nm}^{(1)}$, $\mathbf{N}_{nm}^{(1)}$ and $\mathbf{M}_{nm}^{(3)}$, $\mathbf{N}_{nm}^{(3)}$ can be found later in this supplementary material. In Eq.A.1 and Eq.A.2, $(a_{nm}, b_{nm})$ and $(c_{nm}, d_{nm})$ correspond to the expansion coefficients of the wave functions. By matching the interface conditions on the boundary of the sphere, the cofficients can be linked via a transmission matrix **T**,

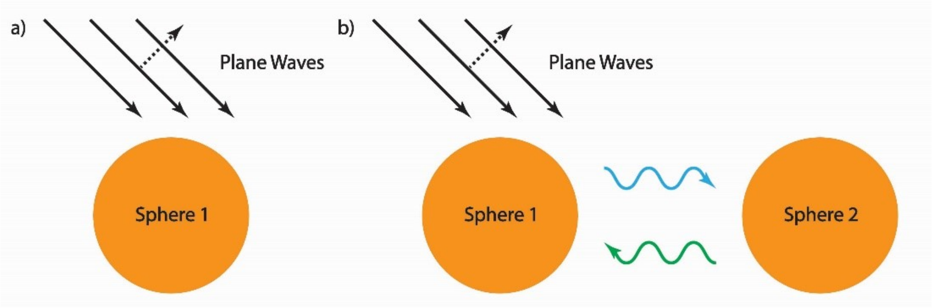

Fig. A.1 Illustration of single sphere and the two-sphere scattering problems. In (a) and (b), the propagation direction and the polarization direction of the incoming plane wave are marked by solid and dashed black lines respectively. In (b), the scattered fields generated by Sphere 1 and Sphere 2 are marked by the green and the blue arrows respectively.

$$\begin{pmatrix} c_{nm} \\ d_{nm} \end{pmatrix} = \mathbf{T} \cdot \begin{pmatrix} a_{nm} \\ b_{nm} \end{pmatrix}. \tag{A.3}$$

Secondly, we consider the scattering of a plane wave by two spheres next to each other in A.1(b) [1]. The following procedures can be taken to generalise the original Mie theory in Eq.A.1. - A.3. Firstly, we see the scattered field generated by Sphere 1 as an incident field (see blue arrow in Error! Reference source not found.b) to Sphere 2, and find a relation between the scattered field generated by Sphere 1 and the scattered field generated by Sphere 2 (see green arrow in Fig.A.1(b) similar to Eq.A.3. Secondly, we take the scattered field generated by the 2nd sphere as the secondary incident field to the 1st sphere and expand this field in terms of the standing spherical wave functions. In this context, Eq.A.3 is modified as

$$\begin{pmatrix} c_{nm} \\ d_{nm} \end{pmatrix} = \mathbf{T} \cdot \left[ \begin{pmatrix} a_{nm} \\ b_{nm} \end{pmatrix} + \begin{pmatrix} a'_{nm} \\ b'_{nm} \end{pmatrix} \right] = \mathbf{T} \cdot \left[ \begin{pmatrix} a_{nm} \\ b_{nm} \end{pmatrix} + \mathbf{R} \cdot \begin{pmatrix} c_{nm} \\ d_{nm} \end{pmatrix} \right]. \tag{A.4}$$

In the above equation, the matrix **R** is the relation described in step 1 and $\left(a'_{nm}, b'_{nm}\right)$ are the expansion coefficients noted in step 2. In this work, we further consider the case where the second scatterer is a layered structure (see Fig.A.2) which includes three regions: region 1 filled by an isotropic medium characterized by $(\varepsilon_1, \mu_1)$, region 2 filled by a uniaxial medium characterized by a tensor permittivity and a permeability (see Error! Reference source not found.), and region 3 filled by a isotropic medium characterized by $(\varepsilon_3, \mu_3)$. The complete topology of the structure is shown in Fig.A.2.

In the following, we present the theory behind the computational scheme of this work. The presentation is organized as follows. Firstly, in subsection A.0.2, we define the spherical

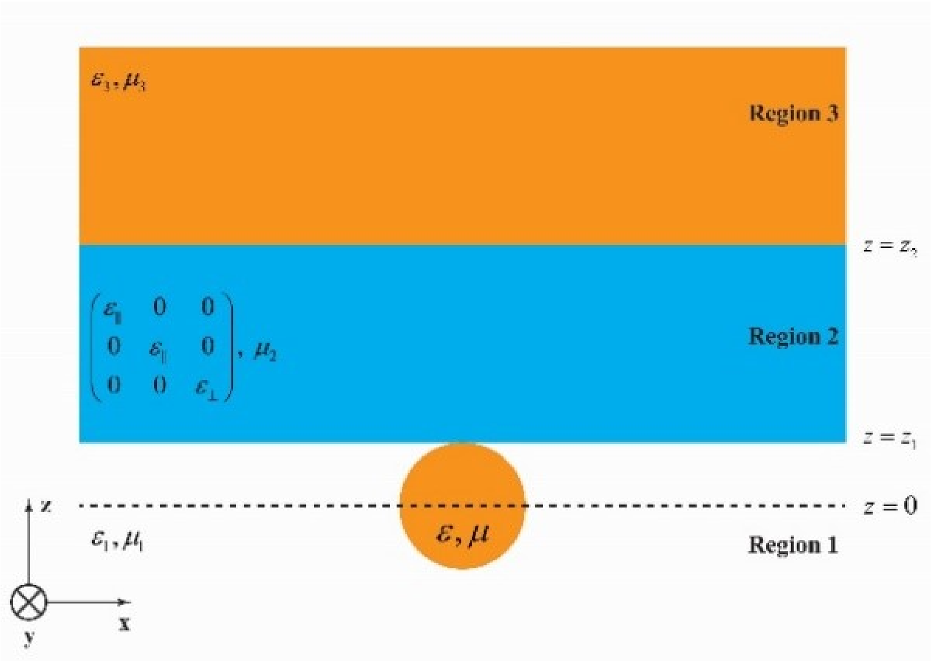

Fig. A.2 Illustration of the targeted structure. The original of coordinate system is set at the centre of the sphere. The first interface separating region 1 from region 2 is located at $z = z_1$ and the second interface separating region 2 from region 3 is located at $z = z_2$.

waves used in this work, expand these spherical waves in terms of plane waves and finally construct the R matrix in Eq. (4). Secondly, in subsections S2 and S3, in order to construct the R matrix, the interaction of plane waves with the layered structure in Fig.A.2 is understood via an approach based on the concept of the S matrix [2].

## A.0.2 Spherical Waves and the R matrix

### Spherical Harmonics, Vector Spherical Harmonics and Spherical Vector Wave Functions

First, we define the spherical harmonics $Y_{nm}$ as,

$$Y_{nm}(\mathbf{r}) = N_{nm} P_n^m [\theta(\mathbf{r})] e^{im\varphi(\mathbf{r})}. \tag{A.5}$$

In Eq.A.5, $n$ and $m$ are the degree and order of the associated Legendre polynomial $P_n^m$ and $N_{nm}$ is defined as,

$$N_{nm} = \sqrt{\frac{(@n-m)!}{(n+m)!} \frac{2n+1}{4\pi}}. \tag{A.6}$$

The spherical harmonics is a function of a vector $\mathbf{r}$, which is

$$\mathbf{r} = x\hat{\mathbf{x}} + y\hat{\mathbf{y}} + z\hat{\mathbf{z}}. \tag{A.7}$$

In Eq. A.7, $x$, $y$ and $z$ are the Cartesian components of $\mathbf{r}$, while r is the magnitude of this vector. $\theta(\mathbf{r})$ and $\varphi(\mathbf{r})$ are the elevation angle and azimuthal angle associated with $\mathbf{r}$. It is noted that the components of the vector $\mathbf{r}$ are not restricted to real values, but also can take complex values. Secondly, we define the angular functions $\tilde{\pi}_{nm}$ and $\tilde{\tau}_{nm}$,

$$\tilde{\pi}_{nm}(\mathbf{r}) = N_{nm}\frac{1}{\sin\theta}\frac{\partial P_n^m[\theta(\mathbf{r})]}{\partial\varphi}, \tilde{\tau}_{nm}(\mathbf{r}) = N_{nm}\frac{\partial P_n^m[\theta(\mathbf{r})]}{\partial\theta}. \tag{A.8}$$

Thirdly, we define the vector spherical harmonics $\mathbf{X}_{nm}$ and $\mathbf{Z}_{nm}$ respectively,

$$\mathbf{X}_{nm}(\mathbf{r}) = \left\{\tilde{\pi}_n^m[\theta(\mathbf{r})]\,\hat{\theta}(\mathbf{r}) - \tilde{\tau}_n^m[\theta(\mathbf{r})]\,\hat{\varphi}(\mathbf{r})\right\}e^{im\varphi(\mathbf{r})}, \tag{A.9}$$

$$\mathbf{Z}_{nm}(\mathbf{r}) = \left\{\tilde{\tau}_n^m[\theta(\mathbf{r})]\,\hat{\theta}(\mathbf{r}) + \tilde{\pi}_n^m[\theta(\mathbf{r})]\,\hat{\varphi}(\mathbf{r})\right\}e^{im\varphi(\mathbf{r})}. \tag{A.10}$$

In Eq. (9) and Eq. (10), $\hat{\theta}$ and $\hat{\varphi}$ are the unit vectors associated with the vector $\mathbf{r}$,

$$\hat{r}(\mathbf{r}) = \frac{x}{r}\hat{\mathbf{x}} + \frac{y}{r}\hat{\mathbf{y}} + \frac{z}{r}\hat{\mathbf{z}}, \hat{\theta}(\mathbf{r}) = \frac{z}{r}\frac{x}{\rho}\hat{\mathbf{x}} + \frac{z}{r}\frac{y}{\rho}\hat{\mathbf{y}} - \frac{\rho}{r}\hat{\mathbf{z}}, \hat{\varphi}(\mathbf{k}) = -\frac{y}{\rho}\hat{\mathbf{x}} + \frac{x}{\rho}\hat{\mathbf{y}}. \tag{A.11}$$

In Eq. A.11, $\rho$ is defined as $\sqrt{x^2+y^2}$. Lastly, the spherical vector wave functions $\mathbf{M}_{nm}$ and $\mathbf{N}_{nm}$ are defined as,

$$\mathbf{M}_{nm}(k\mathbf{r}) = z_n(kr)\,\mathbf{X}_{nm}(\mathbf{r}), \tag{A.12}$$

$$\mathbf{N}_{nm}(k\mathbf{r}) = n(n+1)\frac{z_n(kr)}{kr}Y_{nm}(\mathbf{r})\,\hat{\mathbf{r}} + \frac{1}{kr}\frac{\partial[rz_n(kr)]}{\partial r}\mathbf{Z}_{nm}(\mathbf{r}). \tag{A.13}$$

In Eq. A.12 and Eq. A.13, $k$ is the wavenumber and $z_n(kr)$ can be the spherical Bessel function $j_n(kr)$ for the standing wave case, or the spherical Hankel function of the first kind $h_n(kr)$ for the radiating wave case. Correspondingly, the superscripts $(1)$ and $(3)$ are used to denote the standing spherical vector wave functions, $\mathbf{M}_{nm}^{(1)}$, $\mathbf{N}_{nm}^{(1)}$, and the radiating ones, i.e., $\mathbf{M}_{nm}^{(3)}$, $\mathbf{N}_{nm}^{(3)}$, respectively.

### Expansion of Spherical Wave Functions in terms of Plane Wave Functions

It is known [3] that radiating spherical vector wave functions can be expanded in terms of plane vector wave functions as defined in Eq. A.31,

$$\begin{pmatrix} \mathbf{M}_{nm}^{(3)}(k\mathbf{r}) \\ iZ\cdot\mathbf{N}_{nm}^{(3)}(k\mathbf{r}) \end{pmatrix} = \begin{pmatrix} 1 & 0 \\ 0 & -Z \end{pmatrix} \cdot \frac{1}{2\pi i^n} \int_0^{2\pi} \int_0^{+\infty} \begin{pmatrix} \tilde{\pi}_n^m[\theta(\mathbf{k}^\pm)] & -\tilde{\tau}_n^m[\theta(\mathbf{k}^\pm)] \\ \tilde{\tau}_n^m[\theta(\mathbf{k}^\pm)] & \tilde{\pi}_n^m[\theta(\mathbf{k}^\pm)] \end{pmatrix} e^{im\varphi(\mathbf{k}^\pm)} \cdot \begin{pmatrix} \hat{\theta}(\mathbf{k}^\pm) \\ \hat{\varphi}(\mathbf{k}^\pm) \end{pmatrix} e^{i\mathbf{k}^\pm\cdot\mathbf{r}} \frac{k_\rho dk_\rho d\varphi}{k_z k}. \tag{A.14}$$

In Eq. A.14, a homogeneous space filled with an isotropic medium is assumed and $Z$ is the wave impedance of the space. It can be observed from this equation that the radiating vector spherical waves $\mathbf{M}_{nm}^{(3)}$, $\mathbf{N}_{nm}^{(3)}$ can be expanded as a spectrum of p- and s- polarized (TM- and TE- polarized) plane waves. We note that $\hat{\theta}(\mathbf{k})$ and $\hat{\varphi}(\mathbf{k})$ are the p- polarized plane waves and the s- polarized plane waves, respectively and their definitions can be found in Eq. A.31. The wave vector of these plane waves is $\mathbf{k}^\pm$ where the + sign corresponds to the upgoing waves for the $z > 0$ case and the – sign corresponds to the down-going waves for the $z < 0$ case. In the Cartesian coordinate system, $\mathbf{k}^\pm$ can be expressed as

$$\mathbf{k}^\pm = k_\rho \cos\varphi\hat{\mathbf{x}} + k_\rho \sin\varphi\hat{\mathbf{y}} \pm k_z\hat{\mathbf{z}}. \tag{A.15}$$

### Construction of the R matrix

When planar layers are present in the space (see Fig. A.2), the p- and s- polarized plane waves propagating along the positive z direction interact with all the interfaces and take reflection coefficients,

$$\begin{pmatrix} \hat{\theta}(\mathbf{k}_1^+) \\ \hat{\varphi}(\mathbf{k}_1^+) \end{pmatrix} e^{i\mathbf{k}_1^+\cdot\mathbf{r}} \to \begin{pmatrix} r_p(k_\rho) & 0 \\ 0 & r_s(k_\rho) \end{pmatrix} e^{2ik_{1z}z_1} \cdot \begin{pmatrix} \hat{\theta}(\mathbf{k}_1^-) \\ \hat{\varphi}(\mathbf{k}_1^-) \end{pmatrix} e^{i\mathbf{k}_1^-\cdot\mathbf{r}}. \tag{A.16}$$

In Eq. A.16, $\mathbf{k}_1$ is the wave vector of a plane wave propagating in region 1 and its superscripts ± denote the plane waves propagating along the positive z and the negative z directions, respectively, while $r_p$ and $r_s$ correspond to the reflection coefficients for the p- and s- polarized waves. The evaluation of these coefficients will be shown in Eq. A.57. Based on Eq. A.16, the “reflected” spherical wave functions $\mathbf{M}_{nm}^{(3,R)}$, $\mathbf{N}_{nm}^{(3,R)}$ can be constructed by collecting all the plane waves (i.e., an inverse Fourier transform),

$$\begin{pmatrix} \mathbf{M}_{nm}^{(3,\mathrm{R})}(\mathbf{r}) \\ iZ_1\cdot\mathbf{N}_{nm}^{(3,\mathrm{R})}(\mathbf{r}) \end{pmatrix} = \begin{pmatrix} 1 & 0 \\ 0 & -Z_1 \end{pmatrix}\cdot\frac{1}{2\pi i^n}\int_0^{2\pi}\int_0^{+\infty}\begin{pmatrix} \tilde{\pi}_n^m\left[\theta\left(\mathbf{k}_1^+\right)\right] & -\tilde{\tau}_n^m\left[\theta\left(\mathbf{k}_1^+\right)\right] \\ \tilde{\tau}_n^m\left[\theta\left(\mathbf{k}_1^+\right)\right] & \tilde{\pi}_n^m\left[\theta\left(\mathbf{k}_1^+\right)\right] \end{pmatrix}\cdot$$
$$\ldots e^{im\varphi\left(\mathbf{k}_1^+\right)}\cdot\begin{pmatrix} r_p\left(k_\rho\right) & 0 \\ 0 & r_s\left(k_\rho\right) \end{pmatrix}e^{2ik_{1z}z_0}\cdot\begin{pmatrix} \hat{\theta}\left(\mathbf{k}_1^-\right) \\ \hat{\varphi}\left(\mathbf{k}_1^-\right) \end{pmatrix}e^{i\mathbf{k}_1^-\cdot\mathbf{r}}\frac{k_\rho dk_\rho d\varphi}{k_{1z}k_1}. \tag{A.17}$$

Further, we note that the vector plane wave functions can be expanded in terms of standing spherical wave functions [4],

$$\begin{pmatrix} \hat{\theta}\left(\mathbf{k}_1^-\right) \\ \hat{\varphi}\left(\mathbf{k}_1^-\right) \end{pmatrix}e^{i\mathbf{k}_1^-\cdot\mathbf{r}} = \sum_{n'm'} -\frac{4\pi i^{n'}}{n'\left(n'+1\right)}\begin{pmatrix} \tilde{\pi}_{n'}^{m'}\left[\theta\left(\mathbf{k}_1^-\right)\right] & i\tilde{\tau}_{n'}^{m'}\left[\theta\left(\mathbf{k}_1^-\right)\right] \\ \tilde{\tau}_{n'}^{m'}\left[\theta\left(\mathbf{k}_1^-\right)\right] & -i\tilde{\pi}_{n'}^{m'}\left[\theta\left(\mathbf{k}_1^-\right)\right] \end{pmatrix}\cdot$$
$$\ldots e^{-im'\varphi\left(\mathbf{k}_1^-\right)}\cdot\begin{pmatrix} \mathbf{M}_{n'm'}^{(1)}\left(k_1\mathbf{r}\right) \\ \mathbf{N}_{n'm'}^{(1)}\left(k_1\mathbf{r}\right) \end{pmatrix}. \tag{A.18}$$

Substituting Eq. A.18 into Eq. A.17, we end up with the R matrix required in Eq. A.4

$$\begin{pmatrix} \mathbf{M}_{nm}^{(3,R)}\left(k_1\mathbf{r}\right) \\ \mathbf{N}_{nm}^{(3,R)}\left(k_1\mathbf{r}\right) \end{pmatrix} = \mathbf{R}\cdot\begin{pmatrix} \mathbf{M}_{n'm}^{(1)}\left(k_1\mathbf{r}\right) \\ \mathbf{N}_{n'm}^{(1)}\left(k_1\mathbf{r}\right) \end{pmatrix}. \tag{A.19}$$

In detail, the R matrix is

$$\mathbf{R} = \begin{pmatrix} 1 & 0 \\ 0 & i \end{pmatrix}\cdot\sum_{n'm}\left[-\frac{4\pi i^{n'-n}}{n'\left(n'+1\right)}\int_0^{+\infty}\mathrm{K}_{nm,n'm}\left(k_\rho\right)e^{2ik_{1z}z_0}\frac{k_\rho dk_\rho}{k_{1z}k_1}\right]. \tag{A.20}$$

We note that in the above equation the following definition has been used.

$$\mathrm{K}_{nm,n'm'}\left(k_\rho\right) = \begin{pmatrix} \tilde{\pi}_n^m\left[\theta\left(\mathbf{k}_1^+\right)\right] & -\tilde{\tau}_n^m\left[\theta\left(\mathbf{k}_1^+\right)\right] \\ \tilde{\tau}_n^m\left[\theta\left(\mathbf{k}_1^+\right)\right] & \tilde{\pi}_n^m\left[\theta\left(\mathbf{k}_1^+\right)\right] \end{pmatrix}\cdot\begin{pmatrix} r_{pp}\left(k_\rho\right) & 0 \\ 0 & r_{ss}\left(k_\rho\right) \end{pmatrix}\cdot$$
$$\ldots\begin{pmatrix} \tilde{\pi}_{n'}^{m'}\left[\theta\left(\mathbf{k}_1^-\right)\right] & i\tilde{\tau}_{n'}^{m'}\left[\theta\left(\mathbf{k}_1^-\right)\right] \\ \tilde{\tau}_{n'}^{m'}\left[\theta\left(\mathbf{k}_1^-\right)\right] & -i\tilde{\pi}_{n'}^{m'}\left[\theta\left(\mathbf{k}_1^-\right)\right] \end{pmatrix}. \tag{A.21}$$

### A.0.3 Plane Waves in a Homogeneous Uniaxial Medium

In this subsection, a homogeneous space is assumed to be filled with an electric uniaxial medium. The electromagnetic property of the space is described by a uniaxial material which has a tensor permittivity $\bar{\varepsilon}$ and a scalar permeability $\mu$,

$$\bar{\varepsilon} = \begin{pmatrix} \varepsilon_{\|} & 0 & 0 \\ 0 & \varepsilon_{\|} & 0 \\ 0 & 0 & \varepsilon_{\perp} \end{pmatrix}, \tag{A.22}$$

where $\varepsilon_{\|}$ and $\varepsilon_{\perp}$ are the parallel (i.e., along the $xy$ plane in Fig. A.2) and perpendicular (i.e., along the z direction in Fig. A.2) permittivities respectively. We start with the well-known vector wave equation,

$$\nabla \times \nabla \times \mathbf{E} - k_0^2 \bar{\varepsilon} \mu \cdot \mathbf{E} = 0. \tag{A.23}$$

Due to the full translational symmetry, we assume a plane wave solution to the above equation,

$$\mathbf{E} = \mathbf{e}_0 e^{i\mathbf{k}\cdot\mathbf{r}}.$$

(24) In the Cartesian coordinate system, $\mathbf{e}_0$ and $k$ represent a constant vector and a wave vector which, respectively, have the form of $e_{0x}\hat{x} + e_{0y}\hat{y} + e_{0z}\hat{z}$ and $k_x\hat{x} + k_y\hat{y} + k_z\hat{z}$. By substituting Eq. (24) into Eq. (23), we have an eigenvalue problem,

$$\begin{pmatrix} k_{\|}^2 + k_x^2 & k_x k_y & k_x k_z \\ k_x k_y & k_{\|}^2 + k_y^2 & k_y k_z \\ k_x k_z & k_y k_z & k_{\perp}^2 + k_z^2 \end{pmatrix} \begin{pmatrix} e_{0x} \\ e_{0y} \\ e_{0z} \end{pmatrix} = k^2 \begin{pmatrix} e_{0x} \\ e_{0y} \\ e_{0z} \end{pmatrix}. \tag{A.24}$$

In the above equation, we have used the following definitions,

$$k_{\|}^2 = \varepsilon_{\|} \mu k_0^2, k_{\perp}^2 = \varepsilon_{\perp} \mu k_0^2. \tag{A.25}$$

The eigenvalues for the problem in Eq. (25) are

$$k_o^2 = k_{\|}^2, k_e^2 = \frac{k_{\perp}^2 - k_{\|}^2}{k_{\perp}^2} k_\rho^2 + k_{\|}^2. \tag{A.26}$$

In the above equation, $k_o$ and $k_e$ are the wave numbers for the ordinary waves and the extraordinary waves, respectively; and $k_\rho$ is the lateral wavenumber defined as $\sqrt{k_x^2 + k_y^2}$. It is convenient to define two physical quantities: an equivalent refractive index n and an equivalent wave impedance Z respectively for the ordinary wave and the extraordinary wave,

$$n_o = \frac{k_o}{k_0}, n_e = \frac{k_e}{k_0}, \tag{A.27}$$

$$Z_o = \frac{\mu}{n_o}, Z_e = \frac{\mu}{n_e}. \tag{A.28}$$

The eigenvectors corresponding to the eigenvalues in Eq. A.27 are

$$\mathbf{e}_o = \hat{\varphi}\left(\mathbf{k}_o\right), \mathbf{e}_e = \left(1 - \frac{k_\parallel^2}{k_\perp^2}\right)\frac{k_\rho k_z}{k_e^2}\hat{k}\left(\mathbf{k}_e\right) + \left(\frac{k_z^2}{k_e^2} + \frac{k_\parallel^2}{k_\perp^2}\frac{k_\rho^2}{k_e^2}\right)\hat{\theta}\left(\mathbf{k}_e\right). \tag{A.29}$$

In Eq. A.30, we have used the so-called (plane wave) vector wave functions that are defined as,

$$\begin{gathered} \hat{k}\left(\mathbf{k}\right) = \tfrac{k_\rho}{k}\left(\tfrac{k_x}{k_\rho}\hat{\mathbf{x}} + \tfrac{k_y}{k_\rho}\hat{\mathbf{y}}\right) + \tfrac{k_z}{k}\hat{\mathbf{z}}, \\ \hat{\theta}\left(\mathbf{k}\right) = \tfrac{k_z}{k}\left(\tfrac{k_x}{k_\rho}\hat{\mathbf{x}} + \tfrac{k_y}{k_\rho}\hat{\mathbf{y}}\right) - \tfrac{k_\rho}{k}\hat{\mathbf{z}}, \\ \hat{\varphi}\left(\mathbf{k}\right) = -\tfrac{k_y}{k_\rho}\hat{\mathbf{x}} + \tfrac{k_x}{k_\rho}\hat{\mathbf{y}}. \end{gathered} \tag{A.30}$$

Therefore, the ordinary wave solution to the vector wave equation in Eq. A.23 is,

$$\mathbf{E}_o = \hat{\varphi}\left(\mathbf{k}_o\right)e^{i\mathbf{k}_o\cdot\mathbf{r}}, \mathbf{H}_o = -\frac{1}{Z_o}\hat{\theta}\left(\mathbf{k}_o\right)e^{i\mathbf{k}_o\cdot\mathbf{r}}. \tag{A.31}$$

We can readily see from Eq. (32) that the ordinary wave solution corresponds to the s-polarized wave or the TE wave. The extraordinary wave solution to the vector wave equation in Eq. A.23 is,

$$\begin{gathered} \mathbf{E}_e = \left(1 - \tfrac{k_\parallel^2}{k_\perp^2}\right)\tfrac{k_\rho k_z}{k_e^2}\cdot\hat{k}\left(\mathbf{k}_e\right)e^{i\mathbf{k}_e\cdot\mathbf{r}} + \left(\tfrac{k_z^2}{k_e^2} + \tfrac{k_\parallel^2}{k_\perp^2}\tfrac{k_\rho^2}{k_e^2}\right)\cdot\hat{\theta}\left(\mathbf{k}_e\right)e^{i\mathbf{k}_e\cdot\mathbf{r}}, \\ \mathbf{H}_e = \left(\tfrac{k_z^2}{k_e^2} + \tfrac{k_\parallel^2}{k_\perp^2}\tfrac{k_\rho^2}{k_e^2}\right)\cdot\tfrac{1}{Z_e}\hat{\varphi}\left(\mathbf{k}_e\right)e^{i\mathbf{k}_e\cdot\mathbf{r}}. \end{gathered} \tag{A.32}$$

We can readily see from Eq. A.33 that the ordinary wave solution corresponds to the p-polarized wave or the TM wave.

### A.0.4 Plane Waves at Planar Interface Between Isotropic Medium and Electric Uniaxial Medium

In principle, the field behavior at a planar interface is determined by the interface conditions,

$$\hat{\mathbf{z}}\times\left(\mathbf{E}_2 - \mathbf{E}_1\right) = 0, \hat{\mathbf{z}}\times\left(\mathbf{H}_2 - \mathbf{H}_1\right) = 0. \tag{A.33}$$

For Eq. A.34, we assume that there are no imposed sources on the planar interface; the normal of the planar interface is along the $z$ direction, i.e., the surface normal is $\hat{z}$. Then, we mark the inner and the outer regions of the interface by the subscript 1 and 2, respectively.

### Tangential Components

It can be immediately seen from the interface conditions from Eq. A.34 that the tangential components of the electric and the magnetic fields are essential. We first look at the tangential components of the (plane wave) vector wave functions (that are defined in Eq. A.31) as these wave functions are the constitutive elements of the ordinary wave solutions and the extraordinary wave solutions (please see Eq. A.32 and Eq. A.33),

$$\hat{\mathbf{z}} \times \hat{k}(\mathbf{k}) = -\frac{k_\rho}{k}\mathbf{X}\left(\mathbf{k}_\parallel\right), \hat{\mathbf{z}} \times \hat{\theta}(\mathbf{k}) = -\frac{k_z}{k}\mathbf{X}\left(\mathbf{k}_\parallel\right), \hat{\mathbf{z}} \times \hat{\varphi}(\mathbf{k}) = -\mathbf{Z}\left(\mathbf{k}_\parallel\right). \tag{A.34}$$

In Eq. A.35, $\mathbf{k}_\parallel$ is the component of a wave vector in parallel with the plane, i.e., $\mathbf{k}_\parallel = k_x\hat{x} + k_y\hat{y}$; and the $X$ function and the $Z$ function, i.e., the planar harmonics, are defined as

$$\mathbf{X}\left(\mathbf{k}_\parallel\right) = \frac{k_y}{k_\rho}\hat{\mathbf{x}} - \frac{k_x}{k_\rho}\hat{\mathbf{y}}, \mathbf{Z}\left(\mathbf{k}_\parallel\right) = \frac{k_x}{k_\rho}\hat{\mathbf{x}} + \frac{k_y}{k_\rho}\hat{\mathbf{y}}. \tag{A.35}$$

The following orthogonal properties can be seen from the definitions of the planar harmonics,

$$\mathbf{X}\left(\mathbf{k}_\parallel\right) \cdot \mathbf{X}\left(\mathbf{k}_\parallel\right) = 1, \mathbf{Z}\left(\mathbf{k}_\parallel\right) \cdot \mathbf{Z}\left(\mathbf{k}_\parallel\right) = 1, \mathbf{X}\left(\mathbf{k}_\parallel\right) \cdot \mathbf{Z}\left(\mathbf{k}_\parallel\right) = 0. \tag{A.36}$$

Secondly, we note that: for the ordinary waves (the TE waves), the tangential components are

$$\begin{pmatrix} \hat{\mathbf{z}} \times \mathbf{E}_o \\ \hat{\mathbf{z}} \times \mathbf{H}_o \end{pmatrix} = \begin{pmatrix} -\mathbf{Z}\left(\mathbf{k}_\parallel\right) \\ \frac{1}{Z_o}\frac{k_{oz}}{k_o}\mathbf{X}\left(\mathbf{k}_\parallel\right) \end{pmatrix} e^{i\mathbf{k}_o \cdot \mathbf{r}}, \tag{A.37}$$

for the extraordinary waves (the TM waves), the tangential components are

$$\begin{pmatrix} \hat{\mathbf{z}} \times \mathbf{E}_e \\ \hat{\mathbf{z}} \times \mathbf{H}_e \end{pmatrix} = \begin{pmatrix} -\frac{k_{ez}}{k_e}\mathbf{X}\left(\mathbf{k}_\parallel\right) \\ -\left(\frac{k_{ez}^2}{k_e^2} + \frac{k_\parallel^2}{k_\perp^2}\frac{k_\rho^2}{k_e^2}\right) \cdot \frac{1}{Z_e}\mathbf{Z}\left(\mathbf{k}_\parallel\right) \end{pmatrix} e^{i\mathbf{k}_e \cdot \mathbf{r}}. \tag{A.38}$$

Lastly, we may project the ordinary and the extraordinary waves onto the planar harmonics and define two matrices, i.e., $\mathbf{O}_o$ and $\mathbf{O}_e$,

$$\mathbf{O}_o\left(\mathbf{k}_o\right) = \begin{pmatrix} \mathbf{Z}\left(\mathbf{k}_\parallel\right) \cdot \hat{\mathbf{z}} \times \mathbf{E}_o \\ \mathbf{X}\left(\mathbf{k}_\parallel\right) \cdot \hat{\mathbf{z}} \times \mathbf{H}_o \end{pmatrix} = \begin{pmatrix} -1 \\ \frac{1}{Z_o}\frac{k_{oz}}{k_o} \end{pmatrix} e^{i\mathbf{k}_o \cdot \mathbf{r}}, \tag{A.39}$$

$$\mathbf{O}_e\left(\mathbf{k}_e\right)=\left(\begin{array}{c}\mathbf{X}\left(\mathbf{k}_{\|}\right)\cdot\hat{\mathbf{z}}\times\mathbf{E}_e\\ \mathbf{Z}\left(\mathbf{k}_{\|}\right)\cdot\hat{\mathbf{z}}\times\mathbf{H}_e\end{array}\right)=\left(\begin{array}{c}-\frac{k_{ez}}{k_e}\\ -\frac{1}{Z_e}\left(\frac{k_{ez}^2}{k_e^2}+\frac{k_{\|}^2}{k_{\perp}^2}\frac{k_{\rho}^2}{k_e^2}\right)\end{array}\right)e^{i\mathbf{k}_e\cdot\mathbf{r}}. \tag{A.40}$$

### Case I: Inner region is electric uniaxial medium, outer region is isotropic medium

For the TE waves, we match the interface conditions in Eq. A.34 which leads to,

$$\mathbf{O}_o\left(\mathbf{k}_{1,o}^+\right)a_1^+ + \mathbf{O}_o\left(\mathbf{k}_{1,o}^-\right)a_1^- = \mathbf{O}_o\left(\mathbf{k}_2^+\right)a_2^+ + \mathbf{O}_o\left(\mathbf{k}_2^-\right)a_2^-. \tag{A.41}$$

In the above equation, the superscripts + and – represent the up and down-propagating waves respectively; the subscripts 1 and 2 refer to the inner and the outer regions, respectively; and the coefficients a are the amplitudes of the TE waves. We note that 1) $k_o$ is the wave vector of the ordinary wave in the uniaxial medium; and 2) in an isotropic medium the ordinary waves and the extraordinary waves become degenerate, i.e., the wavenumbers $k_{\|}$ and $k_{\perp}$ are equal. For the TM waves, we match the interface conditions in Eq. A.34 which leads to,

$$\mathbf{O}_e\left(\mathbf{k}_{1,e}^+\right)b_1^+ + \mathbf{O}_e\left(\mathbf{k}_{1,e}^-\right)b_1^- = \mathbf{O}_e\left(\mathbf{k}_2^+\right)b_2^+ + \mathbf{O}_e\left(\mathbf{k}_2^-\right)b_2^-. \tag{A.42}$$

Comparing to Eq. A.41, the coefficients b are now the amplitudes of the TM waves, and $k_e$ is the wave vector of the extraordinary wave in the uniaxial medium.

### Case II: Inner region is isotropic medium, outer region is electric uniaxial medium

For the TE waves, we match the interface conditions in Eq. A.34 which leads to,

$$\mathbf{O}_o\left(\mathbf{k}_1^+\right)a_1^+ + \mathbf{O}_o\left(\mathbf{k}_1^-\right)a_1^- = \mathbf{O}_o\left(\mathbf{k}_{2,o}^+\right)a_2^+ + \mathbf{O}_o\left(\mathbf{k}_{2,o}^-\right)a_2^-. \tag{A.43}$$

Again, in the above equation, the superscripts + and – represent the up and down-propagating waves, respectively; the subscripts 1 and 2 refer to the inner and the outer regions, respectively; and the coefficients a are the amplitudes of the TE waves. We note that 1) $k_o$ is the wave vector of the ordinary wave in the uniaxial medium; and 2) in an isotropic medium the ordinary waves and the extraordinary waves become degenerate, i.e., the wavenumbers $k_{\|}$ and $k_{\perp}$ are equal.

For the TM waves, we match the interface conditions in Eq. A.34 which leads to,

$$\mathbf{O}_e\left(\mathbf{k}_1^+\right)b_1^+ + \mathbf{O}_e\left(\mathbf{k}_1^-\right)b_1^- = \mathbf{O}_e\left(\mathbf{k}_{2,e}^+\right)b_2^+ + \mathbf{O}_e\left(\mathbf{k}_{2,e}^-\right)b_2^-. \tag{A.44}$$

Different from Eq. A.44, the coefficients b are the amplitudes of the TM waves, and $k_e$ is the wave vector of the extraordinary wave in the uniaxial medium.

### S-matrix for a single planar interface

Since Eq. A.41 – Eq. A.44 are of the same mathematical form, they can be treated in the same manner. For the TE system, Eq. A.43 can be recast as,

$$\left[\begin{array}{c} a_1^- \\ a_2^+ \end{array}\right] = S_{TE} \left[\begin{array}{c} a_1^+ \\ a_2^- \end{array}\right]. \tag{A.45}$$

In Eq. A.45, $S_{TE}$ is defined as,

$$S_{TE} = \left[\begin{array}{cc} +\mathbf{O}_o\left(\mathbf{k}_{1,o}^-\right) & -\mathbf{O}_o\left(\mathbf{k}_2^+\right) \end{array}\right]^{-1} \left[\begin{array}{cc} -\mathbf{O}_o\left(\mathbf{k}_{1,o}^+\right) & +\mathbf{O}_o\left(\mathbf{k}_2^-\right) \end{array}\right]. \tag{A.46}$$

Since $S_{TE}$ links the amplitudes of the incoming waves towards the planar interface with the amplitudes of the outgoing waves towards the planar interface, it is an S matrix. For the TM system, Eq. A.44 can be recast as,

$$\left[\begin{array}{c} b_1^- \\ b_2^+ \end{array}\right] = S_{TM} \left[\begin{array}{c} b_1^+ \\ b_2^- \end{array}\right]. \tag{A.47}$$

In Eq. A.47, $S_{TM}$ is defined as,

$$S_{TM} = \left[\begin{array}{cc} +\mathbf{O}_e\left(\mathbf{k}_{1,e}^-\right) & -\mathbf{O}_e\left(\mathbf{k}_2^+\right) \end{array}\right]^{-1} \left[\begin{array}{cc} -\mathbf{O}_e\left(\mathbf{k}_{1,e}^+\right) & +\mathbf{O}_e\left(\mathbf{k}_2^-\right) \end{array}\right]. \tag{A.48}$$

Further, we note two general properties of the S matrix. On the one hand, the S matrix is a function of the lateral wave number, i.e., $k_\rho = \sqrt{k_x^2 + k_y^2}$, and the spatial position of the interface, i.e., the $z$ coordinate, and contains all the phase information. On the other hand, the S matrix has the following generic form,

$$S = \left(\begin{array}{cc} S_{11} & S_{12} \\ S_{21} & S_{22} \end{array}\right) \tag{A.49}$$

In Eq. A.49, $S_{11}$ and $S_{21}$ relate the incoming wave amplitude in the inner region $a_1^+$ with the outgoing wave amplitude in the inner region $a_1^-$ and with the outgoing wave amplitude in the outer region $a_2^+$. Here $S_{12}$ and $S_{22}$ relate the incoming wave amplitude in the outer region $a_2^-$ with the outgoing wave amplitude in the inner region $a_1^-$ and with the outgoing wave amplitude in the outer region $a_2^+$ (see A.3 for the definition of the incoming and the outgoing waves).

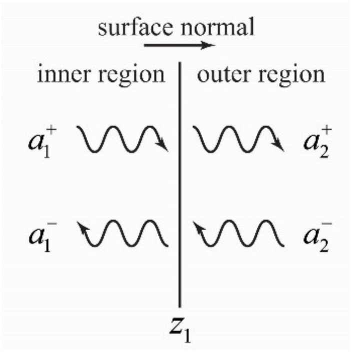

Fig. A.3 Illustration of incoming and outgoing waves.

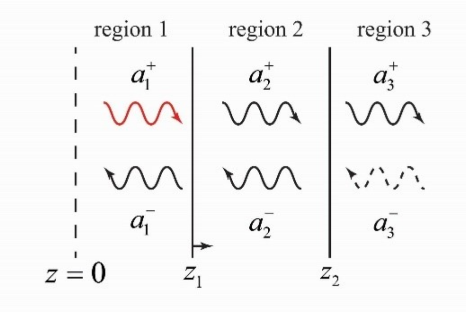

Fig. A.4 Illustration of reflection and transmission through three-region structure. The three regions are separated by two interfaces located at $z_1$ and $z_2$. $(a_1^+, a_1^-)$, $(a_2^+, a_2^-)$ and $(a_3^+, a_3^-)$ correspond to the wave amplitudes in region 1, region 2 and region 3, respectively. The superscripts + and – mark waves propagating along the positive and negative z directions. The wave amplitude of the excitation plane wave is denoted by the red color. Since there is no reflection from the far side, $a_3^-$ is zero and hence the wave propagating along the negative z direction is marked by a dashed line. Lastly, the zero-phase point is defined at $z$=0 which is marked by a dashed line.

## A.0.5 Concatenation of S-matrices

In this subsection, given the S matrices of two interfaces and an incoming wave from the left-most region (see Fig. A.4), we derive the wave amplitudes for the plane waves in each layer.

Assume that the S matrices of the interfaces are

$$\begin{aligned} \begin{pmatrix} a_1^- \\ a_2^+ \end{pmatrix} &= S^{(1)} \begin{pmatrix} a_1^+ \\ a_2^- \end{pmatrix} = \begin{pmatrix} S_{11}^{(1)} & S_{12}^{(1)} \\ S_{21}^{(1)} & S_{22}^{(1)} \end{pmatrix} \begin{pmatrix} a_1^+ \\ a_2^- \end{pmatrix}, \\ \begin{pmatrix} a_2^- \\ a_3^+ \end{pmatrix} &= S^{(2)} \begin{pmatrix} a_2^+ \\ a_3^- \end{pmatrix} = \begin{pmatrix} S_{11}^{(2)} & S_{12}^{(2)} \\ S_{21}^{(2)} & S_{22}^{(2)} \end{pmatrix} \begin{pmatrix} a_2^+ \\ a_3^- \end{pmatrix}. \end{aligned} \tag{A.50}$$

By eliminating $a_2^-$ and $a_2^+$ in Eq. A.50, an S matrix for the entire structure can be derived,

$$\begin{pmatrix} a_1^- \\ a_3^+ \end{pmatrix} = S^{(12)} \begin{pmatrix} a_1^+ \\ a_3^- \end{pmatrix} = \begin{pmatrix} S_{11}^{(12)} & S_{12}^{(12)} \\ S_{21}^{(12)} & S_{22}^{(12)} \end{pmatrix} \begin{pmatrix} a_1^+ \\ a_3^- \end{pmatrix}. \tag{A.51}$$

The elements of the S matrix in Eq. A.51 read

$$S_{11}^{(12)} = S_{11}^{(1)} + S_{12}^{(1)} \left(1 - S_{11}^{(2)} S_{22}^{(1)}\right)^{-1} S_{11}^{(2)} S_{21}^{(1)}, \tag{A.52}$$

$$S_{22}^{(12)} = S_{22}^{(2)} + S_{21}^{(2)} \left(1 - S_{22}^{(1)} S_{11}^{(2)}\right)^{-1} S_{22}^{(1)} S_{12}^{(2)}. \tag{A.53}$$

We note that the excitation plane wave comes from the left-most of the structure and set $a_1^+$ to 1 and $a_3^-$ to zero. As a result, the reflection coefficient and the transmission coefficient of the structure are

$$r = \frac{a_1^-}{a_1^+} = S_{11}^{(12)}, t = \frac{a_3^+}{a_1^+} = S_{21}^{(12)}. \tag{A.54}$$

We also evaluate the amplitudes of the waves propagating in the sandwiched layer,

$$a_2^+ = \left(1 - S_{11}^{(2)} S_{22}^{(1)}\right)^{-1} \left(S_{11}^{(2)} S_{21}^{(1)} a_1^+ + S_{12}^{(2)} a_3^-\right), \tag{A.55}$$

$$a_2^- = \left(1 - S_{22}^{(1)} S_{11}^{(2)}\right)^{-1} \left(S_{21}^{(1)} a_1^+ + S_{22}^{(1)} S_{12}^{(2)} a_3^-\right). \tag{A.56}$$

Lastly, the reflection coefficient $r$ in Eq. A.56 can be used in Eq. A.21 for the evaluation of the R matrix. $(r,t)$ and $\left(a_2^+, a_2^-\right)$ can be used in combination with Eq. A.14 to evaluate the fields in all the layers presented in Fig. A.4.

## References

1. J. Bruning and L. Yuen, "Multiple scattering of EM waves by spheres part I–Multipole expansion and ray-optical solutions," IEEE Transactions on Antennas and Propagation, vol. 19, no. 3, pp. 378-390, 1971, doi: 10.1109/TAP.1971.1139944.

2. D. M. Pozar, Microwave engineering. John Wiley and Sons, 2009.

3. R. C. Wittmann, "Spherical wave operators and the translation formulas," IEEE Transactions on Antennas and Propagation, vol. 36, no. 8, pp. 1078-1087, 1988, doi: 10.1109/8.7220.

4. J. D. Jackson, "Classical electrodynamics," ed: AAPT, 1999.

## A.1 Values used for circuit model calculations

Unless otherwise stated in the chapter, the following values were used in order to calculate the dipole antenna mode positions as shown in chapter 5:

- Plasma wavelength for a Au nanoparticle $\lambda_p = 140nm$. This is calculated from the average values of references[65–71] gathered from [25]
- $\varepsilon_m = n_m^2$ - dielectric constant of the surrounding medium
- $\varepsilon_\infty = 9.38 - 0.00339 \times 2R + 0.00021(2R)^2$ - dielectric permittivity for NPoM structure taking into account variation with nanoparticle radius
- $\varepsilon_0 = (2.9979 \times 10^8)^2 \times 4\pi \times 1e - 7)^{-1}$ - vacuum permittivity
- $\chi \approx 0.5$
- $\beta \approx 0.15$ - calculated from the angle from the centre of the sphere setting the plasmon mode width in the gap

## A.2 The Removal of Contaminants From the Gap

The study of hexagonal-Boron Nitride in NPoM has led to important discoveries about the NPoM system as a whole, the use of layered materials and the consequences of adsorbands in the gap. However, in order to access the very thinnest gaps and study more exciting and potentially non-classical effects, the removal of adsorbands should be a priority for thin layered material spacers in NPoM. Various methods were attempted in order to achieve this and these are presented here.

### A.2.1 Alternative deposition methods

To address the question as to whether the presence of citrate depends on deposition method thorough checks were completed, comparing various deposition techniques.

The most common deposition method, and the one used in previous works on graphene, $MoS_2$ and $WSe_2$ is the long term immersion of the substrate surface in Au nanoparticle solution without the addition of salt[8, 9, 5]. Due to the hydrophobic surface of most layered materials, deposition using this method must continue for more than 12 hours in order to achieve a reasonable density on the vdW crystal surface. This method is not very reproducible, leading to highly variable densities dependent on substrate charge and significantly larger

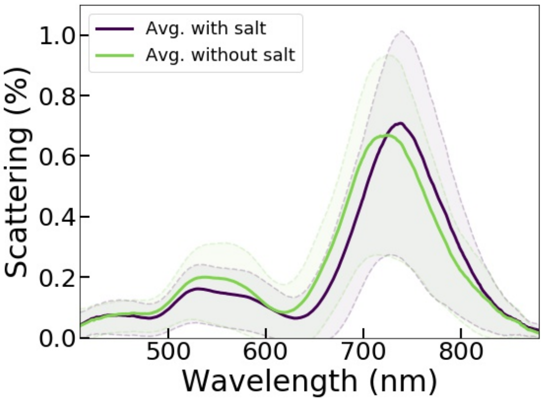

Fig. A.5 Comparison of the average spectrum for 80nm nanoparticles with NaCl added after 20 minutes on Au.

amounts of impurities are also deposited due to the longer exposure time. The Au region surrounding the layered material is found to be more hydrophilic than the layered material, meaning that using this method the density of nanoparticles is too high to gain measurements from individual nanoparticles on the Au surface. By taking spectra from 100 nanoparticles deposited using each method, the original deposition technique was compared with the salt method used in this thesis in order to confirm whether the presence of adsorbands in the gap was a result of the *NaCl* deposition technique (Fig.A.6). It is clearly seen that the resultant spectra on Au are approximately equivalent, but that there may be a slight increase in contaminant thickness when salt is not used. This demonstrates that the presence of adsorbands in the gap is weakly dependent on the addition of salt. This measurement was also taken on template stripped Au, showing a very weak dependence on the peak position compared to the evaporated Au used in this work as expected.

Next it was found that before deposition of nanoparticles from solution, the sample could be heated to a temperature of $120°C$ in order to remove adsorbands such as moisture on the sample surface. It was found that when this was done, nanoparticles would deposit within 1-5 seconds onto the hBN without the addition of salt. This suggests that the repulsion of nanoparticles from the surface of layered materials in solution is related to the presence of adsorbands from the ambient environment which likely equilibrate charge on the surface. As shown in Fig.A.5, it was found that the spectra from NPoM on monolayer hBN deposited in this way do not differ significantly for the same monolayer hBN sample (cut from the same substrate used in this chapter), although there is a slight red-shift. This implies that during deposition from solution the adsorbands evaporated during heating are displaced from the surface, most likely leading to mostly citrate ligands in the gap. The slight red-shift indicates that a small amount of water may increase gap size on Au or decrease

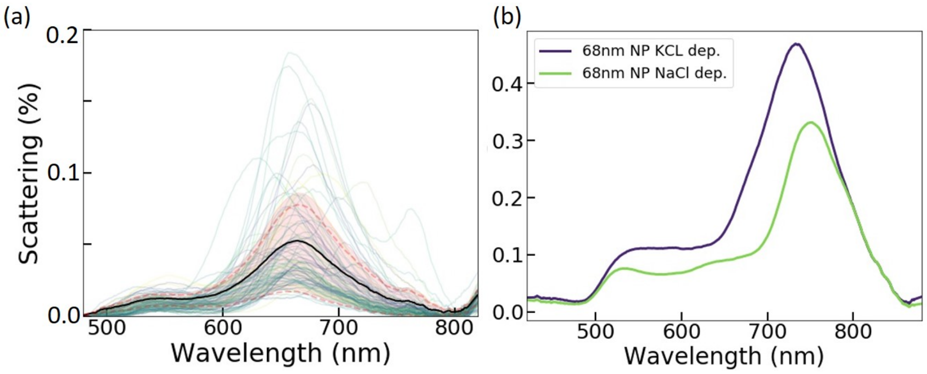

Fig. A.6 (a)The average spectrum for 60nm nanoparticles on monolayer hBN post-heating to $120^oC$ to remove other adsorbands such as water from the surface. (b) The scattering of 68nm nanoparticles prepared in-house also do not allow for ligand displacement and the change of salt to KCl rather than NaCl makes little difference.

refractive index, therefore although it makes little difference to the results it would be a future recommendation to use this method as opposed to salt deposition for simple deposition onto vdW materials.

Finally, $68nm$ nanoparticles prepared in our lab by Dr. Andrew Salmon and deposited using NaCl and then KCL in the same 50:50 water/salt ratio. There remained adsorbands in the gap for the nanoparticles grown in our lab and the position of the dipole antena mode corresponded approximately to the same thickness and refractive index of citrate estimated in this chapter and supported by literature[141](Fig.A.5(a)). KCL instead of NaCl made little difference to the position of the coupled mode wavelength (Fig.A.5(b)).

### A.2.2 Gas phase nanoparticle deposition

Work on the gas-phase deposition of Au nanoparticles was begun by myself in collaboration with the Boies group at the department of engineering and continued further by graduate student George Lewis of the NanoDTC, Cambridge, to whom I acted as daily supervisor for the project and wrote the project proposal.

By generating pure gas phase Au nanoparticles and firing these onto the Au substrate all of the deposition processes which cause contamination in the gap can be removed. These nanoparticles can be made to be highly spherical and monodisperse.

At the beginning of the collaboration, apparent $> 60nm$ nanoparticles were deposited on Au using a thermal evaporation technique followed by biasing of the Au substrate. Nanoparticles generated in this way were deposited directly onto gold to confirm the lack of contaminants in the gap, and initial dark-field results of this experiment indicated that the nanoparticles were indeed $> 60nm$ in diameter and in direct contact with the Au substrate

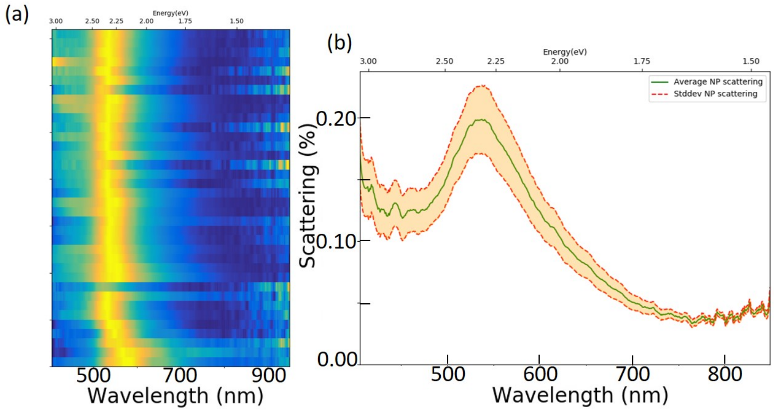

Fig. A.7 Promising preliminary results for $\sim 60nm$ Au nanoparticles on Au, showing the transverse mode alone, as expected for NPoM with no material in the gap (conductive contact).

beneath (Fig.A.7). However, following this experiment we were unable to reproduce these results. The system showed highly variable nanoparticle sizes and required 24 hour deposition times for densities of $> 1$ nanoparticles per $10\mu m^2$.

For this reason, the setup was modified. The latest process steps are as follows:

1. Spark generation: via vapourisation of Au electrodes with inert gas plasma [170]
2. Sintering: agglomerates are heated at slightly below melting point ina furnace to allow primary particles to reorganise into spheres
3. Size selection: using an aerodynamic aerosol classifier (AAC, Fig.A.8) which uses the centrifugal force generated between two rotating cylinders to to separate particles based on diameter, avoiding charging issues [171]
4. Enlargement: by using the particles as seeds for supersaturated butanol condensation
5. Deposition: via impaction. The substrate is placed directly in the flow of the particle beam so that particles with too much inertia are deposited
6. Counting: to find the density on the substrate. This is done using a condensation particle counter (CPC)

A custom built spark generator with 1mm diameter Au wire electrodes, was used to generate gold particles with a high voltage power supply (5kV, 1mA) connected to a custom capacitor supplying the discharge potential. The use of the spark generator greatly increased the particle production rates. Nitrogen was used as the carrier gas, with a flow rate of 2 standard litres per minute (SLPM) controlled by a mass flow controller. A cooling coil was

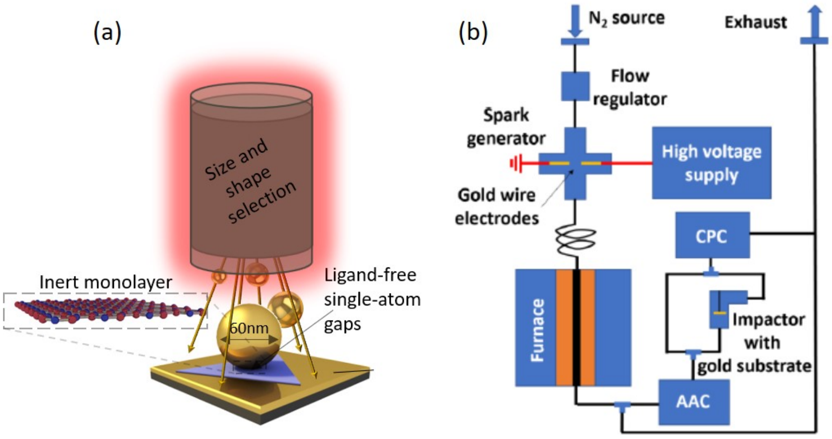

Fig. A.8 The a depiction of gas-phase deposited NPs (a), and description of the experimental setup for gas-phase deposition of Au nanoparticles onto vdW materials, courtesy of G.L. (b).

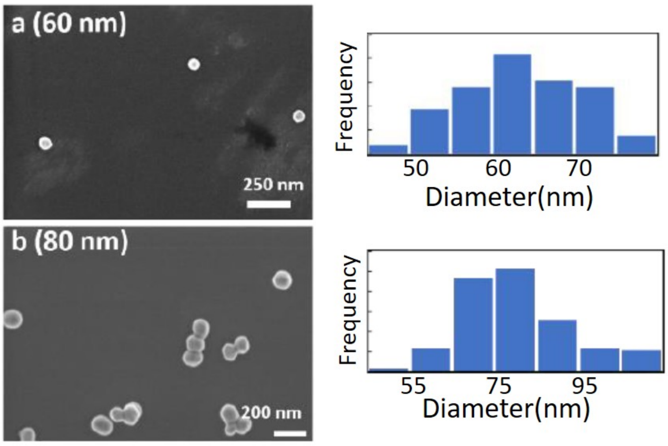

Fig. A.9 The resultant 60nm (a) and 80nm (b) Au nanoparticles produced using the setup in Fig.5.30b along with the corresponding size distributions. Courtesy of G.L.

used for coagulation and then particles were sintered in a tube furnace before passing to the AAC for size selection. Particles were deposited onto $4\times4mm$ Au substrates inside a $4.6mm^2$ impactor and remaining particles were counted on the CPC extracting a flow rate of 1.5 SLPM.

The resultant nanoparticles using this setup are shown in Fig.A.9, demonstrating the potential for this method. However, although the method is able to produce nanoparticles of large enough diameter, as yet it is unable to produce tight size distributions (Fig.A.9).

Upon deposition onto the substrate, coupled mode peaks also appeared for gas-phase nanoparticles (60nm NPs Fig.A.10). The most likely explanation for this is that when deposited onto the surface of Au or hBN are highly energetic, therefore the nanoparticles remain hot and mobile, leading to surface aggregation of the particles as shown for 80nm nanoparticles . This increases scattering as seen in the figure and leads to high variability and apparent plasmonic coupling. Thus, while the method is promising, it requires significant improvement before it will be suitable for NPoM.

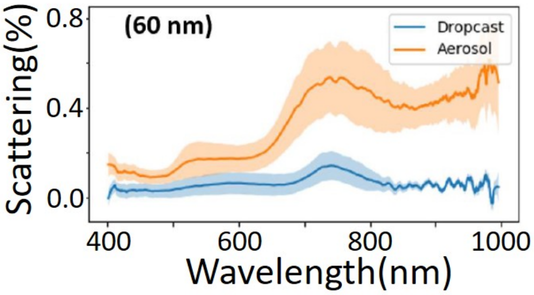

Fig. A.10 Averaged dark field spectra on Au for 60nm solution deposited nanoparticles compared to 60nm nanoparticles produced with gas-phase deposition. Dark-field was taken by G.L.

### A.2.3 $O_2$ plasma etching

Highly energetic charged ions in an oxygen plasma can break down any adsorbands in the gap. A Su substrate sample was placed in and O2 plasma etch (30W, 1 minute) and results from this process on for 60nm nanoparticles previously deposited on Au using the usual techniques are shown in Fig.A.11. It is clearly seen that post-etch the transverse mode becomes the dominant mode as expected, however other modes remain, indicating some remaining contaminants in the gap. The average of the remaining modes coincides closely with the position of the coupled mode wavelength for 80nm nanoparticles on Au.

Monolayer hBN samples were additionally treated in this way, but unfortunately significant damage was observed on the layered material by the process. This requires further careful work in order to optimise this process, resulting in removal of ligands without altering the Au substrate surface, hBN or nanoparticle in the process. This is a highly promising technique in order to resolve the problems encountered in this chapter and would be one

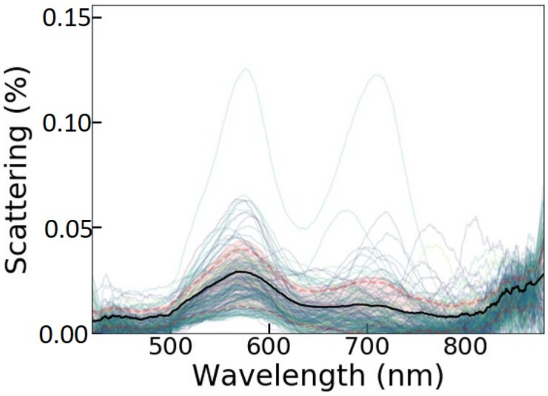

Fig. A.11 Results from 150 60nm NaCl deposited nanoparticles post-plasma etch showing, the average (black) and standard deviation for data (red-dashed)

of the first recommended approaches for somebody aiming to continue work on layered materials with NPoM.